UNIVERSITY OF CALIFORNIA
SANTA CRUZ

LATE HOLOCENE CLIMATE VARIABILITY AND COASTAL CHANGE OF THE YUCATAN PENINSULA, MEXICO

A dissertation submitted in partial satisfaction
of the requirements for the degree of

DOCTOR OF PHILOSPHY

in

EARTH SCIENCES

by

Kyle Houston Broach

June 2020

The Dissertation of
Kyle Houston Broach
is approved:

_____
Professor Matthew Clapham, chair

_____
Dr. Adina Paytan

_____
Professor Christina Ravelo

_____
Professor Andrew Fisher

_____
Quentin Williams
Acting Vice Provost and Dean of Graduate Studies

Table of Contents

List of Figures

1. Introduction

2. Late Holocene foraminiferal assemblages and paleoenvironmental change of the Celestun Lagoon estuary (Yucatan, Mexico)

3. A 5,000-year paleosalinity record from Celestun Lagoon (Yucatan, Mexico): separating geomorphic and climatic controls on groundwater discharge

4. Investigating δ11B variability in shallow benthic foraminifera Ammonia parkinsoniana and potential application as a paleospring discharge proxy of low-pH springs in the Yucatan Peninsula, Mexico

List of Tables

2. Late Holocene foraminiferal assemblages and paleoenvironmental change of the Celestun Lagoon estuary (Yucatan, Mexico)

3. A 5,000-year paleosalinity record from Celestun Lagoon (Yucatan, Mexico): separating geomorphic and climatic controls on groundwater discharge

4. Investigating δ11B variability in shallow benthic foraminifera Ammonia parkinsoniana and potential application as a paleospring discharge proxy of low-pH springs in the Yucatan Peninsula, Mexico

Abstract

Late Holocene climate variability and coastal change

of the Yucatan Peninsula, Mexico

Kyle Houston Broach

The following dissertation contains three studies that use sediment cores to reconstruct past changes in the climate and environment of a tropical lagoon system. These studies provide insight into past droughts and coastal change during geologically recent climate variability and sea-level rise by investigating relationships between geochemical and biological parameters sensitive to different processes occurring on the coast of the Yucatan Peninsula, Mexico.

Chapter one is a foraminiferal fossil record reconstruction of the Celestun Lagoon environment, assessing ecologic response to a change in lagoon salinity and vegetation over the Late Holocene (5,300 years to present). The record and modern environment suggests foraminiferal community composition changes predictably with salinity, but lagoon salinity decreased primarily from restriction of seawater input to the lagoon, and hence reduced mixing between groundwater and seawater, rather than climate-induced increase of groundwater discharge, though climate is a secondary control. The cause of reduced mixing appears to be accumulation of barrier islands

and sand spits that progressively isolated the northern lagoon, reducing mixing between groundwater discharge and seawater and shifting the environment from an open marine coast to estuarine lagoon. The transition was accompanied by expansion of the mangrove forest fringing the coastline. Superimposed on this trend, excursions of foraminifera taxa signify higher salinity coinciding with regionally dry periods and indicate that climate is a second-order control on lagoon mean salinity.

Chapter two is a more detailed paleosalinity reconstruction where relations between modern lagoon salinity and both trace metals and isotopes in foraminiferal tests are applied to samples from cores collected along a transect from the northern to southern lagoon. The benthic species *Ammonia parkinsoniana* is used due to its abundance throughout the lagoon, and paleosalinity tracers recorded in *A. parkinsoniana* calcite tests are the elemental ratios Sr/Ca, and Ba/Ca and isotopes $\delta^{18}O$ and $^{87}Sr/^{86}Sr$. Ba/Ca ratios exhibit the highest correlation with salinity while $\delta^{18}O$ and $^{87}Sr/^{86}Sr$ indicate two types of groundwater discharge to the lagoon—a fresh and a brackish source. A mixing model constructed from $\delta^{18}O$ and $^{87}Sr/^{86}Sr$ show that long-term decrease in salinity was due to increased proportions of the brackish groundwater endmember—consistent with the Chapter 1—and decreases in the freshwater endmember coincide with major dry periods in the Yucatan recorded in other paleoclimate archives of the region. Furthermore, sedimentation rates increase briefly at 3,400 and 2,000 years ago, time periods characterized by large-scale reorganization of atmospheric and oceanic currents in the North Atlantic with atmospheric teleconnections to tropical

climate. These increases in accumulation rate are interpreted as periods of rapid barrier island accumulation as trade winds and the Loop Current weaken in the Gulf of Mexico and deposit sediments during longshore drift. Chapter two suggests that atmospheric patterns resulting in drought in the Yucatan Peninsula also result in rapid sedimentation and apparent decrease in salinity in coastal lagoons, thus demonstrating the value of a multi-proxy approach in reconstructing paleoenvironmental history in dynamic coastal environments.

Chapter three contributes data and a new hypothesis to the growing body of literature on the boron isotope system. The boron isotope ratio $^{11}B/^{10}B$ records pH of ambient water in the carbonate shells, proving to be a powerful tool in reconstructing past ocean acidification and atmospheric carbon dioxide concentrations. However, $\delta^{11}B$ has not previously been used as a proxy for low-pH spring water discharge. In Celestun Lagoon, boron measurements in *A. parkinsoniana* are characterized by high variability both in surface sediments along the lagoon and in downcore samples and exhibit weak but significant relationships with the paleosalinity proxies $^{87}Sr/^{86}Sr$ and Ba/Ca and with the vegetation proxy $\delta^{13}C$. Lower pH caused by respiration of organic matter, recorded in $\delta^{13}C$ of calcite, appears to contribute to $\delta^{11}B$ variability, yet mean $\delta^{11}B$ values of calcite reflect calculated $\delta^{11}B$ values of borate based on present understanding of boron systematics, thus indicating that spring discharge exerts a first-order control on lagoon pH and $\delta^{11}B$ recorded in foraminifera. This finding is of particular interest to the deep-time paleocommunity because prior to the evolution of

foraminifera, and because deep sea sediments older than 180 million years are rare, many calcareous fossils available for $\delta^{11}B$ analysis thrived in shallow marine habitats. As efforts continue to find deep-time analogs to modern ocean acidification, low-pH groundwater discharge in coastal zones may complicate interpretations of $\delta^{11}B$ results but may be addressed by a rigorous multi-proxy approach.

This dissertation provides a record of coastal and climate change during recent periods of climate variability and sea-level rise over the last 5,000 years to provide context for current climate change in the tropics and an understanding of drivers of variability in the past and the future at low latitude sites.

Acknowledgements

It takes a village to raise a dissertation, and I have been fortunate to be part of a marvelous village. I owe much gratitude to my adviser, Adina Paytan, who has been warm and supportive since our first meeting on her couch. Adina is a wonderful mentor, teaching me to plumb deeper, to push the boundaries of geochemistry, and to persist, persist, persist. She has freely shared life's great joys – good food, good friends, and good conversation – which have made for a most enriching journey through science. I am especially thankful for her tireless edits to improve the clarity of my ideas, for support for science education and outreach, and for myriad opportunities to travel and meet new collaborators.

I am grateful to the many collaborators and scientists who have offered support and assistance over the years. I would like to thank my committee for their patience throughout this winding path and interest in surprising findings along the way. Through classes and conversation, Christina Ravelo always filled knowledge gaps with impeccable timing, advancing my understanding and ideas at key junctions of writing and analysis. Andy Fisher has been a fountain of hydrologic knowledge, changing the course of this dissertation with a single question (How long have those barrier islands been there?). His advice and precision with language will continue to improve my science communication for years. Matthew Clapham has immeasurably improved my understanding of the statistical foundations of earth science. His data

class in R provided the most versatile skill I have learned during my doctorate, and I take joy in coding every day.

Paul Koch and Jim Zachos have been wonderful mentors as well, and I am grateful for their knowledge of isotopes and paleoclimate and frequent invitations to join lab meetings and lunches with invited speakers. I appreciate the inclusion and support. This research would not have been possible without the insight, expertise, and instrument wizardry of Colin Carney and Rob Franks. I must also thank my past mentors Bridget Adkins, Molly Miller, and Pat Tellinghuisen for support and teachings early in my education of chemistry and geology.

I am grateful for my lab mates who have been like family. All have provided helpful instruction in the lab and comradery in Santa Cruz. Thank you to Joe Street who was good-humored about my incessant questions regarding fieldwork and sample inventory. I am glad I became so close with Ana Martinez-Fernandez in our shoebox of an office. Thanks to Delphine Defforey, Alanna Lecher, and Katie Roberts for wisdom to live by in the Paytan Lab and analytical assistance. Karen Lykkebo is a treasure, and Kim Mayfield is the best travel partner I could hope for in our global pursuit of geochemistry. This research would not have been possible without the extensive lab help from CJ Vigil, Brendan Chapman, Chelsey Lindo, and Frankie Lon. Thank you for your time and effort, and especially for the opportunity to improve my mentoring abilities. Countless other friends provided the social network

so necessary in graduate school. Dustin Harper, Tali Babila, Sarah White, Michelle Drake, Stephan Bitterwolf, and Abbey Chrystal have my gratitude.

Words cannot describe my luck in finding housemates Karen Lykkebo, Wilson Sauthoff, and Carver and Alicia Bierson. You were the best graduate home anyone could ask for, and I will forever cherish our adventures indoors and outdoors. Long live Dufour.

Lastly, I would like to thank my mother Joy Broach who instilled love of science and field work early in life and fostered calm rationale to weather any storm. I would like to thank my father Ron Broach for encouraging ingenuity, creativity, and sense of fun so useful for work and play. I know he would be proud.

To my husband Scott Hardage, who has the patience of nature, I am forever grateful. Thank you all.

Chapter 1

1. Introduction

As the evidence of human influence on global climate grows with greenhouse gas emissions, climate research has increasingly focused on developing an understanding of how global warming translates to climate variability on regional and local scales. Regional-scale climate controls seasonal patterns of precipitation and aquifer recharge, temperature and evaporation, and soil moisture response to regional hydrologic perturbations, all of which present challenges to municipal water resource managers and planners of human societies (Lutz et al., 2000; Gleick, 2000). While recent research suggests a greater range in precipitation between wet and dry seasons across the globe (Chou and Lan, 2012; Chou et al., 2013), reliable instrument records of the last century are too short to offer a complete view of predictive patterns of climate change and processes driving variability of regional precipitation, creating a need for records of longer duration.

Paleoclimate archives such as lake and ocean sediments and cave deposits record the biogeochemistry and environmental conditions at the time of deposition, extending our understanding of climate processes farther back in time and providing data against which to test climate models to predict future change, especially with respect to hydrologic balance and water resource availability (Koutsoyiannis 2009). However, it has become clear that even geographically adjacent regions experience

local-scale hydrologic effects with differences between catchments of lakes and caves translating into uncertainty in the timing and magnitude of severe drought and ecologic response (Peterson and Haug, 2005; Metcalfe et al., 2015; Douglas et al., 2016b). The goal of this dissertation is to develop a regionally integrated signal of rainfall over the Yucatan Peninsula from coastal sediment archives influenced by the regional groundwater table and to differentiate climatic controls from other contemporaneous processes such as sea level rise and local hydrogeologic effects. This research provides insight into the complexities of coastal paleoclimate archives, demonstrating the importance of local geomorphic controls on paleoenvironmental change while exploring techniques to extract hydroclimate signals reflecting variability in regional precipitation derived from changes in atmospheric circulation patterns. For the Yucatan Peninsula region of Mexico, the extreme seasonality of precipitation leaves the area vulnerable to drought if climate patterns shift, with the prospect of negative economic and ecological consequences (Koutsoyiannis et al., 2009).

The Yucatan Peninsula (Figure 1.1) is famous in part for the Mayan Civilization that thrived from 2,000 BCE to 1,000 CE and declined severely over several decades a millennium ago (Gill, 2001), with much evidence pointing to a series of droughts that diminished rain-recharged groundwater availability and agricultural production (Hodell et al., 1995; Brenner et al., 2002; Peterson and Haug, 2005; Beach et al., 2009; Douglas et al., 2015). The karst peninsula is also famous for the most complex

network of caves in the world (Perry et al., 2003) which contribute to the lack of surface water features like major rivers. Precipitation over the peninsula rapidly percolates through caves and fractures to the groundwater table (Figure 1.2) where it flows to the coasts to discharge at spring sites (Figure 1.3). The field site Celestun Lagoon (Figure 1.1) is a groundwater-influenced estuary on the northwestern shoreline of the Peninsula, from which a series of sediment cores recovered sedimentary records beginning at 5,300 years before present (BP). The hypothesis is that the salinity increases in the lagoon as groundwater spring discharge decreases in response to decreased precipitation. The corresponding water geochemistry recorded in carbonates of shelled fauna thus provides a measure precipitation over the catchment area of the springs spanning nearly a quarter of the northwestern peninsula (Bauer-Gottwein et al., 2011).

Despite this regionally-integrated advantage, paleoenvironmental reconstruction is a challenge due to competing physical and chemical controls on final sediment deposition. Most paleolimnological environmental reconstruction occurs in relatively stable lake systems on continental interiors where geochemical changes may be interpreted as primarily climatic, and assume that change in lake physical characteristics is minimal (Holmes, 1996; Leng and Marshall, 2004). In the coastal context of Celestun Lagoon, influence of sea level rise and ocean currents, in addition to climatically-driven spring discharge, adds variability that can best be addressed by using a multi-proxy approach - that is, to use different biological and geochemical

signals that respond differently in magnitude and direction to local drivers of change. The three chapters of this dissertation thus focus exclusively on Celestun Lagoon microfossils and geochemistry with each chapter focusing on a different dataset to understand and compare different processes impacting the lagoon to other Holocene climate and sea-level records of the Yucatan and Caribbean regions.

The first chapter establishes the paleoenvironmental history of Celestun Lagoon by differentiating climate from coastal geomorphology as drivers of local change. Foraminifera microfossil communities (assemblages) are commonly used to infer holistic environmental change because, in addition to local salinity, these organisms respond to changes in sediment porewater oxygenation, water column suspended particle load, wave energy, and sediment and vegetation substrate type (Culver and Buzas, 1982; Debenay et al., 2000; Debenay et al., 2002; Debenay and Guillou, 2002; Sen Gupta, 2003; Murray, 2006) which are properties that respond to non-climatic forcing (e.g., a blocked lagoon outlet). Thus, assemblages have the advantage of reflecting change in local coastal conditions, irrespective of climate, that influence final lagoon salinity and geochemistry. Similarly, ratios of carbon to nitrogen (C:N) and carbon stable isotopes (expressed as $\delta^{13}C$) of sediment organic matter trace vegetation sources, and as vegetation type changes in response to salinity or shoreline orientation, C:N and $\delta^{13}C$ values change as well. For Celestun Lagoon, organic carbon derives primarily from mangrove and seagrass vegetation with some contributions from marine primary producers (Gonneea et al., 2004). Thus, the

assemblage, C:N and $\delta^{13}C$ proxies serve as the basis for paleoenvironmental interpretation by comparing values observed in the modern lagoon to values of the lagoon's past (Figure 1. 4).

Results reveal that Celestun has not remained a semi-protected lagoon over its 5,300-year history and in fact has evolved with four stages of ecosystem development. With sea level about 2.5 meters lower around 5,300 BP, the northern lagoon was a low salinity (< 10) inland mangrove pond dominated by *Discorinopsis* foraminifera (Figure 1.5). BY 4,900 BP, the site was open shoreline dominated by *Archaias* and *Laevipeneroplis* foraminifera that thrive in marine *Thalassia* seagrass beds - a habitat common to modern Florida coasts but not observed in the northwestern Yucatan (Hallock and Peebles, 1993). From about 4,500 BP to present, the lagoon transitioned from marine shoreline to brackish protected mangrove lagoon, accompanied by faunal succession of assemblages implying a gradual decrease in salinity from > 30 to the modern range of 15 to 20. In the modern lagoon, foraminifera taxa cluster primarily into a northern assemblage of low salinity and muddy substrate and a southern assemblage of protected but otherwise marine-influenced embayment. The modern distribution is remarkably similar to assemblage change from 4,500 BP to present (Figure 1.4), as though the lagoon mouth propagated southward, isolating the northern region from ocean influence. Indeed, modern coastal sedimentology studies observe barrier island and spit formation along the coast with accretion rates of up to 0.5 km per year (Appendini et al., 2012; Cuevas et al., 2013; Lowery and Rankey,

2017), a rate consistent with forming the lagoon's 21 km western bank over a 5,000 year timespan.

This chapter reveals that barrier island formation for the northwestern Yucatan coast has occurred at least over the Late Holocene, greatly influencing the coastal environment of the Celestun region. The same process may influence other Yucatan coastal sedimentary records (Figure 1.1) and, importantly, climatic interpretation of those records. Coastal geomorphic change reduces mixing between fresh groundwater and seawater, giving the appearance of increased groundwater discharge and thus increased rainfall. Thus, to extract climate history from coastal records influenced by groundwater, lagoon paleoenvironmental change and coastal geomorphology must be known. This work has been accepted to the *Journal of Paleolimnology* in 2020.

The goal of chapter two is to separate geomorphic and climatic influence on lagoon salinity to address the original intent of providing an integrated (i.e., groundwater) signal of rainfall. Precipitation falling on the Peninsula percolates rapidly through the karst terrain to the groundwater table (Figure 1.2) where it flows to coasts on timescales of months, discharging as seeps and springs at shorelines (Figure 1.3; (Perry et al., 1989; Perry et al., 2003; Bauer-Gottwein et al., 2011). As groundwater flows, it dissolves the carbonate bedrock, taking on trace metals (strontium and barium, or Sr and Ba) and isotopic values ($^{87}Sr/^{86}Sr$) of limestone and evaporite bedrock lithology (Perry et al., 2009a). The result is a water source geochemically

distinct from seawater. Combining these aquifer-source geochemical signatures with the oxygen isotopic value ($\delta^{18}O$) of groundwater reveals there are in fact two distinct groundwater sources to Celestun Lagoon (Young et al., 2008; Stalker et al., 2014), and when mixed with seawater form a three endmember mixing system that controls the final lagoon salinity and trace metal concentration and isotopic compositions. In turn, these elemental values are recorded as the ratios Sr/Ca and Ba/Ca in the calcite tests of the foraminifera *Ammonia parkinsoniana* (Figure 1.5) which calcifies in such waters, providing a proxy of paleosalinity and a quantitative estimate of the proportions of groundwater and seawater mixing over time.

A. parkinsoniana tolerates a wide range of salinity conditions (4 to 41, (Murray, 2006), coincides with the salinity gradient in the modern lagoon, and is observed throughout most of the sedimentary record at this site, thereby providing a consistent archive of paleosalinity information in space and time. The Sr/Ca and Ba/Ca results from this chapter confirm observations in chapter 1, that in the northern lagoon, low salinity (around 5) conditions prevailed at 5,300 BP with mangrove-dominant vegetation and the *Discorinopsis* assemblage; near-marine salinities >30 occur at 4,900 BP, coincident with the *Archaias-Laevipeneroplis* assemblage and marine *Thalassia* seagrass; and salinity declines from 30 to 20 over the last 4,500 years, indicating an increase in groundwater, a decrease in seawater, or a combination of the two. In addition, cores from the central and southern lagoon reveal that these areas remain relatively unchanged in their salinity values (around 26 and 30, respectively).

Furthermore, the values of $^{87}Sr/^{86}Sr$ and $\delta^{18}O$ show that the proportion of the seawater endmember has decreased over time for the northern lagoon more so than the central or southern areas, consistent with the interpretation of barrier islands propagating south and restricting seawater incursion to the northern site. Thus, the formation of the lagoon may have been initiated by sea-level rise and subsequent barrier island accretion, gradually restricting seawater input to the lagoon inducing a long-term freshening trend.

But what of the climate signal? Though mean salinity may decline over time, climate-induced fluctuations in groundwater discharge would still cause salinity fluctuations about mean lagoon salinity. Assuming the rate of barrier island growth is relatively constant since initiation at 4,500 BP (a reasonable assumption given the relatively steady decline in salinity), geomorphic influence on salinity can be modeled using a fifth-order polynomial. Residuals values of salinity around this polynomial reflect deviations from the mean value, thus detrending the salinity data and removing geomorphic influence on the salinity signal. Detrended data reveals increases in lagoon salinity between 2 to 3 salinity units and thus drier conditions from 3,500-3,100 BP, 2,400-2,000 BP, and 1,300 BP (or 700 CE, the start of the Mayan Droughts). The large area recharging the groundwater springs of Celestun Lagoon suggests the dry periods impacted the western half of the Peninsula which is confirmed by paleoclimatic records (primarily lacustrine) in the west and southwestern peninsula while records farther south in Belize and Guatemala appear

wetter (Mueller et al., 2009; Wahl et al., 2014; Douglas et al., 2016b; Akers et al., 2016).

The droughts appear to be caused by external forcing of solar radiation and internal forcing of ocean and atmospheric currents manifested as high variability due to the Peninsula's unique location at the nexus of several important circulation patterns (Bond et al., 2001; Mayewski et al., 2004; Steinhilber et al., 2009; Metcalfe et al., 2015; Bhattacharya et al., 2017). Among the most important of these are the Intertropical Convergence Zone (ITCZ) - a band of moisture along the Equator that drives the wet and dry seasons of the tropics - and the Loop Current, which brings warm sea surface temperatures and associated moisture from the Caribbean into the Gulf of Mexico (Molinari and Morrison, 1988; Molinari and Morrison, 1988; Giddings and Soto, 2003; Poore et al., 2004; Metcalfe et al., 2015). Comparison of the Celestun Lagoon paleosalinity excursions with other lacustrine and speleological records reveals that widespread droughts occur when the average position of the ITCZ moves south, reducing rainfall over the peninsula. At the same time, continued decrease in long-term salinity and increase in sedimentation rates in Celestun Lagoon during dry periods points to a link between coastal longshore sediment transport and climate aberrations. Longshore sediment transport is driven by the easterly Trade Winds and Loop Current and Yucatan Current for this area (Herrera-Silveira and Morales-Ojeda, 2010; Enriquez et al., 2010; Cuevas et al., 2013), and average position of the Loop Current in the Gulf of Mexico is related to the average position

of the ITCZ (Poore et al., 2009) which both move north or south together. Dry periods centered at 3,200 and 2,000 BP coincide with cooling of the north pole and southward drift of sea ice and cold fronts - known as Bond Events (Bond et al., 2001) - which cool the North Atlantic, push the ITCZ and Loop Current farther south, and result in drought in the Yucatan Peninsula (Gill, 2001; Haug et al., 2001; Bond et al., 2001; Haug et al., 2003) but also apparently increased deposition of sediments on the north coast of the Yucatan as easterly trade winds and the Loop Current weaken. Such periods of rapid atmospheric circulation change coincide with sharp but short-lived decreases in lagoon salinity despite drought on the Peninsula interior. This is consistent with temporary increase in rates of barrier island formation. The implication is that the response of coastal (lower salinity) and continental lacustrine (higher salinity) records may respond oppositely to the same forcing (Bond Event and associated ITCZ excursion), but the contradiction is reconciled if geomorphic history of the field site in question is understood. This is good news the paleoclimate and paleoecologic communities studying the circum-Caribbean region, for coastal records provide insight to regional response of hydroclimate forcing and represent a relatively unexplored source of climate information despite widespread occurrence of coastal lagoon ecosystems around the Gulf of Mexico and Caribbean sea (Peros et al., 2007b; Peros et al., 2015). In addition, knowing the relationship between coastal transport currents and atmospheric circulation can improve future general circulation models assessing the risks of climate change and sea level rise for coastal communities. This chapter is in preparation to be submitted to the journal *Paleoclimatology and*

Paleoceanography.

While chapters one and two focus on the paleoecology and paleosalinity of Celestun Lagoon, chapter three attempts to reconstruct paleo-pH of the estuary using the boron isotope system, expressed as $\delta^{11}B$ and a relatively new paleoceanographic proxy (Hemming and Hanson, 1992; Hemming and Hönisch, 2007). The proxy is based on acid-base equilibrium between boric acid ($B(OH)_3$) and borate ($B(OH)_4^-$) by the equation:

$$B(OH)_3 + H_2O \leftrightarrow B(OH)_4^- + H^+ \quad (1.1)$$

Equation 1.1 shows that $[H^+]$ and thus pH is a driver of speciation of boron. The second key aspect of this system is the partitioning of boron isotopes ^{11}B and ^{10}B into ($B(OH)_3$) and ($B(OH)_4^-$), respectively. As the boron molecules change from one molecular species to the other over the pH range 6 to 11, ^{11}B and ^{10}B fractionate with a value of 27.2 ‰ (Klochko et al., 2006) between ($B(OH)_3$) and ($B(OH)_4^-$) (Figure 1.6). ($B(OH)_4^-$) is the primary constituent incorporated into carbonate, replacing the CO_3^{2-} ion (Branson, 2018; Rae, 2018), thus recording in carbonate the boron fractionation driven by changes in pH.

The $\delta^{11}B$ of marine carbonate in the open ocean generally records the pH of water from which carbonate precipitated (Foster and Rae, 2016; Rae, 2018; Hönisch et al.,

2019). The behavior of $\delta^{11}B$ in coastal systems is much less clear with only one other study investigating $\delta^{11}B$ in shallow carbonate sediments (Zhang et al., 2017). In the coastal ecosystem of Celestun Lagoon, spring discharge is low in pH (<7) relative to the ocean, correlating significantly with spring salinity (Pearson $r = 0.67$, $p = 0.002$). Increases in spring discharge would thus decrease lagoon pH and lower $\delta^{11}B$ values in foraminiferal calcite (Figure 1.6), providing an opportunity to explore $\delta^{11}B$ behavior in shallow low-pH carbonate systems influenced by groundwater.

Results were far more complicated than this simple relationship would suggest. The mean $\delta^{11}B$ of all data collected in Celestun Lagoon indeed reflects mean lagoon pH, but the variability and range in $\delta^{11}B$ (8 to 18 ‰) at this site was as great as all previously published data from the global surface and deep oceans (12 to 22 ‰) (Rae et al., 2011; Hönisch et al., 2019). High variability in parameters that control pH (salinity, temperature, [Mg], [Ca], total inorganic carbon, and total alkalinity) translates to high variability of $\delta^{11}B_{borate}$ incorporated into foraminiferal calcite. In Celestun lagoon, mean geochemistry that determines the final $\delta^{11}B_{borate}$ value are controlled by low-pH springs. Spring discharge explains about 76% of variability seen across important pH-controlling parameters (mentioned above) measured in lagoon water and about 44% of variability in trace metal and $\delta^{11}B$ values measured in foraminiferal calcite. Furthermore, $\delta^{11}B$ measurements in calcite show greater variability within 1 km of the largest spring discharge site, suggesting greater sensitivity of the proxy when closer to the source of pH change. This is an intuitive

result, for pH is not conservative (like dissolved metals) and can change rapidly over short spatial and temporal scales as temperature and dissolved CO_2 change from physical and biological processes (Hofmann et al., 2011). This supports the hypothesis that low-pH spring discharge is a first-order control of $\delta^{11}B_{calcite}$ of benthic foraminifera. Another 18% of the variability in foraminiferal $\delta^{11}B$ geochemistry is explained by respiration of organic matter, which further reduces porewater pH, in this productive mangrove estuary ecosystem. Applying the $\delta^{11}B$ proxy downcore shows that pH at this shallow coastal site has been as variable over the last 3,000 years as is observed at present, ranging from 6.9 to 8.1. Despite the variability in $\delta^{11}B_{calcite}$, boron response to low-pH springs may offer some utility as a tracer for paleospring discharge in coastal environments, provided that $\delta^{11}B_{calcite}$ measurements are extensively paired with multiple proxies to understand impacts of salinity, temperature, source boron, photosynthesis, and microbially-mediated respiration of organic matter.

Chapter three provides new $\delta^{11}B_{calcite}$ to compare to other shallow marine carbonate environments of the Bahamas and Belize (Zhang et al., 2017). In addition to expanding understanding of the limitations of $\delta^{11}B_{calcite}$ in general, this study also provides the first look at $\delta^{11}B_{calcite}$ as a paleospring discharge proxy. Coastal spring discharge may have substantial impact on baseline pH of coastal waters, where calcareous fauna of interest reside (e.g., corals), and hence impact baseline $\delta^{11}B_{borate}$ recorded in biogenic carbonates of shallow marine communities. In deep time, prior

to the evolution of foraminifera or extant corals, most carbonate organisms such as sponges, corals, and brachiopods have lived in shallow carbonate environments (Benton and Harper, 2009). As we observe the effect of CO_2 emissions and ocean acidification on modern carbonate reefs and lagoons (Feely et al., 2009; Doney et al., 2014) and reconstruct past ocean acidification (Hönisch et al., 2019), it is important to consider the hydrogeologic processes that may also impact $\delta^{11}B_{borate}$ and thus $\delta^{11}B_{calcite}$ in shallow shelf environments adjacent to coastal groundwater discharge of the past. This work is in preparation to be submitted to the journal *Geochimica et Cosmochimica Acta.*

This dissertation contributes to a growing body of paleoclimatic work demonstrating important consequence of climate change and associated variability on groundwater resources while advancing our understand of a relatively new proxy system to better study past oceanic ocean acidification via atmospheric carbon dioxide. The strength of these three chapters lies in the multi-variate dataset of diverse proxies - biological, sedimentological, and geochemical - that respond in non-linear and complex ways to climatic and coastal forcing, providing detailed insight to the processes that control the final coastal sedimentary and geochemical record of the northern Yucatan coastline. The approaches and proxies described herein may be applied to both previously collected coastal records and to future coastal sampling campaigns in this region, opening the door to new paleoenvironmental archives detailing complex hydrologic interactions between the atmosphere, the ocean, and the societies living in

between. Beyond the earth science community of paleontologists, geochemists, climatologists, and oceanographers, this work is of interest to archaeologists and resource conservationists seeking to understand Mayan societal turmoil under the stress of drought and modern resource planning under the threat of drought again. In the words of Petersen and Haug (2005), "If Maya civilization could collapse under the weight of natural climate events, it is of more than academic interest to ponder how modern society will fare in the face of an uncertain climate in the years ahead."

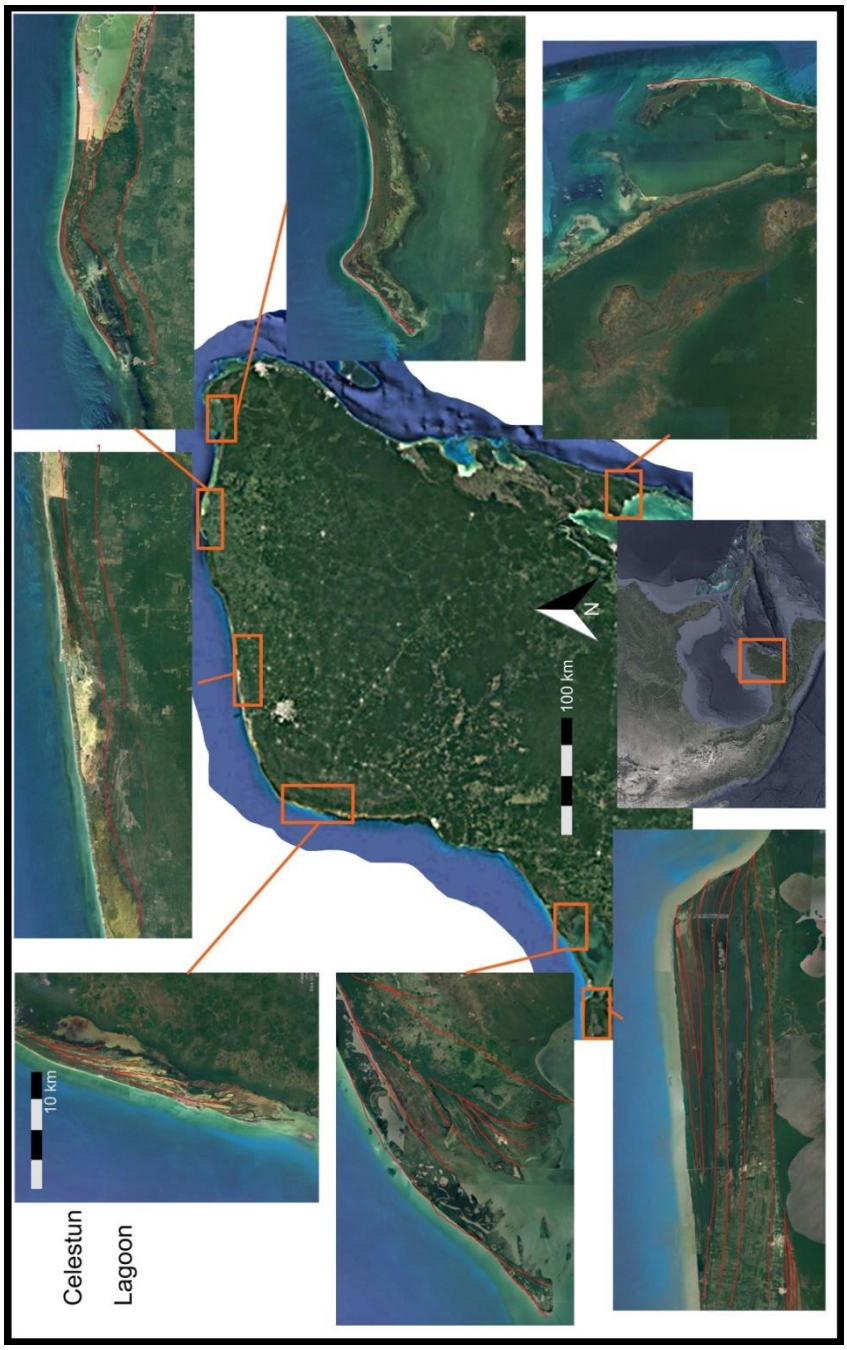

Figure 1.1
Imagery of the Yucatan Peninsula (central image) derived from Google Earth®. The field site Celestun Lagoon is in the northwestern corner of the Peninsula. Linear features of the western bank of Celestun Lagoon (marked in red) are sediment spits and barrier islands that have accumulated over time. Similar features are noted at other lagoon sites around the Yucatan coastline.

Figure 1.2
Aerial photograph of the northeastern coast of the Yucatan Peninsula near Cancun. Precipitation over the peninsula (note clouds) rapidly percolates through the karst terrain to the groundwater table and then flows toward the coasts to discharge as springs and seeps.

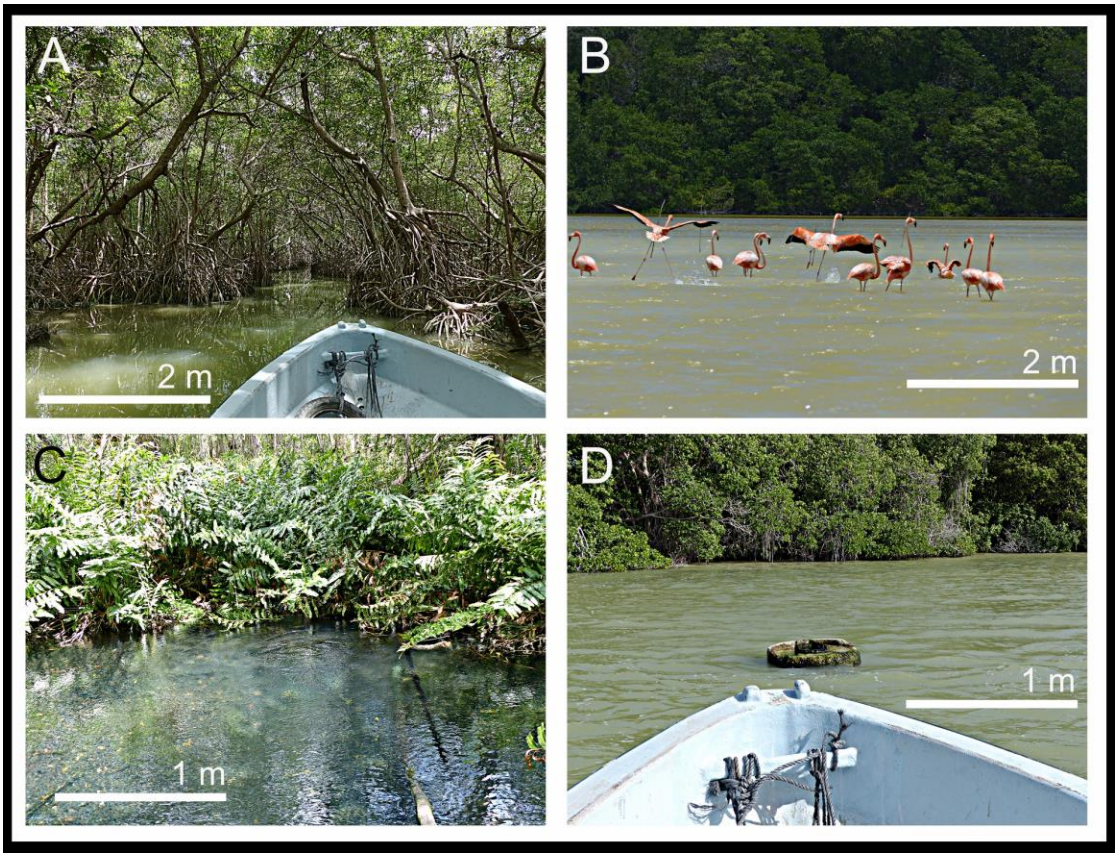

Figure 1.3
A Channel within the mangrove forest on the eastern side of Celestun Lagoon. **B** High biodiversity, including megafauna like flamingos and calcareous meio- and microfauna within sediments, characterize the shallow lagoon. **C** Large spring site discharge low-brackish groundwater to the central lagoon. **D** Drowned well within the main lagoon. Groundwaters of C and D derive from rainfall and are geochemically distinct from seawater entering the lagoon from the southern opening.

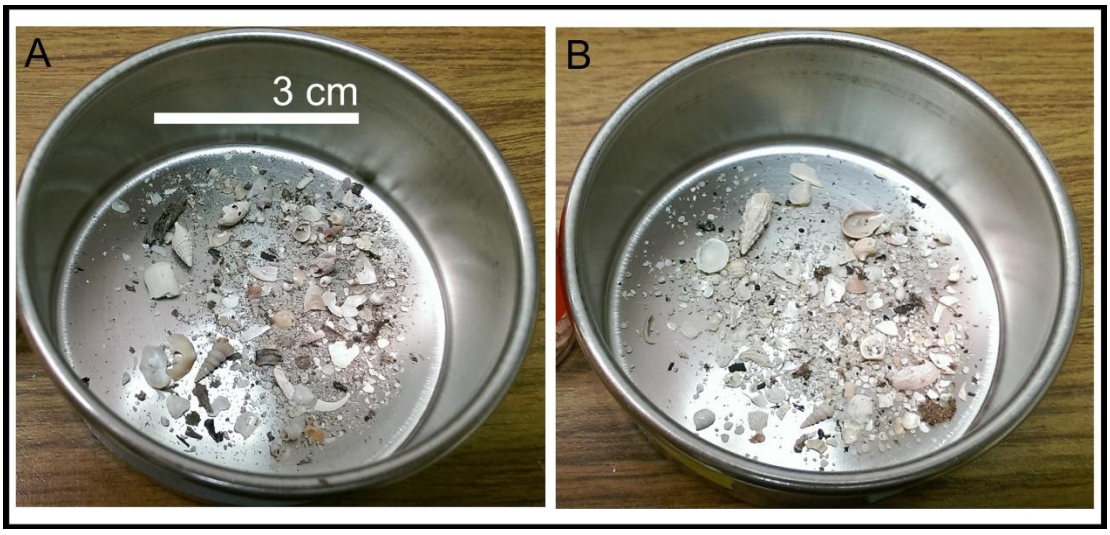

Figure 1.4
A Carbonate sediment and calcareous fauna observed in the top 3 cm of sediment in the southern lagoon near the ocean. **B** Carbonate sediment and calcareous fauna from a northern lagoon core at a depth of 200 cm and dated to 4,800 years before present. Note the similarity in appearance.

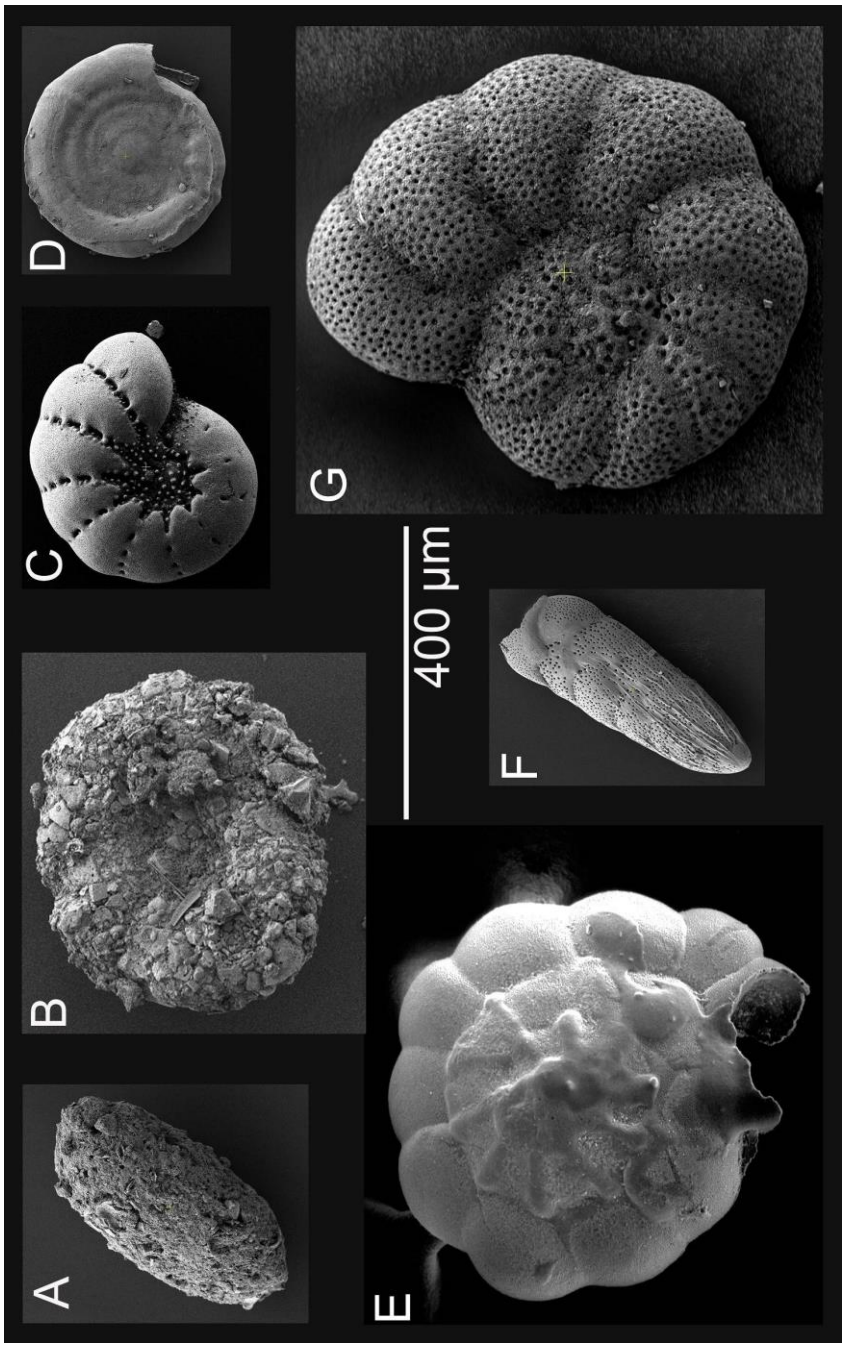

Figure 1.5
Selected scanning electron microscope images of foraminifera taxa in Celestun lagoon sediments. **A** *Miliammina fusca*, agglutinated **B** *Trochammina sp.*, agglutinated **C** *Haynesina germanica*, hyaline **D** *Cornuspira involvens*, porcelaneous **E** *Ammonia parkinsoniana*, hyaline **F** *Bolivina sp.*, hyaline **G** *Discorinopsis aguayoi*, hyaline. *Discorinopsis* was only observed in northern lagoon sediments dating to 5,300 years before present.

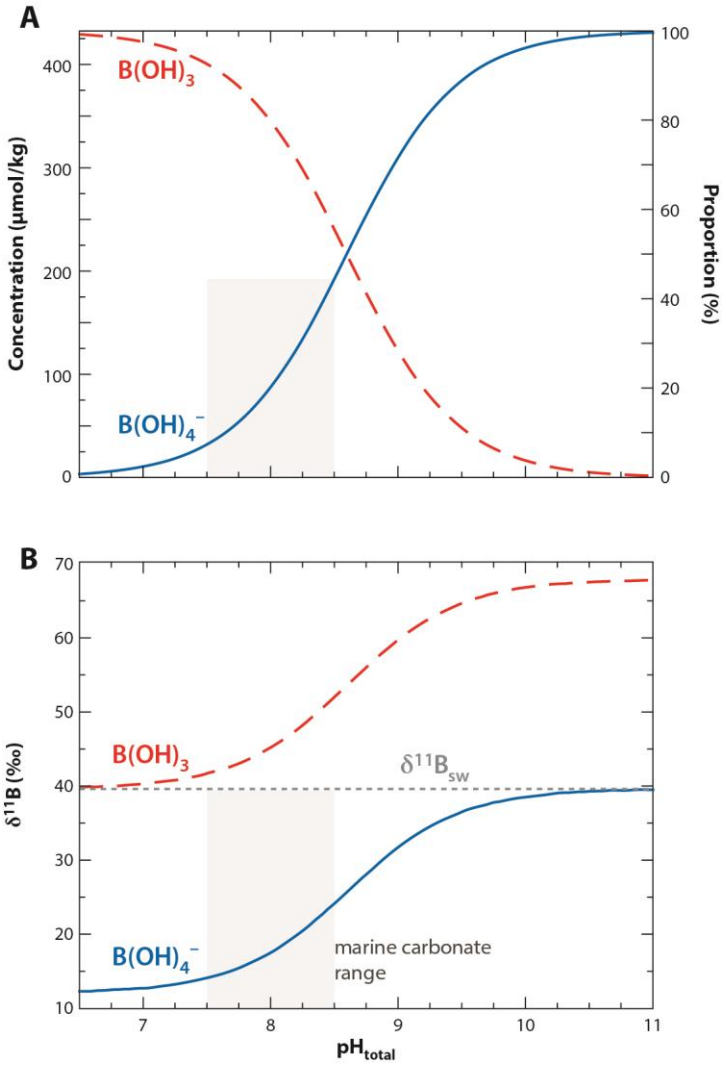

Figure 1.6

A Bjerrum plot for boric acid $B(OH)_3$ and borate $B(OH)_4^-$. **B** Fractionation of ^{11}B and ^{10}B from bulk seawater values ($\delta^{11}B_{sw}$) into $B(OH)_3$ and borate $B(OH)_4^-$. Gray box in both panels represent the range of $B(OH)_4^-$ in the modern ocean and the $\delta^{11}B_{sw}$ value of $B(OH)_4^-$ recorded in marine carbonates. Figure calculated from spreadsheet given in Rae (2018).

Chapter 2

Late Holocene foraminiferal assemblages and paleoenvironmental change of the Celestun Lagoon estuary (Yucatan, Mexico)

2.1 Abstract

Foraminiferal assemblages fluctuate in response to natural environmental changes. This study utilizes foraminiferal assemblages, C isotope ratios ($\delta^{13}C$) and C:N ratios of sedimentary organic matter in sediment cores from Celestun Lagoon, Yucatan, Mexico to describe environmental changes over the past 5,300 years. Specimens of the >125 μm size fraction from modern core top sediments reveal three assemblages: a brackish mangrove assemblage of agglutinated *Miliammina* and *Ammotium* taxa and hyaline *Haynesina*; an inner-shelf marine assemblage of *Bolivina, Hanzawaia*, and *Rosalina*; and a brackish assemblage dominated by *Ammonia* and *Elphidium*. Assemblages change along the lagoon in response to changes in salinity and vegetation type (seagrass and mangrove). In addition to these three assemblages, lagoon sediments representing the past 5,300 Cal yr BP (hereafter BP) are comprised of two additional assemblages defined by *Archaias* and *Laevipeneroplis* indicating marine *Thalassia* seagrasses and *Discorinopsis* indicating inland mangrove ponds. Celestun Lagoon exhibits four phases of paleoenvironmental development: inland mangrove pond (5,300 BP); open coastline with marine seagrass and barrier island aggradation (4,900 BP); protected brackish lagoon (3,000 BP); and protected lagoon

surrounded by mangroves (1,700 BP). The temporal change in assemblages from core bottom to coretop resemble the spatial distribution seen in the modern lagoon from the southern marine lagoon to the brackish northern lagoon. Similar patterns have been reported from Yucatan Peninsula lagoons and cenotes (Nichupte, Aktun Ha) suggesting a regional coastal response to sea level rise and climate change, including geomorphic controls (longshore drift) on lagoon salinity observed today. Barrier island development progressively protected the northwestern Yucatan coastline, reducing mixing between seawater and rain-fed submarine groundwater springs. If the freshening trend associated with restriction of seawater mixing due to barrier island development is removed, Celestun Lagoon foraminiferal assemblages reflect regional wet and dry climatic episodes similar to those recorded in lake archives (Chichancanab, Salpeten) and explain freshening in local cenote salinity records (Cenote San Jose) that conflict with interpreted periods of drought. Our results emphasize the need to consider coastal geomorphic evolution when using lagoon sedimentary archives for paleoclimate reconstruction. Such coastal records can provide integrated rainfall records from basin-scale groundwater drainage.

2.2 Introduction

Coastal lagoons and estuaries are dynamic environments, and changes in local sea level, storm wave energy, coastal geomorphology and climate all affect these ecosystems and the organisms that live there. Sedimentary archives from coastal

lagoons record environmental conditions such as storm surge, sea level rise, catchment hydrochemistry, as well as biological productivity and diversity. Thus, such archives provide insight into paleoclimatic and paleoenvironmental change that control these properties and may affect coastal human communities (Collins et al., 1999; Debenay and Guillou, 2002; Murray, 2006; van Hengstum et al., 2011; Hawkes and Horton, 2012; Peros et al., 2015; Collins et al., 2015). Coastal estuaries and lagoons are abundant around the Caribbean and particularly the Yucatan Peninsula, but relatively few coastal paleoecologic studies are available from this region (Peros et al., 2007).

Here we present a microfossil and vegetation record spanning the last 5,300 years from Celestun lagoon in the northwestern corner of the Yucatan Peninsula, Mexico. The lagoon's proximity to ocean currents and storms, dune-ridge complexes, mangrove forest, and the presence of groundwater springs yields an estuary sensitive to climate and coastal changes across the peninsula lowlands.

2.2.1 Background

The Yucatan Peninsula is a carbonate platform dominated by karst geomorphology (Perry et al., 1995; Perry et al., 2003) where rainfall percolates rapidly into groundwater (within months), flows toward the coasts and discharges as submarine springs (Herrera-Silveira, 1994; Perry et al., 2003). In the northern Yucatan, the

discharge location of these submarine springs is determined by the Chicxulub impact crater which focuses discharge in Celestun and Dzilam Lagoons (Perry et al., 2002; Perry et al., 2003; Bauer-Gottwein et al., 2011). Rainfall is variable, and the Yucatan climate is seasonal subtropical with most rainfall occurring from June to October (Herrera-Silveira, 1994; Bauer-Gottwein et al., 2011). Seasonality of precipitation is driven primarily by migration of the Intertropical Convergence Zone about the equator (Haug et al., 2001), but interannual variability in the position of this humid zone is caused by additional ocean-atmospheric circulation patterns, including the Bermuda High Pressure Zone in the Atlantic, Walker circulation across the Pacific, and solar insolation across both ocean basins (Bond et al., 2001; Laskar et al., 2004; Sutton and Hodson, 2005; Douglas et al., 2016a; Bhattacharya et al., 2017).

Regional climatic variability (compounded with local hydrologic variability) is expressed in paleoclimate records across the Yucatan peninsula including lake and cenote records (Hodell et al., 1995; B. Leyden et al., 1996; Hodell et al., 2005; Douglas et al., 2016b), Caribbean coastal cave sediments (Gabriel et al., 2009; van Hengstum et al., 2010; Collins et al., 2015), and regional speleothem chemistry (Webster et al., 2007; Medina-Elizalde et al., 2010; Kennett et al., 2012; Douglas et al., 2016b; Akers et al., 2016). These records are variable in timing and inconsistent in the severity of recorded drought events, resulting in difficulty reconstructing past atmospheric circulation and raising the need for an integrated rainfall record. New

records from coastal lagoons that represent integrated regional climate (via groundwater with a large catchment) could reconcile some of these discrepancies.

Assemblages of foraminifera and organic matter geochemistry ($\delta^{13}C$, C:N ratios) are useful tools in reconstructing coastal paleoecology and environmental conditions that respond to climatic changes. Modern foraminifera species are distributed along gradients of salinity, wave energy, water stratification, and substrate type, making them sensitive indicators of change in the physical and chemical environment (Debenay and Guillou, 2002; Murray, 2006; Schönfeld et al., 2012). Coastal paleoenvironments reconstructed from foraminifera utilize groups, or clusters, to represent a particular environment (e.g., brackish estuary, protected lagoon, open coast) and individual species to indicate specific habitat (e.g., mangrove swamp, seagrass beds, suboxic sediment) (Sen Gupta, 1999). Both methods are used to characterize the coastal environment in the Yucatan and Caribbean regions. In particular, tropical estuaries are characterized by a landward fine-sediment assemblage containing *Ammotium*, *Miliammina*, and *Trochammina* spp. transitioning to brackish mixed assemblages of *Ammonia*, *Elphidium*, and *Quinqueloculina* spp. before culminating in an ocean end-member assemblages containing *Bolivina* and *Rosalina* spp., among other marine taxa (Debenay and Guillou, 2002).

In carbonate-rich mangrove estuaries of the Caribbean, species richness increases with distance from more protected inland coastal settings, where a few species of

agglutinated foraminifera dominate, to the nearshore, where more diverse hyaline and porcelaneous taxa live. For example, *Trochammina* and other agglutinated taxa live in fringing mangroves of Puerto Rico while *Rosalina*, *Peneroplis*, and *Archaias* live near the open coastal ocean, away from the protected mangroves (Culver, 1990). Change in the coastal environment will affect this distribution, as in Nichupte lagoon, Quintana Roo (northeastern Yucatan peninsula coast) where barrier islands restricted circulation and changed the foraminiferal assemblages from marine genera such as *Triloculina* and *Quinqueloculina* to brackish-tolerant *Ammonia* and *Elphidium* (Hart and Kaesler, 1986). Species diversity also decreases with environmental instability associated with change (Hart and Kaesler, 1986; Sen Gupta, 1999). Specific species indicators (e.g., *Archaias angulatus* and *Peneroplis proteus*) are used around the Caribbean to identify coral reef and seagrass habitat because these species require marine salinities and seagrass beds of *Thalassia* (Sen Gupta, 1999; Gischler and Hudson, 2004). The agglutinated *Miliammina fusca* requires hyposaline muddy environments, and assemblages composed entirely of agglutinated specimens often mark inner mangrove swamps (Sen Gupta, 1999).

Carbon isotopes ($\delta^{13}C_{org}$) and C:N elemental ratios in sedimentary organic matter (OM) are useful in tracing sources of OM to lacustrine and marine sediments. These proxies have been used around the Yucatan Peninsula to infer changes in vegetation and to determine causes for such changes, including Mayan agricultural practices (C3 vs. C4 plants), climate (moist vs. arid), and sea level rise (mangroves) (Gonneea et

al., 2004; Polk et al., 2007; van Hengstum et al., 2010). In particular, $\delta^{13}C$, C:N, and microfossil assemblages records elucidate changes in rainfall variability and its effect on dominant vegetation and cave flooding events during climatic wet periods (Polk et al., 2007; van Hengstum et al., 2010). These studies demonstrate the utility of OM proxies in documenting ecologic change when paired with other hydroclimate and sea level proxies (e.g., $\delta^{18}O$, microfossils, and peat).

In this study we present modern benthic foraminiferal assemblage data and a 5,300 year sedimentary record of assemblages, $\delta^{13}C$, and C:N of sediment OM from Celestun Lagoon (Yucatan, Mexico). We reconstruct the paleoenvironmental history of the lagoon with particular focus on controls of lagoon salinity in order to compare our record to other paleoenvironmental and paleoclimatic records from the northwestern peninsula and other coastal paleoenvironments in this region.

2.3 Materials and methods

2.3.1 Site description

Celestun Lagoon is a narrow (0.5-2.4 km) and long (21.2 km) estuarine lagoon situated along the coastline in the northwestern Yucatan Peninsula in southern Mexico (Figure 2.1A). The lagoon is protected from ocean waves by a series of coquina dune ridges about 30 km long (Lowery and Rankey, 2017). The lagoon

interior is characterized by autochthonous carbonate sediments ranging in size from fine carbonate muds in the protected northern lagoon to coarse mollusk and gastropod shells and fragments near the southern lagoon which opens to the ocean. Benthic foraminifera are found throughout the lagoon. The lagoon depth ranges from 0.5 m in the north to 3 m in the south, and bottom sediments in the center of the lagoon remain submerged at low tide (Young et al., 2008; Lowery and Rankey, 2017). Red and black mangroves (*Rhizophora mangle* and *Avicennia germinans*, respectively) fringe all sides of the lagoon, and abundant, brackish water-tolerant seagrass beds (*Halodule wrightii, Ruppia mexicana*) dominate the central lagoon channel (Herrera-Silveira et al., 1998). These polyhaline flora and fauna are supported by submarine groundwater springs discharging brackish (salinity of 3-9) groundwater predominantly in the northern lagoon, giving the lagoon its estuarine characteristics with a persistent but seasonally variable salinity gradient (Herrera-Silveira, 1996; Gonneea et al., 2004). Peak groundwater discharge (during the month of December) at Celestun Lagoon lags peak rainfall by one to two months (Perry et al., 2002), and prolonged wet periods accompany prolonged low-salinity conditions in the northern lagoon (Herrera-Silveira, 1994; Herrera-Silveira et al., 1998). The interior of Celestun Lagoon is a low-energy settling basin, and the exterior (ocean-side, Figure 2.1B) is high energy characterized by ocean currents and winter storm waves that cause longshore transport of bioclastic carbonate sediments. Longshore sediment transport and accumulation result in a net barrier island and spit formation equaling 200 meters over 33 years (Lowery and Rankey, 2017).

2.3.2 Sediment and water sampling

Three expeditions to Celestun Lagoon (May 2006, June 2009, and May 2015, Table 2.1) collected sediment cores and contemporaneous *in situ* water salinity and temperature data, measured with a Yellow Springs Instruments model 63 (handheld sonde). Water depth was not measured but is estimated at about 50 cm for all cores. Short cores (N = 5) were collected using 30 cm push cores along a lagoon transect from north to south (Figure 2.1A, Table 2.1). Push cores were immediately extruded and sectioned into 2 cm intervals to ensure sufficient mass for ^{210}Pb dating. Longer sediment cores (N = 8) were collected using piston Bolivia and Livingston corers (LacCore, University of Minnesota) and imaged with a Geotek Corescan-V camera provided by the National Lacustrine Core Facility (Minnesota, USA, Figure 2.2). Core 4A was collected in three drives, and Core 4B, 3m away from core 4A, was collected in three drives (Table 2.1) and used only for additional radiocarbon dating. Bulk wet density was measured with a gamma densitometer for cores 4A and 4B (Figure 2.2) and used in Corelyzer software v.2.0.4 to match radiocarbon ages from core 4B to appropriate depths in core 4A. Auxiliary core UL-5 was collected in 2 drives (200 cm total length, Figure S2.1) and was used to corroborate age-depth models and general trends observed in core 4A. Sediment cores 4A and UL-5 were subsampled every ~5 cm, split into aliquots, and separated for organic matter δ^{13}C and C:N atomic ratio analyses and benthic foraminiferal assemblages.

2.3.3 Chronology

Basal peat and terrestrial macro-organics (roots, leaves, and seeds) were picked from wet-sieved sediments and used for radiocarbon dating. Autochthonous organic carbon (e.g., seagrass) was avoided where identifiable due to carbon reservoir effects that occur in karst systems (Fletcher et al., 2017). Radiocarbon data from cores 4A and 4B were combined to create one age-depth model for core 4A. All radiocarbon dates (N = 15, Table 2.2) were calibrated to calendar years using IntCal13 as detailed in Blaauw and Christen, (2011). ^{210}Pb activity (N = 7) was determined using 10 mL samples of homogenized bulk sediment sealed in vials for 24 hours and measured in a high purity germanium (HPGe) well detector using established methods and calibration reference materials (Swarzenski et al., 2006). Sediment accretion rates were calculated from $^{210}Pb_{excess}$ below 6 cm, which we infer was not mixed, and corrected for extruding compaction of 5% (Gonneea et al., 2004). The age-depth model (Figure 2.3) was developed using the R package 'rbacon' v. 2.4.0 which uses Bayesian inference models of the radiocarbon and ^{210}Pb-derived sediment accumulation rate (Blaauw and Christen, 2011).

2.3.4 Foraminiferal assemblages

Foraminifera were visually identified from ~30 mg sediment aliquots dry sieved to 125 µm (Table 2.3). Foraminifera between 63-125 µm were commonly covered in

calcareous precipitates which could not be dislodged with sieving or sonicating, rendering identification inconsistent or impossible and hence were excluded. Individual foraminifera were counted until at least 300 specimens (living or dead) were obtained. Counts were used to calculate relative abundance, and sediment aliquots were weighed to determine absolute abundance (individuals mg^{-1} of sediment) to address varying volumes of sample used (Schönfeld et al., 2012). This method was applied to coretop samples and core 4A down core samples. We define coretop as the upper 5 cm intervals of sediment which we assume was mixed, inferred from ^{210}Pb profiles (Figure 2.3). In core UL-5, foraminiferal counts were performed on the > 250 μm. This size fraction was chosen due the common occurrence of large benthic foraminifera along the Yucatan coast (Martinez et al., 2018) and at this site. Data from core UL-5 (Supplemental Material) was not collected at high resolution and was only used to corroborate the trends observed in core 4A.

2.3.5 Carbon isotope analysis

Organic matter $\delta^{13}C$ and C:N ratios were analyzed simultaneously via gas-sourced Carlo Erba elemental analyzer isotope ratio mass spectrometry. A 2 mg sample from each sediment interval was acidified repeatedly using chilled 6% sulphurous acid following Verardo et al. (1990), with an added sonication between acidifications to promote complete decarbonation. This method minimized effervescence and sample loss in sediments containing ~95% carbonate mud (all samples in this study,

excluding peat). Values are reported in reference to VPDB with instrumental reproducibility of $\delta^{13}C = 0.2‰$ (UC Santa Cruz Stable Isotope Lab). The C:N atomic mass ratio is reported as dry weight % organic C to dry weight % total N with a reproducibility of 0.1.

2.3.6 Statistical analyses

All statistical analyses were performed in R software (v. 3.5.0) with packages vegan (v. 2.5.2) and rioja (v. 0.9.21). Species richness (S), Shannon diversity (H), and evenness (E) were determined from equations presented in Buzas and Hayek (1998). Wisconsin double standardization was applied to raw abundance counts to maximize influence of rare species, and Q-mode and R-mode agglomerative clustering were performed using the Bray-Curtis dissimilarity matrix and Ward's linkage method (Sen Gupta, 1999). Foraminiferal assemblage names were assigned based on R-mode results, and depth intervals of assemblage occurrence were assigned based on Q-mode results. Cluster cophenetic correlation coefficient , which describes data distortion in cluster dendrograms, was determined using Pearson's correlation between the Bray-Curtis dissimilarity matrix and cluster cophenetic matrix (Davis, 2002). Non-metric multidimensional scaling (NMDS) was performed using Bray-Curtis dissimilarity matrix of the Wisconsin standardized data with $k = 3$ dimensions. Continuous variables were natural log-transformed for plotting as vectors.

PERMANOVA and beta-dispersion statistical tests were performed to determine significant differences between cluster centroids and between cluster spreads, respectively (Anderson, 2001; Anderson et al., 2006). To check for significant difference between centroid positions determined from PERMANOVA—which gives a significant result for centroid position or variance—a randomized resampling was performed to simulate a p value for centroid position alone. Clusters were pooled, randomly sampled without replacement, plotted with NMDS ordination, and distance was measured between NMDS centroids of the randomized clusters. A total of 10,000 iterations were performed and compared to the original centroid distance. Kendall correlation was performed for non-normally distributed continuous variables.

2.4 Results

2.4.1 Modern salinity gradient

Lagoon water salinity increases from a minimum of 14 in the northern lagoon (with variability near springs) to 33 in the southern lagoon close to the ocean (Table 2.1). Based on observations in the field, wave energy is lower in the northern region (more protected) than in the southern region close to the coastline.

2.4.2 Sedimentology

Core 4A provided the longest sedimentary record (262 cm, Figure 2.2), hence most analyses were performed on core 4A. The stratigraphy consists of a basal peat layer from 262–230 cm with a transition from 230–228 cm to massive carbonate mud from 228–0 cm with increasing brown pigmentation upcore (Figure 2.2). Fossil bivalves, gastropods, foraminifera, and fragments thereof are rare in peat and common in carbonate mud. Pieces of charcoal and organic matter <1mm occur occasionally in the carbonate mud. Interval 210–170 cm contains more gastropods than other calcareous microfossils, and interval 170–140 cm contains more carbonate mud with brown pigmentation and frequent occurrence of gastropods, ostracods, and foraminifera. From 140–112 cm, coarse-grained material (1 cm clams) and carbonate mud predominate, and bivalves disappear above 112 cm. Interval 112–0 cm is characterized by carbonate mud, frequent gastropods, and abundant foraminifera. From 36–34 cm a coarse (0.5–1 mm) layer of foraminifera and gastropods occurs with a notable color transition from light to dark beige (Figure 2.2B). Core 4B exhibits nearly identical stratigraphy (Figure 2.2A) and consists of basal peat layer followed by massive carbonate mud and fossil bivalves, gastropods, and foraminifera from 230–0 cm, and a coarse layer of gastropod and foraminifera from 36–34 cm (Figure 2.2B). Wet bulk density agrees between the two cores with 1.3 g/mL in the peat layer, a maximum of 1.9 g/mL just above the peat–mud transition (229 cm), and a trend to 1.4 g/mL at present (Figure 2.2A). Based on stratigraphy, wet sediment density, and core proximity, we assume depths in 4A and 4B core represent the same strata.

The coarse-grained layer centered on 35 cm observed in cores 4A and 4B is also observed in cores 2A (31-29 cm), 8A (35-31 cm), and 6A (33-28 cm), but was not observed in 7A (Figure 2.2B). The layer is thickest (5 cm) in the southern lagoon core 6A and decreases to 2 cm in the northern lagoon. The remaining short cores (Table 2.1) did not sample below 30 cm depth.

2.4.3 Radioisotopes and age depth models

^{210}Pb activity in the 0-5 cm interval of short push cores was variable (Table 2.2) and thus excluded from accretion rate calculations. ^{210}Pb activity in the interval 6-13 cm suggests an accretion rate of 1.5 ± 0.2 mm yr^{-1} (Figure 2.3 inset). Radiocarbon data for cores 4A and 4B show expected increased age with depth, although four age inversions occur (Table 2.2). Three ^{14}C age inversions are observed in core 4A from 4A-3L-1 265.5 cm to 4A-2B-1 80.5 cm (495 ^{14}C years), 4A-2B-1 193.5 cm to 4A-1P-1 148.5 cm to (135 ^{14}C years), and 4A-1P-1 90.5 cm to 60.5 cm (135 ^{14}C years), and). One inversion occurs in core 4B from 4B-3L-1 269.5 to 236.5 to (140 ^{14}C years), and one in UL-5 (Supplemental Material). Mean ^{14}C age inversion (N = 5) is 263 uncalibrated years across a mean sediment interval of 27 ± 7 cm.

The Bayesian age-depth model for core 4A (Figure 2.3) implies a long-term sediment accumulation rate between 0.4 and 0.6 mm yr^{-1}. Assuming the lagoon-wide coarse

sediment layer at ~35 cm depth (Figure 2.2B) is a hiatus event, the age model for core 4A indicates a hiatus span of 800 years from 1,300 to 500 Cal yr BP (hereafter BP).

2.4.4 Benthic foraminifera identification and distribution

More than 27,000 foraminifera were counted in 90 samples, and 26 species were identified (Table 2.3). Foraminifera appeared pristine with no pitting or dissolution noted in coretop or downcore specimens.

For all modern and fossil samples, the dominant species are *Ammonia parkinsoniana* (34.7%), *Quinqueloculina laevigata* (14.8%), *Elphidium gunteri* (14.1%), *Elphidium poeyanum* (11.7%), *Triloculina trigonula* (6.5%), Agglutinated taxa (6.0%), *Discorinopsis aguayoi* (3.7%), *Elphidium galvestonense* (2.7%), *Ammonia tepida* (1.3%), and *Haynesina germanica* (1.1%) which comprise 96.6% of all taxa observed. Absolute abundance for all taxa is 11.9 individuals per mg sediment (N mg^{-1}) with the highest absolute abundances occurring for *A. parkinsoniana* (4.1 N mg^{-1}), *Q. laevigata* (1.8 N mg^{-1}), *E. gunteri* (1.7 N mg^{-1}), and *E. poeyanum* (1.3 N mg^{-1}). Remaining taxa absolute abundances are < 1N mg^{-1}.

The relative abundance of fossil taxa in core 4A (Figure 2.4A) is *A. parkinsoniana* (41.4%), *E. poeyanum* (13.0%), *E. gunteri* (11.9%), *Q. laevigata* (8.6%), *D. aguayoi* (6.5%), Agglutinated taxa (5.6%), *E. galvestonense* (4.6%), *T. trigonula* (2.8%).

Other taxa included *Borelis pulchra*, *Trochammina macrascens*, and unknown taxa (1.2%), and *Quinqueloculina linneiana* (1%). Together, these taxa comprise 96.7% of taxa observed in core 4A. Total absolute abundance is 9.7 N mg^{-1}, dominated by *A. parkinsoniana* (4.0 N mg^{-1}), *E. poeyanum* (1.3 N mg^{-1}), and *E. gunteri* (1.2 N mg^{-1}) with remaining taxa < 1 N mg^{-1}. *D. aguayoi* was observed only in interval 262-229 cm (5,300 – 4,900 BP), *Laevipeneroplis proteus* and *Archaias angulatus* were observed only in interval 229-227 cm (4,900 – 4,800 BP), and other taxa are distributed from 227-0 cm (4,800 BP – present).

The relative abundance of taxa in modern coretop samples (Figure 2.4B) was *A. parkinsoniana* (25.7%), *Q. laevigata* (23.0%), *E. gunteri* (17.0%), *T. trigonula* (11.4%), *E. poeyanum* (9.9%), Agglutinated taxa (6.4%), *H. germanica* (2.1%), and *A. tepida* (1.9%) which comprise 97.7% of taxa observed in coretop samples. Absolute abundance for all coretop taxa was 16.8 N mg^{-1} sediment, distributed as *A. parkinsoniana* (4.4 N mg^{-1}), *Q. laevigata* (3.9 N mg^{-1}), *E. gunteri* (2.9 N mg^{-1}), *T. trigonula* (1.9 N mg^{-1}), *E. poeyanum* (1.7 N mg^{-1}), Agglutinated taxa (1.1 N mg^{-1}), *H. germanica* (0.4 N mg^{-1}), and *A. tepida* (0.3 N mg^{-1}) with all other taxa equal to or lower than 0.1 N mg^{-1}. *E. lanieri*, *D. aguayoi*, *L. proteus*, and *A. angulatus* which were not observed in any coretop sample.

2.4.5 Stable carbon isotopes of organic matter

The core 4A peat in interval 262–229 cm (5,300–4,900 BP) is characterized by mean $\delta^{13}C_{org}$ = -27.96‰ and mean C:N = 23.8. At 227 cm (4,800 BP) in the carbonate mud, $\delta^{13}C_{org}$ = -19.27‰ and C:N = 8.6. From 227-135 (4,800-3,000 BP) mean $\delta^{13}C_{org}$ = -19.90‰ and C:N = 8.3, and from 135-0 cm (3,000 BP – Present), $\delta^{13}C_{org}$ changes from -19.90‰ to -24.04‰ and C:N changes from 8.3 to 8.9 (Figure 2.4A). In the modern lagoon, values of $\delta^{13}C_{org}$ and C:N ratios are -23.74‰ and 8.8, respectively, in the northern lagoon and -20.89‰ and 11.5 in the southern lagoon (Figure 2.4B).

2.4.6 Diversity, clustering, and statistical relationships

R-mode cluster analysis of fossil and modern foraminifera indicates 5 clusters of commonly co-occurring taxa with a cophenetic correlation coefficient of 0.61 (Figure 2.5A). We refer to these clusters by a simplified assemblage names which are *Bolivina-Hanzawaia-Rosalina, Discorinopsis*, *Archaias-Laevipeneroplis, Ammonia-Elphidium,* and *Agglutinated-Haynesina*. All five assemblages were observed in core 4A while assemblages *Archaias-Laevipeneroplis* and *Discorinopsis* were absent from modern coretop sediments.

Q-mode unconstrained cluster analysis of core 4A resulted in 4 common clusters with a cophenetic correlation coefficient of 0.71 (Figure 2.5B). In Figure 2.4, clusters are colored shades of gray and describe dominant assemblages at the following depth intervals: Cluster IV occurs from 262-240 cm (5,330-5,150 BP) and is characterized

by the *Discorinopsis* and *Ammonia-Elphidium* assemblages with foraminiferal distribution of *D. aguayoi* (57%), *Borelis pulchra* and Other taxa (10%), *E. poeyanum* (10%, *A. parkinsoniana* (9%), *T. trigonula* (7%), *Q. laevigata* (4%), *A. tepida* (2%), and <1% *of E. gunteri*, *Q. linneiana*, and agglutinated taxa. Cluster III occurs from 210-170 cm (4,550-3,400 BP) and is characterized by both the *Ammonia-Elphidium* and *Bolivina-Hanzawaia-Rosalina* assemblages with a taxa distribution of *E. poeyanum* (41%), *A. parkinsoniana* (21%), *T. trigonula* (10%), *Q. linneiana* (7%), *E. gunteri* (4%), *Q. laevigata* (4%), *Bolivina* sp. (4%), *Triloculina* sp. (3%), *E. galvestonense* (1%), and rare occurrence of other taxa including *C. involvens* and *Rosalina* sp. Cluster II is most prominent from 160-65 cm (3,400-1,850 BP) and is characterized by the *Ammonia-Elphidium* assemblage with *A. parkinsoniana* (58%), *E. gunteri* (17%), *E. poeyanum* (9%), *E. galvestonense* (8%), agglutinated taxa (2.5%), *Q. laevigata* (2%), *T. trigonula* (1%), and <3% of other taxa. Cluster II includes the *Agglutinated-Haynesina* assemblage ca. 1,900 BP. Cluster I contains samples from 60-0 cm (1,700 BP - Present) and is characterized by the *Agglutinated-Haynesina* assemblage.

Q-mode cluster analysis of coretop samples (Figure 2.5C) indicates two sample clusters with a cophenetic correlation coefficient of 0.64. Cluster 1 occurs in the northern lagoon from 0 to 11.5 km along the lagoon (Figure 2.4B) , is characterized by the *Agglutinated-Haynesina* assemblage, and includes *Quinqueloculina laevigata* (38%), *Ammonia parkinsoniana* (19%), agglutinated *Ammotium* sp. and *Miliammina*

fusca (12%), *Elphidium gunteri* (11%), *E. poeyanum* (10%), low abundances of *Triloculina* (<5%), and rare occurrences of *Haynesina* and other species. Cluster 2 occurs in the southern lagoon from 11.5 to 17.5 km (Figure 2.4B), is characterized by the *Bolivina-Hanzawaia-Rosalina* assemblage, and includes *A. parkinsoniana* (34%), *E. gunteri* (23%), *T. trigonula* (20%), *E. poeyanum* (10%), *Q. laevigata* (7%), and the presence of taxa not found in Cluster 1, including *Hanzawaia concentrica, Rosalina* sp., *Cornuspira involvens*, *Bolivina* sp., *E. galvestonense*, *E. discoidale* and *Borelis pulchra* (grouped in Other).

Diversity indices S, H, and E change with the faunal succession upcore in 4A (Figure 2.4A). From Phases 1 to 4 (dashed lines in Figure 2.4A), respective mean S changed from 8.8 – 11.8 – 8.9 – 7.6, mean H from 1.05 – 1.31 – 0.44 – 0.52, and mean E from 0.36 – 0.34 – 0.44 – 0.52. S is a maximum of 18 at 229 cm (4,900 BP) and a minimum of 6 at 170cm (3,400 BP). Diversity H follows a similar trend but remains high for the last 2,900 BP due to an increase in absolute abundance, and E increases over time. In modern samples, the northern lagoon has values of S = 9, H = 1.64, and E = 0.57, and the southern lagoon has values of S = 11, H = 1.71, and E = 0.53 (Figure 2.4B).

NMDS of core 4A clusters and environmental vectors are presented in Figure 2.6 and represent statistical relationships given in Table 2.4. All four clusters plot without overlap in ordination space (Figure 2.6A), and foraminiferal composition of each

cluster is distinct and significantly different (Figure 2.6C and Table 2.4, PERMANOVA Source: Cluster, $p = 0.003$; Bootstrapping Source: Cluster, $p << 0.01$) with no significant difference in cluster dispersion (Beta dispersion Source: Cluster, $p = 0.111$). Bulk sediment $\delta^{13}C_{org}$ and C:N ratio significantly correlate with cluster composition ($p = 0.001$ for both). Correlations between $\delta^{13}C_{org}$ and E (Kendall $\tau = -0.291$, $p = 0.014$) and S (Kendall $\tau = 0.370$, $p = 0.003$) also show a significant but weak relationship. S and H showed no significant correlations but plot as long vectors in the general direction of $\delta^{13}C_{org}$ (Figure 2.6A).

NMDS of modern coretop Clusters 1 and 2 show no overlap (Figure 2.6B) and are significantly different in assemblage composition (Figure 2.6D and Table 2.4, PERMANOVA Source: Cluster, $p = 0.001$; Bootstrapping Source: Cluster, $p << 0.01$) but are not significantly different in the variance of species abundance (Beta dispersion Source: Cluster, $p = 0.128$). The largest gradients (longest vectors) along the lagoon transect are $\delta^{13}C_{org}$, C:N ratio, and salinity (Figure 2.6B). PERMANOVA results are significant for salinity, $\delta^{13}C_{org}$, and cluster composition ($p = 0.001$, Table 2.4), and temperature is significant ($p = 0.014$). Species richness (S), $\delta^{13}C_{org}$, and C:N ratios are significantly correlated (Kendall correlation, $\tau = 0.-460$ and 0.46, respectively, $p = 0.002$ for both), but no significant correlation is observed between the $\delta^{13}C_{org}$ and assemblage diversity (H) or evenness (E). S is significantly correlated with distance along the transect from the northern to southern lagoon (Table 2.4), coincident with observed decrease in lagoon wave energy from north to south.

Results and figures of auxiliary core UL-5 are described in Section 2.8 Supplemental Material.

2.5 Discussion

2.5.1 Modern environment in Celestun Lagoon

2.5.1.1 Distributions of flora and fauna

Foraminiferal and geochemical analyses in surface sediments and water along Celestun Lagoon reveal differences between the northern and southern lagoon regions. The *Agglutinated-Haynesina* assemblage occurs only in the northern lagoon while the *Bolivina-Hanzawaia-Rosalina* assemblage occurs only in the southern lagoon (Figure 2.4B). *Ammonia-Elphidium* assemblage is common in both regions. The *Discorinopsis* and *Archaias-Laevipeneroplis* assemblages were not observed in the modern lagoon. Maximum species richness (15) and diversity (1.96) both occur in the middle of the lagoon about 13 km from the southern opening where assemblages overlap (Figure 2.4B) and habitat transitions from protected low-salinity lagoon to higher energy marine-influenced lagoon. The assemblage distribution aligns with gradients in salinity, temperature, $\delta^{13}C$, and C:N of OM (Figure 2.6B). Strong association (clustering) of foraminiferal assemblages with specific salinity and carbon

isotope ranges suggests that the distribution of benthic foraminifera in Celestun Lagoon is controlled in part by salinity, vegetation, and, to a lesser extent, temperature. PERMANOVA results support a significant relationship among these variables (Table 2.4).

Thus, clusters dominated by the *Agglutinated-Haynesina* assemblage represent brackish salinity and shallow lagoon mangroves, and clusters dominated by the *Bolivina-Hanzawaia-Rosalina* assemblage represent inner marine shelf and seagrass habitat, which are the environments in which species of these assemblages have been found around the Caribbean (Table 2.3). Low wave energy and muddy substrate in the enclosed northern lagoon also promote the abundance of agglutinated foraminifera like *Miliammina fusca* (Debenay and Guillou, 2002). Lagoon water temperature is weakly correlated with cluster composition (Table 2.4, Figure 2.6B) but does not exhibit large changes in mean temperature among sites sampled (29.2 ± 2.6 °C, Table 2.1). Salinity exhibits the greatest variability in the lagoon. Although *Discorinopsis* and *Archaias-Laevipeneroplis* were not observed in modern Celestun, we infer their habitats based on modern occurrence in other sites in the Gulf of Mexico and Caribbean. *Discorinopsis aguayoi* occurs in inland mangrove ponds in Bermuda (Javaux and Scott, 2003) and thus represents low-salinity, isolated mangrove ponds with minimal ocean influence (Table 2.3). *Archaias angulatus* and *Laevipeneroplis proteus* (also known as *Peneroplis proteus*) inhabit marine seagrass of the genus *Thalassia* off the coasts of Belize and Florida (Hallock and Peebles,

1993; Sen Gupta, 1999). Thus, the *Archaias-Laevipeneroplis* assemblage represents marine-salinity, shallow-shelf environments with *Thalassia* seagrass vegetation (Table 2.3).

In the marine-brackish conditions of southern Celestun Lagoon, euryhaline *Ammonia* and *Elphidium* were found alongside epiphytic *Quinqueloculina* and *Rosalina* taxa, suggesting seagrass vegetation may contribute to assemblage diversity but alone is insufficient in determining modern assemblage distribution. The importance of salinity is further demonstrated by benthic foraminifera observed 10 km south of Celestun lagoon, in Isla Arena, which has similar sedimentology, geometry, and vegetation as Celestun but with higher salinity due to greater seawater input (Lowery and Rankey, 2017). As a result of this higher salinity, the Isla Arena assemblages are dominated by miliolid and peneroplid foraminifera that prefer near-marine salinity.

Variable salinity in coastal environments restricts foraminifera occurrence to only those that can withstand a large and fluctuating salinity range (Sen Gupta, 1999). Such conditions occur in the northern lagoon and result in low species richness (low S values, Figures 2.4B, 2.6B). The pattern of assemblage change along a salinity gradient is found in other Caribbean and Atlantic coastal systems with large salinity ranges. On the mangrove forest coast of French Guiana, Debenay et al. (2002) noted that seasonal salinity oscillations from 20 to 35 are accompanied by assemblage compositional changes from *Miliammina*-dominated (agglutinated) to *Ammonia*- and

Elphidium-dominated. A narrow estuary of Brazil exhibited shallow protected brackish water assemblages of agglutinated *Miliammina* and *Ammotium* taxa and seaward marine-influenced assemblages dominated by *A. tepida*, *E. gunteri*, and *Bolivina* taxa (Debenay et al., 1998), similar to the southern opening of Celestun Lagoon. Collectively, these studies point to salinity as being the most important environmental parameter impacting foraminiferal distribution in Celestun Lagoon. Based on these associations we interpret changes in down core assemblages as representing changes in salinity in the northern lagoon over time.

We acknowledge that analyzing the >125 µm size fraction possibly excludes some foraminifera species or smaller adult specimens of the species we identified (Table 2.3, Murray 2006). However, benthic foraminifera at our site and other coastal Yucatan sites are characterized by abundant large (>250 µm) specimens (Martinez et al., 2018), suggesting we observed most taxa present. Based on the number of taxa identified (N = 26, Table 2.3), the number of specimens counted (N = 27,000), and the striking differences in assemblage composition observed in the >125 µm fraction (Figure 2.4), we consider the statistical relationships noted between environmental parameters and assemblage composition (Table 2.4) to be real patterns for the modern system despite small foraminifera exclusion. Furthermore, $\delta^{13}C$ and C:N of bulk sediment OM are independent of foraminifera size fractions and are proxies for mangrove and seagrass vegetation that are also distributed along the lagoon salinity gradient (Gonneea et al., 2004; Khan et al., 2017; Carnero-Bravo et al., 2018),

supporting interpretation of environments inferred from assemblages. It is possible that drying the samples prior to counting may affect preservation of agglutinated taxa (Murray and Alve, 1999) and bias assemblage composition. However, the hyaline foraminifera *Haynesina germanica* observed in low-energy muddy substrate preferred by agglutinated taxa provides additional constraint on the distribution of the *Agglutinated-Haynesina* assemblage in space and time. We thus are confident in using assemblages defined in the modern environment to infer paleoenvironmental properties, specifically changes in salinity, downcore.

2.5.1.2 Lagoon salinity changes - geomorphic processes and climate changes

distinct processes that affect the relative contribution of seawater and fresh/brackish groundwater inputs to the lagoon. These are physical geomorphic changes to the coastline (i.e., lagoon restriction or sea level changes) that determine the amount of seawater input to the lagoon, and climatic changes that impact regional and local precipitation which control the amount of groundwater input. Longshore sediment transport along the Yucatan coastline can build barrier island complexes within decades. Based on a barrier island progradation rate of 200 m per 33 years near Celestun Lagoon (Lowery and Rankey, 2017), a 600 m barrier can develop within a century or around 30 km in 5,000 years. Volumetric rates of sediment transport also concur with this timescale (Appendini et al., 2012). These rates of barrier island development imply gradual accretion of the western Celestun Lagoon bank, resulting

in a gradual increase in lagoon length over time and a parallel increase in the restriction of seawater mixing into the northern lagoon. We note similar barrier-dune complexes from Google Earth™ near Holbox, Ria Lagartos, Dzilam de Bravo, and Progreso, on the northern Yucatan coast and near Isla Arena and Terminos on the western coast. In Terminos Lagoon, the dune-barrier complex called Isla de Carmen consists of 38 km of shelly coquina (Phleger and Ayala-Castanares, 1971). Based on the progradation rate determined by Lowery and Rankey (2017), Carmen Island took 6,300 years to accumulate, consistent with the island's estimated age of 7,000 years based on Holocene sea level terraces (Phleger and Ayala-Castanares, 1971). These studies all indicate that the rate and scale of longshore transport and barrier island formation observed today were similar over the Late Holocene. While the gradual restriction of seawater into Celestun Lagoon will result in a gradual decrease salinity, variability superimposed on this trend may be linked to climate-induced changes in groundwater input. Specifically, an increase in the salinity would suggest lower precipitation and possibly drought conditions.

2.5.2 Reconstruction of the northern lagoon environmental setting

Based on comparison between observations from core tops along the present day lagoon transect and downcore data from core 4A in the northern lagoon, we suggest that the northern lagoon environment has experienced four phases of development characterized by distinct environmental settings controlled by climate, sea-level rise,

and coastal geomorphic change (Figure 2.7). We assume these phases are representative of the entire northern lagoon based on general agreement with core UL-5 (Section 2.8 Supplemental Material).

2.5.2.1 Phase 1 (5,300-5,100 BP)

Between 5,300-5,100 BP the northern area of Celestun Lagoon was within a mangrove forest isolated from ocean influence. The peat $\delta^{13}C_{org}$ value of -28.26‰ indicates mangroves and other terrestrial vegetation (Gonneea et al., 2004; Young, 2005) (Figure 2.2A), and peat accumulation suggests the absence of oxidants such as dissolved oxygen and marine sulfate, hence, a water-logged freshwater swamp setting. The oligohaline assemblage *Discorinopsis* observed during this interval is observed today in isolated mangrove pond environments in Bermuda, supporting interpretation of minimal marine influence in Celestun Lagoon (Javaux and Scott, 2003). Regional sea level at this time is estimated to be 2 to 3 m lower than today (Khan et al. 2017), and a bathymetric slope of -0.4 m km^{-1} off the northwestern Campeche Bank near Celestun (Appendini et al., 2012) would place the coastline 5 km to the northwest of the current location of Celestun Lagoon, consistent with reduced marine influence. Groundwater was likely provided via springs in the permeable Ring of Cenotes because this Cretaceous-age feature existed prior to Holocene coastal development of the Yucatan Peninsula (Perry et al., 2002). The environment may have resembled the “Petenes” to the south of Celestun Lagoon, a

periodically flooded black mangrove forest characterized by other marsh and subtropical vegetation, diffuse groundwater inputs, organic-rich sediments, and gastropods (Lowery and Rankey, 2017). Based on the low-salinity habitat of *Discorinopsis* in Bermuda (Javaux and Scott, 2003) and modern groundwater discharge salinity values (Herrera-Silveira, 1996), salinity was likely less than 10 in these mangrove ponds and probably closer to 3, the value of modern groundwater at this site (Young et al., 2008).

We know of no published climate records that span the period between 5,300-5,100 BP in the northwestern Yucatan. However, pollen records suggest mesic (semi-moist) tropical forests in the southwestern and northeastern areas of the Yucatan Peninsula and in Haiti ca. 5,200-4,800 BP (Hodell et al., 1991; Higuera-Gundy et al., 1999; Aragón-Moreno et al., 2012; Vela-Pelaez et al., 2018). Regionally wet conditions would provide groundwater to inland mangrove ponds to support *Discorinopsis* assemblages whose presence in this environment distinguishes this phase from subsequent, more saline conditions in the lagoon.

2.5.2.2 Phase 2 (5,100-3,000 BP)

This longest phase is characterized by persistent change. Between 5,100 and 4,900 BP, the peat in the core transitions to carbonate mud (Figure 2.2A) as $\delta^{13}C_{org}$ increases from -28.26‰ to -20.21‰ and C:N decreases from 25 to 11 (Figure 2.4A).

The *Discorinopsis* assemblage disappeared from Celestun Lagoon, and at 4,900 BP the *Archaias-Laevipeneroplis* assemblage appeared alongside the *Ammonia-Elphidium* assemblage (Figure 2.4A). The $\delta^{13}C_{org}$ shift to lighter carbon indicates an influx of marine particulate matter and seagrass vegetation (Gonneea et al., 2004), corroborated by the *Archaias-Laevipeneroplis* assemblage which inhabits marine *Thalassia* seagrass beds (Table 2.3, Sen Gupta 1999). These data suggest that coastal marine conditions at Celestun lagoon commenced at this time and were probably caused by sea-level rise ca. 5,100 BP (Figure 2.8). On the Caribbean side of the Yucatan Peninsula in Puerto Morelos, mangrove peat layers date to 5,000 (Islebe and Sánchez, 2002), and coastal caves in Belize, Quintana Roo (Yucatan eastern coast), and Florida exhibit basal peats dated to 6,000-4,000 years ago with mixed pollen and marine microfossil assemblages suggesting transition from terrestrial to marine-influenced coastal zones (Polk et al., 2007; Gabriel et al., 2009; van Hengstum et al., 2010; Collins et al., 2015). A composite sea-level curve estimates that at 5,000 BP, sea level was 2.5 m lower than today on the Yucatan north coast (Khan et al., 2017), consistent with the 2.6 m depth at which peat is found in Celestun Lagoon (Figure 2.2A).

Rising sea level may have been coincident with drought in the northwestern Yucatan, indicated by records in lake Chichancanab and Punta Laguna (Figure 2.8)(Hodell et al. 1995; Curtis et al. 1998). The *Ammonia-Elphidium* assemblage suggests brackish groundwater discharge was still present but limited, otherwise the brackish-intolerant

Archaias angulatus would not be observed (Hart and Kaesler, 1986). Furthermore, palynological and sedimentary changes of riverine soils in the southern Yucatan peninsula suggest the onset of droughts ca. 4,800 BP which would impact the catchment area draining to Celestun Lagoon (Bauer-Gottwein et al., 2011; Aragón-Moreno et al., 2018; Vela-Pelaez et al., 2018). These events occur within chronological uncertainty of the appearance of *Archaias-Laevipeneroplis* (4,900 BP) and may also explain the short duration (century-scale drought event) of this assemblage in the lagoon which would disappear once average precipitation had resumed.

By 4,500 BP, the *Archaias-Laevipeneroplis* assemblage was replaced by the *Bolivina-Hanzawaia-Rosalina* assemblage with increased abundance of the *Ammonia-Elphidium* assemblage while $\delta^{13}C$ remained between -19 and -21‰ (Figure 2.4A) indicating persistent seagrass and marine vegetation from 4,500 BP to 3,500 BP. The foraminiferal community of this time interval greatly resembles the modern assemblage in the southern lagoon (Figure 2.4B), so salinity was likely <30, inhospitable to *Archaias* (Hallock and Peebles, 1993) but ideal for the other taxa (Table 2.3). This represents a decrease from a marine salinity supporting *Thalassia* seagrass and *Archaias-Laevipeneroplis* at 4,800 BP, likely due either to increased groundwater discharge or reduced contribution of seawater. Dry conditions persisted from 4,600 BP to 4,400 BP in Belize (Akers et al., 2016), at 4,500 BP in south-central Yucatan (Curtis et al., 1998; Wahl et al., 2014), from 4,700 to 3,600 BP in the

southwestern Yucatan (Islebe et al., 2019), though conditions in the north-central Yucatan Peninsula at this time are unclear. Hence, precipitation-induced increase in groundwater discharge in Celestun Lagoon at 4,500 BP is at odds with available climate data (Figure 2.8).

Alternatively, formation of barrier islands and spits around the northern lagoon, where springs are located (Figure 2.1A), would reduce mixing between groundwater and seawater resulting in a relative decrease in salinity (Figure 2.7). The highest species richness and diversity occur between 4,500 BP and 3,800 BP (S = 17, H = 1.97, Figure 2.4A), similar in magnitude to, and comprised of the same taxa as, the modern south-central lagoon assemblages (Figure 2.4B). High diversity is expected of foraminifera colonizing diverse habitat niches typical to such an environment (fringing mangrove, brackish-tolerant seagrass, semi-protected lagoon, and unrestricted seawater circulation). West of Celestun Lagoon across the Gulf of Mexico (Figure 2.1B), La Mancha lagoon exhibits a rapid change in foraminiferal composition between 6,500 BP and 4,500 BP, attributed to longshore transport and barrier island formation (Arellano-Torres et al., 2019). Initiation of coastal dunes and barrier islands across the Gulf of Mexico as sea-level rose would be consistent with apparent freshening and maximum diversity in Celestun Lagoon despite regionally dry conditions. A more recent example (1,000 BP) of this process has been observed in sediment cores from Nichupte Lagoon on the eastern Yucatan Peninsula (Figure 2.1B) where assemblages shift from an *Archaias* assemblage to *Ammonia-Elphidium*

as barrier islands isolate the lagoon and reduce mixing with seawater (Hart and Kaesler, 1986).

From 4,500 to 3,600 BP, diversity decreases as marine taxa progressively disappear while mean $\delta^{13}C$ (-19.5‰) and C:N (8.2) change little (Figure 2.4A). *Ammonia-Elphidium* assemblage becomes dominant by 3,400 BP while the *Bolivina-Hanzawaia-Rosalina decreases*, indicating salinity ranged from 20-25 based on modern lagoon distributions (Table 2.3, Figure 2.4B). However, sea level rise during this time (Figure 2.8) should have resulted in greater marine influence, not less. The shift to brackish taxa suggests greater influence of groundwater discharge which may be caused by increasingly moist climate between 4,500 and 3,400 BP, reduced contribution of seawater related to sand-bar buildup, or a combination of the two.

Rapid fluctuation between dominant assemblages suggests an unstable environment from climate change rather than the gradual barrier island accumulation. Between 3,600 and 3,400 BP (Figure 2.4A), assemblages oscillate between *Bolivina-Hanzawaia-Rosalina* and *Ammonia-Elphidium*, accompanied by large changes in S and H. Because salinity correlates best with assemblage distribution (Table 2.4), undulations between these two assemblages suggests fluctuating lagoon salinity which is not consistent with the generally uni-directional formation of barrier islands. Instead, lagoon geometry at this time may have increased sensitivity foraminiferal assemblages to fluctuations in groundwater (Figure 2.7) in which relatively small

changes in absolute groundwater discharge greatly affect the proportions of groundwater and seawater and thus salinity in the lagoon. These relatively short-term salinity fluctuations are likely related to climatic changes, such as variability in the ITCZ and regional precipitation manifested in other climate records as high variability during this period (Figure 2.8)(Hughen et al. 1996; Douglas et al. 2016b; Aragón-Moreno et al. 2018). A wet period ca. 3,500 BP is supported by negative oxygen isotope excursions in lake records from Salpeten and mesic forest pollen from lake Silvituc in the southwestern peninsula (Wahl et al., 2006; Douglas et al., 2015; Vela-Pelaez et al., 2018). However, dry conditions are indicated at the same time by the oxygen records from Lakes Chichancanab and Puerto Arturo in the central peninsula (Hodell et al., 1991; Wahl et al., 2014). Indeed, at 3,500 BP our data best matches the Fe/Ca data (a runoff proxy) of La Mancha west of Celestun Lagoon (Figures 2.8, 2.1B), across the Gulf of Mexico, demonstrating the link between climate and assemblage variability in Celestun Lagoon.

In Celestun Lagoon from 3,400-3,000 BP, the *Ammonia-Elphidium* assemblage becomes dominant and *Bolivina-Hanzawaia-Rosalina* decreases in prevalence, indicating decrease in salinity while decrease in $\delta^{13}C$ suggests more mangrove-derived carbon in sediments (Figure 2.4A). It is difficult to say whether these salinity and carbon trends are the result of barrier island growth or climate. Mangrove forest cover in particular may respond to wetter climate or to additional shoreline to colonize. K/Ca ratios in nearby Los Petenes and Fe/Ca ratios in La Mancha suggest

decreased erosion and hence dry conditions across the southern Gulf of Mexico (Roy et al., 2017; Arellano-Torres et al., 2019) while $\delta^{18}O$ records from Punta Laguna and δD records from Lake Salpeten imply wet conditions over the eastern and southern Yucatan Peninsula around 3,000 BP (Figure 2.8)(Curtis et al. 1998; Douglas et al. 2015). The general divide between dry northwest and wet southeast among records in the region may suggest that the specific atmospheric circulation pattern drove precipitation at this time, with previous studies indicating changes in the positions of the ITCZ, Bermuda High, and descending limb of Walker circulation (Metcalfe et al., 2015; Bhattacharya et al., 2017)

Overall, Phase 2 is distinguished by the apparent faunal succession from coastal marine taxa to brackish lagoon taxa (Figure 2.4A), despite sea-level rise of 1 meter (Khan et al., 2017), with occasional oscillations between dominant assemblages during periods of climate variability (Figure 2.8). Close agreement among observed sediment transport rates (Appendini et al., 2012), calculated barrier island aggradation time (Lowery and Rankey, 2017), and transition between dominant foraminiferal assemblages (Figure 2.4A) suggests coastal geomorphology continued to influence the hydrogeology and salinity of Celestun Lagoon during Phase 2 with assemblages exhibiting fortuitous sensitivity to changes in groundwater discharge induced by climate at this time (Figure 2.7).

2.5.2.3 Phase 3 (3,000-1,700 BP)

Between 3,000 and 1,700 BP, species richness decreased and assemblages were dominated by the near-exclusive presence of *Ammonia-Elphidium* (Figure 2.4A). Bulk sediment $\delta^{13}C_{org}$ decreases from -19.51‰ to -23.27‰ by 1,700 BP, indicating vegetation shifted from seagrass/phytoplankton to a greater proportion of mangroves. The decrease in species richness indicates lower salinity, possibly a more homogenous setting (fewer niches) compared to Phase 2 and was probably similar to the modern northern lagoon (Figure 2.4B). Celestun Lagoon salinity was likely15-25, indicated by the *Ammonia-Elphidium* assemblage and decrease in species richness (Figure 2.4B). This trend is consistent with the ongoing barrier island buildup that reduced seawater input. However, at 2,500 BP (105-106 cm) *Quinqueloculina bicarinata* and *Hanzawaia concentrica* appear briefly and *Ammonia-Elphidium* decrease, suggesting a reduction in groundwater and more marine influence in the lagoon (Figure 2.4A). This change corresponds to drought conditions noted in Lake Chichancanab (Central Yucatan), and Macal Chasm (Belize) speleothem records ca. 2,600 BP (Hodell et al., 1991; Akers et al., 2016). Generally drier conditions in the Yucatan from 3,000 to 2,000 BP (Douglas et al., 2015) also match the timing of increased marine influence in Celestun Lagoon suggested by slight carbon isotope changes from -21.7 to -21.5‰ (indicating marine particulate matter). After 2,000 BP, *Ammonia-Elphidium* return, and the conclusion of this phase is the onset of the modern brackish, semi-protected lagoon environment conditions at the present day northern lagoon.

2.5.2.4 Phase 4 (1,700-present BP)

The last 1,700 years are characterized by the appearance of the *Agglutinated-Haynesina* assemblage, low species richness (S = 7), $\delta^{13}C_{org}$ decrease from -22.97 to -24.22‰, and variable C:N (mean = 7.5). *Elphidium galvestonense* disappeared, but other taxa of the *Ammonia-Elphidium* assemblage (Figure 2.5C) remained alongside increased abundance of *Q. laevigata*. These conditions persist to the present, thus representing the onset of modern conditions in the northern lagoon beginning at 1,700 BP. *Agglutinated-Haynesina* assemblage indicates increased muddy substrate observed in the protected mangrove lagoon today and is consistent with mangrove forest expansion indicated by decreasing carbon isotope values (Figure 2.4A). Mangrove expansion around Celestun Lagoon is consistent with expansion of mangrove forest documented elsewhere in the Caribbean (Peros et al., 2007a). Though barrier islands provide more land for mangrove colonization, the effect is local, so a regional expansion of mangroves suggests regional climate influence or regionally-stable sea-level. Onset of moister climate ca. 1,700 BP is consistent with observation in the Chichancanab and Salpeten lake records (Figure 2.8)(Hodell et al. 1995; Douglas et al. 2015).

The age-depth model indicates that the coarse bioclastic layer at 35 cm depth (Figure 2.2B) begins at 1,300 BP, or about 700 Common Era. In core 4A this layer consists of

an increase in absolute abundance of foraminifera in the *Ammonia-Elphidium* assemblage and an acute decrease in agglutinated taxa and H and E indices (Figure 2.4B) while in the southern lagoon, abundant bivalves and fragments are noted. This interval coincides with the well-documented Mayan droughts (Douglas et al., 2016b) which implies decreased groundwater discharge in Celestun Lagoon. While an increase in the polyhaline assemblage *Ammonia-Elphidium* could be a response to increased salinity, the lack of fine mud across the cores would imply that authigenic carbonate precipitation was reduced in the lagoon at the same time. If included in the age-depth model, radiocarbon sampled at 31 cm (Table 2.2, 1,485 ^{14}C yr) causes a rapid change in slope in the age-depth regression line that results in abrupt decrease of sedimentation to 0.2 mm yr^{-1}. This slowed sedimentation rate is not consistent with the 1.5 mm yr^{-1} rate determined in upper sediments (Figure 2.3) or rising sea level at this coastal setting (Figure 2.8)(Khan et al. 2017). We thus interpret this lagoon-wide layer to be a hiatus event caused by storm erosion or a tsunami. Hurricanes are known to sort and transport shelf foraminifera into coastal systems (Murray, 2006), and identifying features of this coarse layer include lack of fine sediments, lack of agglutinated taxa, and rapid increase in absolute abundance of *Ammonia* and *Elphidium* which occurs in hurricane overwash deposits on the Atlantic coast of the United States (Collins et al., 1999). The presence of a hiatus itself provides some climatic information, as other studies suggest increased hurricane activity from 800 to 1350 AD (1,150-600 BP) in the Caribbean (Peros 2015), a time frame consistent with the hiatus interval.

Alternatively, the bioclastic layer could represent a tsunami deposit, likely from submarine continental slope failure. Holocene sea-level rise has been suggested as a cause of slope failure from water overburden pressure (Smith et al., 2013), and in the Gulf of Mexico, sea level has risen 9 m over the last 7.8 ka (Blum et al., 2002). Continental slopes may also fail due to additional sediment load which would be expected from increased continental weathering and riverine transport to coasts. Fe/Ca and K/Rb ratios in sediments of La Mancha Lagoon in Veracruz, Mexico (Figure 2.1B), indicate increased detrital input and coastal weathering at 1,000 BP (Arellano-Torres et al., 2019). The timing is coincident with the apparent hiatus in Celestun Lagoon (Figures 2.2, 2.3), and evidence of a tsunami deposit might be recognized in sediment cores from other lagoons around the southern Gulf of Mexico. South of Celestun in Los Petenes (Figure 2.1B), sediments transition from peat at 38 cm to silt between 35 and 15 cm and are dated around 700 BP (1,300 CE) with a spike in K/Ca that indicates rapid erosion inland (Figure 2.8)(Roy et al. 2017). Rapid erosion is unlikely during Terminal Mayan mega-droughts of this time (Hodell et al., 1995; Douglas et al., 2016b) , further implying a catastrophic depositional event such as a tsunami.

From 500 BP to present, the *Ammonia-Elphidium* and *Agglutinated-Haynesina* assemblages dominate with a notable increase in *A. tepida* at 150 BP, or about 1800 CE (Figure 2.4A). The only other occurrence of abundant *A. tepida* occurred during

Phase 1, 5,200 BP. Thin-walled *A. tepida* thrive in low-salinity, protected conditions (Table 2.3, Murray 2006). Barrier islands aggradation is unlikely to have altered the entire lagoon geometry substantially over just the last few hundred years, so the increase in *A. tepida* may be a response to low salinity conditions induced by wet climate. The nearest speleothem-derived oxygen isotope record at Tecoh Cave (100 km west of Celestun Lagoon) shows three century-scale pulses of relatively wet conditions occurred during the Medieval Warm Periods and Little Ice Age (Medina-Elizalde et al., 2010), and a wet interval is also noted in Belize speleothems (Kennett et al., 2012). A diatom record from Cenote San Jose Chulchaca, 22 km west of Celestun Lagoon indicates a decrease in salinity over the last 800 years (Whitmore et al., 1996; Hodell et al., 2005). However, Whitmore et al. (1996) did not note the same trend in Cenote Sayaucil (north-central Yucatan lowlands). Furthermore, the pollen record from Lake San Jose suggests a decline of forest taxa dependent on high rainfall at the same time the cenote is freshening (Hodell et al., 2005), a trend corroborated by pollen and microfossil observations from Aguada X'caamal (75 km southwest of Celestun Lagoon) that imply drying in the northwestern region during the Little Ice Age (600 to 100 BP)(Hodell et al., 2005). Together these records suggest both increased precipitation and increased evaporation for the northwestern Yucatan which, today, has the highest evapotranspiration potential of the entire region (Bauer-Gottwein et al., 2011). Phase 4 of Celestun Lagoon development is thus characterized by expanding mangrove forests during a period of variable precipitation. *Ammonia-Elphidium* and *Agglutinated-Haynesina* assemblages dominate foraminiferal

composition of the northern semi-protected habitat with a wide range of salinity, features observed in the modern northern lagoon today.

2.6 Conclusion

This study presents the oldest paleoenvironmental record currently available for the northwestern corner of the Yucatan Peninsula. Over the past 5,300 years, Celestun Lagoon on the northwestern Yucatan coast has evolved from an inland mixed mangrove marsh saturated by groundwater to a protected brackish lagoon surrounded by mangrove forest. We identify three primary controls for this change: sea level rise, coastal barrier island buildup and climate change. Geomorphic control of lagoon salinity, via reduced contribution of seawater, is a first-order control on the composition of benthic foraminiferal assemblages that trend from marine to brackish taxa over time. Importantly, the 5,000 year age of our record suggests barrier island aggradation, and thus lagoon formation, occurs on Holocene timescales and are important features of the modern Yucatan coastline. Thus, studies seeking to interpret causes of paleoenvironmental change in the coastal Yucatan will need to account for changes in lagoon basin size and shape that impact the proxy record. When geomorphologic change is considered, excursions from brackish to marine taxa during lagoon development signify decreases in groundwater discharge and hence decreased precipitation over the catchment area recharging the groundwater. Agreement between the Celestun sedimentary record and climate records on the far

western and southern regions of the Gulf of Mexico suggest that Celestun Lagoon sediments reflect region-wide climatic events and thus regionally-integrated precipitation. The paleoecologic variability presented in this study, derived from processes of barrier island aggradation, sea-level rise, and climate-induced change in groundwater discharge, will assist in future interpretation of paleoenvironmental paleoclimatic found along on the Yucatan coast.

2.7 Acknowledgements

We thank the support of UC MEXUS for funding this project and the logistical work and technical assistance with sediment metadata by LacCore. Kyle Broach was supported by the NSF Graduate Research Fellowship Program. Thank you to the Geological Society of America for providing graduate funding for radiocarbon dating at Lawrence Livermore National Lab. We give thanks for the generous instrument use provided by the US Geological Survey for lead-210 dating and UL-5 core imaging, particularly with the assistance of Tom Lorenson and Mike Torreson, and to Dave Wahl for data resources. Thank you to Jenna Hill and two anonymous reviewers for very helpful revisions, Scott Hardage for GIS mapping assistance, Chelsey Lindo and Frankie Lon for lab assistance, and CJ Vigil and Colin Carney for stable carbon analytical expertise.

2.8 Supplemental Material for UL-5

2.8.1 Results for auxiliary core UL-5

Sedimentology

Core UL-5 (Figure S2.1), taken 0.7 km northwest of 4A and 4B (Figure 2.1), exhibits stratigraphy similar to both cores 4A and 4B (see main text section Sedimentology). A basal peat layer occurs from 200-170 cm followed by a transition to carbonate mud from 170-168 cm and massive carbonate mud with bivalves, gastropods, and foraminifera from 150-64.5. Bivalves decrease from 140-110 cm but are dominant from 110-64.5 cm. The interval 64.5-0 cm was lost in the field.

Radioisotopes and age depth models

Radiocarbon data for core UL-5 shows expected increased age with depth. One ^{14}C age inversion occurs between UL-5 199.5 and 178.5 (Table 2.2). This inversion is included in the mean ^{14}C age inversion (n = 5) which is 263 uncalibrated years with a mean core interval of 27 ± 7 cm standard deviation.

The Bayesian age-depth model for core UL-5 (Figure S2.2) agrees within error to the age-depth model of composite core 4A and implies a long-term sedimentation rates between 0.4 and 0.6 mm yr^{-1}. The upper 64.5-0 cm of core UL-5 was lost, thus we could not assess the presence of the coarse-grained layer observed in other cores at ~35 cm depth.

Stable carbon isotopes of organic matter

The core UL-5 peat interval from 200-170 cm (5,200-4,800 BP) has a mean $\delta^{13}C_{org}$ of -25.31‰ and mean C:N of 25.3. The transition from peat to carbonate mud from 170-150 cm (4,800-4,400 BP) is characterized by a shift in $\delta^{13}C_{org}$ from -26.09‰ to -21.81‰ and a shift in C:N from 17.32 to 5.62. From 150-64.5 cm (4,400-1,800 BP) $\delta^{13}C_{org}$ is variable with a mean of -20.76 (min = -24.16, max = -13.51) and C:N mean is 6.9 (min = 5.27, max = 10.73) (Figure S2.3).

Benthic foraminifera identification and distribution

At the fraction > 250 µm, UL-5 included *E. poeyanum* (47.9%), *A. parkinsoniana* and *A. tepida* (24.2% combined), *Quinqueloculina* and *Triloculina* (22% combined), *L. proteus* (2.7%), and *A. angulatus* (1.1%) accounting for >97% of specimens identified (see Table 2.1 for taxa list). Absolute abundance was typically 0.1 N mg^{-1} sediment. *A. angulatus* is present only at depth interval 200-199 cm (22% ca. 5,200 BP), and *L. proteus* is most abundant at 200-199 cm (37.5%) and occurs rarely (2.1%) from 200-170 cm (5,200-4,800 BP). From 170-64.5 cm (4,400-1,800 BP), taxa trend toward fewer *Elphidium* and more *Ammonia* (Figure S2.3).

Diversity, clustering, and statistical relationships

Core UL-5 taxa were grouped by genus, so diversity S ranged from 2 to 5, H ranged from 0.27 to 1.33, and E ranged from 0.36 to 0.96. All three indices reach minima around 180 cm (5,000 BP) and increase to 65.4 cm (1,800 BP) but were variable (Figure S2.3).

R-mode cluster analysis was not performed separately on core UL-5, and instead we apply the R-mode dendrogram in Figure 2.2 to assemblages in UL-5. The assemblages are *Ammonia-Elphidium* and *Archaias-Laevipeneroplis,* though miliolid taxa were also common. While the coarse size fraction used for auxiliary data (> 250 µm) likely excludes some taxa, it is important to note the presence of the *Archaias-Laevipeneroplis* assemblage at 200 cm depth which is not observed in the modern lagoon.

Q-mode cluster analysis for UL-5 identified three clusters and yielded a cophenetic correlation coefficient of 0.76 (Figure S2.4). All three clusters are dominated by the *Ammonia-Elphidium* assemblage, but the *Archaias-Laevipeneroplis* assemblage is present in Cluster 3 samples. Clusters from Figure S2.4 are shaded gray in Figure S2.3 and resemble faunal succession.

NMDS of UL-5 clusters and environmental vectors are presented in Figure S2.5. The three clusters fall in line with the vectors for $\delta^{13}C_{org}$ and C:N. PERMANOVA,

bootstrapping, and beta dispersion indicate the clusters are significantly different and have significantly different dispersions among species ($p < 0.05$, Table 2.4). PERMANOVA also suggests significant influence of $\delta^{13}C_{org}$ on cluster assemblage similar to core 4A ($p < 0.001$). H ($\tau = 0.354$, $p = 0.008$) and E ($\tau = 0.402$, $p = 0.002$) are significantly correlated with $\delta^{13}C_{org}$ (Table 2.4).

2.8.2 Discussion of UL-5

Trends in UL-5

Overall, core UL-5 corroborates observations noted in 4A and suggests the data are representative of the head of the lagoon. The age-depth model of both cores indicates sedimentation rates between 0.4 and 0.6 mm/yr. The sedimentology of both cores shows a peat layer occurring around 5,200 BP followed by carbonate mud to the present. The peat-mud transition coincides with a shift from mangrove-sourced organic to seagrass and marine particulate matter, indicated by the increasing value of $\delta^{13}C_{org}$ and decreasing C:N ratio. Presence of *Archaias* and *Laevipeneroplis* at this time indicates open coast and seagrass beds. The assemblage change from *Archaias-Laevipeneroplis* to *Ammonia-Elphidium* suggests change from marine to brackish conditions between 4,800 and 1,800 BP. The clusters shaded gray in Figure S2.3 produce a faunal succession that looks similar to 4A in timescale and magnitude, despite using the size fraction > 250 µm compared to > 125 µm in 4A. We interpret the similarity between the cores to mean that the northern lagoon experienced basin-

wide changes to the environment that were characterized by a rapid increase in salinity and then a steady decrease to brackish conditions. Sea-level rise around 5,000 BP for this area would rapidly increase salinity the mangrove understory, and the *Archaias-Laevipeneroplis* assemblage indicates this was an open coast with *Thalassia* seagrass. The shift to the *Ammonia-Elphidium* assemblage indicates more brackish groundwater entering the lagoon. The inferred primary cause of this groundwater is the same as for 4A which is barrier island aggradation reduced mixing between groundwater and seawater as the western bank of Celestun Lagoon began to form.

Age models and sediment accumulation

Two of the five radiocarbon age reversals occur between core sections in 4A (Table 2.2), thus core misalignment cannot be excluded, but continuously measured density of core 4A (Figure 2.2A) and visual inspection of discrete shell layers do not suggest resampling or misalignment of core sediments. In addition, the two age reversals in 4B (and one in UL-5) occur within core sections where core section alignment is not a factor, and 60% of age reversals occur in the peat layer at the bottom of the cores. All five ^{14}C age reversals have a mean duration of 263 uncalibrated years over a mean interval of 27 cm which implies mean sediment accumulation rate of about 1 mm yr^{-1} for these age reversal intervals, consistent with the 1.5 mm yr^{-1} rate determined from ^{210}Pb (Figure 2.3). We interpret this to possibly relate to growth of new (young) mangrove roots into deeper (older) sediments, especially when peat was

accumulating, or to minor storm mixing of the sediment-water interface. However, coarse-grained storm layers were not noted in sediments containing the reversed radiocarbon data. The low topographic relief (i.e., low rainfall runoff) around Celestun and the northern Yucatan Peninsula (Appendini et al., 2012) implies the transport of substantially older carbon to the lagoon is unlikely but cannot be ruled out. Whatever the cause of age reversals, they are relatively small and are included in the simulated error of the Bayesian models of age with depth (Blaauw and Christen, 2011). We are thus comfortable with the age-depth model generated (Figure 2.3). Variable ^{210}Pb activity from 5-0 cm of short push cores (Table 2.2) is consistent with other studies (Gonneea et al., 2004) and indicates moderate mixing from bioturbation and/or wind given the shallow (<0.5 m) lagoon depth.

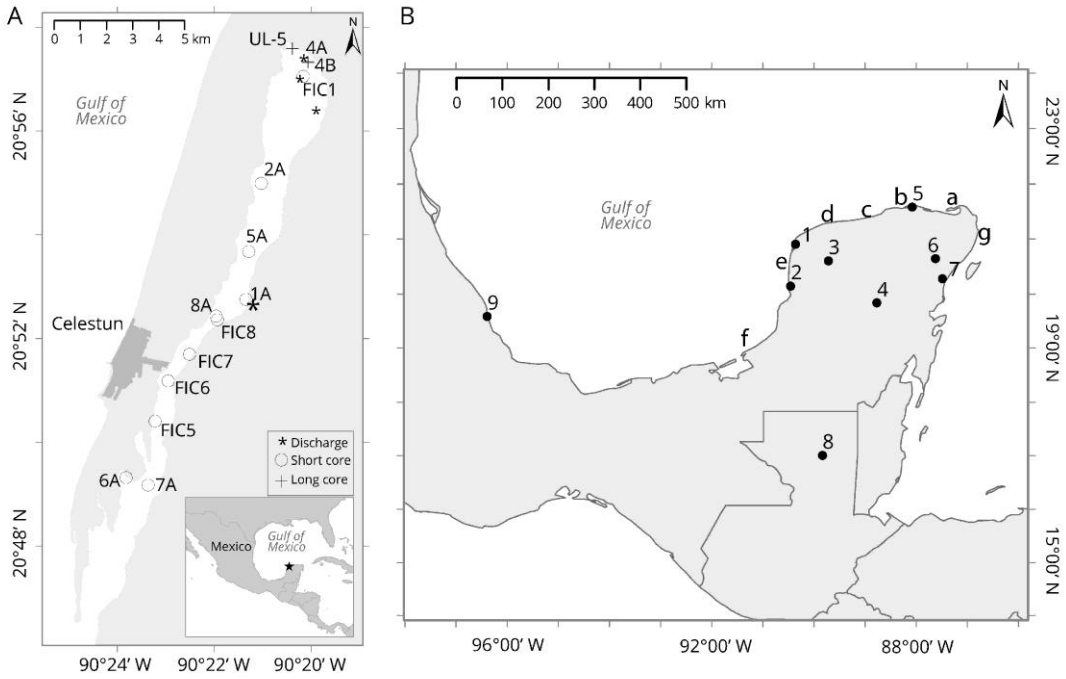

Figure 2.1

A Map of Celestun Lagoon field location with sample sites from the northern lagoon to the southern lagoon (open to the ocean). Site names derive from expeditions (Table 2.1), and water samples were measured at each site. **B** Field sites for comparison in Figure 2.8. 1 Celestun Lagoon (this study), 2 Los Petenes (Roy et al. 2017), 3 Aguada X'caamal (Hodell et al. 2005), 4 Lake Chichancanab (Hodell et al. 1995), 5 Ria Lagartos (Aragon-Moreno et al. 2012), 6 Punta Laguna (Curtis et al. 1998), 7 Aktun Ha (ven Hengstrum et al. 2010), 9 Lake Puerto Arturos (Wahl et al. 2014), 9 La Mancha Lagoon (Arellano-Torres et al. 2019). Letters are coastal sites with geomorphic features similar to Celestun Lagoon: a Holbox, b Ria Lagartos, c Dzilam de Bravo, d Progreso, e Isla Arena, f Terminos, g Nichupte.

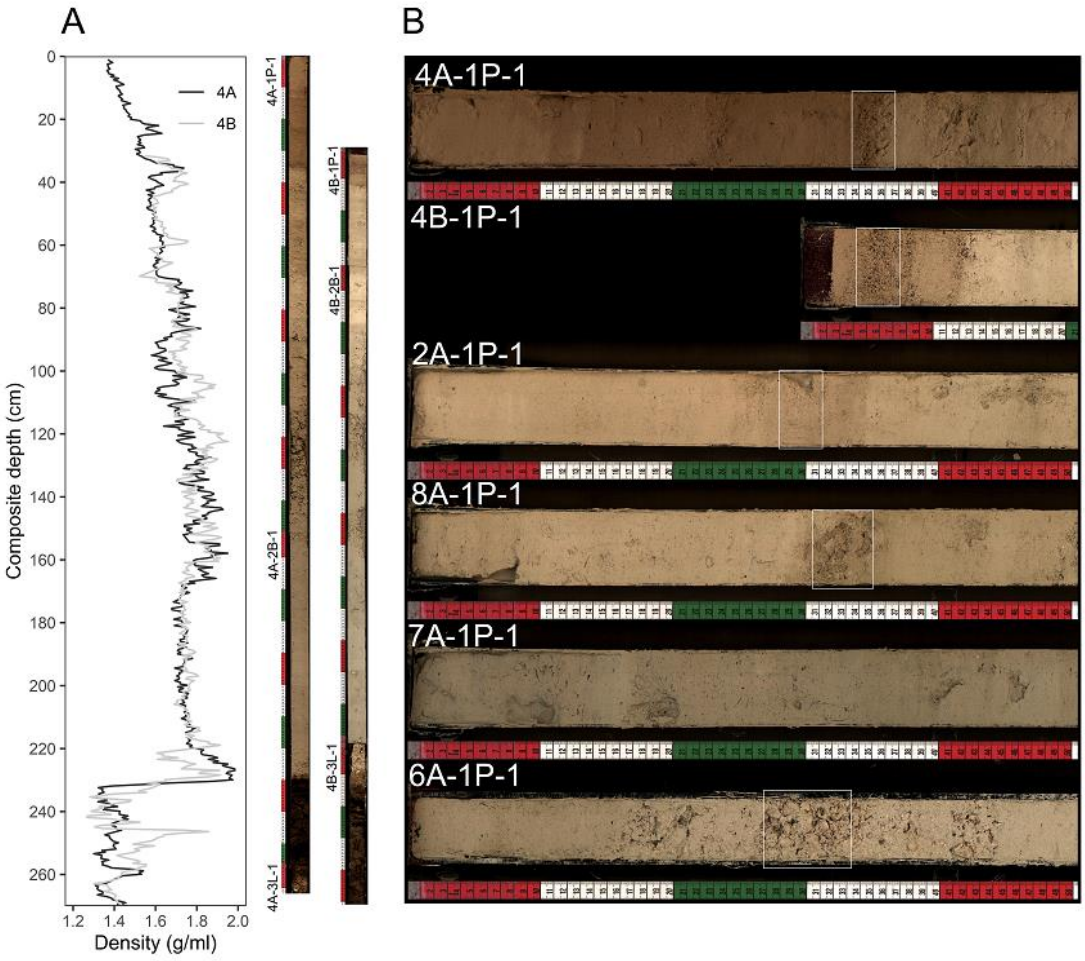

Figure 2.2
A Downcore density measured in cores 4A and 4B (adjacent) to determine composite depth profile for radiocarbon ages. Peat layer begins at 229 cm. **B** Top 50 cm of cores from locations in Figure 2.1. Coarse (> 500 µm) bioclastic sand and shell layer is boxed at ~30 cm. Note increasing thickness from north (4A) to south (6A).

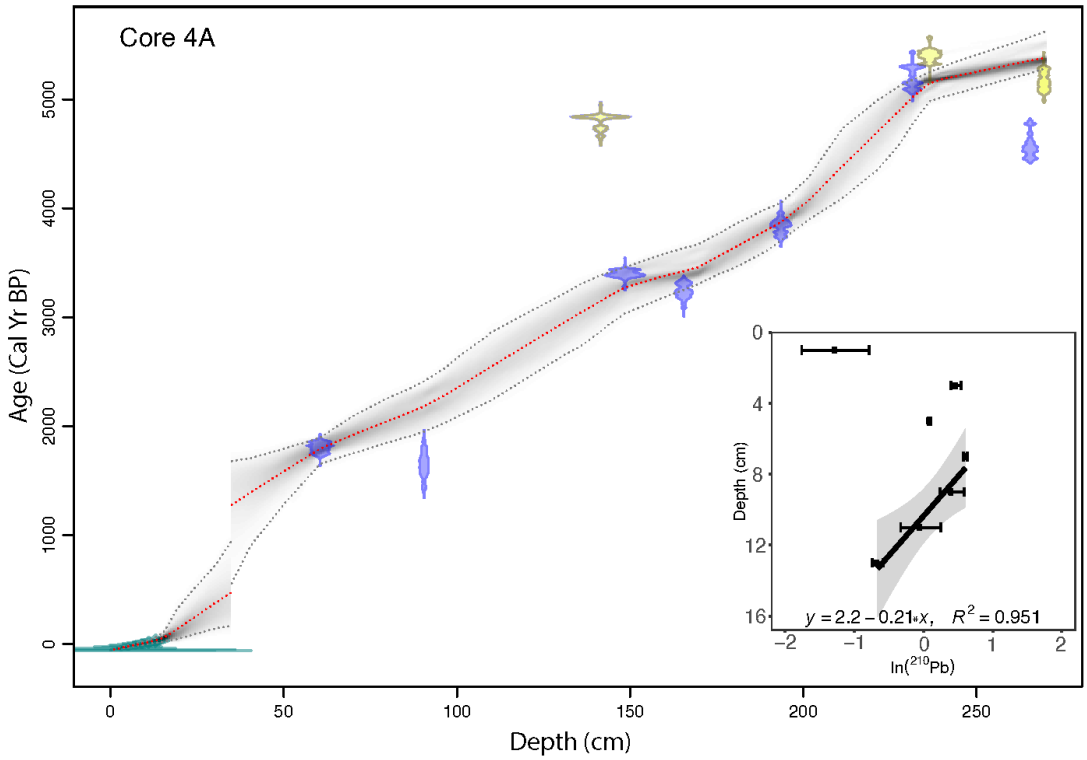

Figure 2.3

Age-depth model for core 4A using radiocarbon dates from 4A (blue) and 4B (light yellow) and ^{210}Pb accretion-derived age (green, accretion rate from inset). Data is presented in Table 2. Gray dotted lines are the 95% confidence interval for ages. Offset at depth 35 cm represents an inferred hiatus (Figure 2.2) estimated at 800 years long for core 4A. **Inset** ^{210}Pb-derived sediment accumulation rate calculated as -0.0311/-0.21 = 0.146 cm yr^{-1} ~ 1.5 mm yr^{-1}. More detail on the age-depth models can be found in Supplemental Material.

Figure 2.4
Stratigraphic diagrams of benthic foraminifera colored by cluster results (from Figure 2.5) and paired with diversity indices and bulk sediment organic carbon isotope data for **A** core 4A, with an age scale obtained from Figure 2.3, and **B** coretop samples from north to south in the lagoon (Figure 2.1). Dashed lines represent stratigraphic transitions between assemblages. Note change in scale on the bottom axis of each panel and the age jump at 35 cm reflecting a hiatus from 1,300 to 500 Cal yr BP.

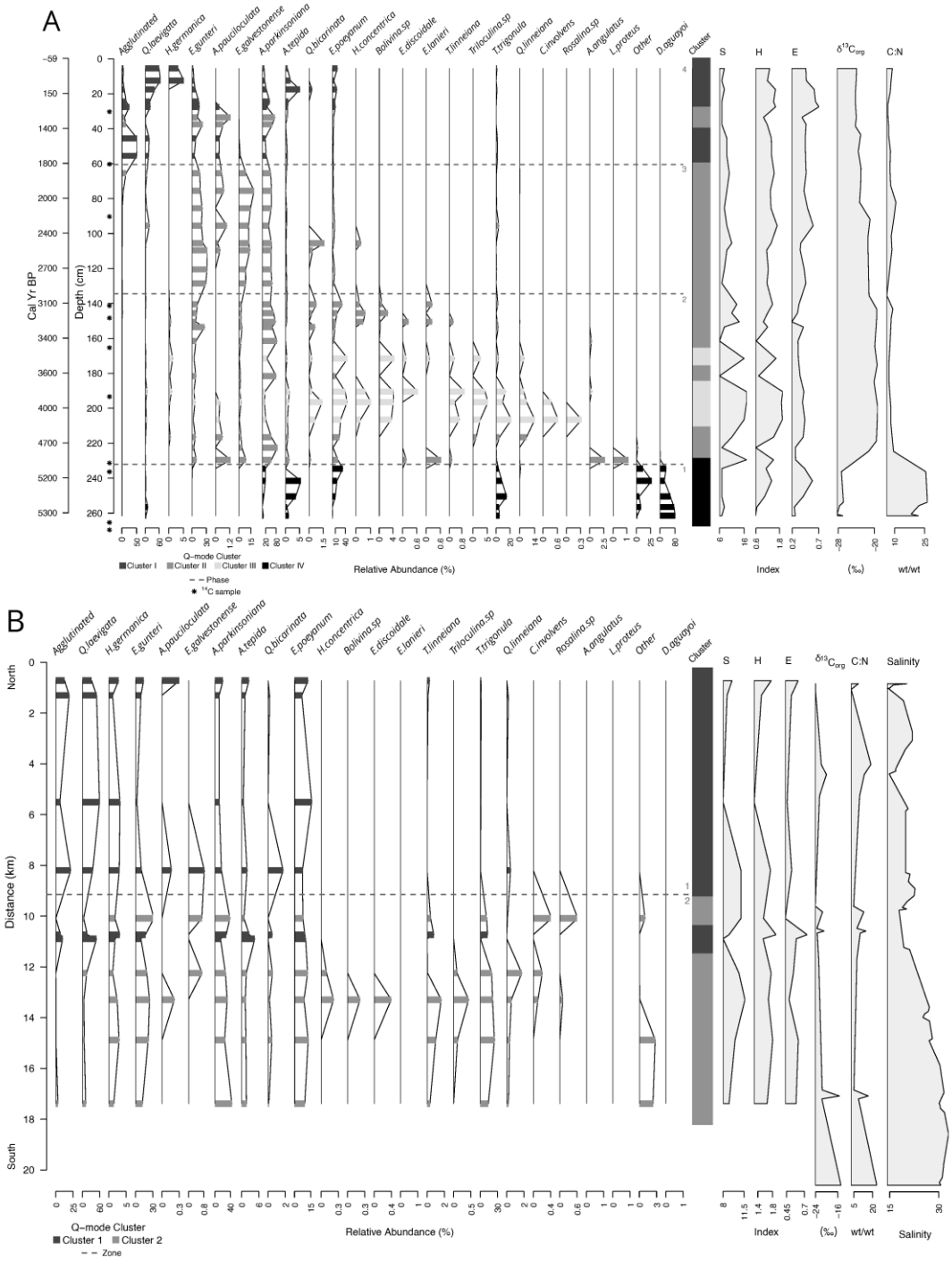
A
Agglutinated
Q.laevigata
H.germanica
E.gunteri
A.pauciloculata
E.galvestonense
A.parkinsoniana
A.tepida
Q.bicornata
E.poeyanum
H.concentrica
Bolivina.sp
E.discoidale
E.lamieri
T.linneiana
Triloculina.sp
T.trigonula
Q.limneiana
C.involvens
Rosalina.sp
A.angulatus
I.proteus
Other
D.oguapoi
Cluster
S
H
E
δ13Corg
C:N
Cal Yr BP
Depth (cm)
Q-mode Cluster
Cluster I
Cluster II
Cluster III
Cluster IV
Phase
14C sample
Relative Abundance (%)
Index
(‰)
wt/wt
B
North
South
Distance (km)
Salinity
Cluster 1
Cluster 2
Zone

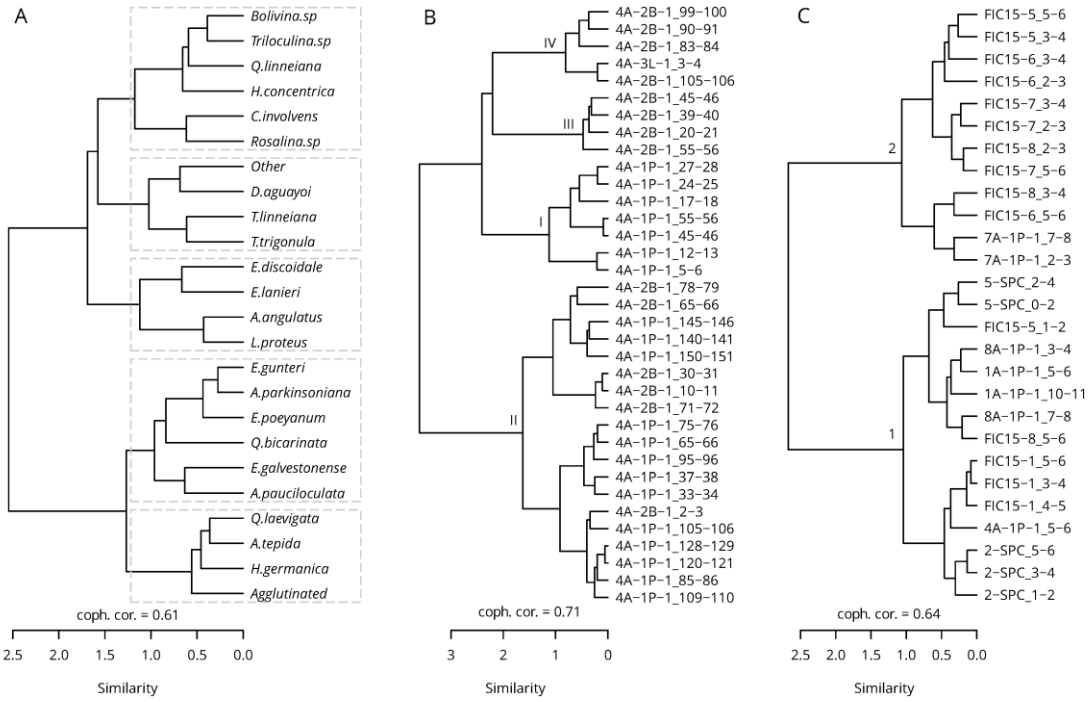

Figure 2.5

A R-mode cluster analysis of all modern and fossil foraminifera observed. Gray dashed boxes encompass co-occurring taxa which are given assemblage names (from top to bottom): *Bolivina-Hanzawaia-Rosalina*, *Discorinopsis*, *Archaias-Laevipeneroplis*, *Ammonia-Elphidium*, and *Agglutinated-Haynesina*. Taxa list given in Table 2.3. Q-mode cluster analysis and cophenetic correlation coefficients of **B** core 4A and **C** coretop samples. Arabic and Roman numeral notations are the clusters colored in Figures 2.4 and 2.6.

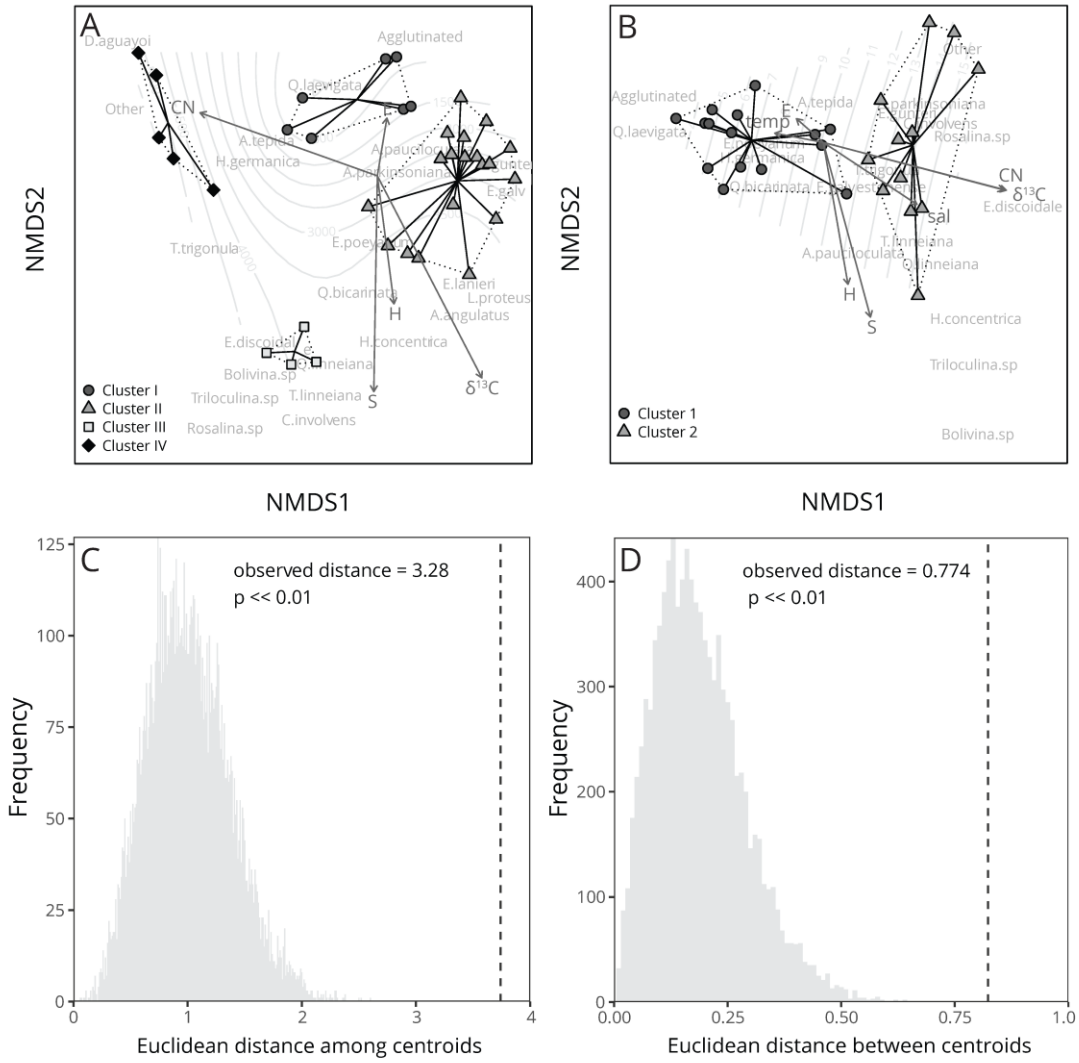

Figure 2.6
NMDS result (k = 3) for **A** core 4A (stress = 0.082) with contours of age and **B** coretop samples (stress = 0.094) with contours of distance. Vectors S, H, and E are indices of species, diversity, and evenness, respectively, and d13C is $\delta^{13}C$ and C:N ratio of bulk sediment organics. In B, temp is temperature (°C) and sal is salinity of the lagoon water column. Clusters are joined at their centroids and outlined by dotted lines, and distributions of Euclidian distances among group centroids are given for **C** core 4A and **D** coretop samples and compared to observed centroid distance (dashed line). C and D represent simulated p-values for the null hypothesis that clusters (faunal distributions) are not significantly different from one another within each panel A and B. Note that absolute value of centroid distances is not meaningful, only the distribution relative to the observed distance.

Figure 2.7
Conceptual diagram of coastal development around Celestun Lagoon. The star represents core 4A in the present day northern lagoon. **A** Phase 1, during low sea level the core site was located within a inland low-salinity mangrove pond with *Discorinopsis* assemblage. **B** Phase 2, sea level rose beginning ~ 5,100 BP, the site is inundated, and coastal marine *Thalassia* seagrass and *Archaias-Laevipeneroplis* assemblages colonized by 4,900 BP. Long-shore drift continued, initiating spits and barrier islands which began a prolonged period of assemblage change. **C** Phase 3, decelerating sea-level rise allowed for spits and barrier islands to accumulate stably. *Bolivina-Hanzawaia-Rosalina* dominated the site but was replaced by *Ammonia-Elphidium* as groundwater lowered salinity the nascent lagoon. **D** Phase 4, sea level stabilized, barrier island coastline expanded, and mangroves colonized new shoreline in the lagoon which increased in length. *Agglutinated-Haynesina* assemblage developed alongside *Ammonia-Elphidium*. Barrier islands continued to accumulate to the present. Precipitation (climate) recharged groundwater throughout all phases, and final assemblage reflects reduction in mixing between the groundwater and seawater as well as absolute decrease in groundwater (and increase in sweater) during droughts.

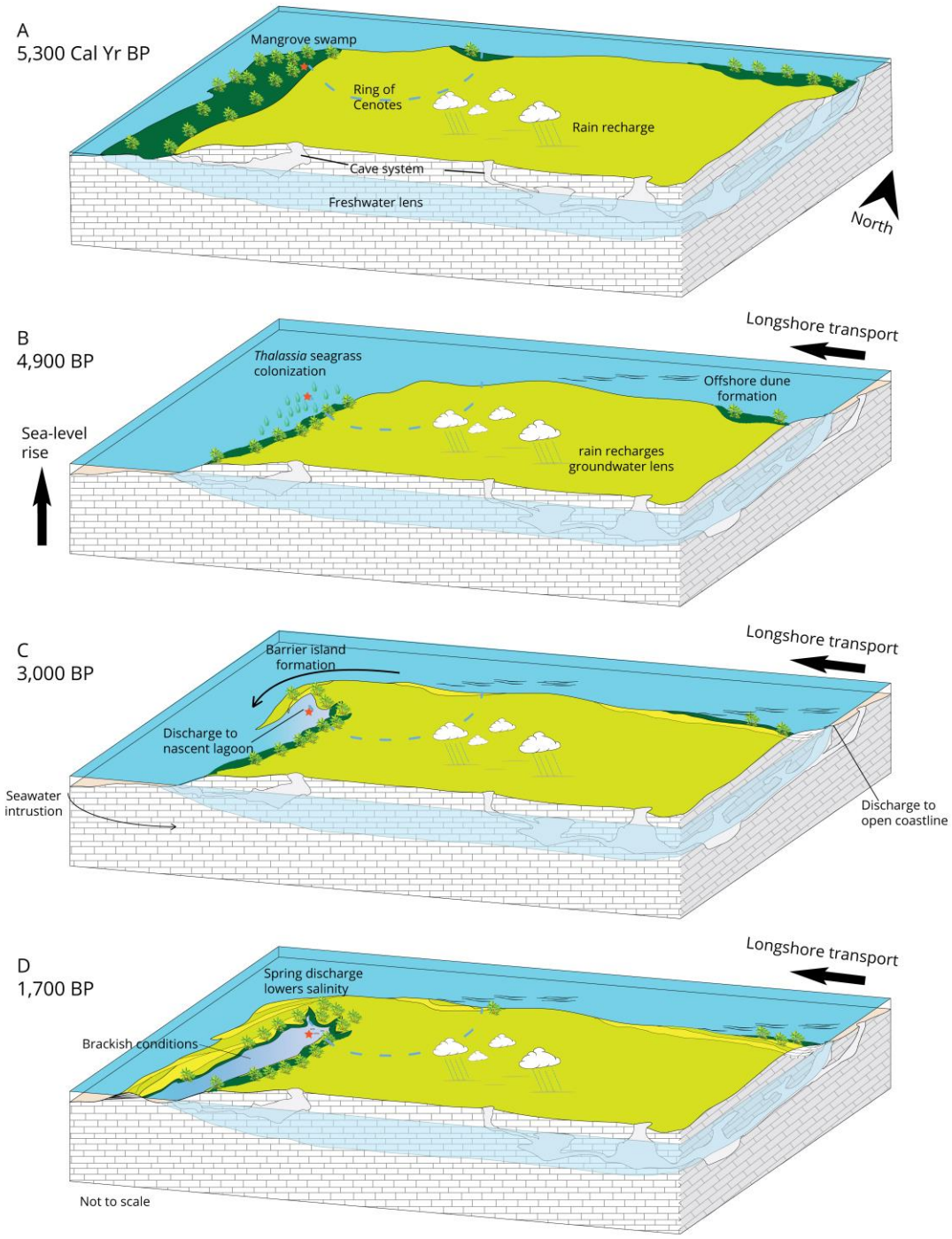
A
5,300 Cal Yr BP
Mangrove swamp
Ring of Cenotes
Rain recharge
Cave system
Freshwater lens
North
B
4,900 BP
Longshore transport
Thalassia seagrass colonization
Offshore dune formation
Sea-level rise
rain recharges groundwater lens
C
3,000 BP
Longshore transport
Barrier island formation
Discharge to nascent lagoon
Seawater intrustion
Discharge to open coastline
D
1,700 BP
Longshore transport
Spring discharge lowers salinity
Brackish conditions
Not to scale

Figure 2.8

Summary of oceanographic and paleoclimate records from coasts and lakes around the Yucatan Peninsula, Mexico. Climate records have been smoothed using a 4-point rolling average to. See Figure 2.1 for site locations. **A** Relative sea-level and 95% confidence shading (Khan et al. 2017). **B** Summer (August) insolation at 20° N (Laskar et al., 2004). **C** Hydrogen isotopes of plant wax from Lake Salpeten (Douglas et al. 2015). **D** NMDS of microfossils and Cenote Aktun Ha (van Hengstrum et al. 2010). **E** $\delta^{18}O$ of *Pyrgophorus sp.* in Lake Punta Laguna (Curtis et al., 1998). **F** $\delta^{18}O$ of *Pyrgophorus coronatus* in Lake Chichancanab (Hodell et al. 1995). **G** $\delta^{18}O$ of Pyrgophorus coronatus in Aguada X'caamal (closed cenote, Hodell et al. 2005). **H** Absolute pollen abundance from Ria Lagartos (Aragon-Moreno et al. 2012). **I** K/Ca of sediment in Los Petenes (Roy et al. 2017). **J** Fe/Ca of sediment in La Mancha lagoon (Arellano-Torres et al. 2019). **K** $\delta^{13}C$ of bulk sediment organic matter in Celestun Lagoon (this study). **L** NMDS scores of foraminiferal assemblages (see Figure 2.6A). **M** H diversity (reflecting total species and absolute abundance) of assemblages. **N** Phase of lagoon development for Celestun Lagoon (see conceptual diagram, Figure 2.7). ^{14}C data points are for this study (Table 2.2). Shaded columns represent documented dry periods for the north-central Yucatan Peninsula. Dotted box represents possible storm or tsunami deposit in coastal records from the west, south, and east of Celestun Lagoon (Figure 2.1). Note that NMDS scores in **D** and **L** cannot be directly compared and are presented to show relative trends.

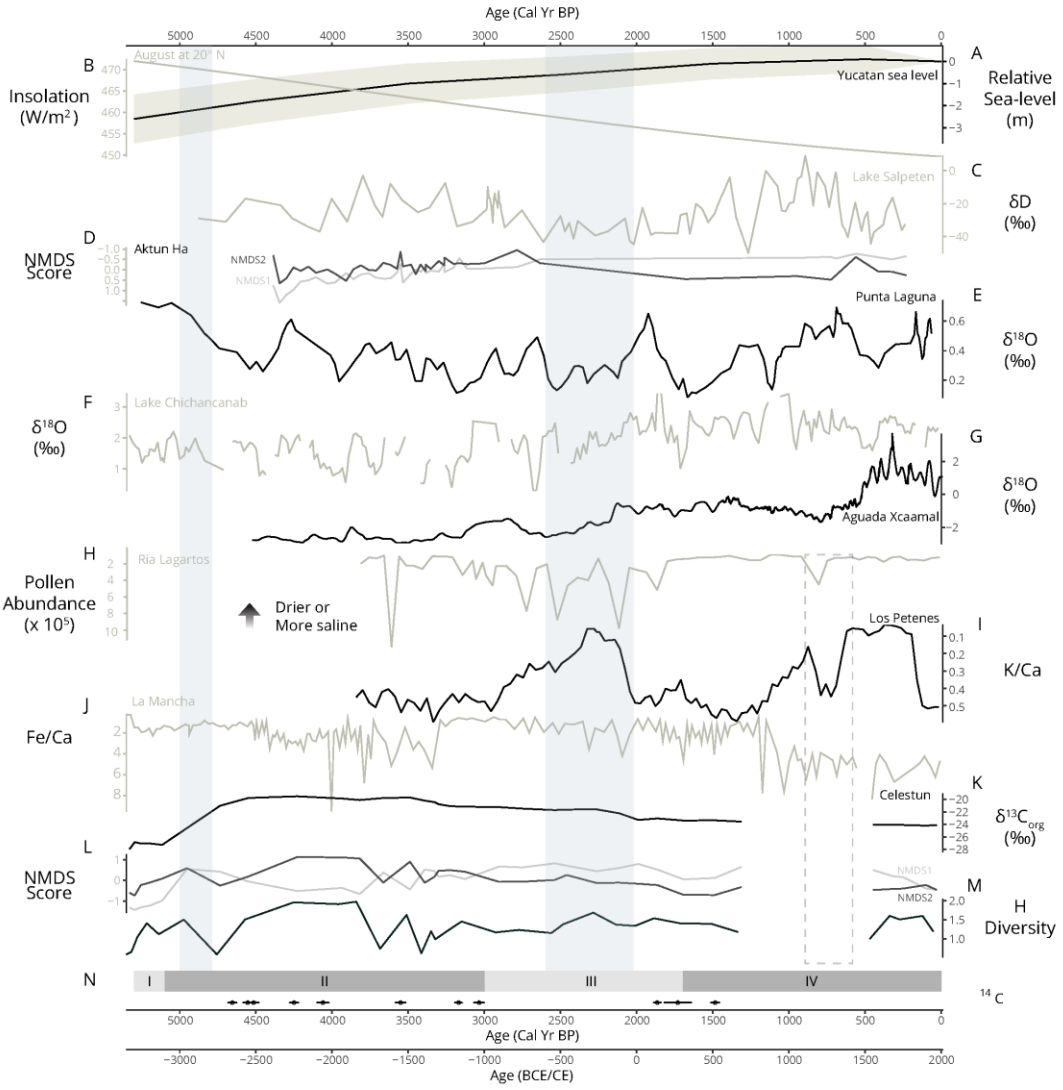
Age (Cal Yr BP)
5000
4500
4000
3500
3000
2500
2000
1500
1000
500
0
B
August at 20° N
Insolation (W/m²)
470
465
460
455
450
A
Yucatan sea level
Relative Sea-level (m)
0
−1
−2
−3
C
Lake Salpeten
δD (‰)
0
−20
−40
D
NMDS Score
Aktun Ha
NMDS2
NMDS1
−1.0
−0.5
0.0
0.5
1.0
E
Punta Laguna
δ18O (‰)
0.6
0.4
0.2
F
Lake Chichancanab
δ18O (‰)
3
2
1
G
Aguada Xcaamal
δ18O (‰)
2
0
−2
H
Ria Lagartos
Pollen Abundance (x 10⁵)
2
4
6
8
10
Drier or More saline
I
Los Petenes
K/Ca
0.1
0.2
0.3
0.4
0.5
J
La Mancha
Fe/Ca
2
4
6
8
K
Celestun
δ13Corg (‰)
−20
−22
−24
−26
−28
L
NMDS Score
1
0
−1
NMDS1
NMDS2
M
H Diversity
2.0
1.5
1.0
N
I
II
III
IV
14C
5000
4500
4000
3500
3000
2500
2000
1500
1000
500
0
Age (Cal Yr BP)
−3000
−2500
−2000
−1500
−1000
−500
0
500
1000
1500
2000
Age (BCE/CE)

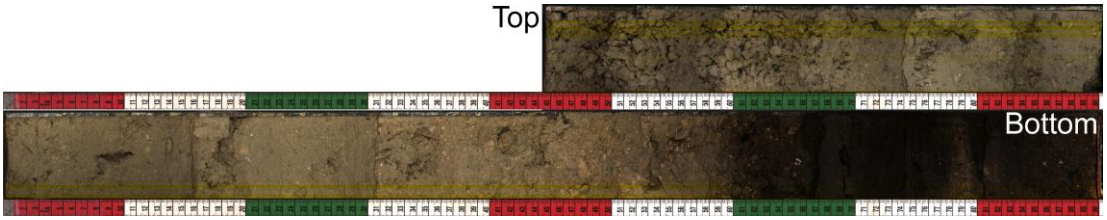

Figure S2.1
Scanned core images core UL-5. Top refers to the uppermost section of core at 64.5 cm below the sediment-water interface, and 64.5-0 cm was lost in the field. Note the peat layer and transition to carbonate mud.

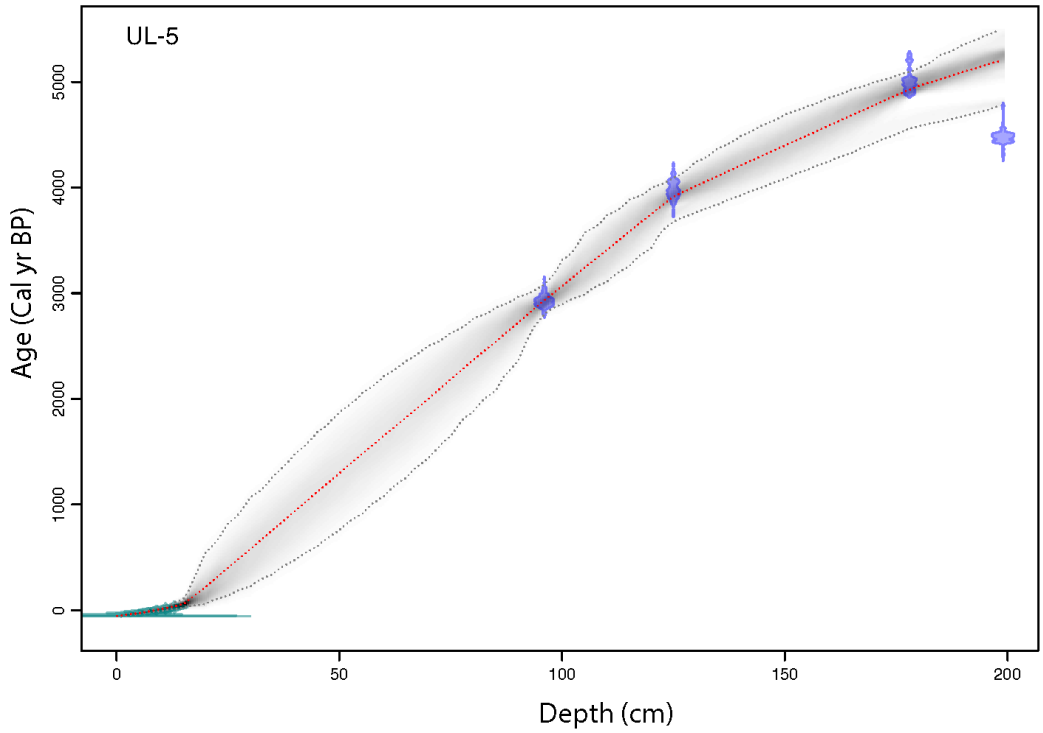

Figure S2.2
Age-depth model for core UL-5 using radiocarbon dates (blue) from UL-5 and ^{210}Pb accretion-derived age (green, see Figure 2.3 inset). Data is presented in Table 2.2. Gray dotted lines are the 95% confidence interval for ages. Hiatus is not presented at ~35 cm depth because this section of core was lost.

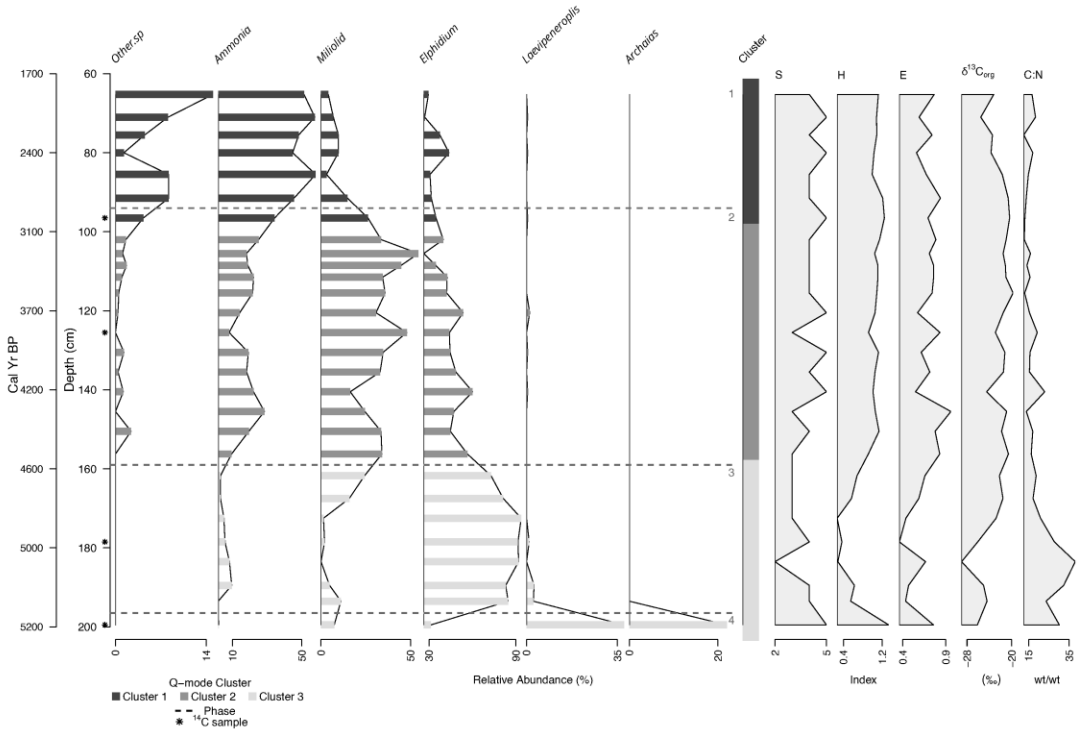

Figure S2.3
Stratigraphic diagrams of benthic foraminifera colored by cluster results (from Figure S2.4) and paired with diversity indices and bulk sediment organic carbon isotope data.

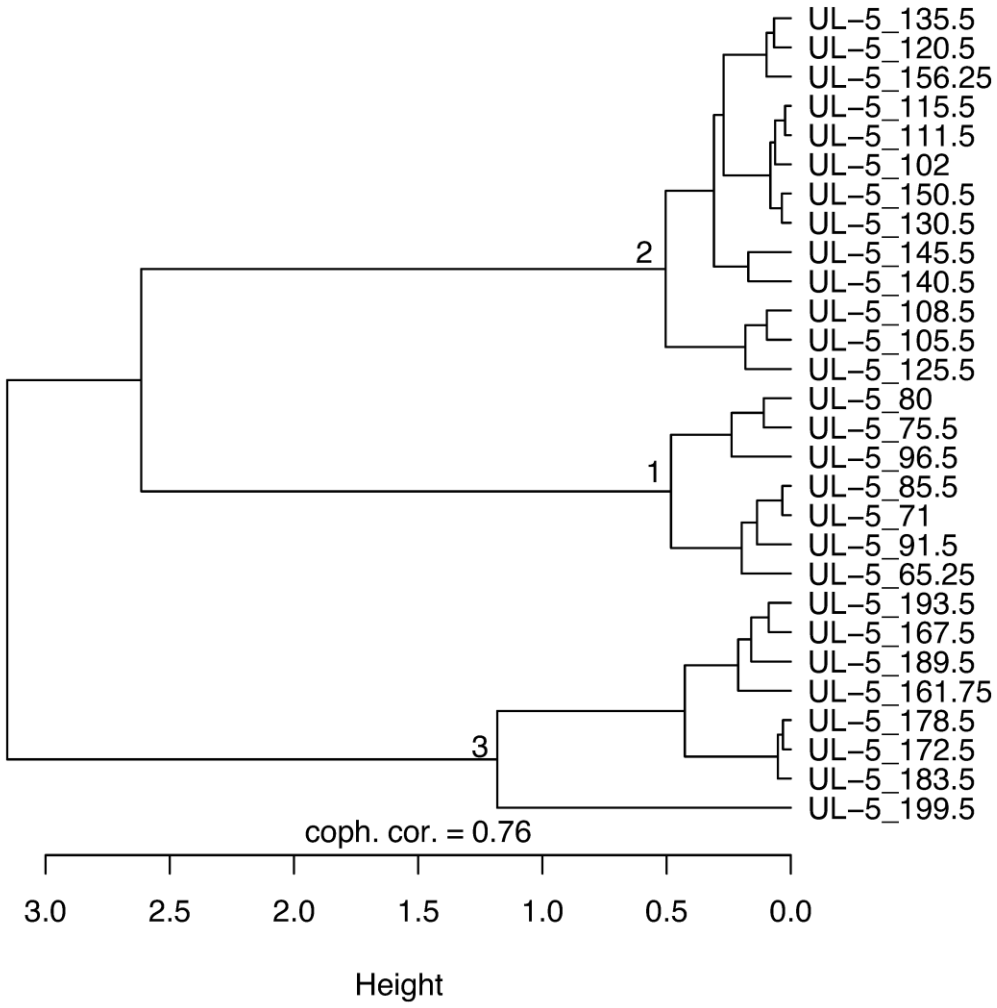

Figure S2.4
Q-mode cluster dendrogram of core UL-5 samples (cophenetic correlation = 0.76) of benthic foraminifera at the >250 µm fraction identified at the genus level. Clusters are used to color clusters presented in Figures S2.3 and S2.5. Assemblages assigned to clusters come from R-mode cluster analysis in Figure 2.5A of the main text.

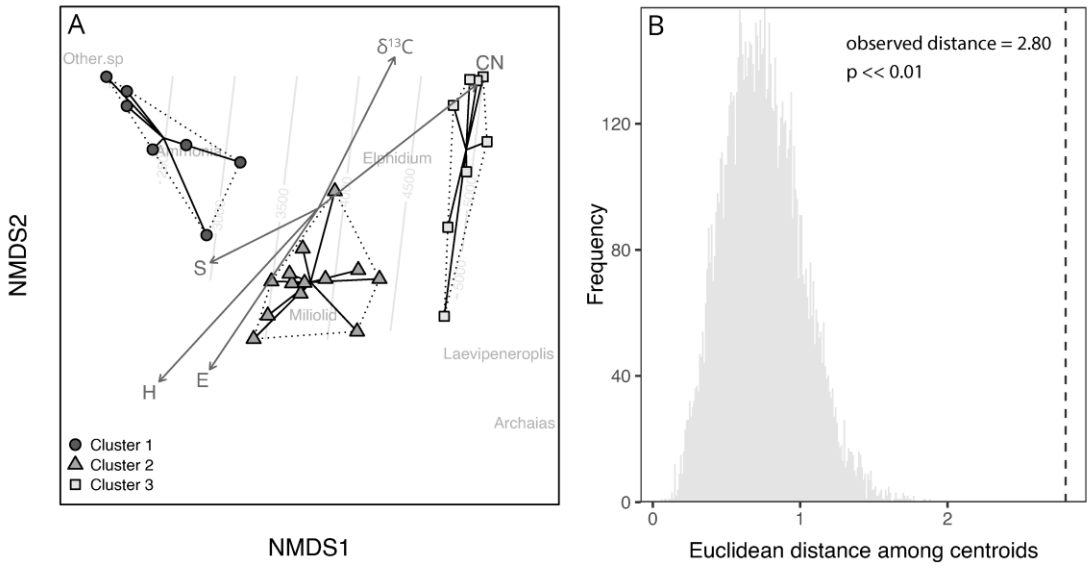

Figure S2.3

A NMDS of core UL-5 samples (k = 3, stress = 0.026) with contours of age. Vectors S, H, and E are indices of species, diversity, and evenness, respectively, and $\delta^{13}C$ and C:N ratio are of bulk sediment organics. Clusters are joined at their centroids and outlined by dotted lines. **B** Distribution of Euclidian distances among group centroids which represents simulated p-values for significant difference between cluster compositions (i.e., cluster faunal compositions are significantly different, p <<0.01).

Table 2.1 Sediment sampling locations and modern environmental parameters measured at each site

Core	Section ID*	Interval (cm)	Expedition Year	Latitude	Longitude	Distance† (km)	Salinity (psu)	Temperature (°C)	$\delta^{13}C_{org}$ (‰)	C:N (atomic)
UL-5	UL-5-1	0-110	2006	20.9589	-90.3406	0.21	23	-	-24.17	8.8
	UL-5-2	110-200								
4A	4A-1P-1	0-148	2009	20.9548	-90.3354	0.72	29	32.3		
	4A-2B-1	148-262	2009	20.9548	-90.3354	0.72	29	32.3	-23.74	8.8
	4A-3L-1	251-262	2009	20.9548	-90.3354	0.72	29	32.3		
4B	4B-1P-1	0-67	2009	20.9548	-90.3354	0.72	29	32.3	-23.74	8.8
	4B-2B-1	67-184	2009	20.9548	-90.3354	0.72	29	32.3	-23.74	8.8
	4B-3L-1	184-240	2009	20.9548	-90.3354	0.72	29	32.3	-23.74	8.8
FIC15-1	FIC15-1	0-30	2015	20.9501	-90.3370	1.30	16	28.6	-23.64	8.9
2A	2A-1P-1	0-119	2009	20.9157	-90.3513	5.51	26	32.8	-22.92	9.5
1A	1A-1P-1	0-30	2009	20.8783	-90.3567	10.09	14	23.7	-22.14	10.3
8A	8A-1P-1	0-135	2009	20.8731	-90.3670	10.73	25	30.6	-22.03	10.4
FIC15-21	FIC15-21	0-30	2015	20.8718	-90.3666	10.89	23	28.2	-22.00	10.4
FIC15-20	FIC15-20	0-30	2015	20.8607	-90.3762	12.24	24	27.9	-21.77	10.6
FIC15-19	FIC15-19	0-30	2015	20.8522	-90.3835	13.29	25	28.7	-21.59	10.8
FIC15-18	FIC15-18	0-30	2015	20.8392	-90.3880	14.88	31	28.3	-21.32	11.1
6A	6A-1L-1	0-81	2009	20.8216	-90.3978	17.03	29	26.9	-22.19	11.0
7A	7A-1P-1	0-149	2009	20.8197	-90.3904	17.39	33	31.2	-20.89	11.5

*For cores collected in 2009, coring device is denoted after the first dash as P = piston, B = Bolivia, L = Livingstone.
All others are piston devices.
†Distance is from the northern lagoon (0 km) to the southern lagoon (20 km).

Table 2.2 Radionuclide data used in age-depth models in the R package rbacon

Lab ID	Site	Core	Interval (cm)	Composite depth (cm)	$^{210}Pb_{excess}$ (dpm g^{-1})	$^{210}Pb_{excess}$ error (dpm g^{-1})	$^{14}C_{uncalibrated}$ (yr)	$^{14}C_{uncalibrated}$ error (yr)
-	5A	5-SPC	0-2	1	0.280	1.624	-	-
-	5A	5-SPC	2-4	3	1.605	1.076	-	-
-	5A	5-SPC	4-6	5	1.097	1.018	-	-
-	5A	5-SPC	6-8	7	1.836*	0.972	-	-
-	5A	5-SPC	8-10	9	1.512*	1.191	-	-
-	5A	5-SPC	10-12	11	0.962*	1.336	-	-
-	5A	5-SPC	12-14	13	0.517*	0.927	-	-
CAMS #177919	4A	4A-1P-1	30-31	30.5	-	-	1485†	30
CAMS #150117	4A	4A-1P-1	60-61	60.5	-	-	1865	25
CAMS #150118	4A	4A-1P-1	90-91	90.5	-	-	*1730*	*90*
CAMS #150119	4A	4A-1P-1	148-149	148.5	-	-	3170	25
CAMS #150120	4A	4A-2B-1	14-15	165.5	-	-	*3035*	*35*
CAMS #177920	4A	4A-2B-1	42-43	193.5	-	-	3550	35
CAMS #147318	4A	4A-2B-1	80-81	231.5	-	-	4555	30
CAMS #147319	4A	4A-3L-1	7-8	265.5	-	-	*4060*	*40*
CAMS #150121	4B	4B-2B-1	75-76	141.5	-	-	4250	30
CAMS #147320	4B	4B-3L-1	18-19	236.5	-	-	4655	30
CAMS #147321	4B	4B-3L-1	51-52.5	269.5	-	-	*4515*	*35*
CAMS #128506	UL-5	UL-5	96-97	96.5	-	-	2820	35
CAMS	UL-5	UL-5	125-126	125.5	-	-	3650	50

#128505								
CAMS #128504	UL-5	UL-5	178-179	178.5	-	-	4410	35
CAMS #128503	UL-5	UL-5	199-200	199.5	-	-	*4000*	*35*

*Only ^{210}Pb data below 6 cm was used to determine accumulation rate. †Value excluded from Bacon age model.
Italics represent age inversions.

Table 2.3 Foraminifera species and modern environment

Species	General salinity tolerance (psu) and environment	Reference
Ammonia parkinsoniana	Infaunal, euryhaline, 4-41psu, silty sand to calcareous mud, estuaries with variable sedimentation and high organics, protected mangrove lagoons	Murray (1991, 2006); Hayward et al. (2004); Poag (2015)
Ammonia tepida	Same as *A. parkinsoniana*, more sensitive to salinity variability	Poag (2015)
Ammonia pauciloculata	Infaunal, euryhaline, rare along Texas inner shelf estuaries	Poag (2015)
Ammotium sp. or *Ammobaculites sp.*	Infaunal, 4-41psu, silty mud, intertidal mudflats	Murray (1991, 2006)
Archaias angulatus	Epifaunal, epiphytic, 34-37psu, carbonate-rich sediments with seagrasses (*Thalassia sp.*), shallow warm marginal marine	Murray (1991, 2006); Poag (2015); Sen Gupta (1999); Javaux and Scott (2003)
*Borelis pulchra**	Epifaunal, epiphytic, 35psu, macroalgal substrates, back-reef lagoons and tropical seagrass beds	Javaux and Scott (2003); Poag (2015); Murray (2006)
Brizalina sp.	Infaunal, 31-35psu, tolerates dysoxia, marine inner/outer shelf	Murray (1991, 2006)
Cornuspira involvens.	Epiphytic, seagrass beds, widespread inner shelf, nearshore marine lagoons	Murray (2006)
*Discorinopsis aguayoi**	Epifaunal, brackish salinity, characteristic of landlocked mangrove ponds, common to Bermuda and brackish inner lagoons of Florida, Bahamas, and Belize	Javaux and Scott (2003); Murray (2006)
Elphidium discoidale	35-37psu, clastic sediments, warm water bays and estuaries	Poag (2015); Sen Gupta (1999)
Elphidium galvestonense	Epifaunal, epiphytic, marshes, lagoons, and estuaries	Murray (2006); Poag (2015)
Elphidium gunteri	Euryhaline, 25-31psu, sandy mud, common to marshes, lagoons, estuaries	Murray (1991, 2006); Poag (2015)
Elphidium lanieri	Protected nearshore lagoons and back-reefs	Javaux and Scott (2003); Poag (2015)
Elphidium poeyanum	Epifaunal, euryhaline, 35-81psu, warm-temperate silty lagoons and estuaries	Murray (1991, 2006); Sen Gupta (1999)
Hanzawaia concentrica	Epifaunal, 34-36psu, warm marine inner shelf, bays, estuaries	Sen Gupta (1999); Poag (2015); Murray (19912006)
Haynesina germanica	Infaunal, common to salt marshes and estuaries with variable mud and organics	Murray (2006); Poag (2015)
Laevipeneroplis proteus	Epifaunal, epiphytic, 35psu, warm carbonate-rich lagoon seagrass and macroalgae beds in lagoons and innermost shelf	Murray (2006); Poag (2015); Sen Gupta (1999)
Miliammina fusca	Epifaunal, euryhaline, 7-19psu, silty mud, shallow lagoons and estuaries	Murray (2006)
Quinqueloculina Bicarinata	Epifaunal, carbonate-rich brackish-marine bays, lagoons, inner shelf, commonly near seagrass beds	Javaux and Scott (2006); Poag (2015); Murray (1991, 2006); Sen Gupta (1999)
*Quinqueloculina laevigata**	Epifaunal, 10-47psu, seagrasses and algae beds, common to mangroves of the Caribbean	Murray (2006); Javaux and Scott (2003), Sen Gupta (1991)
Quinqueloculina linneiana	Epifaunal, nearshore bays and lagoons similar to *Q. bicarinata*	Poag (2015)
Rosalina sp.	Epifaunal, clinging to seagrasses, warm marine lagoons, mangroves, and	Murray (2006); Poag (2015); Sen Gupta

	back-reef	(1999); Javaux and Scott (2003)
Triloculina sp.	Likely similar to T trigonula, 35-81psu	Murray (1991, 2006)
Triloculina linneiana	carbonate-rich mud, nearshore marine lagoons and mangroves	Javaux and Scott (2003); Murray (2006)
Triloculina trigonula	Epifaunal, clinging to vegetation, marine to hypersaline, carbonate-rich inner shelf, low tidal marsh, and nearshore mangrove	Poag (2015); Murray (2006); Sen Gupta (1991); Javaux and Scott (2003)
*Trochammina macrascens**	Epifaunal, clinging to vegetation, organic-rich mud, common to mid, high marsh and mangroves	Javaux and Scott (2003); Murray (1991, 2006)

*identification from Javaux and Scott (2003); other identifications from Poag (2015), and environments from remaining listed references

Table 2.4 Multivariate analyses of clusters and environmental parameters

	PERMANOVA							Beta dispersion						Bootstrapping		Kendall tau		
	Source	df	SS	MS	Pseudo *F*	R^2	*p**	Source	df	SS	MS	*F*	*p**	Source	*p*‡	Source	*τ*	*p*
Coretop >125 µm	salinity	1	0.504	0.504	10.01	0.149	**0.001**	Cluster	1	0.013	0.013	2.248	0.128	Cluster	<<**0.01**	S: $\delta^{13}C_{org}$	-0.460	**0.002**
	$\delta^{13}C_{org}$	1	0.786	0.786	15.60	0.232	**0.001**	Residuals	25	0.147	0.006	—				H: $\delta^{13}C_{org}$	-0.268	0.056
	Temperature	1	0.150	0.150	2.98	0.044	**0.014**									E: $\delta^{13}C_{org}$	0.132	0.345
	Cluster	1	0.346	0.346	6.86	0.102	**0.001**									S:CN	0.460	**0.002**
	Salinity×$\delta^{13}C_{org}$	1	0.104	0.104	2.07	0.031	0.076									H:CN	0.268	0.056
	$\delta^{13}C_{org}$×CN	1	0.153	0.153	3.04	0.045	**0.029**									E:CN	-0.132	0.345
	Salinity×Temperature	1	0.142	0.142	2.82	0.042	**0.026**									S:salinity	0.228	0.127
	$\delta^{13}C_{org}$×Temperature	1	0.174	0.174	3.46	0.051	**0.012**									H:salinity	-0.026	0.850
	Salinity×Cluster	1	0.061	0.061	1.21	0.018	0.29									E:salinity	-0.380	**0.007**
	$\delta^{13}C_{org}$×Cluster	1	0.065	0.065	1.29	0.019	0.238									S:distance	0.460	**0.002**
	Residuals	14	0.113	0.113	—	0.034	—									H:distance	0.268	0.056
	Total	24	0.078	—	—	1.000	—									E:distance	-0.132	0.345
4A Downcore >125 µm	$\delta^{13}C_{org}$	1	1.531	1.531	12.95	0.188	**0.001**	Cluster	3	0.031	0.010	2.200	0.111	Cluster	<<**0.01**	S: $\delta^{13}C_{org}$	0.370	**0.003**
	CN	1	1.265	1.265	10.69	0.155	**0.001**	Residuals	31	0.144	0.004	—				H: $\delta^{13}C_{org}$	0.096	0.429
	Cluster	1	0.435	0.434	3.67	0.053	**0.006**									E: $\delta^{13}C_{org}$	-0.291	**0.014**
	$\delta^{13}C_{org}$×CN	1	0.201	0.201	1.70	0.025	0.096									S:CN	0.013	0.919
	$\delta^{13}C_{org}$×Cluster	1	1.079	1.079	9.12	0.132	**0.001**									H:CN	-0.210	0.078
	CN×Cluster	1	0.387	0.387	3.27	0.047	**0.004**									E:CN	-0.213	0.073
	$\delta^{13}C_{org}$×CN×Cluster	1	0.071	0.071	0.60	0.009	0.760											
	Residuals	27	3.193	0.118	—	0.391	—											
	Total	34	8.163	—	—	1.000	—											
UL-5 Downcore > 250 µm	$\delta^{13}C_{org}$	1	0.561	0.561	11.701	0.196	**0.001**	Cluster	1	0.045	0.045	7.820	**0.015**	Cluster	<<**0.01**	S: $\delta^{13}C_{org}$	-0.075	0.620
	CN	1	0.669	0.669	13.940	0.233	**0.001**	Residuals	23	0.132	0.006	—				H: $\delta^{13}C_{org}$	0.354	**0.008**
	Cluster	1	0.509	0.509	10.607	0.177	**0.001**									E: $\delta^{13}C_{org}$	0.402	**0.002**
	$\delta^{13}C_{org}$×CN	1	0.020	0.020	0.414	0.007	0.715									S:CN	-0.111	0.464
	$\delta^{13}C_{org}$×Cluster	1	0.046	0.046	0.960	0.016	0.422									H:CN	-0.458	**0.001**
	CN×Cluster	1	0.077	0.077	1.608	0.027	0.219									E:CN	-0.363	**0.007**
	$\delta^{13}C_{org}$×CN×Cluster	1	0.029	0.029	0.595	0.010	0.637											
	Residuals	20	0.959	0.048	—	0.334	—											
	Total	27	2.869	—	—	1.000	—											

*based on 999 permutations. ‡based on 10,000 iterations. **Bold** indicates significance at the 95% confidence interval

Table S2.1 Foraminifera counts >125µm in coretop sediments

Sample ID (site-core_cm interval)	*A. parkinsoniana*	*A. tepida*	*A. paucicloculata*	*E. poeyanum*	*E. gunteri*	*E. galvestonense*	*E. lanieri*	*E. discoidale*	*H. germanica*	*D. aguayoi*	*T. trigonula*	*T. linneiana*	*Triloculina sp.*	*Q. bicarinata*	*Q. linneiana*	*Q. laevigata*	*H. concentrica*	*Rosalina sp.*	*C. involvens*	*Bolivina sp.*	*L. proteus*	*A. angulatus*	*Agglutinated*	*Other*	Sum	Sediment (mg)	S	H	E	$\delta^{13}C_{org}$	CN
2-SPC_1-2	32	4	0	16	27	0	0	0	0	0	5	0	0	2	2	178	0	0	0	0	0	0	77	0	343	13.9	9	1.41	0.46	-23.74	9.5
2-SPC_3-4	42	6	0	19	35	0	0	0	5	0	4	0	0	0	0	153	0	0	0	0	0	0	50	0	314	17.4	8	1.52	0.57	-22.92	9.5
2-SPC_5-6	30	2	0	29	30	0	0	0	5	0	6	1	0	0	0	143	0	0	0	0	0	0	59	0	305	23.9	9	1.55	0.52	-22.92	9.5
5-SPC_0-2	49	6	1	17	24	5	0	0	9	0	1	0	0	5	2	97	0	0	0	0	0	0	88	0	304		12	1.77	0.49	-22.46	9.9
5-SPC_2-4	75	8	0	39	55	0	0	0	13	0	2	0	0	8	1	171	0	0	0	0	0	0	60	0	432		10	1.72	0.56	-22.46	9.9
1A-1P-1_5-6	59	9	1	35	63	0	0	0	19	0	7	2	0	0	0	133	0	0	0	0	0	0	35	0	363	29	10	1.79	0.60	-22.92	10.3
1A-1P-1_10-11	76	8	1	46	33	0	0	0	1	0	6	0	0	0	0	83	0	0	0	0	0	0	48	0	302	34.3	9	1.73	0.63	-22.14	10.3
FIC15-1_3-4	39	20	0	34	31	0	0	0	7	0	2	0	0	0	0	189	0	0	0	0	0	0	37	0	359	17.2	8	1.51	0.57	-22.14	8.9
FIC15-1_4-5	37	10	0	40	34	0	0	0	6	0	2	0	0	0	0	161	0	0	0	0	0	0	36	0	326	18.9	8	1.54	0.59	-23.64	8.9
FIC15-1_5-6	65	16	0	28	30	0	0	0	5	0	2	0	0	0	0	142	0	0	0	0	0	0	25	0	313	21.3	8	1.58	0.61	-23.64	8.9
FIC15-5_1-2	78	6	0	49	48	7	0	0	1	0	42	0	0	5	6	87	0	0	1	0	0	0	0	0	330	103.6	11	1.84	0.57	-23.64	11.1
FIC15-5_3-4	169	12	0	64	124	0	0	0	13	0	157	1	0	0	12	62	0	0	2	0	0	0	1	0	617	12.1	11	1.77	0.53	-21.32	11.1
FIC15-5_5-6	107	4	0	38	85	0	0	0	3	0	74	0	1	0	5	27	1	0	0	0	0	0	0	0	345	17.3	10	1.67	0.53	-21.32	11.1
FIC15-6_2-3	68	4	2	33	57	0	0	0	8	0	85	10	4	0	5	28	1	1	0	2	0	0	1	0	309	5.1	15	1.96	0.47	-21.32	10.8
FIC15-6_3-4	85	8	0	33	64	0	0	3	14	0	71	5	0	1	0	18	1	0	1	0	0	0	0	1	305	4.8	13	1.86	0.49	-21.59	10.8
FIC15-6_5-6	222	0	0	23	168	0	0	1	0	0	65	0	0	1	0	9	0	0	0	0	0	0	0	0	489	8.5	7	1.24	0.49	-21.59	10.8
FIC15-7_2-3	85	5	0	42	64	0	0	0	12	0	81	0	0	2	0	22	0	0	0	0	0	0	1	0	314	8.8	9	1.72	0.62	-21.59	10.6
FIC15-7_3-4	75	4	0	41	67	0	0	0	8	0	74	6	1	2	3	15	0	0	0	0	0	0	0	8	304	14.2	12	1.86	0.54	-21.77	10.6
FIC15-7_5-6	70	5	0	33	72	0	0	0	7	0	72	3	0	0	0	21	0	0	0	0	0	0	0	17	300	20.1	9	1.82	0.68	-21.77	10.6
FIC15-8_2-3	171	11	0	52	43	0	0	0	5	0	74	4	0	0	0	36	0	0	0	0	0	0	0	17	413	27.7	9	1.71	0.61	-21.77	10.4
FIC15-8_3-4	175	0	0	9	54	0	0	0	1	0	46	0	0	0	0	28	0	0	0	0	0	0	9	10	332	13.3	8	1.43	0.52	-22.00	10.4

FIC15-8_5-6	123	8	0	43	31	0	0	0	9	0	34	0	0	1	2	57	0	0	0	0	0	0	22	0	330	20.4	10	1.81	0.61	-22.00	10.4
7A-1P-1_2-3	126	1	0	14	100	0	0	0	1	0	35	0	0	0	0	19	0	2	2	0	0	0	0	6	306	11.6	10	1.47	0.44	-22.00	11.5
7A-1P-1_7-8	182	7	0	55	159	7	0	0	16	0	55	4	0	0	1	14	0	3	1	0	0	0	0	0	504	13.7	12	1.64	0.43	-20.89	11.5
8A-1P-1_3-4	87	11	0	31	54	0	0	0	14	0	38	5	0	0	0	57	0	0	0	0	0	0	26	0	323	25	9	1.95	0.78	-20.89	10.4
8A-1P-1_7-8	96	6	0	29	55	0	0	0	6	0	43	0	0	3	0	51	0	0	0	0	0	0	17	0	306	25.8	9	1.83	0.69	-22.03	10.4

S = richness, H = diversity, E = evenness from Murray (2006) and references therein. Genera names are given in Table 2.3. *Trochammina macrascens* is found only in core FIC15-7 and grouped with Agglutinated.

Table S2.2 Foraminifera counts >125µm in downcore sediments

Sample ID (site-core_cm interval)	*A. parkinsoniana*	*A. tepida*	*A. pauciloculata*	*E. poeyanum*	*E. gunteri*	*E. galvestonense*	*E. lanieri*	*E. discoidale*	*H. germanica*	*D. aguayoi*	*T. trigonula*	*T. linneiana*	*Triloculina sp.*	*Q. bicarinata*	*Q. linneiana*	*Q. laevigata*	*H. concentrica*	*Rosalina sp.*	*C. involvens*	*Bolivina sp.*	*L. proteus*	*A. angulatus*	*Agglutinated*	*Other*	Sum	Sediment (mg)	S	H	E	$\delta^{13}C_{org}$	CN
4A-1P-1_5-6	35	2	0	50	8	0	0	0	10	0	4	0	0	0	0	187	0	0	0	0	0	0	18	0	314	15.8	8	1.30	0.46	-24.04	8.4
4A-1P-1_12-13	51	6	0	17	14	0	0	0	18	0	0	0	0	0	0	228	0	0	0	0	0	0	14	0	348	9.1	7	1.19	0.47	-24.09	8.1
4A-1P-1_17-18	73	16	0	44	21	0	0	0	0	0	4	0	0	1	0	127	0	0	0	0	0	0	26	0	312	14.5	8	1.60	0.62	-24.15	7.6
4A-1P-1_24-25	128	3	0	23	43	0	0	0	0	0	1	0	0	0	0	58	0	0	0	0	0	0	45	0	301	24.3	7	1.50	0.64	-24.11	7.0
4A-1P-1_27-28	83	2	1	30	47	0	0	0	0	0	0	0	0	0	0	66	0	0	0	0	0	0	77	0	306	13.7	7	1.60	0.71	-24.11	7.1
4A-1P-1_33-34	221	2	4	14	35	0	0	0	0	0	0	0	0	0	0	4	0	0	0	0	0	0	29	0	309	27.3	7	0.99	0.39	-24.05	6.9
4A-1P-1_37-38	175	0	2	13	68	1	0	0	0	0	0	0	0	0	0	5	0	0	0	0	0	0	41	0	305	28.7	7	1.18	0.46	-23.76	7.0
4A-1P-1_45-46	53	1	1	11	24	1	0	0	0	0	6	0	0	0	0	54	0	0	0	0	0	0	162	0	313	26.7	9	1.39	0.45	-23.57	7.9
4A-1P-1_55-56	74	2	1	9	15	6	0	0	0	0	7	0	0	0	0	47	0	0	0	0	0	0	166	0	327	17.3	9	1.40	0.45	-23.27	7.9
4A-1P-1_65-66	183	1	2	15	62	33	0	0	0	0	2	0	0	0	1	26	0	0	0	0	0	0	53	0	378	25	10	1.54	0.46	-23.01	7.9
4A-1P-1_75-76	224	0	3	14	74	80	0	0	0	0	2	0	0	0	1	3	0	0	0	0	0	0	23	0	424	27.8	9	1.34	0.42	-22.27	8.9
4A-1P-1_85-86	159	1	0	16	66	45	0	0	0	0	2	0	0	0	0	19	0	0	0	0	0	0	3	0	311	19.1	8	1.37	0.49	-21.56	9.7
4A-1P-1_95-96	112	1	3	23	61	37	0	0	0	0	12	0	0	0	0	57	0	0	0	0	0	0	3	0	309	14.5	9	1.68	0.60	-21.45	9.3
4A-1P-1_105-106	291	1	1	29	128	68	0	0	0	0	1	0	0	9	0	19	2	0	0	0	0	0	7	0	556	21.9	11	1.38	0.36	-21.44	8.6
4A-1P-1_109-110	256	1	2	5	161	68	0	0	0	0	0	0	0	2	0	4	0	0	0	0	0	0	3	0	502	30.5	9	1.15	0.35	-21.33	8.4
4A-1P-1_120-121	172	1	0	26	108	29	0	0	0	0	2	0	0	0	0	4	0	0	0	0	0	0	1	0	343	49.6	8	1.23	0.43	-21.30	7.8
4A-1P-1_128-129	295	2	0	30	155	46	0	0	0	0	0	0	0	0	0	4	0	0	0	0	0	0	6	0	538	26.5	7	1.17	0.46	-21.24	7.4
4A-1P-1_140-141	178	2	0	119	43	12	1	0	1	0	10	0	0	3	0	9	1	0	0	3	0	0	4	0	386	16.8	13	1.45	0.33	-20.29	7.9
4A-1P-1_145-146	205	1	0	47	30	9	0	0	1	0	0	0	0	1	0	3	2	0	0	8	0	0	7	0	314	14.2	11	1.20	0.30	-19.82	8.4
4A-1P-1_150-151	292	2	0	39	28	10	1	1	3	0	7	1	0	0	1	1	2	0	0	1	0	0	0	0	389	26.5	14	0.99	0.19	-19.27	9.2
4A-2B-1_2-3	177	0	0	27	83	13	0	0	1	0	10	0	0	2	0	0	0	0	0	1	0	0	0	0	314	25.8	8	1.20	0.41	-19.38	8.9

4A-2B-1_10-11	290	0	0	16	28	9	0	0	1	0	0	0	0	0	0	0	0	0	0	0	0	1	0	0	345	46.3	6	0.62	0.31	-19.43	8.2
4A-2B-1_20-21	172	3	0	308	28	4	1	1	9	0	22	2	17	2	26	22	0	0	0	29	0	0	2	0	648	28.1	16	1.62	0.32	-19.61	7.8
4A-2B-1_30-31	185	0	0	23	18	5	0	0	1	0	0	0	0	0	0	1	0	0	0	0	0	0	0	0	233	30.5	6	0.74	0.35	-19.72	7.3
4A-2B-1_39-40	49	4	0	123	12	4	0	2	3	0	41	3	13	1	12	23	2	0	0	13	0	1	1	0	307	10	17	1.97	0.42	-19.64	7.5
4A-2B-1_45-46	37	3	1	132	18	8	0	0	1	0	27	1	15	4	19	5	3	0	1	12	0	0	1	0	288	9.7	17	1.90	0.40	-19.59	7.8
4A-2B-1_55-56	63	2	1	81	8	2	0	0	0	0	69	2	8	2	44	15	1	1	2	11	0	0	0	0	312	16.6	16	1.95	0.44	-19.38	8.2
4A-2B-1_65-66	178	3	2	75	24	10	0	0	2	0	17	0	4	0	22	5	0	0	0	0	0	0	0	0	342	29.5	11	1.50	0.41	-19.50	8.6
4A-2B-1_71-72	271	1	0	9	11	12	0	0	0	0	0	0	0	0	0	0	0	0	0	0	0	0	1	7	312	134	7	0.59	0.26	-20.34	9.0
4A-2B-1_78-79	327	8	8	108	57	55	4	1	0	16	4	1	0	1	1	5	0	0	0	0	7	17	2	0	622	0	17	1.50	0.26	-22.25	13.6
4A-2B-1_83-84	44	0	0	78	2	0	0	0	0	79	8	0	0	0	2	0	0	0	0	0	0	0	0	28	241	126.1	7	1.12	0.44	-23.54	16.6
4A-2B-1_90-91	46	14	0	37	0	0	0	0	0	61	21	0	0	0	0	7	0	0	0	0	0	0	0	70	256	129.1	7	1.41	0.58	-25.05	20.8
4A-2B-1_99-100	23	9	0	24	0	0	0	0	0	141	38	0	0	0	0	3	0	0	0	0	0	0	0	12	250	123.4	7	1.05	0.41	-26.84	26.4
4A-2B-1_105-106	1	2	0	2	0	0	0	0	0	293	15	0	0	0	0	43	0	0	0	0	0	0	1	30	387	70.8	8	0.65	0.24	-27.25	24.3
4A-3L-1_3-4	19	3	0	2	0	0	0	0	0	225	13	0	0	0	0	9	0	0	0	0	0	0	0	4	275	51.3	7	0.59	0.26	-27.96	20.2

S = richness, H = diversity, E = evenness from Murray (2006) and references therein. Genera names are given in Table 2.3. *Borelis pulchra* is found only below 4A-2B-1_65-66 and grouped with *Other*.

Table S2.3 Foraminifera counts >250µm in UL-5 downcore sediments

Sample ID (site-core_cm interval)	*Ammonia spp.*	*Elphidium spp.*	*Triloculina* + *Quinqueloculina*	*L. proteus*	*A. angulatus*	*Other*	Sum	Sediment (mg)	S	H	E	$\delta^{13}C_{org}$
UL-5_65.25	161	93	13	0	0	47	314	2150	4	1.12	0.77	-23.22
UL-5_71	149	70	18	1	0	21	259	2960	5	1.08	0.59	-25.54
UL-5_75.5	149	116	30	0	0	14	309	2370	4	1.09	0.74	-23.45
UL-5_80	101	99	22	1	0	3	226	2950	5	1.03	0.56	-23.70
UL-5_85.5	149	79	8	0	0	21	257	3060	4	0.99	0.67	-21.68
UL-5_91.5	111	77	36	0	0	20	244	3330	4	1.21	0.84	-20.62
UL-5_96.5	80	81	61	1	0	10	233	2800	5	1.24	0.69	-20.37
UL-5_102	64	102	86	0	0	4	256	3150	4	1.14	0.79	-20.99
UL-5_105.5	47	69	142	0	0	3	261	2950	4	1.04	0.71	-21.53
UL-5_108.5	45	83	107	0	0	4	239	3600	4	1.11	0.76	-21.13
UL-5_111.5	66	127	103	0	0	3	299	2900	4	1.11	0.76	-21.03
UL-5_115.5	47	92	78	0	0	1	218	2810	4	1.09	0.74	-19.75
UL-5_120.5	34	129	74	3	0	1	241	3960	5	1.05	0.57	-21.52
UL-5_125.5	19	105	114	0	0	0	238	2610	3	0.92	0.83	-22.92
UL-5_130.5	45	105	82	1	0	3	236	2720	5	1.12	0.61	-21.22
UL-5_135.5	41	110	75	0	0	1	227	2880	4	1.05	0.71	-21.47
UL-5_140.5	57	155	42	1	0	3	258	3290	5	1.01	0.55	-24.48
UL-5_145.5	58	96	50	0	0	0	204	2930	3	1.06	0.96	-20.90
UL-5_150.5	33	76	57	0	0	4	170	2990	4	1.13	0.78	-21.81
UL-5_156.25	18	108	65	0	0	0	191	3650	3	0.91	0.83	-20.58
UL-5_161.75	6	147	49	0	0	0	202	2620	3	0.68	0.66	-22.20

UL-5_167.5	6	164	32	0	0	0	202	2340	3	0.57	0.59	-21.56
UL-5_172.5	11	205	3	0	0	0	219	3920	3	0.27	0.44	-22.79
UL-5_178.5	11	181	4	2	0	0	198	1090	4	0.37	0.36	-26.09
UL-5_183.5	7	78	0	0	0	0	85	430	2	0.28	0.66	-28.98
UL-5_189.5	10	87	5	3	0	0	105	1740	4	0.63	0.47	-25.04
UL-5_193.5	2	99	13	3	0	0	117	1350	4	0.55	0.43	-24.42
UL-5_199.5	6	101	24	121	71	0	323	2010	5	1.33	0.76	-26.15

S = richness, H = diversity, E = evenness from Murray (2006) and references therein. Genera names are given in Table 2.3.

Chapter 3

A 5,000-year paleosalinity record from Celestun Lagoon (Yucatan, Mexico): separating geomorphic and climatic controls on groundwater discharge

3.1 Abstract

Paleo-precipitation reconstructions from lakes and speleothems in the Yucatan Peninsula, Mexico, disagree on the frequency and magnitude of Holocene changes in precipitation. We reconstruct paleosalinity in Celestun Lagoon (northwestern peninsula), which sources water from the regional water table, during the Late Holocene using isotopes ($\delta^{18}O$, $^{87}Sr/^{86}Sr$) and trace metals (Sr, Ba) incorporated into benthic foraminifera *Ammonia parkinsoniana*. Three water sources (seawater SW, brackish groundwater BW, and fresh groundwater FW) were identified from $\delta^{18}O$ and $^{87}Sr/^{86}Sr$, and mixing models indicate source contributions in the northern lagoon changed from 64%-34%-2% SW-BW-FW 4,000 years before present (BP) to 20%-51%-29% at present. Present-day correlations between salinity and Sr/Ca (R^2 = 0.607) and Ba/Ca (R^2 = 0.678) in *A. parkinsoniana* result in paleosalinities of 5 to10 at 5,300 BP, 33 at 4,400 BP, and 21 at present, reflecting change in source waters likely driven by sea-level rise and subsequent barrier island formation, restricting seawater mixing into the lagoon. Detrending paleosalinity reveals salinity oscillations of ±4 units contemporaneous with North Atlantic Bond Events and southward shift of tropical moisture. Paleosalinity peaks temporally match known drought events at

3,500 BP, 2,400 BP and 1,300 suggesting that these events were peninsula-wide, impacting the regional groundwater table that sources spring discharge to the field site. Despite abundance of coastal lagoons in the Yucatan region, coastal lagoon sediments are untapped archives for paleoclimatology and paleoceanography that link regionally integrated rainfall to large-scale atmospheric perturbations, but coastal geomorphic evolution must be known to extract the climatic signal.

3.2 Introduction

The past decade of paleoclimate research in the Caribbean and Gulf of Mexico region has advanced our understanding of Holocene climate variability in the region. Predictive understanding of regional climate change impacts on groundwater resources is especially important for areas like the Yucatan Peninsula which derives municipal water sources nearly exclusively from the regional water table (Escolero et al., 2000). However, climate reconstructions based on pollen, microfossils, isotopes, and trace metals reveal considerable differences in the timing, magnitude, and locale of droughts (Akers et al., 2016; Bhattacharya et al., 2017; Douglas, et al., 2016a; Douglas, 2016b; van Hengstum et al., 2010; Medina-Elizalde et al., 2016; Wahl et al., 2014). A continued difficulty with these proxy archives is deciphering if records represent local conditions at the study site or whether they integrate regional precipitation signals that express the combined effects of ocean and atmospheric climate drivers (e.g., Intertropical Convergence Zone, Walker Circulation, and

Atlantic Meridional Overturning) (Hodell et al., 2001; Haug et al., 2001; Giddings and Soto, 2003; Méndez and Magaña, 2010; Douglas et al., 2016b; Bhattacharya et al., 2017). Coastal lagoon sediment archives represent potential sources of climate records in the Yucatan Peninsula, as regionally integrated precipitation impacts these coastal lagoons through groundwater springs. However, coastal lagoon sedimentary archives remain relatively unexplored despite their abundance around the region's coastlines (Peros et al., 2015).

The Yucatan Peninsula has few surface rivers due to the porous karst geology; thus, rain-fed groundwater percolating into the extensive caves and conduits flows toward the coasts, discharging near the coastline and in coastal lagoons (Perry et al., 2003; Gonneea et al., 2004; Young et al., 2008; Bauer-Gottwein et al., 2011). Groundwater discharge seeps and springs create estuarine-like conditions in coastal lagoons in which salinity oscillates with precipitation amount (Herrera-Silveira, 1994). Authigenic and biogenic carbonate sediments in these lagoons record the lagoon water hydrochemistry which is controlled by the groundwater discharge and, hence, represents an integrated record of rainfall. A key assumption for interpreting sedimentary records of these systems, however, is that lagoon salinity change reflects absolute change in groundwater discharge rather than relative change in mixing between source waters. While this is generally true on short (years to decades) timescales, on millennium timescales this assumption is more tenuous because coastal lagoons will also be impacted by sea-level rise and coastal geomorphic change (e.g.,

barrier island formation; (Peros et al., 2015; Lowery and Rankey, 2017) which can change a lagoon's shape and thus the relative proportions of groundwater and seawater mixing into the lagoon. It is therefore challenging but necessary to decipher controls on lagoon paleosalinity in order to separate the regional climatic signal (absolute freshwater inputs) from the local geomorphic signal (relative inputs). In turn, this requires use of multiple biological and geochemical proxies of paleoenvironmental change in order to interpret coastal paleosalinity (Chapter 2).

Here we present a 5,000-year paleosalinity record from Celestun Lagoon in the northwestern corner of the Yucatan Peninsula (Figure 3.1a) and compare this record to regional hydroclimate records and known changes in regional atmospheric and oceanic circulation. Only a few paleoclimate records exist for the northwestern peninsula (e.g., sinkhole lakes and speleothems), and these existing records may be affected by local watershed hydrology, particularly due to sedimentation and isolation from the regional water table (B. W. Leyden et al., 1996; Whitmore et al., 1996; Hodell et al., 2005; Medina-Elizalde et al., 2010). In contrast, salinity (and thus paleosalinity) in Celestun Lagoon derives from groundwaters spanning much larger aquifer of the western half of the Yucatan Peninsula (Perry et al., 2003; Bauer-Gottwein et al., 2011). Previous work at this site established that barrier island formation is a primary driver of paleoecologic change, including paleosalinity, which results in long-term freshening due to reduced relative mixing between groundwater and seawater (Chapter 2). Research presented here expands on prior work by

reconstructing paleosalinity more precisely with trace metal proxies and removing geomorphically-induced (relative) freshening from the absolute freshening caused by climate variability. Because the northwestern Yucatan Peninsula supports the largest city of the peninsula (Merida with population exceeding 600,000; Escolero et al., 2000) and a rapidly growing ecotourism industry that may strain fragile water resources, understanding regional-scale changes in the water table during periods of past climate change is critically important for future resource management while also broadly advancing efforts in regional-scale modeling of future change in climate and hydrologic cycling.

3.2.1 Regional climate and hydrogeology

Climate in the Yucatan region is semi-arid tropical with minimal seasonal variation in temperature but notable seasonality in precipitation. Most rain falls between June and October during the wet season driven by the north-south oscillation of the Intertropical Convergence Zone (ITCZ), although other ocean-atmosphere circulation patterns also affect precipitation (e.g., Walker Circulation in the Pacific and the Atlantic Bermuda high pressure zone)(Herrera-Silveira, 1994; Hodell et al., 2001; Haug et al., 2001; Giddings and Soto, 2003). Rainfall over the peninsula ranges from 600 mm/yr in the northern coastal region to 1,600 mm/yr in the southern highlands (Bauer-Gottwein et al., 2011; Douglas et al., 2016b).

Paleocene to Miocene-age carbonate rock comprises the Yucatan Platform with evaporites occurring in central and western regions of the peninsula (Weidie, 1985; Perry et al., 2003; Perry et al., 2009a). Holocene coastal plains lie along the north and western peninsula coasts, and longshore sediment transport continues to build coastal dune fields (Cuevas et al., 2013; Lowery and Rankey, 2017). There are few rivers in the region, and precipitation rapidly percolates into the groundwater aquifer (Perry et al., 2003; Bauer-Gottwein et al., 2011). Groundwater flows are intercepted by structural features, including the Cretaceous-age Chicxulub impact crater and associated Ring of Cenotes (sinkhole lakes) in the north, the Holbox Fracture Zone in the east, and the Ticul Fault Zone in the south-central regions of the peninsula (Bauer-Gottwein et al., 2011). These structures direct groundwater flow to the coast, where it discharges through groundwater springs and seeps. Such springs are abundant in Celestun and Dzilam Lagoons in the northwestern corner of the peninsula (Young et al., 2008; Bauer-Gottwein et al., 2011). Based on oxygen and hydrogen isotopes of water from hurricane rainfall pulses, the residence time of groundwater in the platform is on the order of months (Perry et al., 2003), resulting in predictable seasonal and interannual salinity change in Celestun lagoon which depend on rainfall amount and timing (Figure 3.1b).

Geochemical investigations of groundwater reveal characteristic signatures attributed to water-rock interactions within the limestone aquifer. Groundwaters passing through the limestone and evaporite deposits have ion concentrations that are

relatively higher ([Sr^{2+}],[Ba^{2+}], [SO_4^{2-}]) or lower ([Mg^{2+}], [Cl^-]) than seawater as well as isotope values (^{18}O, $^{87}Sr/^{86}Sr$, ^{223}Ra, ^{224}Ra, ^{226}Ra, ^{228}Ra) distinct from seawater (Young et al., 2008; Stalker et al., 2014). Mass balance and mixing-models of groundwater inputs to coastal waters yield present day groundwater discharge estimates of 45 ± 20 $m^3\ m^{-1}\ d^{-1}$ along the north and west coasts of the Yucatan (Perry et al., 2002; Perry et al., 2009a; Null et al., 2014; Gonneea et al., 2014), in agreement with estimated discharge range of 26-35 $m^3\ m^{-1}\ d^{-1}$ on the east coast (Bauer-Gottwein et al., 2011). Depending on the catchment area, coastal spring discharge volumes represent 17-70% of recharge provided from inland rainfall (Bauer-Gottwein et al., 2011).

Because groundwater discharge carries chemical and isotopic signatures that are distinct from those of seawater, incorporation of major ions into biogenic carbonates close to spring discharge sites can serve as tracers of groundwater discharge to the coast and, hence, reflect precipitation farther inland.

3.2.2 Geochemical proxies

Abundant benthic foraminifera inhabit Celestun Lagoon (Chapter 2) and may serve as potential archives for the water chemistry in which they lived. Temperature, pH, calcite saturation state, and carbonate ion concentration affect the incorporation of metals into biogenic carbonates, and these effects are species-specific. The benthic

species we used for analysis is *Ammonia parkinsoniana* (Figure 3.1c, molecular type T9 from Hayward et al., 2004) due to the abundance of this species throughout most of the sediment record we recovered.

3.2.3 Trace metal ratios in the genus *Ammonia*

Ammonia benthic foraminifera typically live in shallow, brackish nearshore environments and are adapted to fluctuating temperature, salinity, and carbonate chemistry characteristic of these environments (Sen Gupta, 1999). Brackish waters discharging in the lagoon have concentrations of [Mg], [Sr], and [Ba] different from seawater, therefore Mg/Ca, Sr/Ca, and Ba/Ca in the foraminifera shells could serve as potential proxies for climate-induced changes in groundwater input to the lagoon and hence in lagoon salinity and water chemistry.

Mg/Ca is used as a temperature proxy with several recent studies focusing on *Ammonia*. Toyofuku et al. (2011) observed an exponential increase in Mg/Ca from 1 to 3 mmol/mol over a temperature range of 10 to 28 °C in *Ammonia 'beccarii'* (author's quotation) and observed no effect of salinity on Mg/Ca ratios. Dissard et al. (2010a) and Geerken et al. (2018) found that both higher temperature and higher salinity resulted in higher Mg/Ca ratios of *A. tepida*. Raitzsch et al. (2010) observed a relationship between saturation state and Mg/Ca of *A. tepida*, and Mewes et al. (2015) determined that Mg/Ca and Sr/Ca are positively correlated because these elements

compensate each other for strain within the calcite mineral lattice. These lab-based culture studies demonstrate multiple controls on the variability of Mg/Ca in *Ammonia*.

Sr/Ca is often studied alongside Mg/Ca. Early observations suggested temperature has little impact on Sr/Ca of benthic foraminifera, but Sr/Ca ratios decreased in deep-sea specimens with increasing depth, suggesting the influence of pressure or saturation state (Rosenthal et al., 1997). In shallow coastal waters, Sr/Ca in *A. tepida* calcite was not impacted by changes in saturation state when salinity was held at marine values (Raitzsch et al., 2010; Dueñas-Bohórquez et al., 2011). Dissolved inorganic carbon (DIC), however, positively correlates with Sr/Ca calcite in *A. tepida* over a salinity range of 20-33 (Dissard et al., 2010b; Keul et al., 2017). Sr/Ca correlation with DIC was attributed to the ability of *Ammonia* to moderate internal saturation state by removing calcium, thereby increasing the Sr/Ca ratio of calcite (Keul et al., 2017). Such a mechanism would explain the generally low trace metal to calcium ratios of *Ammonia* compared to other genera (often an order of magnitude smaller) (Raitzsch et al., 2010; Diz et al., 2012a). Despite these various geochemical controls, Sr/Ca of *Ammonia* calcite generally reflects ambient water [Sr]/[Ca] (Langer et al., 2016) and correlates well with water salinity over a range of salinity, temperature, and DIC conditions (Dissard et al., 2010a; Diz et al., 2012b; Geerken et al., 2018).

Barium to calcium ratios (Ba/Ca) in planktic foraminifera have been used to reconstruct open ocean alkalinity (Lea and Spero, 1994; Henderson, 2002). Few field studies have focused on Ba/Ca in *A. tepida* or *A. parkinsoniana*, but available data suggests incorporation of [Ba] into *Ammonia* sp. calcite is dependent only on ambient [Ba] concentrations and not affected by pH, temperature, or salinity (Havach et al., 2001; Hönisch et al., 2011; de Nooijer et al., 2017). Although open seawater Ba concentrations may have changed over time, because Ba is enriched in estuaries, and particularly in waters of the Yucatan Coast (Coffey et al., 1997; Gonneea et al., 2014), changes in seawater Ba concentrations relative to local groundwater derived Ba contributions are likely small, so Ba/Ca of *A. parkinsoniana* is expected to be a reliable groundwater discharge tracer for Celestun Lagoon.

3.2.4 Strontium isotopes

The $^{87}Sr/^{86}Sr$ ratio recorded in carbonates represents the ratio in the water in which it formed. The long residence time (2 million years) of strontium in seawater means that both the concentration (86 µM) and radiogenic strontium isotopic composition (0.70916) of the modern oceans have not changed much throughout the Holocene (Peros et al., 2007b; Beck et al., 2013). Surface water and groundwaters from terrestrial sources, however, acquire $^{87}Sr/^{86}Sr$ values from interaction with rocks. Terrestrial waters in the Yucatan typically have high [Sr^{2+}] concentrations (> 200 µmolar) and low $^{87}Sr/^{86}Sr$ ratios (around 0.70800 from Miocene carbonates)(Perry et

al., 2009a). Thus, $^{87}Sr/^{86}Sr$ can be used to calculate the proportions of seawater and groundwater in coastal estuaries (Ingram and Sloan, 1992; Reinhardt et al., 1998; Peros et al., 2007b). In Celestun Lagoon, multiple groundwater types discharge to the system, resulting in a three-endmember mixing regime for strontium concentrations and isotopes (Young et al., 2008; Stalker et al., 2014).

3.2.5 Oxygen isotopes

The oxygen isotope value of calcite ($\delta^{18}O_c$) depends on the temperature and oxygen isotope value of water ($\delta^{18}O_w$) in which calcite forms (Urey et al., 1951). Ambient $\delta^{18}O_w$ values, in turn, are affected by several global and regional processes, and detailed reviews of known controls can be found elsewhere (Leng and Marshall, 2004; Ravelo and Hillaire-Marcel, 2007). On glacial-interglacial timescales, change in ice volume affects the global ocean $\delta^{18}O_w$ value, but this effect is negligible for the tropics during the Late Holocene (last 5,000 years) when ice volume did not change appreciably (Lambeck et al., 2014). Along the north coast of the Yucatan Peninsula, the primary controls on lagoon water $\delta^{18}O_w$ are coastal upwelling (relatively high $\delta^{18}O_w$), balance of evaporation and precipitation (E/P ratio to which $\delta^{18}O_w$ responds), and mixing of isotopically distinct water sources, e.g., seawater and groundwater (relatively high and low $\delta^{18}O_w$, respectively). The northwestern region of the Yucatan has the highest E/P ratio on the peninsula (Bauer-Gottwein et al., 2011) which promotes $\delta^{18}O_w$ values up to +4.0 ‰ in surface waters. However, the residence time

of waters affected by seasonal changes in E/P is on the order of months for coastal lagoons (Herrera-Silveira, 1994) and ephemeral compared to the persistent input of distinct groundwater sources. Thus, mixing of seawater and groundwater will impact the $\delta^{18}O_w$ value of lagoon water and hence foraminifera in Celestun.

The other primary control on $\delta^{18}O_c$ is temperature. However, tropical seasonal and interannual temperature variability is small relative to precipitation effects (Curtis et al., 1998). Temperature inversely correlates with $\delta^{18}O_c$ of *Ammonia 'beccarii'* in waters of 10-27 °C (Toyofuku et al., 2011), but in the smaller temperature range of Yucatan coastal waters (25-30 °C) the effect is likely muted and contributes less to the $\delta^{18}O_c$ of *A. parkinsoniana* than the variability related to source waters. Biological or 'vital' effects do not appear significant in *Ammonia* which calcifies in near-equilibrium with ambient water (Toyofuku et al., 2011). Salinity itself does not appear to affect the incorporation of $\delta^{18}O$ into calcite of *Ammonia* sp. (Toyofuku et al., 2011), thus $\delta^{18}O_c$ should reflect ambient salinity conditions.

3.2.6 Bias and taphonomic alteration

Life-modes of *Ammonia* may bias the geochemical proxy record, and post-depositional processes further influence proxy values in calcite. First, the seasonality of an environment (sunlight, temperature, groundwater flux and associated carbonate chemistry, and food availability) influence timing and rates of calcification over the

lifespan of *Ammonia* in mid-latitude waters. Diz et al. (2009) note that these species tend to calcify primarily during periods of low salinity and moderate temperature. Preferential calcification during the Yucatan wet season (June – October) would bias the geochemical record in favor of wetter conditions. *A. parkinsoniana* lives for several months (Murray, 2006), and additional research is needed to determine if seasonality in calcification affects the Yucatan lagoon records. Bioturbation, which can be intense in coastal zones, mixes sediments and decreases the temporal resolution of geochemical proxies (Peros et al., 2007b), and storm transport may bring geochemically distinct (seawater) foraminifera into brackish regimes of inner lagoons (Hippensteel and Martin, 1999). Such storm events are also accompanied by changes in faunal assemblage, however, and thus can be identified (Chapter 2; Collins et al., 1999), and tidal transport is likely not a problem for the low tidal regime of the Yucatan (Young et al., 2008; Diz et al., 2009).

Dissolution of calcite in high-pCO_2 porewaters preferentially dissolves some elements like Mg from tests (Martin & Lea, 2002; McCorkle et al., 1995), so dissolution alteration of geochemical signatures must be carefully considered. Much of the sediment on the Yucatan coast is authigenic and biogenic carbonate (Lowery and Rankey, 2017), suggesting a robust buffering ability against dissolution within coastal sediments. We also did not note dissolution in any fossil specimens which were smooth and resembled modern, pristine specimens.

3.3 Materials and methods

3.3.1 Field site

Celestun Lagoon is a long and narrow (21.2 km by 2.4 km) shallow (0.5 to 3 m) estuary on the coast of the northwestern Yucatan Peninsula, Mexico (Figure 3.1a). A series of accreting dune ridges protect the lagoon from ocean waves, and the lagoon interior is characterized by fine carbonate muds and abundant calcareous mollusks and foraminifera (Lowery and Rankey, 2017). Vegetation consists of red and black mangroves (*Rhizophora mangle* and *Avicennia germinans*, respectively) fringing the lagoon edges, and brackish water-tolerant seagrass beds (*Halodule wrightii, Ruppia mexicana*) along the lagoon channel (Herrera-Silveira et al., 1998). Groundwater springs discharge brackish water (salinity 9 to 21) predominantly in the northern and central lagoon, creating a persistent but seasonally variable salinity gradient (Herrera-Silveira, 1996; Gonneea et al., 2004). At least two types of groundwater have been identified in the lagoon based on trace metal and ion concentrations and radium activity, although discharge amounts of each type are difficult to constrain (Young et al., 2008; Stalker et al., 2014). Peak seasonal rainfall precedes peak groundwater discharge by about one month (Perry et al., 2002), as shown in Figure 3.1b. Lagoon water residence time varies seasonally between < 150 days to > 280 days (Herrera-Silveira et al., 1998), although recent coast-wide discharge measurements (25 to 40

m^3 m^{-1} day^{-1}) suggest a residence time between 37 and 60 days for Celestun Lagoon (Bauer-Gottwein et al., 2011; Gonneea et al., 2014).

3.3.2 Field methods

Sediment and water samples were taken on three occasions (May 2006, June 2009, and May 2015) at approximately similar sample stations, though not all stations were sampled in each expedition (Figure 3.1a). *In situ* water temperature and salinity were measured with a Yellow Springs Instruments model 63 handheld sonde. Water samples were filtered through 0.45 µm filters into acid-washed plastic bottles for analysis of oxygen and strontium isotope and trace metals. Short push cores (n = 28, mean depth = 30 cm) were collected along the length of the lagoon (Figure 3.1a) and immediately extruded in 2 cm intervals for chronological and foraminiferal sub-sampling. Longer sediment cores (n = 6, max depth = 269 cm) were collected in 1.5 m sections using piston, Bolivia, and Livingstone corers (LacCore, University of Minnesota; Supplemental Table S3.1). Long cores were halved, imaged, and stored at 4 °C at LacCore. Sediments were sub-sampled every 2 to 5 cm and split into aliquots for radiocarbon dating and foraminiferal trace metal analysis.

3.3.3 Chronology

Identifiable terrestrial macro-organics (seeds, roots, and leaves) were picked, dried, and analyzed for radiocarbon via Accelerator Mass Spectrometry at Lawrence Livermore National Labs (Livermore, CA, USA). Bulk homogenized 10 mL sediment samples from the upper 30 cm of cores were used to determine lead-210 activity in high purity germanium (HPGe) well detector (Princeton Gamma Tech Instruments, Inc.) at the US Geological Survey Coastal Science Center (Santa Cruz, CA, USA) using established methods (Swarzenski, 2014) and reference materials (RGU-1, RGTh-1, and IAEA-300). The slope of natural log(^{210}Pb) vs. depth yields sediment accretion rates which were corrected for 5% compaction (Gonneea et al., 2004). Bayesian accumulation models (rBacon v. 2.3.8) incorporating calculated accretion rates and ^{14}C ages were used to develop the age-depth models of sediment cores following the method Blaauw and Christen (2011). Core 7A age model (southern lagoon near the ocean, Figure 3.1a) was derived from ^{14}C data in an adjacent core (6A), and the core 2A age model was derived from ^{14}C measurements in core 4A (Table 3.1) which was matched to appropriate depths in core 2A using scandium peaks from X-ray fluorescence (Supplemental Figure S1). Scandium presented the best signal-to-noise ratio of the elements measured in bulk sediment.

3.3.4 Analytical methods

Water samples were split into aliquots for $\delta^{18}O_w$ analysis and $^{87}Sr/^{86}Sr$ isotope and trace metal analysis at the University of California Santa Cruz. Oxygen isotopes were

determined by equilibrium exchange of the water oxygen with 0.3% carbon dioxide gas analyzed on a ThermoFinnigan Delta Plus XP isotope ratio mass spectrometer. Lab-calibrated standards yield precision of ±0.06‰, and results are reported relative to Vienna Standard Mean Ocean Water. An acidified (1 M nitric acid, Optima-grade) aliquot of water was diluted by a factor of 100 and analyzed for Mg, Ca, Sr, and Ba concentrations on a Thermo Scientific Element XR using lab-prepared solution standards. External reproducibility was assessed with repeated measurements of a lab-prepared standard and is reported as ±1 standard deviation of each element measured.

For each 1 cm sediment interval, approximately 20 specimens of the benthic foraminifera *A. parkinsoniana* in the size fraction 250-500 µm (Figure 3.1c) were picked, crushed between two glass plates, and split into aliquots for trace metal and isotope ratio analysis. A 300 µg aliquot of crushed foraminifera was added to acid-cleaned microcentrifuge vials and cleaned for trace metals analysis following the methods of Martin and Lea (2002) and Barker et al. (2003) (acid-leach omitted). Cleaned samples were dissolved in 400 µL 0.075 nitric acid (Optima-grade) and analyzed on a Thermo Scientific Element XR for Mg, Ca, Sr, and Ba concentrations and reported as elemental ratios Mg/Ca, Sr/Ca, and Ba/Ca. External reproducibility was assessed with repeated measurements of lab-prepared foraminifera consistency standards and is reported as ±1 standard deviation. Foraminiferal calcite $\delta^{18}O$ was assessed using a Kiel IV Carbonate Device connected to a ThermoScientific MAT-

253 dual-inlet isotope ratio mass spectrometer. Results are reported relative to Vienna PeeDee Belemnite, and long-term reproducibility was determined with repeated measurements of standard reference material NBS-19 limestone (±0.08‰).

Radiogenic strontium isotopes of both water and foraminiferal calcite were measured on a Neptune multi-collector inductively coupled plasma mass spectrometer at National Cheng Kung University (Tainan, Taiwan) following Liu et al. (2012). Crushed foraminifera (3 mg) were dissolved in 800 µL of 3 M nitric acid and passed through 0.25 mL of Eichrom Sr resin columns to separate strontium from calcium. For lagoon water, 100 µL of each lagoon water sample was passed through Eichrom resin. Reproducibility was determined from IAPSO seawater standard (±0.00007 2SD) and NIST 987 strontium carbonate standard (±0.00006 2SD).

3.3.5 Geochemical modeling and statistical analysis

All statistical analyses were performed in R software (v. 3.6.1). Pearson correlations were used to confirm the association of salinity with different metal concentrations or isotope values. Predictive relationships between core top foraminiferal elemental ratios and salinity were assessed first with multiple regression and then with simple linear regression based on the best fit of the Akaike information criterion (Akaike, 1974). Outlier data points with substantial influence on the regression adjusted R^2 were assessed using Cook's distance and removed (Fox and Weisberg, 2018).

Linear regression equations were used to reconstruct paleosalinity from foraminiferal geochemistry in downcore samples, and reconstructed salinity followed non-linear trends. To observe deviations from long-term trends, paleosalinity trends were first fit with fifth-order polynomial regressions in R software. Residual fitted values about these regressions were then plotted against age determined from age-depth models of cores. Uncertainty in detrended salinity values is represented by the standard error of each fitted value to the polynomial regression.

To determine relative contributions of lagoon water sources to paleosalinity, we follow a three-endmember mixing model for Celestun Lagoon water samples developed by Young et al. (2008) with the following equations:

$$f_{SW} + f_{FW} + f_{BW} = 1 \tag{3.1}$$

$$f_{SW}[A]SW + f_{BW}[A]BW + f_{FW}[A]FW = [A]L \tag{3.2}$$

$$f_{SW}[B]SW + f_{BW}[B]BW + f_{FW}[B]FW = [B]L \tag{3.3}$$

where f_{SW}, f_{FW}, and f_{BW} represent fractions of seawater, fresh groundwater, and brackish groundwater, respectively. $[A]$ and $[B]$ represent the isotope signatures of selected tracers for each endmember (SW, BW, and FW) and for the measured lagoon sample (L). In our model, we use foraminiferal isotope values from samples that best reflect endmember isotope composition and add a 20% tolerance following Gonneea

et al. (2004). Replacing *A* with $\delta^{18}O$ and *B* with $^{87}Sr/^{86}Sr$, the equations were solved by substitution following Moore (2003):

$$f_{FW} = \frac{\left(\frac{[^{87}Sr/^{86}Sr]L - [^{87}Sr/^{86}Sr]SW}{[^{87}Sr/^{86}Sr]BW - [^{87}Sr/^{86}Sr]SW}\right) - \left(\frac{[\delta^{18}O]L - [\delta^{18}O]SW}{[\delta^{18}O]BW - [\delta^{18}O]SW}\right)}{\left(\frac{[^{87}Sr/^{86}Sr]FW - [^{87}Sr/^{86}Sr]SW}{[^{87}Sr/^{86}Sr]BW - [^{87}Sr/^{86}Sr]SW}\right) - \left(\frac{[\delta^{18}O]FW - [\delta^{18}O]SW}{[\delta^{18}O]BW - [\delta^{18}O]SW}\right)} \quad (3.4)$$

$$f_{BW} = \frac{[^{87}Sr/^{86}Sr]L - [^{87}Sr/^{86}Sr]SW - f_{GWf} * ([^{87}Sr/^{86}Sr]FW - [^{87}Sr/^{86}Sr]SW)}{[^{87}Sr/^{86}Sr]BW - [^{87}Sr/^{86}Sr]SW} \quad (3.5)$$

$$f_{SW} = 1 - f_{FW} - f_{BW} \quad (3.6)$$

To assess changes in paleoprecipitation in our record, we exploit the relationship between precipitation in the western Yucatan Peninsula and changes of salinity in Celestun Lagoon (see section 1.1). Based on monthly hydrologic data from Herrera-Silveira (1994) collected between sites 4A and 8A (Figure 3.1b), we plot Celestun Lagoon salinity lagged by 1 month, exclude the highly variable "nortes" season data (October to December), and plot the remaining wet and dry seasonal data against monthly mean precipitation for the western Yucatan (Figure 3.1b). The resulting linear equation is as follows:

$$S_{northern\ lagoon} = 23.6 - 0.0456 * P, R^2 = 0.936 \quad (3.7)$$

where *S* is mean salinity of the northern lagoon and *P* is precipitation. Using paleosalinity reconstructed from Ba/Ca in the northern lagoon, we estimate

corresponding precipitation recharging groundwater over the northwestern region of the peninsula.

3.4 Results

3.4.1 Age-depth models and sedimentation rates

Measured ^{14}C and ^{210}Pb data are given in Table 3.1. Radiocarbon ages were not reservoir corrected. Reservoir effects are unknown for the Yucatan aquifer, and we assume that mangrove organics chosen for analysis reflect atmospheric ^{14}C with minimal reservoir effects. Age-depth models for cores 4A and UL-5 are reported in Chapter 2, and age-depth models for the other cores (3A, 8A, and 7A) are given in Figure 3.2. X-ray fluorescence peak matching between cores 4A and 2A are given in Supplemental Figure S1. A hiatus interval reported in Chapter 2 for core 4A (at 35 cm sediment depth) also occurs in cores 2A (30 cm depth), 3A (29 cm depth), 8A (33 cm depth), and 7A (31 cm depth). Estimated missing time intervals vary for each hiatus and range from 350 years (core 8A) to 1,800 years (core 7A). Dates are given as calibrated years before present (Cal Yr BP) and referenced hereinafter as BP. Age-depth models also suggest slight increases in sedimentation (Figure 3.2d) in the northern lagoon at 3,300 BP (1mm/yr) and 1,900 BP (0.8 mm/yr) compared to the long-term lagoon average of 0.5 mm/yr based on radiocarbon data of core 4A.

3.4.2 Water chemistry and salinity

Water metal concentrations [Mg], [Sr], and [Ba], and isotope values of $^{87}Sr/^{86}Sr$ and $\delta^{18}O_w$ in lagoon water are significantly correlated with lagoon salinity (Pearson correlation, r and p values in Figure 3.3). [Mg] and $^{87}Sr/^{86}Sr$ exhibit the strongest correlation, followed by [Ba], [Sr], and $\delta^{18}O$. Correlation for [Ba] improves when using the ratio [Ba]/[Ca] from r = 0.74 to r = 0.92, respectively. [Mg]/[Ca] relationship to salinity is similar to that of [Mg], and [Sr]/[Ca] correlation is not significant compared to [Sr] alone (Figure 3.3). Samples of salinity of 17.1 from the northern lagoon contained the highest values for $\delta^{18}O_w$, [Sr], [Ba], and an intermediate value for $^{87}Sr/^{86}Sr$ (Table 3.2). There is no significant correlation between temperature and salinity despite the observation that springs typically discharge colder (24.4 °C) low-salinity (9) water (Figure 3.3; Table 3.2).

3.4.3 Coretop foraminiferal calcite geochemistry

Foraminiferal calcite metal/calcium ratios compared to water salinity generally followed the same patterns as metal concentrations in the water (Figure 3.3). In all cases of multiple regression that used salinity, temperature, and metal/calcium of water samples, the Akaike information criterion indicated that salinity alone was sufficient to explain foraminiferal metal/calcium values. Using simple regression, Ba/Ca, Sr/Ca, and $^{87}Sr/^{86}Sr$ have the highest R^2 coefficients while $\delta^{18}O_c$ and Mg/Ca

exhibited little relationship with water salinity (Figure 3.4). We note that foraminiferal Sr/Ca more closely matched [Sr]/[Ca] of the water column from mid to high salinities (15-35) rather than [Sr] alone (Figure 3.3). The correlation with temperature is not significant for foraminiferal Sr/Ca (Pearson correlation, $r = 0.13$, $p = 0.52$), Mg/Ca (Pearson correlation, $r = 0.17$, $p = 0.41$), or $\delta^{18}O_c$ (Pearson correlation, $r = 0.28$, $p = 0.16$) (Supplemental Figure S2).

3.4.4 Downcore foraminiferal calcite geochemistry

Foraminiferal calcite measurements for $\delta^{18}O_c$, Mg/Ca, Ba/Ca, Sr/Ca, and $^{87}Sr/^{86}Sr$ in three sediment cores—one each in the northern, central, and southern lagoon—are shown in Figure 3.5a-c, and three additional Ba/Ca records are shown in Figure 3.5d-f. Trace metal to calcium rations in sediment cores from the northern lagoon (4A, 3A, and 2A) exhibit viability in trace metal ratio values with depth. Ba/Ca and Sr/Ca increase over time in the northern lagoon cores from a mean and standard deviation of 4.9 ± 2.3 to 8.5 ± 3.3 µmol/mol and 2.2 ± 0.8 to 2.7 ± 0.2 mmol/mol, respectively, between 4,500 BP and present. No consistent trends are noted in middle and southern lagoon cores 8A and 7A. Mg/Ca values exhibit no trend in any of the cores with a mean and standard deviation value of 4.9 ± 0.9 and a range of 3.1 to 8.1 mmol/mol.

In cores 4 and UL-5 from the northern lagoon, $^{87}Sr/^{86}Sr$ of *A. parkinsoniana* records lower than seawater values (0.70804and 0.70807, respectively,) around 5,200 BP,

rapidly increasing to 0.70906 and 0.70886 ca. 4,700 BP, and then gradually decreasing to 0.70837 at present (Figure 3.5). The $^{87}Sr/^{86}Sr$ values fall within those expected for endmember source waters to Celestun Lagoon (Table 3.3). A decrease in $^{87}Sr/^{86}Sr$ is also noted in core 7A in the middle lagoon from 0.70901 to 0.70883 between 4,000 and 2,300 BP, though the $^{87}Sr/^{86}Sr$ values are higher relative to cores 4A and UL-5. Over the same period, core 8A in the southern lagoon exhibited minimal variation in $^{87}Sr/^{86}Sr$ but increased from 0.70852 to 0.70875 between 800 BP and present.

Values and trends of $\delta^{18}O_c$ are more variable among cores (Figure 3.5a-c). For the northern lagoon core 4A, $\delta^{18}O_c$ values are relatively high ca. 5,000 BP (-0.85 ‰ and -0.88 ‰), low ca. 2,500 BP (-2.54 ‰ and -2.26 ‰) and higher at present (-1.40 ‰). In cores 7A and 8A, $\delta^{18}O_c$ values are variable without a notable trend (core 7A: -1.87 ± 0.23 ‰, core 8A: -2.94 ± 0.32 ‰,) (Figure 3.5).

3.4.5 Paleosalinity

We apply the regression equations for Sr/Ca and Ba/Ca (Figure 3.4), which exhibited the strongest relationship between coretop foraminiferal calcite chemistry and water column salinity, to downcore foraminiferal calcite measurements (Figure 3.5) to reconstruct paleosalinity for each sediment core (Figure 3.6), plotted separately for inspection and together for comparison. Paleosalinity uncertainty comes from

propagating the 95% confidence interval bands around regression lines in Figure 3.4. Three salient features are observed in Figure 3.6: 1) each proxy produced similar results with Sr/Ca and Ba/Ca in better agreement with each other than $^{87}Sr/^{86}Sr$; 2) the modern salinity gradient of ~35 at south lagoon to ~25 in the mid-lagoon to ~18 in the northern lagoon is portrayed; and 3) the salinity gradient is a relatively recent feature of the lagoon that developed primarily from 2,500 BP to present. The general trends noted in proxy measurements (Figure 3.5) are also reflected in Figure 3.6 with a decrease in lagoon salinity from ~4,000 BP to present in the northern lagoon and variability but no trend in the middle and southern lagoon (cores 7A and 8A). Decrease in salinity is most dramatic for cores 2A, 3A, and 4A. Ba/Ca paleosalinity reconstructions best match modern conditions. Using this proxy, we note salinity trends as follows: core 4A from 30.4 ± 3.9 to 21.2 ± 1.4 (4,700 BP-present); core 3A from 33.5 ± 3.2 to 17.1 ± 2.37 (4,400 BP-present); core 2A from 29.2 ± 2.2 to 21.4 ± 1.34 (3,300 BP-present). Initial and final salinity is similar for core 8A with salinity 26.1 ± 1.3 to 24 ± 1.1 (2,600 BP-present) and core 7A with salinity 31.5 ± 2.7 to 29.6 ± 2.14 (4,500 BP-present) (Figure 3.6). Paleosalinity across all cores representing the time interval of 4,600 BP suggests that the salinity gradient in the lagoon was muted at 4,600 BP, ranging only between 29 and 34 compared to 14 to 35 at present.

3.4.5.1 Endmember mixing models

Based on values of $\delta^{18}O_w$, $^{87}Sr/^{86}Sr$, [Mg], [Ca], [Sr], [Ba] and salinity in water samples, Celestun Lagoon water is a mixture of three geochemically distinct endmembers(Figure 3.7a, Table 3.3). Seawater (SW) from the Gulf of Mexico is characterized by [Sr] = 90.2 µmolar, [Ba] = 44 nmolar, [Mg] = 49.4 mmolar, $^{87}Sr/^{86}Sr$ = 0.70916, and $\delta_{18}O$ = 1.56 ‰ (Hsieh and Henderson, 2017). Fresh groundwater (FW) is characterized by [Sr] = 38.7 µmolar, [Ba] = 253 nmolar, [Mg] = 6.2 mmolar, $^{87}Sr/^{86}Sr$ = 0.70821, and $\delta^{18}O$ = -3.70 ‰. Brackish groundwater (BW) is characterized by [Sr] = 109 µmolar, [Ba] = 331 nmolar, [Mg] = 33.7 mmolar, $^{87}Sr/^{86}Sr$ = 0.70832, and $\delta^{18}O$ = 4.27 ‰. These are the same endmember water sources described in previous studies (Young et al., 2008; Stalker et al., 2014). Isotopic composition of coretop foraminiferal calcite collected closest to water endmember sources reflects source geochemistry (Figure 3.7b) with a mean offset $\delta^{18}O_c$ of 3.01 ‰ between water and calcite samples. No foraminifera were observed immediately adjacent to FW source waters. Some foraminiferal data points fall outside of the mixing triangle, which may reflect seasonal conditions of some specimens not captured in our endmember samples. Therefore, following Gonneea et al. (2004), we add a 20% tolerance to each endmember so the triangle encompasses the spread of data encountered in both the coretop and downcore samples. Because groundwater is the most important freshwater source to the lagoon and discharges year-round, summer direct precipitation is unlikely to be a substantial endmember for this system (Stalker et al., 2014).

Because cores 4A, 8A, and 7A in the northern, central, and southern sections of the lagoon, respectively offer the most complete datasets for $\delta^{18}O_c$ and $^{87}Sr/^{86}Sr$, data from these cores were used for mixing models. Oldest data (> 5,000 BP) in the northern lagoon comes from cores 3A and UL-5. Using the foraminiferal values for endmember $\delta^{18}O_c$ and $^{87}Sr/^{86}Sr$ (Figure 3.7b, Table 3.3) and equations 4-6, we found that BW is the most important contributor to the modern northern lagoon, FW is the major contributor in the modern middle lagoon, and in the southern lagoon SW is the most important, but the proportions of each endmember at these sites have changed over the last 4,000 BP (Figure 3.7). The middle and southern lagoons have remained relatively consistent in composition while the northern lagoon water sources fluctuated considerably over time. In the northern lagoon prior to 3,200 BP SW was the main water source but around 3,200 BP the FW contribution began increasing. At approximately 2,400 BP, BW increased while both FW and SW decreased. From 2,000 to 1,300 BP, FW increased markedly while SW increased modestly and BW decreased. The hiatus interval spans ca. 1,300 to 500 BP hence no data is available for that 800 years time interval, and the last 500 years have remained consistent in overall composition (Figure 3.7).

The mixing model shows decreasing salinity was accompanied by increased proportions of groundwater sources relative to seawater (Figure 3.7). Because Ba/Ca in the foraminifera is closely related to groundwater and not affected by temperature or saturation state, we detrend the Ba/Ca-derived salinity reconstructions (Figure 3.6)

and plot residuals (Figure 3.8) to extract short-term changes in spring discharge which are superimposed on the long term trend. Paleosalinity was detrended by taking the residuals of fifth-order polynomial fits to paleosalinity of cores 4A and 8A (Figure 3.8). Lagoon salinity deviations from the trend range from -4 to +3 salinity units for all sites. Notable low-salinity conditions in core 4A occur at 3,300 BP (salinity decreased by 4.1), 2,400 BP (decrease by 2.9), and 2,000 BP (decrease of 3.5) while higher salinity is observed from 3,300 to 3,100 BP (1.5 more saline) and 2,300 to 2,100 BP (1.9 more saline). A general increasing salinity trend in 4A is observed from ca. 2,000 BP to 1,300 BP (relative change of ~6). Core 8A record is shorter but also indicates salinification from ca. 2,000 to 1,000 BP (relative salinity change ~3) with another notable increase in salinity ca. 2,200 BP (~3 units increase).

Paleosalinity, detrended residuals, and accretion rate of core 4A are plotted against other lacustrine and marine records as well as coastal lagoon records from the region (Figures 3.9, 3.10) with wet and dry periods denoted by shading.

3.4.5.2 Paleoprecipitation estimates

Equation 3.7, which describes the relation between regional precipitation and salinity in Celestun Lagoon (Figure 3.1b), indicates that for the salinity range 15 to 30, each unit increase of salinity in Celestun Lagoon corresponds to approximately 20 mm decrease in rain recharging the springs that discharge to the lagoon. Based on a

modern measured mean precipitation of approximately 1,100 mm/yr (Bauer-Gottwein et al., 2011) and an estimated 950 mm/yr average for the last 1,500 years recorded in speleothems (Medina-Elizalde et al., 2016) for the central Yucatan, we assume that 1,000 mm/yr is representative of average annual precipitation for the catchment area that recharges the groundwater feeding the springs in Celestun Lagoon. A 1 unit decrease in lagoon salinity is thus equal to about 20 mm / 1,000 mm or 2% reduction in mean annual precipitation for the western-central Yucatan Peninsula.

3.5 Discussion

3.5.1 Celestun lagoon salinity responses to groundwater input and precipitation

Groundwater input is the primary source of low-salinity water to Celestun lagoon. This groundwater is characterized by high [Sr] and [Ba], low [Mg], and low values of $^{87}Sr/^{86}Sr$ when compared to seawater (the other major water source to the lagoon) (Figure 3.3). These metals and isotopes mix conservatively along the length of the lagoon from the northern enclosed terminus, where much of the groundwater discharges, to the southern lagoon, where most seawater enters (Figure 3.1). Closer inspection of the metal and isotope distributions reveals variable [Sr] and $\delta^{18}O_w$ of the groundwater which indicates that the two groundwater types (aquifers) discharging into the lagoon, previously described (Young et al., 2008; Stalker et al., 2014;), differ in their Sr and O isotope ratios (Table 3.3, Figure 3.7a). Fresh groundwater (FW)

$\delta^{18}O$ of -3.70 ‰ best represents meteoric water with short residence time in the carbonate aquifer. Brackish groundwater (BW) $\delta^{18}O$ of 4.27 ‰ suggests interaction with evaporites (high [Sr]) and evaporation in the Ring of Cenotes (enriched $\delta_{18}O$, Stalker et al., 2014, Figure 3.11) and possibly mixing with some seawater prior to discharge (Figure 3.3). Stalker et al. (2014) suggest that 80% of the fresh and brackish water in Celestun is derived from the springs and that runoff from rainwater is not an important contributor in this system. Indeed, monthly monitoring of salinity indicates that the salinity in Celestun lagoon varies seasonally and between years in response to rain events (Figure 3.1b, Bauer-Gottwein et al., 2011; Herrera-Silveira, 1994; Perry et al., 2003) yet the salinity gradient of low salinities at the northern lagoon terminus and near-seawater salinity at the mouth in the south persists (Herrera-Silveira, 1994). Accordingly, changes in salinity at any location in the lagoon over time may be indicative of changes in the relative contribution of saline seawater and lower salinity groundwater. Furthermore, several of the geochemical parameters measured here correlate well with salinity, with correlation coefficients (r) ranging from 0.98 (for Mg) to 0.72 (for Sr) at a significance level of << 0.01 (Figure 3.3). Thus if any of these parameters is recorded in carbonate shells without modification by other environmental or vital effects, it may be possible to reconstruct past salinity changes in at different locations in the lagoon (where cores are available) and evaluate the causes of salinity change, e.g., climate-induced change in precipitation and hence groundwater discharge.

3.5.2 Mid-Holocene salinity reconstructions

Of the suite of potential salinity proxies recorded in *A. parkinsoniana* carbonate tests examined here (Mg/Ca, Sr/Ca, Ba/Ca, $^{87}Sr/^{86}Sr$, and $\delta^{18}O_c$) Ba/Ca and Sr/Ca in the tests have the best correspondence to salinity (Figure 3.4) while $^{87}Sr/^{86}Sr$, and $\delta^{18}O_c$ most clearly differentiate endmember water sources (Figure 3.7b). Accordingly, we use the relation between present-day Ba/Ca in foraminifera and salinity (Ba/Ca equation in Figure 3.4) to reconstruct Celestun paleo-salinity over the last 5,300 years (Figures 3.5 and 3.6) and assess changes in water inputs from the different endmembers (SW, FW, BW) (Figure 3.7c) to the lagoon. We also compare our data to other Yucatan hydroclimatic records (Figure 3.8).

At 5,300 BP, the Ba/Ca and Sr/Ca records (Core 4A) indicate a salinity between 3 and 20 (Figure 3.6) which suggests substantial groundwater influence and limited marine influence. This is consistent with the $\delta^{18}O_c$ value of -2.89‰ and the $^{87}Sr/^{86}Sr$ value of 0.70804. Mean sea level at that time was -2.6 m below the current level for this region (Khan et al., 2017), placing the coastline about 5 km to the northwest of the core site (Appendini et al., 2012). Mangrove peat deposits and foraminiferal assemblages of *Discorinopsis aguayoi* at the bottom of the core (2.59-2.3 m) further suggest the study site in the northern lagoon was within an inland mangrove-dominated freshwater pond suggesting that the narrow lagoon had not developed at that time (Chapter 2). Several hundred years later (at ~4,900 BP), Ba/Ca of 2.4

µmol/mol suggests salinity in the northern lagoon increased dramatically to ~30, and contribution form seawater was substantial. Indeed an increase in $\delta^{18}O_c$ to -0.85 ‰ and near-seawater values of $^{87}Sr/^{86}Sr$ are consistent with increased contribution from seawater (Figure 3.5). As sea level rose (Toscano and Macintyre, 2003; Khan et al., 2017), the coastline approached the location of the current northern lagoon and the freshwater inland mangrove ponds became inundated with seawater. Indeed, the presence of the marine seagrass foraminifera *Archaias* and *Laevipeneroplis* is indicative of a predominantly marine coastal environment (Chapter 2). It is possible that at the same time dry conditions between 5,000 and 4,500 BP as reported for the central and southwestern peninsula by Mueller et al. (2009) and Wahl et al. (2014) resulted in lower groundwater discharge to Celestun Lagoon also contributing to the observed increase in salinity.

From 4,900 BP to present, the northern part of Celestun Lagoon (cores 3A, 4A, and UL-5, Figures 3.1, 3.5) generally exhibits a long term increase in foraminiferal Ba/Ca and Sr/Ca, indicating freshening in the northern lagoon from a salinity of about 30 to salinity of 14 (Figure 3.6) while $^{87}Sr/^{86}Sr$ and $\delta^{18}O_c$ indicate increasing proportions of the freshwater endmember (Figure 3.7d). These data suggest decrease in salinity at the site which has been attributed to reduced mixing between seawater and groundwater as barrier island accretion formed the lagoon(Chapter 2). Notably, this long-term trend is not observed in the middle (8A) and lower lagoon (7A) (Figures

3.5, 3.6) cores as these sites were closer to the lagoon mouth and seawater input was not yet restricted.

3.5.3 Climate driven barrier island formation and associated change in salinity

The relatively consistent decrease in salinity (i.e., reduction in seawater influence) beginning at 4,900 BP to the present day (Figures 3.6, 3.7) is best explained by accretion of barrier islands along the coast, restricting seawater input to the lagoon, rather than a continuous increase in freshwater input due to increased precipitation during the Late Holocene (see Figure 2.7 for conceptual diagram). Precessionally-driven decrease in insolation of the northern hemisphere over the last 8,000 years progressively shifted the ITCZ south of the Caribbean region (Douglas, et al., 2016b; Giddings & Soto, 2003; Haug et al., 2001) and caused a long-term decrease in average precipitation, as indicated by paleoclimate records in lakes and speleothems of the Yucatan (Akers et al., 2016; Douglas, et al., 2016a). Decreased precipitation and related decrease in groundwater discharge to Celestun would be accompanied by a long-term decrease in Ba concentration in the lagoon and a reduction in Ba/Ca and an increase in $^{87}Sr/^{86}Sr$ toward seawater values, contrary to our observations (Figure 3.5). Because sea level also rose in this region during this time (and should increase salinity), freshening in the lagoon, indicate some other mechanism for the observed decrease is salinity and influence of seawater in the lagoon.

Regional reorganization of climate patterns in the tropics of the Americas at ~4,000 BP moved the ITCZ south, causing the Loop Current to experience less incursion into the Gulf of Mexico (Poore et al., 2004). In turn, Gulf of Mexico sea surface temperatures decreased and reduced moisture flow from the Gulf of Mexico, weakening the North American Monsoon around 4,000 BP (Metcalfe et al., 2015). The combined effects of a truncated Loop Current path and reduced easterly wind flow reduced wave energy that drives longshore drift along the Yucatan Peninsula north coast (Enriquez et al., 2010; Appendini et al., 2012) causing sediments to accumulate at abrupt changes in shoreline orientation (Cuevas et al., 2013) (Figure 3.11). Thus, the northwest corner of the Peninsula became a prime location for barrier island aggradation during this climate transition period. Other lagoons in the southern and western Gulf of Mexico also exhibit decreased input of seawater contemporaneously with Celestun Lagoon (Phleger and Ayala-Castanares, 1971; Arellano-Torres et al., 2019), suggesting that barrier island development was widespread along the southern half of the Gulf of Mexico and therefore a response to regional climate and/or sea-level forcing (e.g., change in circulation patterns). Today, barrier island-dune complexes are observed accumulating along the Celestun coastline (Appendini et al., 2012; Lowery and Rankey, 2017) at a rate (~200 m/yr) consistent with forming the 25 km barrier-dune complexes bounding the western side of Celestun lagoon in about 5,000 years. This coincides with the peat layer and low salinity (based on Sr/Ca and foraminifera assemblage) at that time, which indicate the site being a coastal pond several kilometers away from ocean influence prior to the

initiation of barrier island-dune. As sea level increased, the location transformed into a coastal setting impacted by seawater and spring water; not yet an isolated lagoon, which became more and more isolated from the ocean gradually as the barrier island-dune complex grew.

Aerial imagery of Celestun Lagoon shows the barrier islands accumulate from northeast to southwest (Lowery and Rankey, 2017). It is therefore expected that northern lagoon will become restricted and receive less seawater before such conditions are manifested in the lower reaches of the lagoon. Indeed, we note the divergence of salinity among lagoon sections beginning around 3,000 BP (Figure 3.6) in which the northern lagoon trends toward fresher values while the southern lagoon remains with brackish-marine salinity values (~30). Assuming a constant rate of accretion beginning at 4,900 BP near core 4A, barrier islands would reach from the northern lagoon terminus to site 8A (Figure 3.1a) by approximately 2,000 BP (Supplemental Figure S3.3). Adjacent to site 8A is the largest spring source of the FW endmember (Figure 3.1a, Table 3.3). Barrier island extension south of 8A would effectively change the northern lagoon from a three endmember system of SW, BW, and FW to a two endmember-mixing system (FW and BW) while the southern lagoon (still open coastline at this time) would be expected to continue to be dominated by SW. Core 4A in the northern lagoon exhibits water source proportions that appears to fall along the mixing line between FW and BW beginning at 2,000 BP (Figure 3.7c) while core 7A is comprised primarily of seawater as expected from their respective

location along the lagoon (Figure 3.7f). Thus, greater FW contribution to core 4A in the upper lagoon between 2,000 BP and 1,600 BP may be related to the timing that the FW mid-lagoon springs were incorporated into the expanding lagoon. Importantly, the first agglutinated foraminiferal assemblages associated with protected, low-salinity, fine-substrate lagoon conditions emerge in Celestun Lagoon around 1,800 BP (Chapter 2), coincident with a brief doubling of long-term sedimentation rates in the northern lagoon (Figure 3.2d). High sedimentation rates would be expected in a protected lagoon with limited wave induced washout of sediment, yet the high sedimentation rate is not sustained.

Interestingly, higher sedimentation rates also occur during the first rapid increase of the FW endmember at 3,200 BP (Figures 3.2d, 3.8d), suggesting a link between periods of rapid sediment accumulation and proportions of the FW endmember in the lagoon. Though groundwater here is elevated in total inorganic carbonate (> 6,000 µmol/kg, Gonneea et al., 2014) relative to seawater, it is also undersaturated with respect to calcite and facilitates dissolution of carbonates when mixing with seawater (Perry et al., 2002; Perry et al., 2003). Reduction in corrosive mixing between FW and SW (via less SW) combined with a dry, evaporative environment associated with drought may facilitate rapid sedimentation of authigenic carbonates during such periods, returning to long-term sedimentation rates when average conditions resume. The timing of these FW and sedimentation rate increases in Celestun Lagoon at 3,200 and 1,900 BP seem to coincide with Bond cooling events in the North Atlantic during

the Holocene (Bond et al., 2001). These events have been linked to decreased solar output resulting in cool periods in the North Atlantic that effectively push the ITCZ and thus Loop Current farther south in the Gulf of Mexico with particular excursions centered on 5,200, 4,200, 3,200, and 1,900 BP (Poore et al., 2003; Poore et al., 2004). Reduced Loop Current penetration in the Gulf of Mexico and associated decrease in ocean energy may increase sedimentation along the Yucatan Peninsula north coast while the southward shift in the ITCZ results in less precipitation falling on the Yucatan Peninsula. Climatically, Bond events appear to manifest as drought, with some authors referring to the period ca. 1,900 BP as a megadrought after observing the lowest precipitation levels of the last 2,000 years during this time (Carrillo-Bastos et al., 2013; Medina-Elizalde et al., 2016). Between 2,000 and 1,500 BP there is a drastic drop in humid jungle taxa with a shift to open forest upland species in Los Petenes south of Celestun Lagoon (Roy et al., 2017) and in Ria Lagartos east of Celestun Lagoon (Aragón-Moreno et al., 2012). Pollen analysis also suggests substantial drought ca. 1,800 BP in Cenote San Jose 22 km east of Celestun Lagoon (B. W. Leyden et al., 1996), ca. 1,900-1,700 BP in Lake Peten Itza in the southern peninsula (Wahl et al., 2006), and ca. 1,700 BP in Belize (Akers et al., 2016). The slight salinity increase noted in core 8A near the FW source (Figures 3.1, 3.5) and increase in SW contribution in the northern lagoon (Figure 3.7d) suggest a decrease in groundwater input possibly in response to these dry events (Figure 3.7d). While the interpretation of paleosalinity controls in Celestun lagoon is complicated for the time period around 1,900 BP, our results suggest that in Yucatan coastal lagoons, changes

in barrier island geomorphology (affecting seawater contributions) and inland precipitation (absolute freshwater input) may respond simultaneously to the same atmospheric/oceanic forcing with opposing effects on lagoon salinity reducing the expression of drought events in lagoon records (Figure 3.9).

To be able to observe any climate induced changes in lagoon salinity it is necessary to removes the expression of geomorphic barrier-sand dune buildup influence on salinity. To do that we have detrended the long-term record of decreasing salinity and investigate excursions about the long-term trend that would indicate climate-induced dry or wet periods (Figure 3.8b).

3.5.4 Climate expression in detrended salinity of Celestun Lagoon

Though long-term salinity decrease is driven by geomorphic change, change in precipitation over the Yucatan Peninsula changes groundwater discharge to Celestun Lagoon (Herrera-Silveira, 1994), resulting in excursions from the decreasing trend. The general east-west divide of groundwater flow in the peninsula (Bauer-Gottwein et al., 2011) implies two main atmospheric patterns that decrease lagoon salinity: southward shift of the average ITCZ position reducing precipitation over the north peninsula lowlands, or eastward shift in rainfall from El Nino Southern Oscillation and Walker Circulation reducing rainfall over the western catchment (Metcalfe et al., 2015). Detrending paleosalinity in Celestun lagoon removes the geomorphic

influence in order to directly compare climatic influence with other paleoclimate archives (Figure 3.9).

The sand-dune barrier buildup started limiting seawater input to the lagoon at around 4,000 BP and as the barrier length increased with time from 4,000 BP to the present seawater input to the upper lagoon gradually decreased resulting in a trend towards lower salinity over time as seen in the Sr/Ca and Ba/Ca records (Figure 3.5). The detrending was a fifth-order polynomial and residuals were plotted in Figure 3.8. In general, changes in freshwater input (hence precipitation) at Celestun can occur due to (1) changes in the average placement of the ITCZ (ITCZ displacements farther south towards Guatemala would reduce groundwater input), or (2) shift of rainfall to movement of ENSO/Hadley cells across the groundwater divide so most of the rain falls on the eastern Peninsula and over the Caribbean and does not feed the groundwater system discharging at Celestun (Figure 3.11; Méndez & Magaña, 2010; Metcalfe et al., 2015). These processes are considered in context with other existing climate records for the region when interpreting the detrended record from 4,000 BP to the present. Prior to 4,000 BP, before the initiation of the barrier islands, seawater fraction increases, coincident with sea-level rise. Data at 4,900 and 5,300 BP fall outside of the tolerance interval over the ternary diagram (Figure 3.7c). At 5,300 BP $^{87}Sr/^{86}Sr$ is 0.70804, lower than the FW endmember which indicates no seawater component. At 4,900 BP, $^{87}Sr/^{86}Sr$ is 0.70906 and $\delta^{18}O$ is -0.86 ‰, suggesting nearly all seawater and possibly warmer temperature or evaporation. These values are

consistent with environments determined from assemblages that suggest the site was an inland freshwater mangrove pond around 5,300 BP and an open marine coast beginning at 4,900 BP (Chapter 2).

From 4,000 to 3,200 BP, Celestun Lagoon average salinity is about 2 salinity units higher than the mean (detrended) conditions (Figure 3.8c) and indicates drier-than-average conditions. Regional climate reorganization around 4,000 BP increased the importance of the Pacific Decadal Oscillation relative to the Atlantic Multidecadal Oscillation (Metcalfe et al., 2015) and strengthened El Nino Southern Oscillation (ENSO) (Wahl et al., 2014; Jones et al., 2015). The result was a relatively wet southeastern region of the Yucatan Peninsula including Belize and the Caribbean during this time (Higuera-Gundy et al., 1999; Webster et al., 2007; Mueller et al., 2009; Akers et al., 2016), while the west and southwest region of the peninsula (which recharge Celestun lagoon) exhibited dry forest conditions between 4,200 and 3,600 BP (Figure 3.10) (Díaz et al., 2017; Vela-Pelaez et al., 2018). This decrease in precipitation, and expected decrease in groundwater discharge, is manifested as rapid increase of salt-tolerant taxa and increased carbonate precipitation in the Los Petenes mangrove region 80 km south of Celestun Lagoon from 4,000 to 3,100 BP (Roy et al., 2017). The dry conditions reversed and between 3,200 and 2,800 BP Lagoon salinity decreased by about 2 units indicating greater input of groundwater. Cooler conditions prevailed in the region at that time as evidenced by a weaker Loop current and reduced evapotranspiration in the south-central Yucatan Peninsula (Poore et al.,

2003; Wahl et al., 2014). Wet conditions also prevail at Ria Lagartos on the north-central Yucatan coast (Carrillo-Bastos et al., 2013).

From 2,400 to 2,100 BP, a relative increase in Ba/Ca suggests salinity rose from 23 to 28 indicating drier than average conditions (Figure 3.8a). From Equation 3.7, a 5 unit rise in salinity in Celestun Lagoon equals a decrease in precipitation of ~100 ± 25 mm which is on the order of a 10% precipitation decline over the western half of the Yucatan Peninsula. A decrease of about 15% in precipitation is noted in Ria Lagartos (Carrillo-Bastos et al., 2013), however, in contrast a 20% increase in precipitation is reported based on speleothem records of the same time for the north-eastern Yucatan (Medina-Elizalde et al., 2016). This suggests spatial variability between the eastern and western halves of the peninsula and is consistent with reconstructed climate patterns and drivers (Metcalfe et al., 2015). This period coincides with warm sea surface temperatures in the Gulf of Mexico (Poore et al., 2003) and dry conditions noted around the western Peninsula, including speleothem and pollen records in Belize (Aragón-Moreno et al., 2012; Kennett et al., 2012), lake records in the central peninsula (Hodell et al., 1995; Wahl et al., 2014), and mangrove pollen records of the northeastern coast (Islebe and Sánchez, 2002) and western Los Petenes region (Roy et al., 2017). Wet conditions occur farther south and east in the Peninsula (Rosenmeier et al., 2002; Díaz et al., 2017), suggesting a general shift in atmospheric delivery of precipitation due to some combination of southward shift of the ITCZ, enhanced

ENSO activity, and dry polar air mass migration from North America (Pérez-Cruz, 2013; Wahl et al., 2014; Metcalfe et al., 2015; Roy et al., 2017).

From 2,100 to 1,600 BP, salinity in the northern lagoon did not deviate appreciably from average conditions, though a slight decrease of 1 to 2 salinity units occurs between 1,800 and 1,700 BP, indicating a wet period which is also noted in the central-north Yucatan (Lakes Chichancanab and Punta Laguna, Hodell et al. 1995). Dry conditions are noted in the southeastern Peninsula and southern Mayan Lowlands at Lakes Salpeten and Puerto Arturo (Rosenmeier et al., 2002; Wahl et al., 2014), which is consistent with the east-west and north-south rain variability resulting from atmospheric circulation (Douglas, et al., 2016b).

From 1,600 to 1,300 BP, the Ba/Ca record suggests salinity increased slightly from 21 to 23, particularly in core 8A near the FW spring (Figure 3.6), which was accompanied by a decrease in the FW endmember in the northern lagoon (Figure 3.8e). Higher salinity and decreased groundwater indicate the onset of dry conditions (leading up to the Classic Mayan droughts of this time). The relative increase of $\delta^{18}O$ from -2.7 to -1.8 ‰ at this time suggests either less precipitation inland or enhanced local evaporation, though both effects may be expected during drought. Just east of Celestun, speleothem records in Tecoh Cave indicate notable decreases in rainfall around 1,400 BP (Medina-Elizalde et al., 2010) and south of Celestun Lagoon, wet-forest taxa nearly vanish in the Los Petenes forest (Roy et al., 2017).The western

Yucatan coast vegetation trended toward dry conditions at the same time of this salinity increase in Celestun Lagoon (Carrillo-Bastos et al., 2013). Dry conditions implied by our record are also consistent with the series of droughts noted in other lacustrine and speleothem records across the Yucatan Peninsula culminating the Terminal Mayan droughts (Alejandro A. Aragón-Moreno et al., 2018; Bhattacharya et al., 2017; Douglas, et al., 2016b, and references therein). These conditions were attributed to a southward shift in the ITCZ that coincides with a Bond event (Figure 3.9).

For the last 500 years, salinity in the northern lagoon has been variable and ranged from around 20 to 14, the same as today's modern range between wet and dry seasons (Herrera-Silveira, 1994). A slight salinity increase between 1 and 2 salinity units is noted between 450 and 400 BP, or about 1500 to 1550 CE. Other authors note dry conditions in the central Yucatan during the Little Ice Age (~500 to 300 BP / 1450 to 1800 CE), although the magnitude of drought was less severe than at the collapse of Mayan civilization (Hodell et al., 2005; Medina-Elizalde et al., 2010; Wahl et al., 2014; Douglas et al., 2016b; Roy et al., 2017). Change in lagoon salinity during the Little Ice Age may thus be smaller than the natural variability imposed by regional climatic processes prominent during prior periods of rapid change caused by Bond Events (Bond et al., 2001). Despite this more recent variability, the 5,000-year paleosalinity record of Celestun Lagoon offers a regionally integrated record of rainfall provided that local coastal geomorphology is well-constrained. Future work at

Celestun Lagoon should include higher resolution sampling of intervals of rapid change in both climate and ocean currents (e.g., Bond events and ENSO activity), and modeling efforts may consider coupling changes in circulation of atmospheric and ocean currents with longshore drift and rates of sediment deposition, as highlighted by (Méndez and Magaña, 2010). More broadly, coastal lagoon paleoenvironmental records around the Caribbean region and Yucatan Peninsula especially should be reassessed for local barrier island effects on salinity and sedimentation rate, and flux of proxies of interest while new lagoon records can be evaluated with these coastal processes in mind.

3.6 Conclusion

The paleosalinity record of the last 5,300 years in Celestun Lagoon, developed from Ba/Ca and Sr/Ca of the benthic foraminifera *Ammonia parkinsoniana,* indicates that this lagoon in the northwestern region of the Yucatan Peninsula, Mexico, developed from a low salinity inland pond dominated by spring water to an open saline coastline to a brackish protected lagoon where groundwater springs discharge and mix with seawater. The marginal marine environment of the lagoon was initiated by sea-level rise while subsequent barrier island accretion gradually restricted seawater input to the lagoon inducing a long-term freshening trend. Detrending the record reveals several periods of increases or decreases in salinity that may be linked to reginal climate trends. Some of the recorded trends in Celestun suggest differences in

regional precipitation patterns with the east and west parts of the Yucatan showing opposites trends (for example at Rio Hondo). In addition, we also show that coastal and inland paleoclimate records may respond to the same atmospheric forcing with opposite expected effects on the paleosalinity of coastal lagoons. For example, cool air masses moving from North America toward the tropics (indicated by Bond events in the North Atlantic) push the moisture band of the ITCZ south resulting in drought over the Yucatan Peninsula while also weakening the Loop Current, causing coastal sediment accumulation and reduced mixing between seawater and groundwater. This suggests that coastal estuarine systems common to the Yucatan region, like Celestun Lagoon, provide complex archives of climate change, but both sea-level rise and geomorphic histories must be known to interpret the paleohydrologic data from these systems.

3.7 Acknowledgements

We thank the funding support from UC MEXUS faculty grants for this project, from the Geological Society of America for radiocarbon dating at Lawrence Livermore National Lab, and from the Dr. Earl H. Myers and Ethel M. Myers Oceanographic and Marine Biology Trust for X-Ray fluorescence data. Kyle Broach was supported by the NSF Graduate Research Fellowship Program. Thank you to LacCore for technical field assistance, to CJ Vigil, Brendan Chapman, Chelsey Lindo, Frankie Lon, and Colin Carney for lab assistance. Thank you to Guil Gualda and Vanderbilt

University for SEM time. Special thanks to Rob Franks for mass spectrometer expertise and to Nancy Prouty for helpful critique of the manuscript.

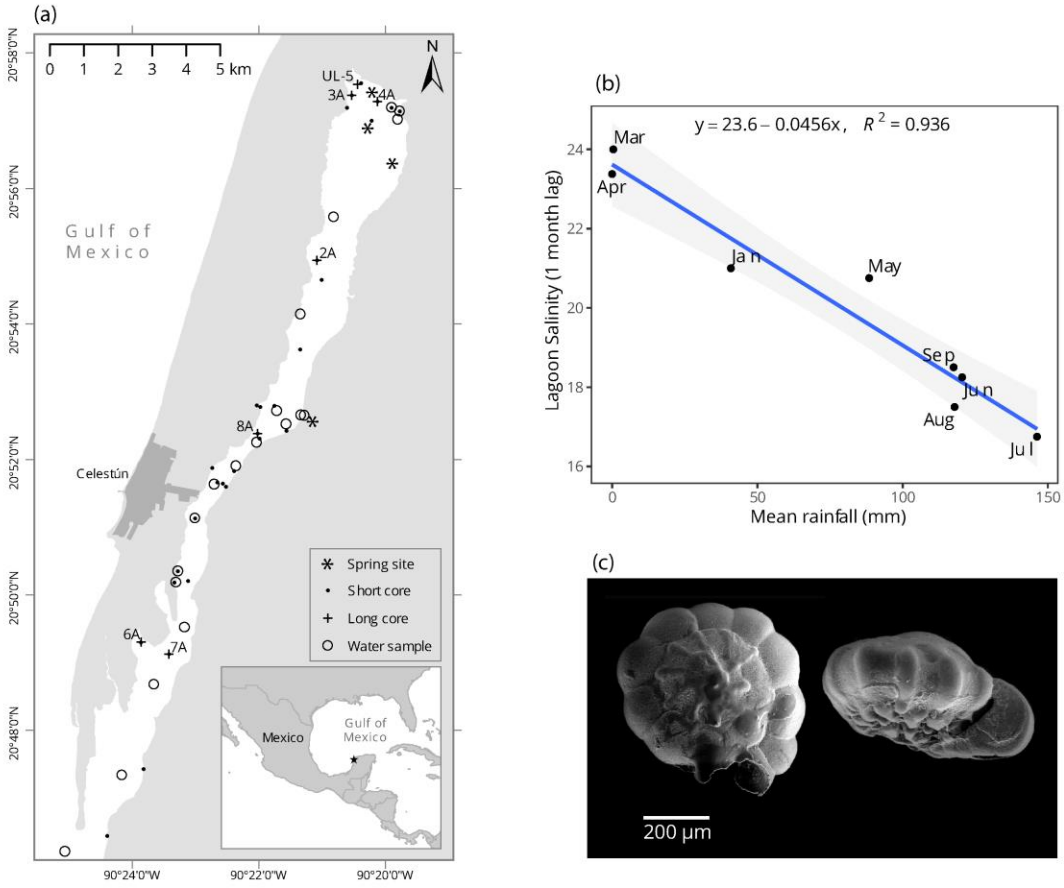

Figure 3.1
(a) Map of Celestun field site showing sample stations for water and sediment. **(b)** Northern lagoon (north of 8A) salinity response to monthly rainfall from wet and dry seasons ("nortes" months of October-December excluded) (Herrera-Silveira 1994). **(c)** Top and side view of the benthic foraminifera *Ammonia parkinsoniana* (molecular type T9, Hayward et al., 2004) used in geochemical analyses. See Figure 3.9 for additional regional context.

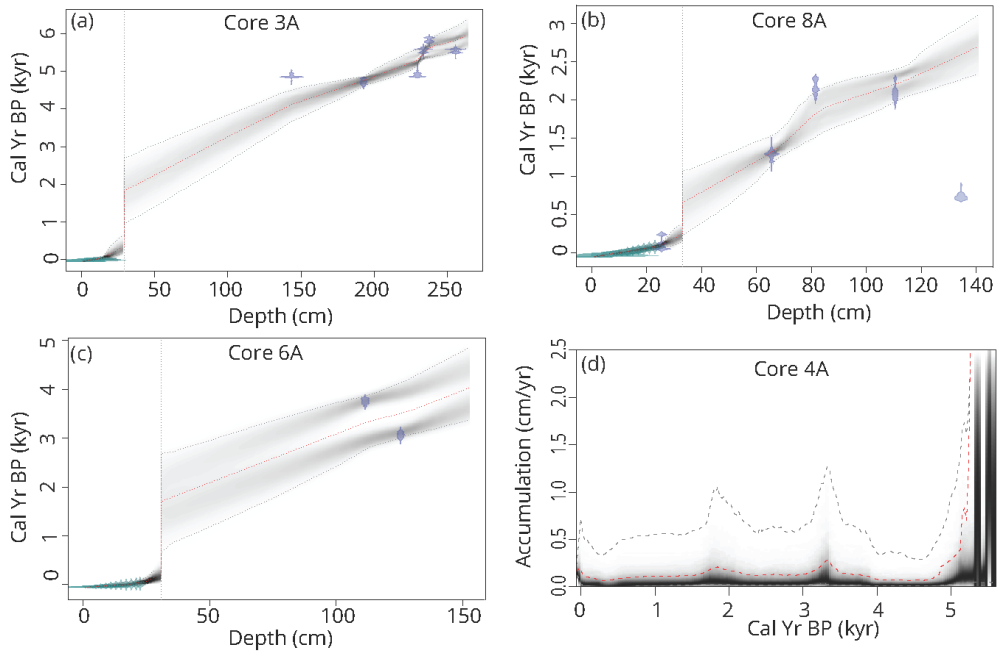

Figure 3.2
Bayesian accumulation age-depth models for **(a)** core 3A in the northern lagoon, **(b)** core 8A in the central lagoon, **(c)** core 6A in the southern lagoon which was used as the age-depth model in core 7A. Vertical lines mark apparent hiatus (Chapter 2). **(d)** Modeled sediment accumulation rate in core 4A (valid after 5 kyr BP), derived from age-depth model of 4A presented in Chapter 2. Upper dashed line is the 95% confidence interval, red dashed line (near bottom axis) is the mean accumulation, and black shading represents Monte Carlo simulations of accretion rates over time (Blaauw and Christen, 2011).

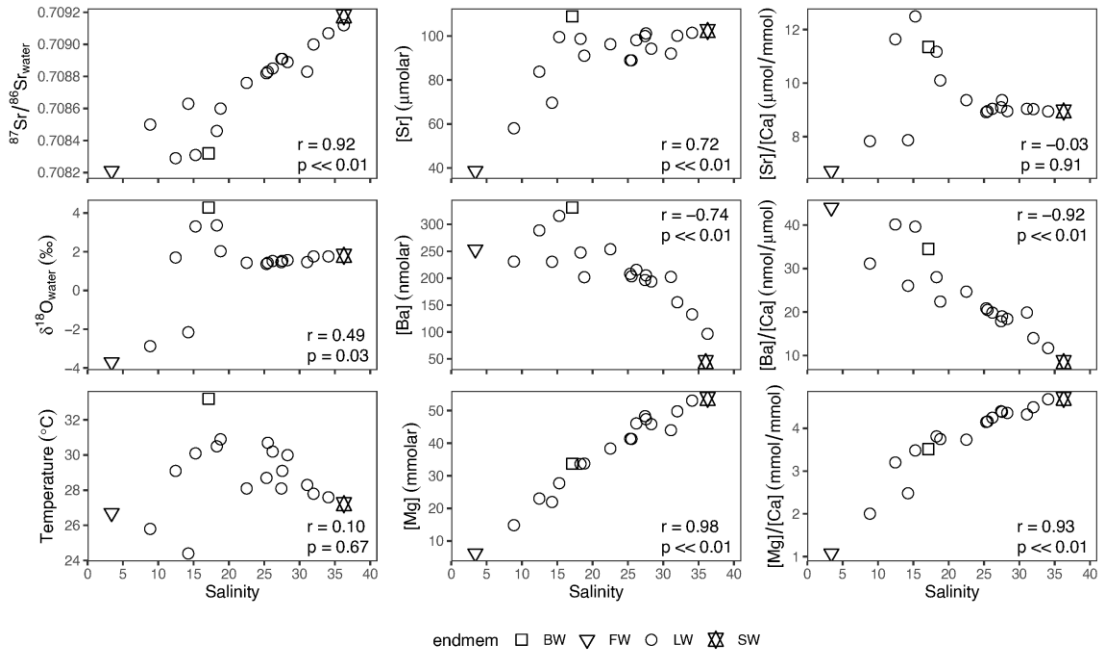

Figure 3.3
Isotope ratios, trace metal concentrations, and parameters of water samples taken along the lagoon, including at spring sites and at the ocean. Pearson's correlation r and associated p values are given in the corner of each graph. [Ca] concentrations (not shown) follow a nearly identical pattern to [Mg] and range from 5.6 to 11.4 mmolar.

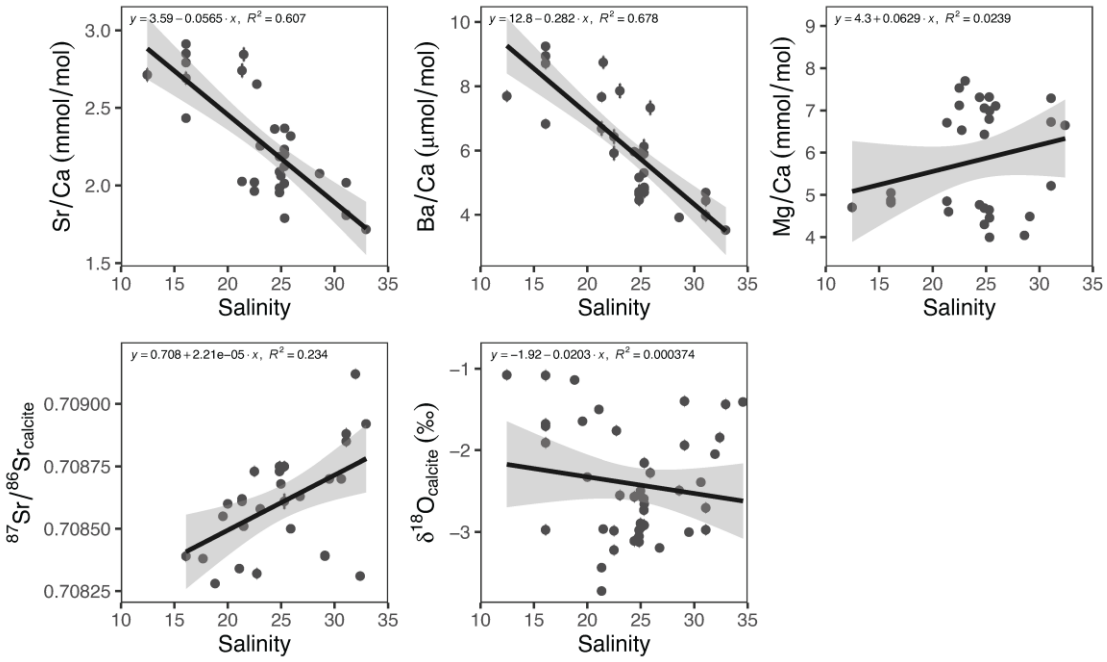

Figure 3.4
Linear regressions between isotope or metal ratios of coretop foraminiferal calcite and salinity of the nearest water column sample.

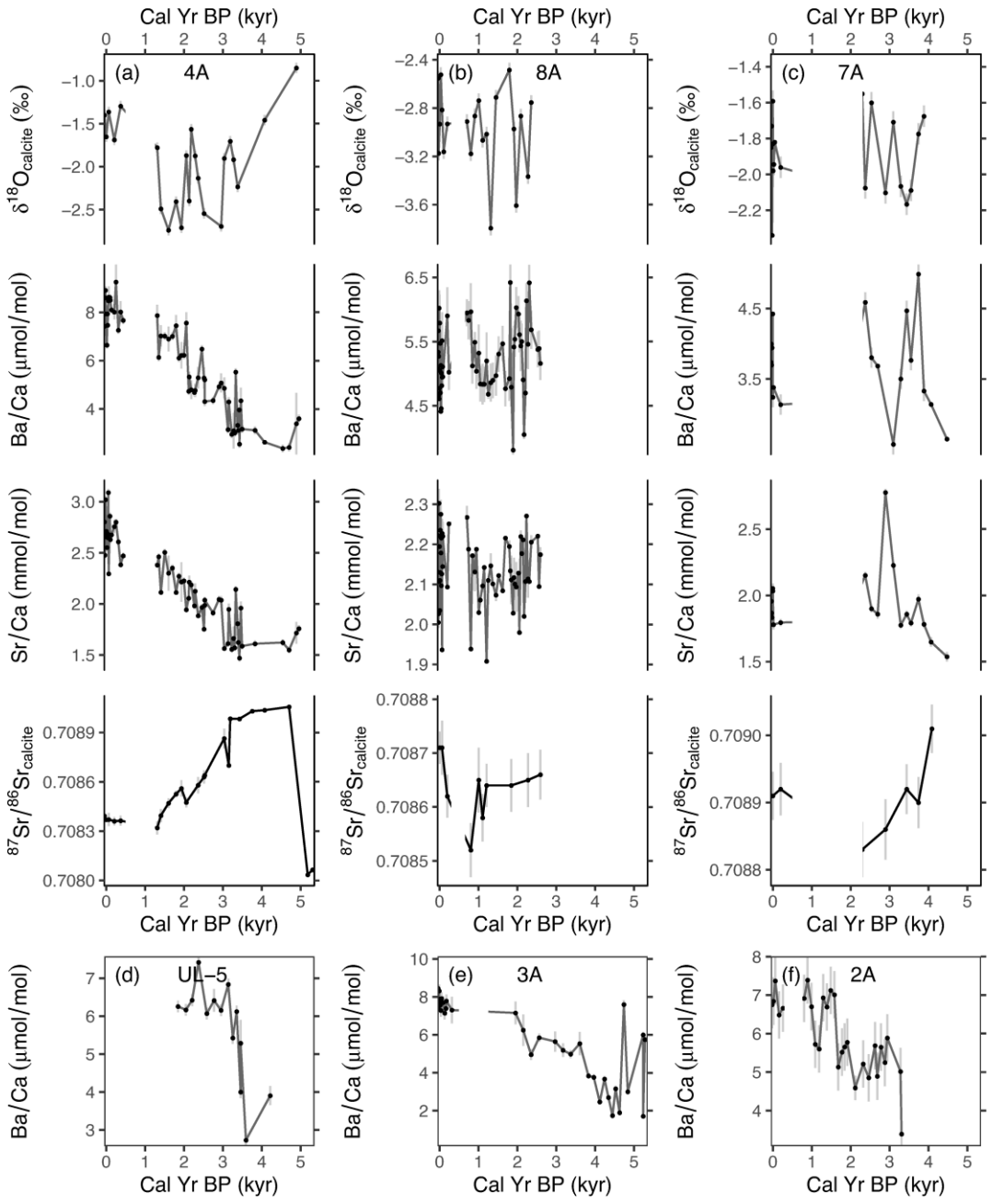

Figure 3.5
Downcore trace metal and isotope records for cores **(a)** 4A **(b)** 8A **(c)** and 7A which provide the most extensive datasets for the northern, central, and southern lagoon, respectively. Note the y-scale changes between each panel. Ba/Ca records for three additional cores **(d)** UL-5 **(e)** 3A and **(f)** 2A which are located in the northern lagoon (Figure 3.1a).

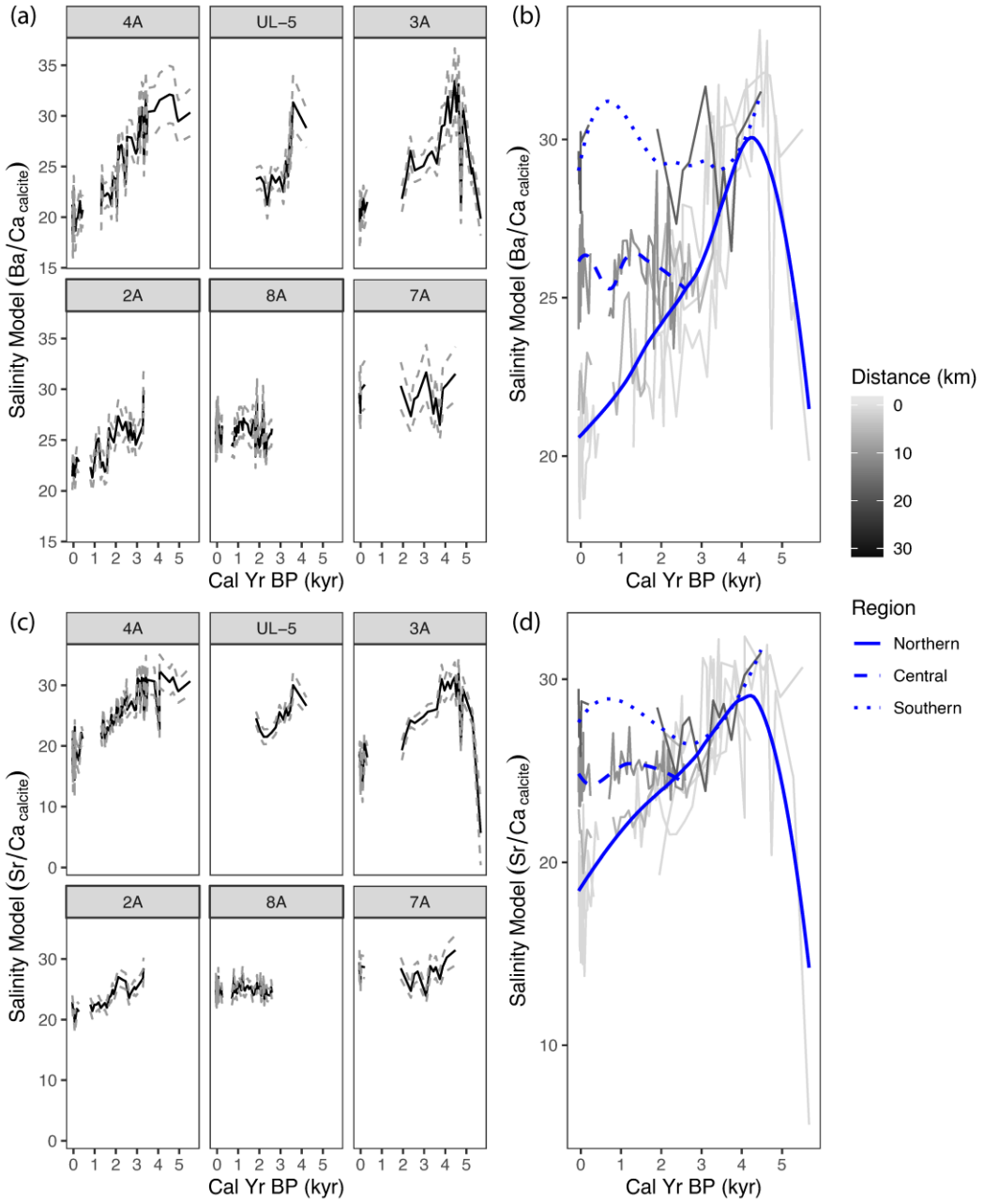

Figure 3.6

(a) Lagoon salinity reconstructed from the Ba/Ca records in Figure *3*.5 using the equation in Figure *3*.4 for salinity and Ba/Ca in foraminifera. Dashed lines represent 95% confidence intervals. **(b)** Salinity reconstructions from (a) plotted together and colored by distance from north (0 km) to south (max 21 km). Curves are LOESS smoothing functions for each region of the lagoon, and 95% confidence intervals have been removed for clarity. **(c)** The same analyses were applied using Sr/Ca for each core and **(d)** plotted together. Note change in y axis in each panel.

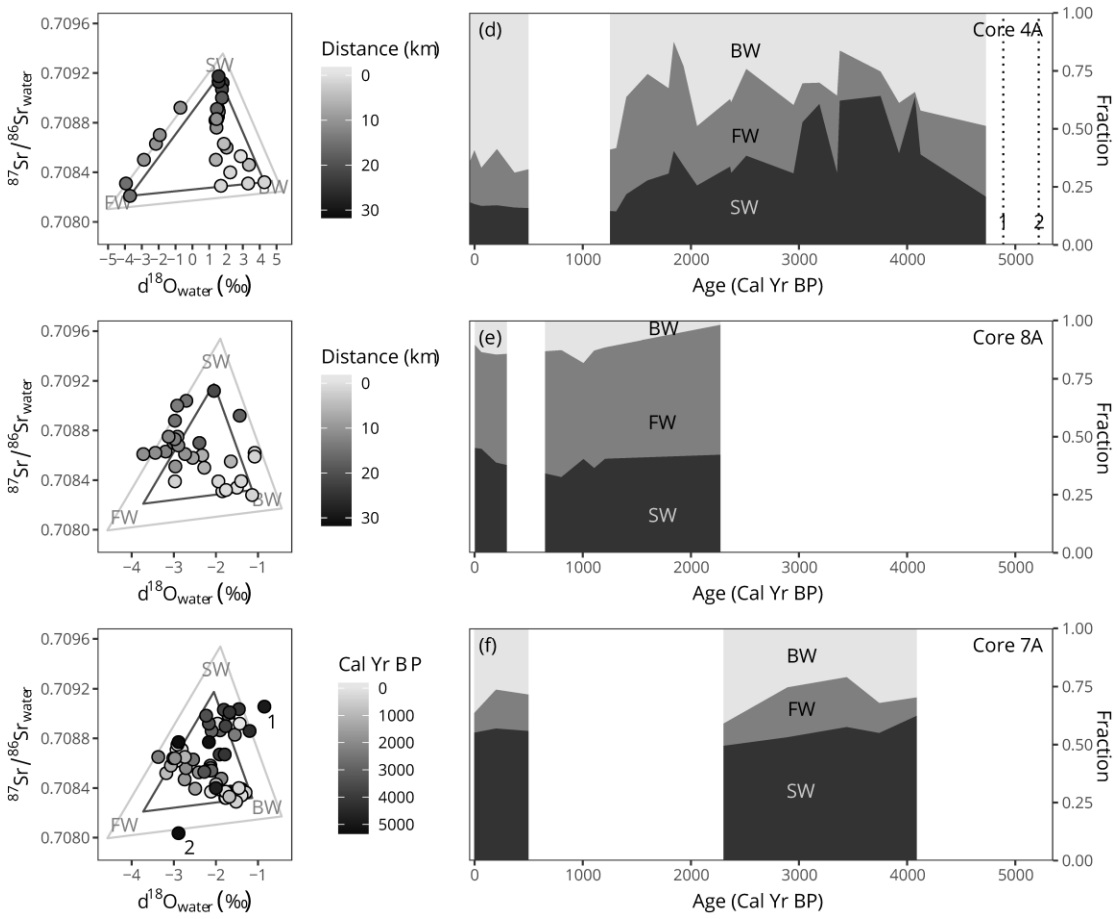

Figure 3.7

Ternary diagrams for $\delta^{18}O$ and $^{87}Sr/^{86}Sr$ values in **(a)** lagoon water samples, **(b)** coretop foraminifera samples, and **(c)** downcore samples. SW = seawater, BW = brackish water, and FW = freshwater, and the subscript $_c$ signifies each endmember as recorded in foraminiferal calcite collected closest to the source water. Distance is measured from the north (0 km) to the south (21 km) of the lagoon. Relative proportions of each endmember, derived from data in (c) and calculated using Equations 5, 6, and 7, are plotted against calibrated age in **(d)** core 4A, **(e)** core 8A, and **(f)** core 7A. Only cores with paired $\delta^{18}O$ and $^{87}Sr/^{86}Sr$ data are shown. White boxes represent hiatus length inferred from age models (Figure *3*.2).

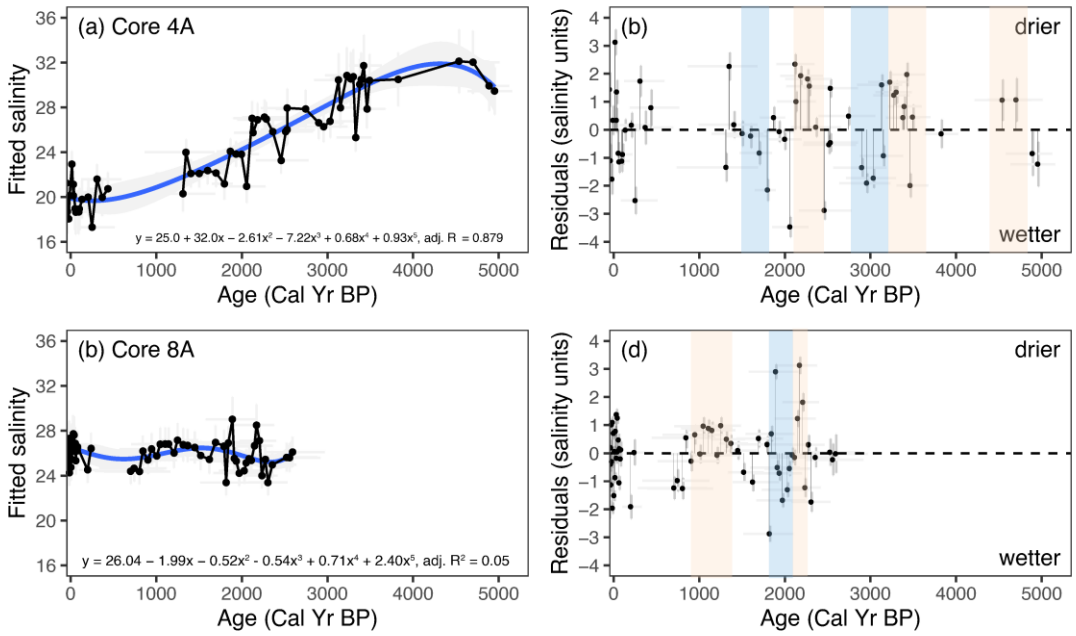

Figure 3.8
(a) Fifth-order polynomial fit to the Ba/Ca-derived salinity shown in Figure 3.6 of core 4A, and **(b)** residuals about the polynomial fit in (a). **(c)** Fifth-order polynomial fit to the Ba/Ca-derived salinity in core 8A, and **(d)** residuals about the polynomial fit in (c). Age uncertainty is the 95% confidence intervals derived from the Bacon age model Monte Carlo simulations. Residual salinity uncertainty is the standard error of fitted values of the polynomial.

Figure 3.9
Celestun Lagoon paleosalinity and sediment accumulation rate (gray box) compared to regional records of the Yucatan Peninsula. Lake and Ocean records (left panel) taken within continental interior or in the open ocean are interpreted to primarily represent climate variability (ocean and atmospheric circulation). Coastal records (right panel) taken within 10 km of shoreline are interpreted to represent a combination of variability in climate, sea level rise, and coastal geomorphic evolution. Site locations are given in Figure 3.10. Orange boxes mark dry periods over the Yucatan region. Blue boxes mark wetter conditions noted in Celestun Lagoon based on residuals of paleosalinity fifth-order polynomial fit in Figure 3.8.

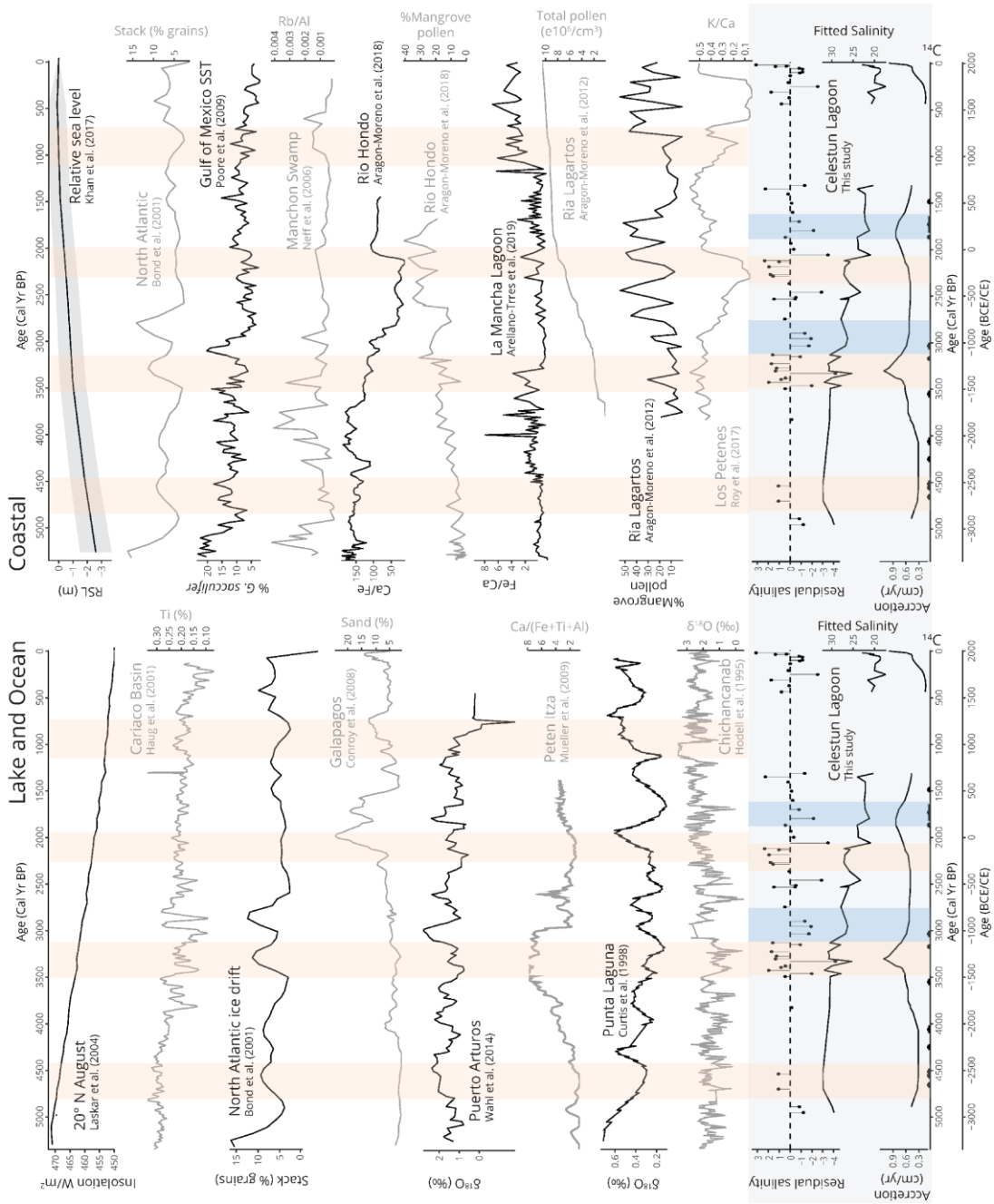
Coastal
Lake and Ocean
Age (Cal Yr BP)
Relative sea level
Khan et al. (2017)
RSL (m)
North Atlantic
Bond et al. (2001)
Stack (% grains)
Gulf of Mexico SST
Poore et al. (2009)
% G. sacculifer
Manchon Swamp
Neff et al. (2006)
Rb/Al
Rio Hondo
Aragon-Moreno et al. (2018)
Ca/Fe
Rio Hondo
Aragon-Moreno et al. (2018)
%Mangrove pollen
La Mancha Lagoon
Arellano-Trres et al. (2019)
Fe/Ca
Ria Lagartos
Aragon-Moreno et al. (2012)
Total pollen (e10⁶/cm³)
Ria Lagartos
Aragon-Moreno et al. (2012)
%Mangrove pollen
Los Petenes
Roy et al. (2017)
K/Ca
Celestun Lagoon
This study
Fitted Salinity
Residual salinity
Accretion (cm/yr)
Age (BCE/CE)
14C
20° N August
Laskar et al. (2004)
Insolation W/m²
Cariaco Basin
Haug et al. (2001)
Ti (%)
North Atlantic ice drift
Bond et al. (2001)
Stack (% grains)
Galapagos
Conroy et al. (2008)
Sand (%)
Puerto Arturos
Wahl et al. (2014)
δ18O (‰)
Peten Itza
Mueller et al. (2009)
Ca/(Fe+Ti+Al)
Punta Laguna
Curtis et al. (1998)
δ18O (‰)
Chichancanab
Hodell et al. (1995)
δ18O (‰)
Celestun Lagoon
This study
Fitted Salinity
Residual salinity
Accretion (cm/yr)
Age (BCE/CE)
14C

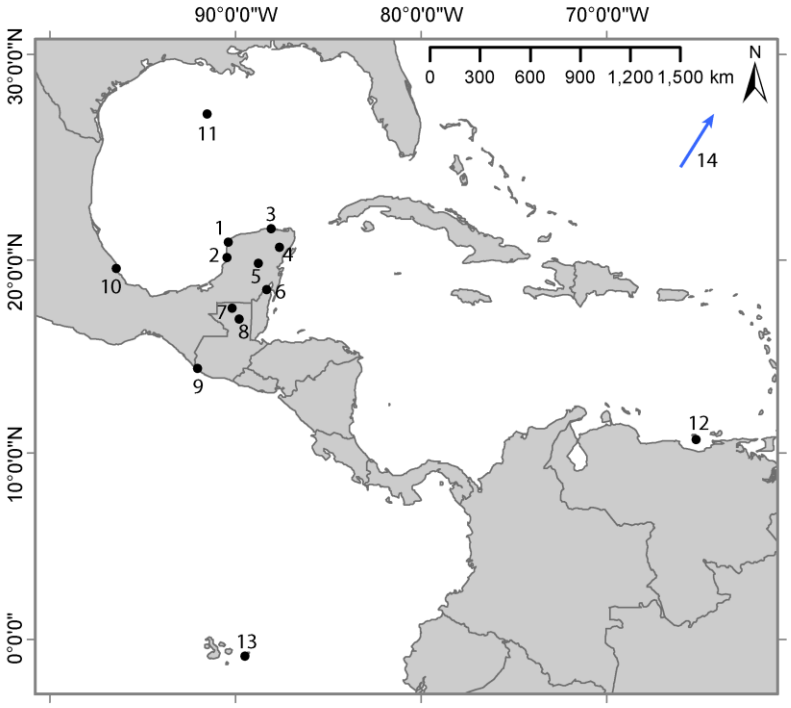

Figure 3.10
Regional records presented in Figure 3.9. 1 Celestun Lagoon, 2 Los Petenes, 3 Ria Lagartos, 4 Punta Laguna, 5 Lake Chichancanab, 6 Rio Hondo, 7 Lake Puerto Arturo, 8 Lake Peten Itza, 9 Manchon Swamp, 10 La Mancha Lagoon, 11 Pygmy Basin (core MD02-2553), 12 Cariaco Basin (ODP site 1002), 13 El Junco Lagoon, 14 (out of frame) North Atlantic drift ice records near Greenland. See Figure 3.9 for references.

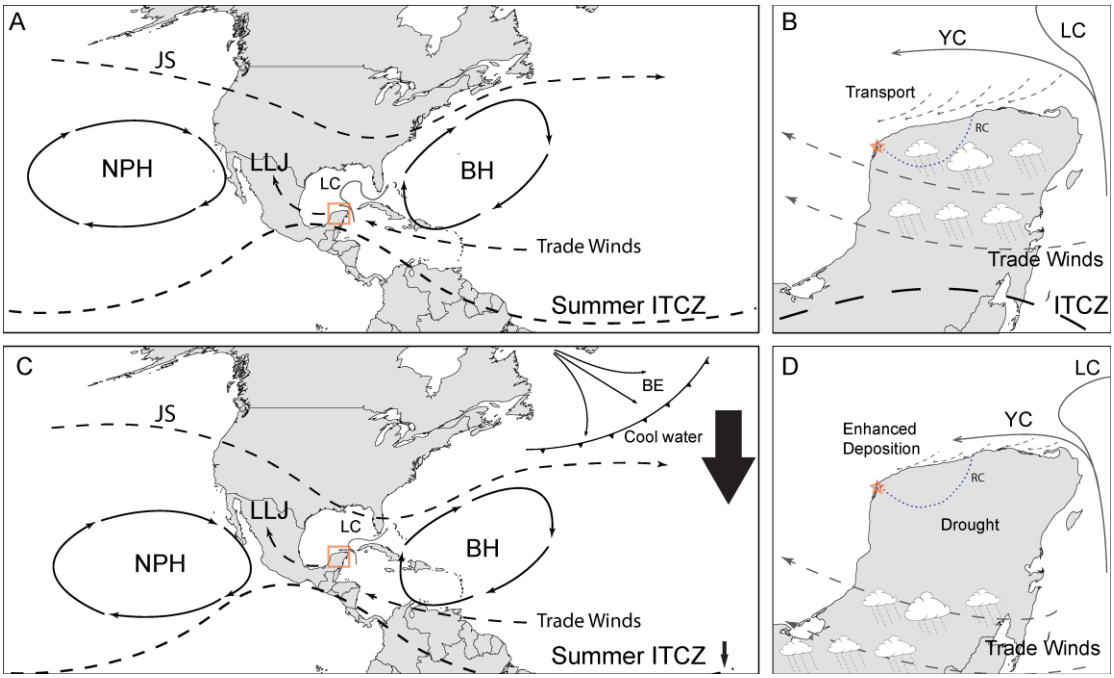

Figure 3.11
Schematic diagram (after Metcalfe et al., 2015) of important atmospheric and oceanic currents around the Gulf of Mexico Region. **(a)** Normal conditions of summer circulation in the region and **(b)** over the Yucatan Peninsula. **(c)** Bond event influence on summer circulation, represented by the large black arrow pushing circulation farther south over the region and **(d)** over the Yucatan Peninsula. Star marks Celestun Lagoon. Enhanced coastal deposition (d) via barrier islands or dunes restricts mixing between groundwater discharge and seawater, decreasing lagoon salinity despite decreased rainfall over spring catchment area denoted by Drought. BE = Bond Event, BH = Bermuda High, ITCZ = Intertropical Convergence Zone, JS = Jet Stream, LC = Loop Current, LLJ = Low-level Jet, NPH = North Pacific High, RC = Ring of Cenotes, YC = Yucatan Current.

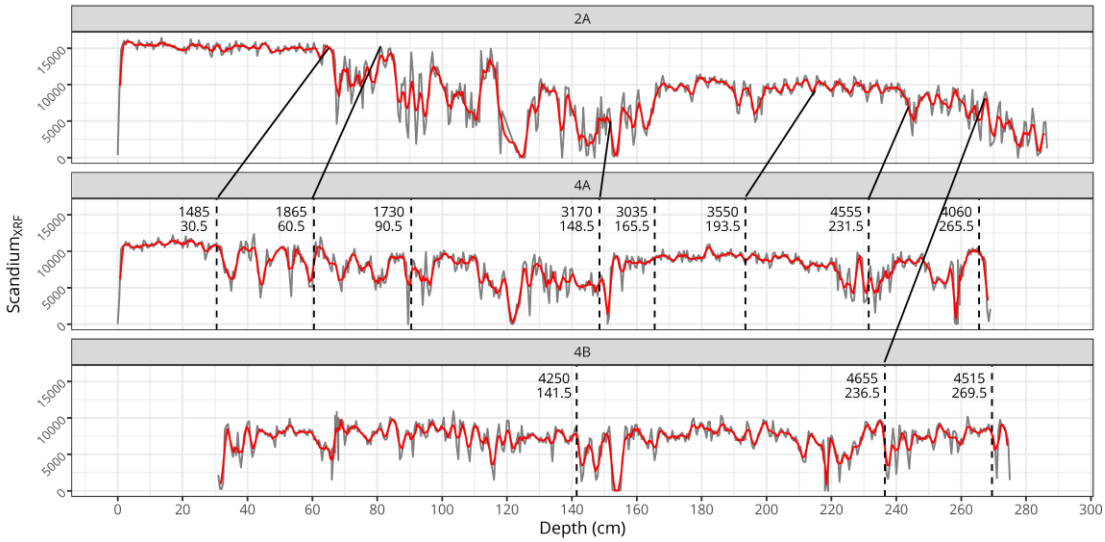

Figure S3.1
Tie-points of radiocarbon ages from cores 4A and 4B to core 2A visually matched by patterns in x-ray fluorescence (XRF) of scandium which presented the best signal-to-noise ratio of the elements measured. Red lines are a 4-point moving average.

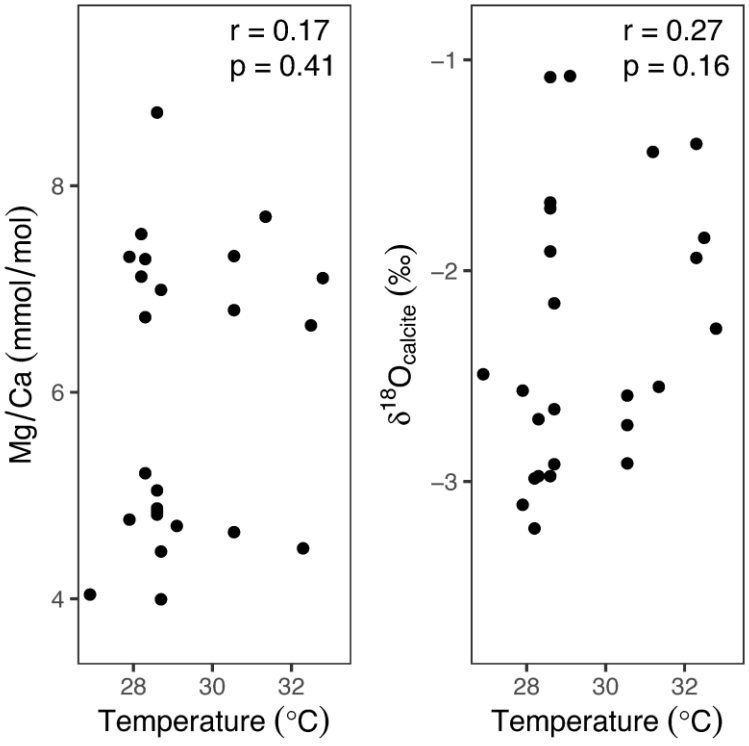

Figure S3.2
No correlation is noted between coretop A. parkinsoniana calcite Mg/Ca ratios (left panel) with water column temperature or between $\delta^{18}O$ of the same calcite samples and water temperature (right panel).

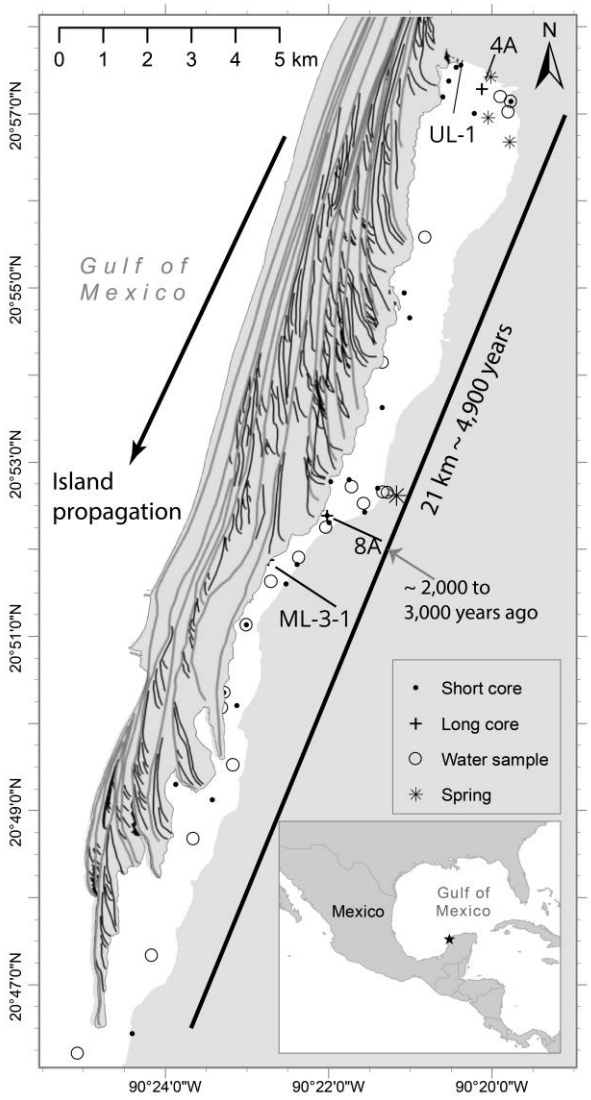

Figure S3.3
Map of Celestun Lagoon with large spring complexes marked by asterisks and accreted barrier-island-dune complexes marked in gray lines, as presented in Lowery and Rankey (2017), who observe modern barrier island accretion rates of 200 m/ 33 years. Assuming a constant, more conservative rate of accretion of 0.5 km / 100 years, the largest spring at 10 km (near 8A) would reside at the lagoon mouth beginning at about 2,500 BP and likely within the lagoon by 2,000 BP.

Table 3.1 Radionuclide data used in Bacon age models

Sample Code	Site	Core	Interval (cm)	Composite depth (cm)	$^{210}Pb_{excess}$ (dpm g^{-1})	$^{210}Pb_{excess}$ error (dpm g^{-1})	$^{14}C_{uncalibrated}$ (yr)	$^{14}C_{uncalibrated}$ error (yr)
-	8A	8-SPC	0-2	1	0.382	0.910	-	-
-	8A	8-SPC	2-4	3	0.152	0.948	-	-
-	8A	8-SPC	4-6	5	1.695	1.185	-	-
-	8A	8-SPC	6-8	7	2.099	0.987	-	-
-	8A	8-SPC	8-10	9	1.392	0.962	-	-
-	8A	8-SPC	10-12	11	0.792	0.860	-	-
-	8A	8-SPC	12-14	13	1.862	1.010	-	-
-	8A	8-SPC	14-16	15	1.445	1.007	-	-
-	8A	8-SPC	16-18	17	2.072	1.053	-	-
-	8A	8-SPC	18-20	19	-0.026	0.945	-	-
-	8A	8-SPC	20-22	21	-0.346	0.927	-	-
-	8A	8-SPC	22-24	23	0.132	0.975	-	-
-	7A	7-SPC	0-2	1	1.772	1.191	-	-
-	7A	7-SPC	2-4	3	0.937	1.246	-	-
-	7A	7-SPC	4-6	5	4.340	1.248	-	-
-	7A	7-SPC	6-8	7	4.475	1.067	-	-
-	7A	7-SPC	8-10	9	2.061	1.049	-	-
-	7A	7-SPC	10-12	11	3.233	0.743	-	-
-	7A	7-SPC	12-14	13	1.236	0.733	-	-
-	7A	7-SPC	14-16	15	2.997	0.779	-	-
-	7A	7-SPC	16-18	17	0.194	0.753	-	-
-	7A	7-SPC	18-20	19	0.717	0.908	-	-
-	7A	7-SPC	20-22	21	0.603	0.760	-	-
-	7A	7-SPC	22-23	22.5	1.974	0.727	-	-
CAMS # 150122	3A	3A-1P-1	13-14	13.5	-	-	4295	30
CAMS # 150123	3A	3A-3L-1	20-21	192.5	-	-	4175	30
CAMS # 147315	3A	3A-3L-1	57-58	229.5	-	-	4325	30
CAMS # 150124	3A	3A-3L-1	83-84	255.5	-	-	4830	30
CAMS # 147316	3A	3A-4L-1	18-19	237.5	-	-	5110	30
CAMS # 147317	3A	3B-2L-1	45-46	233.5	-	-	4840	35
CAMS # 147322	6A	6A-2L-1	28-29	111.5	-	-	3480	30
CAMS # 147323	6A	6A-3L-1	5-6	125.5	-	-	2920	30
CAMS # 177921	8A	8A-1P-1	25-26	25.5	-	-	>Modern	-
CAMS # 177922	8A	8A-1P-1	65-66	65.5	-	-	1370	45
CAMS # 147325	8A	8A-1P-1	80-83	81.5	-	-	2155	40
CAMS # 150116	8A	8A-1P-1	110-111	110.5	-	-	2105	50
CAMS # 177923	8A	8A-1P-1	134-135	134.5	-	-	815	35

Radiocarbon data from 6A was used in conjunction with 7-SPC ^{210}Pb data to generate the age model for 7A. Complementary geochronology data can be found in Chapter 1.

Table 3.2 Water sampling locations and measured parameters

ID	Sample	Latitude	Longitude	Distance km	Salinity PSU	Temperature °C	$\delta^{18}O$ ‰	$^{87}Sr/^{86}Sr$	[Mg] mmolar	[Sr] µmolar	[Ba] nmolar	[Ca] mmolar
FIC2	lagoon water	20.9532	-90.3317	0.92	12.470	29.1	1.70 ± 0.04	0.70829 ± 0.00003	23.1 ± 0.1	83.8 ±0.1	289.0 ± 0.5	7.2 ± 0.01
FIC3	lagoon water	20.9524	-90.3296	1.02	17.129	33.2	4.28 ± 0.05	0.70832 ± 0.00003	33.7 ± 0.2	108.9 ±0.1	331.2 ± 1.0	9.6 ± 0.43
FIC4	lagoon water	20.9503	-90.3300	1.27	15.290	30.1	3.31 ± 0.06	0.70831 ± 0.00003	27.7 ± 0.2	99.5 ±0.1	315.9 ± 0.7	8.0 ± 0.02
FIC1	lagoon water	20.9501	-90.3370	1.30	16.098	28.6	3.77 ± 0.0.4	0.70834 ± 0.00006	-	-	-	-
FIC5	lagoon water	20.9263	-90.3470	4.21	18.301	30.5	3.36 ± 0.04	0.70846 ± 0.00003	33.7 ± 0.4	98.7 ± 0.1	247.7 ± 0.2	8.8 ± 0.02
FIC6	lagoon water	20.9024	-90.3557	7.14	18.832	30.9	2.03 ± 0.06	0.70860 ± 0.00003	33.8 ± 0.4	91.0 ± 0.1	202.0 ± 0.1	9.0 ± 0.02
FIC22	lagoon water	20.8786	-90.3620	10.05	22.522	28.1	1.43 ± 0.05	0.70876 ± 0.00003	38.4 ± 0.4	96.3 ± 0.1	254.0 ± 0.1	10.3 ± 0.03
FIC8	lagoon water	20.8775	-90.3556	10.19	14.266	24.4	-2.15 ± 0.04	0.70863 ± 0.00003	22.0 ± 0.1	69.7 ± 0.1	230.7 ± 0.2	8.8 ± 0.01
FIC7	spring water	20.8775	-90.3546	10.19	8.871	25.8	-2.87 ± 0.03	0.70850 ± 0.00003	14.9 ± 0.1	58.1 ± 0.1	231.1 ± 0.4	7.4 ± 0.03
FIC9	lagoon water	20.8754	-90.3596	10.45	25.516	30.7	1.43 ± 0.06	0.70883 ± 0.00003	41.3 ± 0.5	89.0 ± 0.1	203.6 ± 0.5	9.9 ± 0.03
FIC10	lagoon water	20.8708	-90.3672	11.01	26.199	30.2	1.52 ± 0.05	0.70885 ± 0.00003	46.1 ± 0.6	98.1 ± 0.1	215.6 ± 0.1	10.8 ± 0.05
FIC11	lagoon water	20.8651	-90.3727	11.72	27.567	29.1	1.54 ± 0.04	0.70891 ± 0.00004	47.4 ± 0.6	101.2 ± 0.1	205.4 ± 0.3	10.8 ± 0.01
FIC12	lagoon water	20.8605	-90.3784	12.27	28.313	30	1.57 ± 0.04	0.70889 ± 0.00003	45.9 ± 0.6	94.2 ± 0.2	194.0 ± 0.1	10.5 ± 0.04
FIC19	lagoon water	20.8522	-90.3835	13.29	25.330	28.7	1.37 ± 0.04	0.70882 ± 0.00003	41.4 ± 0.6	89.0 ± 0.1	208.2 ± 0.1	10.0 ± 0.03
FIC18	lagoon water	20.8392	-90.3880	14.88	31.092	28.3	1.47 ± 0.03	0.70883 ± 0.00003	44.0 ± 0.5	92.0 ± 0.1	202.5 ± 0.4	10.2 ± 0.02
FIC17	spring water	20.8364	-90.3885	15.23	3.403	26.7	-3.70 ± 0.02	0.70821 ± 0.00003	6.2 ± 0.1	38.7 ± 0.1	253.5 ± 0.4	5.8 ± 0.01
FIC16	lagoon water	20.8254	-90.3863	16.58	27.436	28.1	1.46 ± 0.04	0.70891 ± 0.00003	48.3 ± 0.7	100.0 ± 0.1	196.7 ± 0.1	11.0 ± 0.03
FIC15	lagoon water	20.8113	-90.3943	18.31	31.995	27.8	1.76 ± 0.06	0.70900 ± 0.00003	49.8 ± 0.7	100.1 ± 0.1	155.4 ± 0.2	11.1 ± 0.05
FIC14	lagoon water	20.7889	-90.4028	21.04	34.091	27.6	1.76 ± 0.05	0.70907 ± 0.00003	53.1 ± 0.7	101.5 ± 0.1	132.9 ± 0.1	11.3 ± 0.04
FIC13	seawater*	20.7701	-90.4178	23.35	36.276	27.2	1.79 ± 0.05	0.70912 ± 0.00003	53.6 ± 0.6	102.2 ± 0.2	96.8 ± 0.1	11.4 ± 0.03

*measured 1 km offshore of lagoon and is higher than West Atlantic average value of ~44 nmolar (Hsieh and Henderson, 2017).
Errors represent 1 standard deviation from replicate standards. Distance is from the northern enclosed lagoon to the southern opening to the Gulf of Mexico.

Table 3.3 Mean endmember compositions for trace metals and isotope of water and foraminiferal calcite

Endmember (water)	Distance km	$\delta^{13}C_w$ ‰	$\delta^{18}O_w$ ‰	$^{87}Sr/^{86}Sr_w$	[Mg] mmolar	[Ca] mmolar	[Sr] µmolar	[Ba] nmolar	Salinity PSU	Temperature °C
Seawater (SW)	24	-	1.56 ± 0.05	0.70916 ± 0.00006	49.4 ± 1.3	11.4 ± 0.1	90.2 ± 0.3	44 ± 0.6	36.2	27.2
Fresh groundwater (FW)	10	-	-3.70 ± 0.02	0.70821 ± 0.00006	6.2 ± 0.1	5.8 ± 0.05	28.7 ± 0.3	253 ± 0.1	3.4	26.7
Brackish groundwater (BW)	1	-	4.27 ± 0.05	0.70832 ± 0.00005	33.7 ± 0.4	9.6 ± 0.06	109 ± 0.01	331 ± 2	17.1	33.2

Endmember (foraminifera)	Distance km	$\delta^{13}C_c$ ‰	$\delta^{18}O_c$ ‰	$^{87}Sr/^{86}Sr_c$	Mg/Ca mmol/mol		Sr/Ca mmol/mol	Ba/Ca µmol/mol		
Seawater (SWc)	21	-5.70 ± 0.13	-2.05 ± 0.06	0.70912 ± 0.00006	5.83 ± 0.79	-	1.86 ± 0.15	3.06 ± 1.6	32.0	-
Fresh groundwater (FWc)	10	-8.02 ± 0.13	-3.73 ± 0.06	0.70861 ± 0.00004	4.85 ± 0.28	-	2.74 ± 0.24	7.67 ± 0.54	21.3	-
Brackish groundwater (BWc)	1	*	-1.13 ± 0.06	0.70828 ± 0.00006	4.49 ± 0.13	-	2.69 ± 0.32	9.35 ± 0.76	18.8	-

* Range from -6.34 to -7.62 for foraminifera in close proximity to the BW source despite similar $\delta^{18}O_c$ (calcite) values.

Table S3.1 Downcore sampling locations and measured parameters

Core Station	Latitude	Longitude
2A, SPC2	20.91572	-90.35133
3A, SPC3	20.95624	-90.34215
3B	20.95626	-90.34219
4A, SPC4	20.95478	-90.33543
4B	20.95476	-90.33543
7A, SPC7	20.81873	-90.39037
8A, SPC8	20.87307	-90.367
UL-5	20.95895	-90.34065

Core	Interval top-bottom cm	Depth cm	$\delta^{13}C$ ‰	$\delta^{18}O$ ‰	$^{87}Sr/^{86}Sr$	Mg/Ca mmol/mol	Sr/Ca mmol/mol	Ba/Ca µmol/mol
2A-1P-1	5-6	5.5	-	-	-	5.01±0.1	2.44±0.05	6.75±0.31
2A-1P-1	10-11	10.5	-	-	-	5.21±0.1	2.43±0.05	6.84±0.31
2A-1P-1	15-16	15.5	-	-	-	4.61±0	2.64±0.05	7.37±0.31
2A-1P-1	20-21	20.5	-	-	-	4.68±0	2.42±0.05	6.48±0.31
2A-1P-1	25-26	25.5	-	-	-	4.5±0	2.46±0.05	6.66±0.31
2A-1P-1	30-31	30.5	-	-	-	4.65±0	2.36±0.05	6.92±0.31
2A-1P-1	35-36	35.5	-	-	-	4.98±0.1	2.45±0.05	7.39±0.31
2A-1P-1	40-41	40.5	-	-	-	5.11±0.1	2.36±0.05	6.7±0.31
2A-1P-1	45-46	45.5	-	-	-	5.09±0.1	2.36±0.05	5.72±0.31
2A-1P-1	50-51	50.5	-	-	-	3.89±0	2.32±0.05	5.6±0.31
2A-1P-1	55-56	55.5	-	-	-	5.84±0.1	2.41±0.05	6.93±0.31
2A-1P-1	60-61	60.5	-	-	-	5.23±0.1	2.37±0.05	6.69±0.31
2A-1P-1	65-66	65.5	-	-	-	5.12±0.1	2.33±0.05	7.12±0.31
2A-1P-1	70-71	70.5	-	-	-	5.81±0.1	2.4±0.05	7.01±0.31
2A-1P-1	75-76	75.5	-	-	-	4.88±0.1	2.26±0.05	5.13±0.31
2A-1P-1	80-81	80.5	-	-	-	4.66±0.1	2.22±0.05	5.52±0.31
2A-1P-1	85-86	85.5	-	-	-	4.6±0.1	2.14±0.05	5.65±0.31
2A-1P-1	90-91	90.5	-	-	-	3.84±0.1	2.2±0.05	5.77±0.31
2A-1P-1	100-101	100.5	-	-	-	4.06±0.1	1.94±0.05	4.59±0.16
2A-1P-1	110-111	110.5	-	-	-	4.38±0.1	1.98±0.05	5.21±0.31

2A-1P-1	117-118	117.5	-	-	-	4.4±0.1	2±0.05	4.85±0.31
2A-2B-1	2-3	125.5	-	-	-	4.89±0.1	2.26±0.05	5.69±0.31
2A-2B-1	5-6	128.5	-	-	-	4.09±0.1	2.2±0.05	4.89±0.31
2A-2B-1	10-11	133.5	-	-	-	4.78±0.1	2.15±0.05	5.65±0.31
2A-2B-1	15-16	138.5	-	-	-	3.79±0.1	2.09±0.05	5.25±0.31
2A-2B-1	18-19	141.5	-	-	-	4.28±0.1	2.13±0.05	5.89±0.31
2A-2B-1	42-43	165.5	-	-	-	4.75±0.1	1.96±0.05	5.02±0.31
2A-2B-1	45-46	168.5	-	-	-	3.86±0.1	1.81±0.05	3.39±0.16
3A-1P-1	2-3	2.5	-6.48±0.13	-1.18±0.06	-	4.75±0.07	2.67±0.01	8.46±0.06
3A-1P-1	7-8	7.5	-6.31±0.13	-1.17±0.06	-	4.79±0.04	2.82±0.01	7.72±0.11
3A-1P-1	12-13	12.5	-7.55±0.13	-1.05±0.06	-	4.8±0.05	2.84±0.01	7.65±0.11
3A-1P-1	20-21	20.5	-7.91±0.13	-1.51±0.06	-	4.52±0.05	2.82±0.01	7.39±0.11
3A-1P-1	27-28	27.5	0.02±0.13	-2.33±0.06	-	4.45±0.05	2.75±0.01	7.31±0.11
3A-1P-1	35-36	35.5	-6.52±0.13	-1.7±0.06	-	4.5±0.05	2.65±0.01	7.15±0.11
3A-1P-1	45-46	45.5	-5.72±0.13	-2.37±0.06	-	4.98±0.04	2.4±0.01	6.25±0.11
3A-1P-1	55-56	55.5	-5.64±0.13	-2.3±0.06	-	4.04±0.05	2.2±0.01	4.96±0.11
3A-1P-1	65-66	65.5	-5.62±0.13	-1.87±0.06	-	3.87±0.05	2.24±0.01	5.85±0.11
3A-1P-1	85-86	85.5	-5.29±0.13	-2.6±0.06	-	4.22±0.05	2.14±0.01	5.65±0.11
3A-1P-1	95-96	95.5	-6.26±0.13	-2.44±0.06	-	4.1±0.05	2.07±0.01	5.19±0.11
3A-1P-1	105-106	105.5	-5.13±0.13	-2.74±0.06	-	4.29±0.05	2.05±0.01	4.98±0.11
3A-1P-1	117-118	117.5	-	-	-	3.77±0.1	2.03±0.05	5.54±0.31
3A-1P-1	128.5-129.5	129	-	-	-	4.64±0.06	1.58±0.02	3.84±0.08
3A-1P-2	5-6	135.5	-	-	-	4.29±0.06	1.75±0.02	3.76±0.08
3A-1P-2	13-14	143.5	-	-	-	5.31±0.03	1.62±0.02	2.47±0.08
3A-1P-2	22-23	152.5	-	-	-	4.54±0.06	1.72±0.02	3.67±0.08
3A-1P-2	30-31	160.5	-	-	-	4.76±0.03	1.61±0.02	2.69±0.08
3A-1P-2	38-39	168.5	-	-	-	4.42±0.06	1.55±0.02	1.74±0.08
3A-3L-1	2-3	175	-	-	-	4.4±0.06	1.84±0.02	3.16±0.08
3A-3L-1	10-11	183	-	-	-	4.49±0.06	1.5±0.02	1.9±0.08

3A-3L-1	52-53	225	-	-	-	4.76±0.03	2.12±0.02	6±0.08
3A-3L-1	55-56	228	-	-	-	5.62±0.03	2.16±0.02	5.75±0.08
3A-4L-1	21-22	240.5	-	-	-	5.91±0.03	3.89±0.02	8.07±0.08
3B-2L-1	3-4	191.5	-	-	-	5.37±0.03	2.55±0.01	7.6±0.11
3B-2L-1	10-11	198.5	-	-	-	4.71±0.06	1.73±0.02	3±0.08
4A-1P-1	1-2	1.5	-7.12±0.13	-1.4±0.06	0.70839±0.00001	4.49±0.04	2.8±0.01	7.43±0.05
4A-1P-1	8-9	8.5	-7.2±0.13	-1.65±0.06	0.70837±0	6.18±0.04	2.69±0.01	24.42±0.05
4A-1P-1	12-13	12.5	-	-	-	5.05±0.03	2.69±0.02	7.94±0.08
4A-1P-1	15-16	15.5	-6.94±0.13	-1.36±0.06	0.70837±0.00002	7.44±0.03	2.3±0.1	8.63±0.22
4A-1P-1	17-18	17.5	-	-	-	4.94±0.03	2.63±0.02	8.51±0.08
4A-1P-1	22-23	22.5	-	-	-	5.24±0.03	2.76±0.01	8.01±0.08
4A-1P-1	24-25	24.5	-	-	-	6.05±0.03	2.8±0.02	9.26±0.36
4A-1P-1	27-28	27.5	-	-	-	5.81±0.03	2.61±0.02	7.26±0.08
4A-1P-1	30-31	30.5	-7.29±0.13	-1.29±0.06	0.70836±0.00002	6.02±0.03	2.38±0.1	8.02±0.22
4A-1P-1	33-34	33.5	-	-	-	5.09±0.03	2.47±0.02	7.67±0.08
4A-1P-1	35-36	35.5	-6.73±0.13	-1.78±0.06	0.70832±0.00002	6.14±0.03	2.38±0.1	7.87±0.22
4A-1P-1	37-38	37.5	-	-	-	4.91±0.03	2.46±0.02	6.14±0.08
4A-1P-1	40-41	40.5	-7.23±0.13	-2.49±0.06	0.7084±0.00002	6.92±0.03	2.11±0.1	7.03±0.22
4A-1P-1	45-46	45.5	-	-	-	5.43±0.03	2.51±0.02	7.02±0.08
4A-1P-1	50-51	50.5	-7.13±0.13	-2.74±0.06	0.70847±0.00002	-	2.3±0.01	6.9±0.12
4A-1P-1	55-56	55.5	-	-	-	6.03±0.03	2.35±0.02	7.01±0.08
4A-1P-1	60-61	60.5	-6.61±0.13	-2.41±0.06	0.70853±0.00001	6.36±0.03	2.11±0.1	7.45±0.22
4A-1P-1	65-66	65.5	-	-	-	4.84±0.03	2.27±0.02	6.11±0.08
4A-1P-1	70-71	70.5	-7.23±0.13	-2.71±0.06	0.70856±0.00003	-	2.21±0.01	6.22±0.12
4A-1P-1	75-76	75.5	-	-	-	4.82±0.03	2.23±0.02	6.23±0.08
4A-1P-1	80-81	80.5	-6.26±0.13	-1.87±0.06	0.70848±0.00002	6.91±0.03	1.94±0.1	7.56±0.22
4A-1P-1	85-86	85.5	-	-	-	4.37±0.06	2.06±0.02	4.73±0.08
4A-1P-1	90-91	90.5	-5.04±0.13	-1.56±0.06	-	3.63±0.04	2.19±0.01	4.8±0.05
4A-1P-1	95-96	95.5	-	-	-	4.65±0.06	1.98±0.02	4.69±0.08

4A-1P-1	100-101	100.5	-5.7±0.13	-2.13±0.06	0.70858±0.00003	6.62±0.03	1.88±0.1	5.29±0.22
4A-1P-1	105-106	105.5	-	-	-	3.85±0.06	1.97±0.02	6.48±0.08
4A-1P-1	108-109	108.5	-6.13±0.13	-2.55±0.06	0.70863±0.00002	5.09±0.03	1.75±0.1	5.28±0.22
4A-1P-1	109-110	109.5	-	-	-	4.8±0.03	1.99±0.02	5.21±0.08
4A-1P-1	120-121	120.5	-	-	-	4±0.06	1.91±0.02	4.35±0.08
4A-1P-1	128-129	128.5	-	-	-	4.89±0.03	2.05±0.02	4.92±0.08
4A-1P-1	135-136	135.5	-5.07±0.13	-1.9±0.06	0.70886±0.00003	5.73±0.03	1.56±0.1	4.86±0.22
4A-1P-1	140-141	140.5	-	-	-	4.94±0.03	1.61±0.02	3.15±0.08
4A-1P-1	145-146	145.5	-	-	-	4.77±0.03	1.56±0.02	2.95±0.08
4A-1P-1	148-149	148.5	-5.56±0.13	-1.92±0.06	-	4.91±0.04	1.66±0.02	3.1±0.08
4A-1P-1	150-151	150.5	-	-	-	4.42±0.06	1.57±0.02	3.01±0.08
4A-2B-1	5-6	143.5	-5.26±0.13	-1.7±0.06	0.70898±0.00001	-	-	-
4A-2B-1	2-3	153.5	-	-	-	4.74±0.03	2.14±0.02	5.53±0.08
4A-2B-1	10-11	161.5	-	-	-	5.64±0.03	1.62±0.02	3.12±0.08
4A-2B-1	14-15	165.5	-	-	0.70898±0.00001	4.13±0.06	1.47±0.02	2.55±0.08
4A-2B-1	20-21	171.5	-	-	-	6.62±0.03	1.59±0.02	3.17±0.08
4A-2B-1	25-26	176.5	-	-	-	-	-	-
4A-2B-1	35-36	186.5	-	-	0.70903±0	-	-	-
4A-2B-1	39-40	190.5	-	-	-	5.77±0.03	1.61±0.02	3.12±0.08
4A-2B-1	42-43	193.5	-	-	-	-	-	-
4A-2B-1	50-51	201.5	-4.63±0.13	-1.46±0.06	0.70904±0.00001	4.55±0.04	2.36±0.02	2.63±0.03
4A-2B-1	60-61	211.5	-	-	-	-	-	-
4A-2B-1	65-66	216.5	-	-	-	4.49±0.06	1.62±0.02	2.37±0.08
4A-2B-1	70-71	221.5	-	-	0.70906±0.00001	4.2±0.06	1.55±0.02	2.41±0.08
4A-2B-1	76-77	227.5	-6.37±0.13	-0.85±0.06	-	-	1.72±0.02	3.39±0.04
4A-2B-1	78-79	229.5	-	-	-	5.06±0.03	1.76±0.02	3.6±0.08
4A-2B-1	80-81	231.5	-	-	-	-	-	-
4A-2B-1	80-81	231.5	-	-	-	-	-	-
4A-2B-1	88-89	239.5	-	-	0.70804±0.00001	-	-	-

4A-2B-1	93-94	244.5	-	-	-	-	-	-
4A-2B-1	106-107	257.5	-	-	0.70807±0.00001	-	-	-
4B-2B-1	20-21	86.5	-6.96±0.13	-2.4±0.06	-	4.37±0.04	2.21±0.01	5.33±0.08
4B-2B-1	30-31	96.5	-5.91±0.13	-1.87±0.06	-	3.67±0.04	2.13±0.01	4.77±0.07
4B-2B-1	43-44	109.5	-	-	0.70864±0	3.85±0.04	2.04±0.01	4.31±0.07
4B-2B-1	65-66	131.5	-5.16±0.13	-2.69±0.06	-	4.36±0.04	2.04±0.01	5.08±0.08
4B-2B-1	75-76	141.5	-	-	0.7087±0	3.63±0.04	1.95±0.01	4.3±0.07
4B-2B-1	93-94	159.5	-5.16±0.13	-2.23±0.06	-	4.18±0.04	1.81±0.01	3.33±0.07
4B-2B-1	103-104	169.5	-	-	-	4.1±0.04	1.96±0.01	4.34±0.08
4B-2B-1	123-134	279.5	-	-	-	4.58±0.06	1.61±0.02	3.2±0.08
7A-1P-1	10-11	10.5	-	-	-	3.32±0.03	1.83±0.01	3.94±0.11
7A-1P-1	15-16	15.5	-6.05±0.13	-1.59±0.27	0.70891±0.00002	4.1±0.07	2.03±0.01	3.24±0.07
7A-1P-1	30-31	30.5	-6.26±0.13	-1.96±0.4	0.70892±0.00002	-	1.8±0.01	3.14±0.07
7A-1P-1	40-41	40.5	-5.04±0.13	-2.07±0.2	-	-	1.81±0.01	3.2±0.07
7A-1P-1	49-50	49.5	-	-	-	-	-	-
7A-1P-1	64-65	64.5	-5.96±0.13	-2.08±0.06	-	4.97±0.07	2.15±0.01	4.59±0.07
7A-1P-1	72-73	72.5	-5.92±0.13	-1.6±0.16	-	4.32±0.07	1.9±0.01	3.8±0.07
7A-1P-1	80-81	80.5	-	-	-	3.75±0.06	1.86±0.02	3.68±0.1
7A-1P-1	90-91	90.5	-5.72±0.13	-2.1±0.08	0.70886±0.00002	4.34±0.07	2.78±0.01	-
7A-1P-1	100-101	100.5	-5.76±0.13	-1.71±0.31	-	8.06±0.07	2.23±0.01	2.57±0.07
7A-1P-1	109.5-110.5	110	-5.58±0.13	-2.07±0.22	-	3.16±0.07	1.78±0.01	3.5±0.07
7A-1P-1	120-121	120.5	-5.76±0.13	-2.17±0.16	0.70892±0.00002	4.51±0.07	1.86±0.01	4.47±0.07
7A-1P-1	128-129	128.5	-5.25±0.13	-2.09±0.07	-	3.54±0.07	1.79±0.01	3.77±0.07
7A-1P-1	138-139	138.5	-5.16±0.13	-1.77±0.06	0.7089±0.00002	-	1.97±0.02	4.99±0.07
7A-1P-1	145-146	145.5	-4.98±0.13	-1.68±0.06	-	3.76±0.07	1.78±0.01	3.33±0.07
7A-2L-1	5-6	154.5	-	-	-	3.95±0.06	1.65±0.02	3.14±0.1
7A-2L-1	25-26	174.5	-	-	-	6.2±0.1	1.54±0.02	2.65±0.1
8A-1P-1	0-2	1	-6.76±0.13	-2.59±0.06	-	4.65±0.02	2.23±0.1	5.3±0.03
8A-1P-1	3-4	3.5	-	-	-	5.93±0.04	2.3±0.1	5.34±0.14

8A-1P-1	5-6	5.5	-7.24±0.13	-3.17±0.06	-	4.53±0.02	2.22±0.1	5.27±0.03
8A-1P-1	7-8	7.5	-	-	-	4.5±0.04	2.11±0.1	6.02±0.14
8A-1P-1	10-11	10.5	-6.94±0.13	-2.93±0.06	0.70871±0.00002	7.97±0.03	2.04±0.1	5.79±0.22
8A-1P-1	12-13	12.5	-	-	-	4.66±0.04	2.13±0.1	5.47±0.14
8A-1P-1	15-16	15.5	-6.55±0.13	-2.52±0.06	-	4.76±0.03	2.18±0.01	5.13±0.08
8A-1P-1	17-18	17.5	-	-	-	4.77±0.04	2.1±0.1	5.01±0.14
8A-1P-1	20-21	20.5	-6.75±0.13	-2.82±0.06	0.70871±0.00003	-	1.94±0.1	5.52±0.22
8A-1P-1	22-23	22.5	-	-	-	4.86±0.04	2.14±0.1	5.11±0.14
8A-1P-1	30-31	30.5	-7.38±0.13	-2.93±0.06	0.70862±0.00002	7.31±0.03	2.09±0.1	5.9±0.22
8A-1P-1	32-33	32.5	-	-	-	4.68±0.04	2.25±0.1	5.02±0.14
8A-1P-1	35-36	35.5	-6.88±0.13	-2.91±0.06	-	5.51±0.03	2.27±0.01	5.95±0.08
8A-1P-1	37-38	37.5	-	-	-	4.38±0.04	2.19±0.1	5.83±0.14
8A-1P-1	40-41	40.5	-6.79±0.13	-3.18±0.06	0.70852±0.00003	-	1.94±0.1	5.97±0.22
8A-1P-1	42-43	42.5	-	-	-	4.28±0.04	2.17±0.1	5.12±0.14
8A-1P-1	45-46	45.5	-7.61±0.13	-2.87±0.06	-	4.54±0.04	2.13±0.01	5.49±0.08
8A-1P-1	47-48	47.5	-	-	-	4.57±0.04	2.19±0.1	5.04±0.14
8A-1P-1	50-51	50.5	-6.82±0.13	-2.74±0.06	0.70865±0.00003	6.7±0.03	2.03±0.1	5.32±0.22
8A-1P-1	52-53	52.5	-	-	-	4.31±0.04	2.06±0.1	4.84±0.14
8A-1P-1	55-56	55.5	-6.48±0.13	-3.07±0.06	0.70858±0.00002	4.99±0.03	2.1±0.01	4.84±0.08
8A-1P-1	57-58	57.5	-	-	-	4.98±0.04	2.14±0.1	4.84±0.14
8A-1P-1	60-61	60.5	-6.64±0.13	-3.02±0.06	0.70864±0.00002	-	1.91±0.1	5.2±0.22
8A-1P-1	62-63	62.5	-	-	-	5.98±0.04	2.11±0.1	4.68±0.03
8A-1P-1	65-66	65.5	-6.81±0.13	-3.79±0.06	-	4.76±0.03	2.15±0.01	4.86±0.08
8A-1P-1	67-68	67.5	-	-	-	4.8±0.04	2.1±0.1	4.9±0.14
8A-1P-1	70-71	70.5	-5.94±0.13	-2.71±0.06	-	4.82±0.04	2.07±0.01	4.97±0.05
8A-1P-1	72-73	72.5	-	-	-	4.85±0.04	2.12±0.1	5.31±0.14
8A-1P-1	75-76	75.5	-	-	-	4.72±0.04	2.08±0.1	5.47±0.14
8A-1P-1	77-78	77.5	-	-	-	3.61±0.04	2.22±0.1	4.77±0.14
8A-1P-1	80-81	80.5	-6.32±0.13	-2.49±0.06	-	3.97±0.04	2.19±0.01	4.92±0.05

8A-1P-1	81-82	81.5	-	-	-	5.03±0.04	2.13±0.1	6.42±0.14
8A-1P-1	82-83	82.5	-	-	-	5.07±0.04	2.11±0.01	4.79±0.05
8A-1P-1	84-85	84.5	-	-	-	4.73±0.04	2.03±0.1	3.81±0.03
8A-1P-1	85-86	85.5	-6.67±0.13	-2.97±0.06	-	4.74±0.04	2.12±0.01	5.42±0.08
8A-1P-1	87-88	87.5	-	-	-	4.93±0.04	2.1±0.1	5.54±0.14
8A-1P-1	90-91	90.5	-7.25±0.13	-3.61±0.06	-	5.33±0.04	2.09±0.01	6.03±0.05
8A-1P-1	95-96	95.5	-	-	-	5.53±0.04	2.13±0.1	5.93±0.14
8A-1P-1	97-98	97.5	-	-	-	3.74±0.04	1.98±0.1	5.61±0.14
8A-1P-1	100-101	100.5	-6.02±0.13	-2.87±0.06	-	4.5±0.04	2.22±0.01	5.43±0.05
8A-1P-1	102-103	102.5	-	-	-	4.69±0.04	2.18±0.1	5.5±0.14
8A-1P-1	105-106	105.5	-	-	-	4.66±0.04	2.21±0.1	4.91±0.14
8A-1P-1	107-108	107.5	-	-	-	4.01±0.04	2.02±0.1	4.05±0.03
8A-1P-1	110-111	110.5	-	-	-	4.97±0.03	2.11±0.01	4.7±0.07
8A-1P-1	112-113	112.5	-	-	-	6.45±0.04	2.27±0.1	6.14±0.14
8A-1P-1	115-116	115.5	-7.1±0.13	-3.37±0.06	0.70865±0.00003	4.56±0.03	2.11±0.01	5.46±0.08
8A-1P-1	117-118	117.5	-	-	-	4.53±0.04	2.11±0.1	6.42±0.14
8A-1P-1	120-121	120.5	-6.41±0.13	-2.75±0.06	-	4.39±0.04	2.21±0.01	5.69±0.05
8A-1P-1	130-131	130.5	-	-	-	4.45±0.04	2.22±0.1	5.38±0.14
8A-1P-1	132-133	132.5	-	-	-	4.7±0.04	2.09±0.1	5.39±0.14
8A-1P-1	134-135	134.5	-	-	0.70866±0.00002	4.97±0.03	2.17±0.01	5.16±0.08
SPC2	0-2	1	-6.85±0.13	-2.28±0.06	0.7085±0.00001	7.11±0.03	2.32±0.1	7.33±0.22
SPC3	0-2	1	-6.31±0.13	-1.84±0.06	0.70831±0.00002	6.65±0.03	2.74±0.1	9.35±0.39
SPC3	2-4	3	-	-	-	4.11±0.1	2.76±0.1	7.43±0.17
SPC3	4-6	5	-	-	-	4.68±0.1	2.73±0.1	7.59±0.17
SPC3	6-8	7	-	-	-	4.41±0.1	3.02±0.1	8.32±0.17
SPC3	8-10	9	-	-	-	3.81±0.1	3.08±0.1	7.89±0.17
SPC3	10-12	11	-	-	-	4.05±0.1	2.86±0.1	7.57±0.17
SPC3	12-14	13	-	-	-	4.26±0.1	2.7±0.1	7.29±0.17
SPC3	14-16	15	-	-	-	4.67±0.1	2.8±0.1	7.92±0.17

SPC3	16-18	17	-	-	-	4.87±0.03	3.15±0.1	7.7±0.17
SPC3	18-20	19	-	-	-	5.2±0.03	2.83±0.1	7.14±0.17
SPC3	20-22	21	-	-	-	5.67±0.03	2.53±0.1	7.79±0.17
SPC4	0-2	1	-7.62±0.13	-1.94±0.06	0.70839	-	-	-
SPC4	2-4	3	-	-	-	5.5±0.1	2.48±0.02	8.61±0.07
SPC4	4-6	5	-	-	-	5.55±0.1	3.02±0.02	8.91±0.08
SPC4	6-8	7	-	-	-	5.17±0.1	2.66±0.02	7.94±0.07
SPC4	8-10	9	-	-	-	5.64±0.1	2.71±0.02	15.29±0.08
SPC4	10-12	11	-	-	-	3.84±0.06	2.55±0.02	6.64±0.07
SPC4	12-14	13	-	-	-	5.09±0.1	2.65±0.02	7.47±0.07
SPC4	14-16	15	-	-	-	4.83±0.1	3.09±0.02	8.49±0.07
SPC4	16-18	17	-	-	-	5.71±0.1	2.86±0.02	8.62±0.07
SPC4	18-20	19	-	-	-	4.77±0.1	2.68±0.02	8.1±0.07
SPC7	0-2	1	-5.7±0.13	-1.44±0.36	0.70892	-	1.72±0.02	3.52±0.03
SPC7	2-4	3	-	-1.85	-	3.29±0.06	1.85±0.02	3.74±0.1
SPC7	4-6	5	-	-	-	-	1.96±0.02	4±0.1
SPC7	6-8	7	-	-1.73	-	3.59±0.06	1.87±0.02	3.7±0.1
SPC7	14-16	15	-	-1.83	-	7.33±0.1	2.05±0.02	4.42±0.1
SPC7	16-18	17	-	-1.98	-	-	-	-
SPC7	18-20	19	-	-	-	4.09±0.06	1.78±0.02	3.38±0.1
SPC7	18-20	19	-	-	-	4.09±0.06	1.78±0.02	3.38±0.1
SPC8	0-2	1	-6.95±0.13	-2.91±0.06	0.70875±0.00002	7.32±0.03	2.01±0.1	6.13±0.22
SPC8	2-4	3	-	-	-	4.79±0.1	2.13±0.02	5.07±0.07
SPC8	0-8	4	-6.59±0.13	-2.55±0.06	-	6.02±0.03	2.01±0.1	5.67±0.22
SPC8	4-6	5	-	-	-	4.84±0.1	2.03±0.02	4.67±0.1
SPC8	6-8	7	-	-	-	4.61±0.06	2.3±0.02	4.61±0.1
SPC8	8-10	9	-	-	-	4.73±0.1	2.19±0.02	4.77±0.07
SPC8	10-12	11	-	-	-	3.84±0.06	2.11±0.02	5.05±0.07
SPC8	12-14	13	-	-	-	5.85±0.1	2.24±0.02	4.7±0.1

SPC8	14-16	15	-	-	-	4.93±0.1	2.28±0.02	4.41±0.1
SPC8	16-18	17	-	-	-	4.12±0.06	2.22±0.02	4.46±0.1
SPC8	18-20	19	-	-	-	4.7±0.06	2.13±0.02	4.81±0.07
SPC8	20-22	21	-	-	-	6.27±0.1	2.23±0.02	4.95±0.07
SPC8	22-24	23	-	-	-	3.97±0.06	2.22±0.02	4.95±0.07
UL-5	64.5-66	65.25	-	-2.13	0.70856±0.00001	6.86±0.03	2.17±0.02	6.26±0.08
UL-5	70-72	71	-	-1.83	-	5.46±0.03	2.36±0.02	6.17±0.08
UL5	75-76	75.5	-	1.94	-	5.36±0.03	2.44±0.02	6.42±0.08
UL5	79-81	80	-	2.15	0.70854±0.00001	6.14±0.03	2.44±0.02	7.42±0.08
UL5	85-87	86	-	1.7	-	3.99±0.06	2.38±0.02	6.07±0.08
UL5	91-92	91.5	5.75±0.13	2.26±0.06	-	4.51±0.03	2.3±0.01	6.42±0.12
UL5	96-97	96.5	-	2.11	0.708-54±0.00001	4.86±0.03	2.07±0.02	6.15±0.08
UL5	101-103	102	-	2.29	-	-	2.19±0.02	6.84±0.08
UL5	105-106	105.5	-	2.29	-	4.93±0.03	2.01±0.02	5.43±0.08
UL5	108-109	108.5	-	2.28	0.70853±0.00001	5.93±0.03	2.12±0.02	6.12±0.08
UL5	111-112	111.5	-		-	6.57±0.1	2.06±0.05	5.29±0.31
UL5	115-116	115.5	-	1.81	-	-	1.67±0.02	2.73±0.08
UL5	120-121	120.5	-			-	-	-
UL5	125-126	125.5	-	1.91	0.70867±0.00001	-	-	-
UL5	130-131	130.5	-	1.59		-	-	-
UL5	135-136	135.5	-	1.79	0.70867±0.00002	-	-	-
UL5	140-141	140.5	-			5.43±0.03	1.98±0.1	3.9±0.13
UL5	145-146	145.5	-	1.2	0.70886±0.00001	-	-	-

Errors, when given, represent 1 standard deviation from replicate standards.
Cores are presented as station, drive and instrument, and section, e.g. station 2A drive 1 Piston corer section 1. P = Piston, B = Bolivia, L = Livingstone

Table S3.2 Coretop sampling locations and measured parameters

Core	Interval cm	Latitude	Longitude	Distance km	$\delta^{13}C$ ‰	$\delta^{18}O$ ‰	$^{87}Sr/^{86}Sr$	Mg/Ca mmol/mol	Sr/Ca mmol/mol	Ba/Ca µmol/mol
UL-1	0-2	20.9593	-90.3398	0.17	-7.07±0.13	-1.76±0.06	0.70832±0.00002	6.53±0.03	2.65±0.02	9.07±0.03
SPC3	0-2	20.9562	-90.3422	0.54	-6.31±0.13	-1.84±0.06	0.70831±0.00002	6.65±0.03	2.74±0.02	9.35±0.03
4A-1P-1	1-2	20.9548	-90.3354	0.72	-7.12±0.13	-1.40±0.06	0.70839±0.00001	4.49±0.04	2.80±0.02	7.43±0.03
SPC4	0-2	20.9548	-90.3354	0.72	-7.62±0.13	-1.94±0.06	0.70839±0.00002	-	-	-
FIC15-3	0-1	20.9532	-90.3317	0.92	-	-	-	-	-	-
FIC15-3	1-2	20.9532	-90.3317	0.92	-	-	-	-	-	-
FIC15-3	0-2	20.9524	-90.3296	1.02	-6.98±0.13	-1.08±0.06	0.70859±0.00002	4.71±0.05	2.71±0.02	7.69±0.03
FIC15-4	0-1	20.9524	-90.3296	1.02	-	-	-	-	-	-
FIC15-4	1-2	20.9524	-90.3296	1.02	-	-	-	-	-	-
FIC15-1	0-1	20.9501	-90.3370	1.30	-6.41±0.13	-1.68±0.06	-	5.05±0.02	2.79±0.02	8.94±0.03
FIC15-1	1-2	20.9501	-90.3370	1.30	-7.21±0.13	-1.91±0.06	-	4.85±0.02	2.85±0.02	8.71±0.03
FIC15-1&2	0-2	20.9501	-90.3370	1.30	-6.34±0.13	-1.08±0.06	0.70862±0.00003	4.82±0.05	2.69±0.02	6.83±0.03
FIC15-2	0-1	20.9501	-90.3370	1.30	-6.68±0.13	-1.70±0.06	-	4.88±0.02	2.91±0.02	9.24±0.03
FIC15-2	1-2	20.9501	-90.3370	1.30	-6.56±0.13	-2.97±0.06	0.70839±0.00002	8.71±0.03	2.43±0.02	8.94±0.03
SPC2	0-2	20.9157	-90.3513	5.51	-6.85±0.13	-2.28±0.06	0.70850±0.00001	7.11±0.03	2.32±0.02	7.33±0.03
SPC5	0-2	20.8938	-90.3558	8.20	-6.48±0.13	-2.55±0.06	0.70858±0.00002	7.70±0.03	2.26±0.02	7.86±0.03
SPC9	0-2	20.8796	-90.3663	9.93	-7.63±0.13	-2.73±0.06	0.70861±0.00003	6.80±0.03	2.12±0.02	5.90±0.03
8A-1P-1	0-2	20.8731	-90.3670	10.73	-6.76±0.13	-2.59±0.06	-	4.65±0.02	2.23±0.02	5.30±0.03
8A-1P-1	0-2	20.8731	-90.3670	10.73	-6.76±0.13	-2.59±0.06	-	4.65±0.02	2.23±0.02	5.30±0.03
SPC8	0-2	20.8731	-90.3670	10.73	-6.95±0.13	-2.91±0.06	0.70875±0.00002	7.32±0.03	2.01±0.02	6.13±0.03
SPC8	0-2	20.8731	-90.3670	10.73	-6.95±0.13	-2.91±0.06	0.70875±0.00002	7.32±0.03	2.01±0.02	6.13±0.03
FIC15-8	0-1	20.8718	-90.3666	10.89	-7.42±0.13	-3.22±0.06	-	7.12±0.03	2.02±0.02	6.43±0.03
FIC15-8	1-2	20.8718	-90.3666	10.89	-7.17±0.13	-2.99±0.06	0.70873±0.00002	7.53±0.03	1.96±0.02	5.92±0.03
ML-3-1	0-1	20.8646	-90.3790	11.77	-6.47±0.13	-2.90±0.06	0.70868±0.00001	9.46±0.03	2.06±0.02	5.92±0.03
ML-3-1	1-2	20.8646	-90.3790	11.77	-7.04±0.13	-2.50±0.06	-	-	-	-

MS-2-1	0-1	20.8638	-90.3732	11.87	-7.02±0.13	-3.12±0.06	0.70875±0.00002	7.06±0.03	1.95±0.02	4.45±0.03
MS-2-1	1-2	20.8638	-90.3732	11.87	-5.88±0.13	-2.55±0.06	-	4.69±0.02	2.19±0.02	4.65±0.03
FIC15-7	0-1	20.8607	-90.3762	12.24	-7.57±0.13	-2.57±0.06	-	4.77±0.02	2.36±0.02	5.96±0.03
FIC15-7	1-2	20.8607	-90.3762	12.24	-6.97±0.13	-3.11±0.06	-	7.31±0.02	-	2.62±0.03
MS-1-2	0-1	20.8600	-90.3754	12.33	-7.17±0.13	-3.05±0.06	-	4.30±0.04	2.09±0.02	5.16±0.03
MS-1-2	1-2	20.8600	-90.3754	12.33	-7.14±0.13	-2.98±0.06	0.70873±0.00001	6.43±0.03	1.98±0.02	4.72±0.03
FIC15-19	0-2	20.8522	-90.3835	13.29	-6.27±0.13	-2.92±0.06	0.70900±0.00003	6.99±0.03	1.79±0.02	4.70±0.03
FIC15-6	0-1	20.8522	-90.3835	13.29	-6.94±0.13	-2.16±0.06	-	3.99±0.02	2.20±0.02	4.85±0.03
FIC15-6	1-2	20.8522	-90.3835	13.29	-7.01±0.13	-2.66±0.06	-	4.46±0.02	2.37±0.02	4.79±0.03
FIC15-18	0-2	20.8392	-90.3880	14.88	-6.79±0.13	-2.70±0.06	0.70904±0.00003	5.22±0.05	2.02±0.02	4.69±0.03
FIC15-5	0-1	20.8392	-90.3880	14.88	-	-	0.70885±0.00002	7.29±0.03	1.81±0.02	4.44±0.03
FIC15-5	1-2	20.8392	-90.3880	14.88	-6.56±0.13	-2.97±0.06	0.70888±0.00002	6.73±0.03	1.81±0.02	3.97±0.03
SPC6	0-2	20.8216	-90.3978	17.03	-5.84±0.13	-2.49±0.06	-	4.04±0.02	2.08±0.02	3.92±0.03
SPC7	0-2	20.8187	-90.3904	17.39	-5.70±0.13	-1.44±0.06	0.70892±0.00002	-	1.72±0.02	3.52±0.03
LL-1	1-2	20.7740	-90.4067	22.88	-6.69±0.13	-0.88±0.06	-	-	-	-
LL-1	0-1	20.7740	-90.4067	22.88	-	-1.41±0.06	-	-	-	-

Errors represent 1 standard deviation from replicate standards. Distance is from the northern enclosed lagoon to the southern opening to the Gulf of Mexico.

Table S3.3 Downcore endmember water contributions

Station	Age (Cal Yr BP)	Age (upper) (Cal Yr BP)	Age (lower) (Cal Yr BP)	Fresh %	Brackish %	Seawater %
4A	-52	-54	-51	29	51	20
4A	-49	-51	-47	17	65	18
4A	-2	-14	11	23	59	18
4A	62	23	115	16	67	17
4A	207	72	424	24	59	17
4A	369	153	697	15	69	16
4A	1311	736	1687	27	58	14
4A	1404	994	1680	42	36	22
4A	1600	1309	1800	46	26	28
4A	1795	1652	1893	37	33	31
4A	1932	1759	2110	43	23	34
4A	2057	1852	2274	26	49	26
4A	2362	2076	2654	29	37	34
4A	2513	2213	2830	37	24	38
4A	3033	2715	3297	17	30	53
4A	3188	2931	3404	9	30	61
4A	3378	3182	3578	22	16	62
4A	4072	3897	4290	2	34	64
7A	-3	-23	19	8	36	55
7A	198	71	415	17	26	57
7A	2296	1423	3128	9	41	49
7A	2894	2172	3593	22	25	53
7A	3441	2926	4035	22	21	58
7A	3742	3183	4468	13	32	55
7A	4088	3404	4928	8	30	62
8A	-53	-54	-52	43	9	48

8A	3	-10	16	44	11	45
8A	62	41	86	42	14	45
8A	198	102	327	47	15	39
8A	803	394	1162	55	13	33
8A	1007	646	1315	41	18	40
8A	1106	790	1390	51	13	36
8A	1208	945	1464	48	12	40
8A	2273	2056	2464	56	2	42
UL-5	1842	1542	2113	47	13	40
UL-5	2372	1872	2750	30	39	31
UL-5	2950	2823	3112	29	40	31
UL-5	3353	3078	3657	34	36	31
UL-5	3753	3565	3954	11	25	64
UL-5	3925	3696	4099	22	39	39
UL-5	4123	3851	4382	19	42	39
UL-5	4729	4376	4958	31	49	21
UL-5	5139	4701	5412	25	28	47
UL-5	5216	4784	5516	42	9	49

Table S3.4 Paleosalinity from Ba and Sr

Station	Age (Cal Yr BP)	Age (upper) (Cal Yr BP)	Age (lower) (Cal Yr BP)	Salinity (Sr fit)	Salinity upper (Sr fit)	Salinity lower (Sr fit)	Salinity (Ba fit)	Salinity upper (Ba fit)	Salinity lower (Ba fit)	Residual (Ba fit)	Standard error (Ba fit)
2A	-52	-54	-51	22.9	24.0	21.8	21.4	22.8	20.1	-	-
2A	-21	-27	-14	21.6	22.8	20.4	22.7	23.9	21.5	-	-
2A	12	-4	29	21.7	22.9	20.5	22.5	23.7	21.3	-	-
2A	61	23	111	19.4	21.0	17.8	21.4	22.7	20.0	-	-
2A	158	54	371	21.8	23.0	20.6	23.3	24.4	22.1	-	-
2A	258	91	530	21.3	22.6	20.1	22.9	24.0	21.7	-	-
2A	804	313	1289	22.5	23.6	21.3	22.3	23.5	21.1	-	-
2A	892	460	1297	21.4	22.6	20.2	21.3	22.7	19.9	-	-
2A	992	585	1373	22.5	23.6	21.3	22.8	24.0	21.6	-	-
2A	1089	686	1444	22.5	23.6	21.3	24.9	26.1	23.7	-	-
2A	1190	800	1511	22.8	23.9	21.7	25.2	26.4	24.0	-	-
2A	1291	931	1586	21.9	23.1	20.7	22.3	23.5	21.1	-	-
2A	1389	1053	1655	22.3	23.5	21.2	22.8	24.0	21.6	-	-
2A	1484	1174	1719	22.7	23.8	21.6	21.9	23.2	20.6	-	-
2A	1581	1299	1787	22.0	23.1	20.8	22.1	23.4	20.9	-	-
2A	1680	1465	1836	23.6	24.6	22.5	26.2	27.5	24.8	-	-
2A	1776	1642	1881	24.0	25.0	22.9	25.3	26.6	24.1	-	-
2A	1845	1715	1968	24.9	26.0	23.8	25.0	26.2	23.9	-	-
2A	1912	1780	2079	24.2	25.3	23.1	24.8	26.0	23.6	-	-
2A	2116	1905	2392	27.0	28.5	25.6	27.3	28.9	25.8	-	-
2A	2321	2057	2639	26.6	27.9	25.2	26.0	27.3	24.7	-	-
2A	2464	2177	2789	26.3	27.7	25.0	26.8	28.2	25.3	-	-
2A	2625	2325	2939	23.5	24.6	22.5	25.0	26.2	23.8	-	-
2A	2684	2386	2991	24.2	25.2	23.1	26.7	28.1	25.2	-	-
2A	2780	2484	3077	24.8	25.9	23.6	25.1	26.2	23.9	-	-

2A	2881	2583	3158	25.4	26.5	24.2	25.9	27.2	24.6	-	-
2A	2942	2655	3207	25.0	26.1	23.9	24.5	25.7	23.4	-	-
2A	3281	3100	3446	26.8	28.2	25.4	26.4	27.8	25.0	-	-
2A	3308	3147	3465	28.4	30.2	26.7	29.9	32.1	27.7	-	-
3A	-52	-54	-51	18.3	20.2	16.4	17.1	19.5	14.7	-	-
3A	-41	-45	-38	19.0	20.7	17.3	19.0	20.9	17.2	-	-
3A	-38	-42	-34	18.1	20.0	16.2	21.2	22.6	19.8	-	-
3A	-23	-30	-17	18.4	20.3	16.6	20.9	22.3	19.5	-	-
3A	-11	-18	-4	15.2	17.8	12.5	19.3	21.1	17.5	-	-
3A	-8	-16	1	17.4	19.5	15.3	20.6	22.1	19.1	-	-
3A	2	-11	15	14.5	17.4	11.7	20.2	21.8	18.7	-	-
3A	16	3	31	17.0	19.2	14.8	20.9	22.4	19.5	-	-
3A	29	10	49	17.2	19.3	15.1	20.7	22.2	19.3	-	-
3A	33	12	58	18.7	20.5	17.0	21.5	22.9	20.2	-	-
3A	50	18	93	17.6	19.6	15.6	20.2	21.8	18.6	-	-
3A	91	32	187	13.8	16.8	10.8	20.7	22.1	19.2	-	-
3A	131	40	310	17.3	19.4	15.2	21.8	23.1	20.6	-	-
3A	163	52	384	17.4	19.5	15.3	21.3	22.7	19.9	-	-
3A	174	59	397	20.6	22.0	19.2	20.5	22.0	18.9	-	-
3A	316	147	621	18.1	20.0	16.2	21.5	22.8	20.2	-	-
3A	1952	1079	2782	19.3	20.9	17.7	21.8	23.1	20.5	-	-
3A	2150	1300	2981	22.0	23.2	20.9	23.8	24.9	22.6	-	-
3A	2353	1522	3132	24.2	25.3	23.1	26.5	28.0	25.1	-	-
3A	2560	1764	3301	23.8	24.9	22.7	24.6	25.8	23.5	-	-
3A	2970	2226	3616	24.8	26.0	23.7	25.1	26.3	23.9	-	-
3A	3173	2469	3769	25.6	26.8	24.4	26.0	27.4	24.7	-	-
3A	3370	2741	3928	25.8	27.0	24.6	26.5	27.9	25.1	-	-
3A	3604	3031	4102	26.1	27.3	24.8	25.3	26.5	24.1	-	-
3A	3828	3303	4295	31.0	33.4	28.6	28.9	30.9	27.0	-	-

3A	3965	3469	4416	29.2	31.1	27.2	29.1	31.1	27.1	-	-
3A	4118	3672	4510	30.6	32.8	28.3	31.9	34.7	29.1	-	-
3A	4241	3822	4596	29.4	31.4	27.5	29.3	31.4	27.3	-	-
3A	4343	3978	4649	30.7	33.0	28.4	31.4	34.0	28.8	-	-
3A	4446	4132	4703	31.3	33.8	28.9	33.5	36.7	30.2	-	-
3A	4527	4238	4753	28.1	29.8	26.4	30.4	32.8	28.1	-	-
3A	4629	4401	4806	31.9	34.5	29.3	33.1	36.2	30.0	-	-
3A	5235	5033	5535	25.1	26.2	23.9	24.3	25.4	23.2	-	-
3A	5280	5108	5566	24.7	25.8	23.5	24.8	26.0	23.7	-	-
3A	5672	5389	5922	5.7	10.9	0.4	19.9	21.5	18.2	-	-
4A	-49	-51	-47	17.6	19.6	15.5	21.2	22.6	19.9	1.4	0.6
4A	-38	-42	-34	21.1	22.4	19.9	18.7	20.6	16.7	-1.1	0.6
4A	-23	-31	-16	15.2	17.8	12.5	18.0	20.2	15.9	-1.8	0.5
4A	-11	-19	-3	19.2	20.8	17.5	20.1	21.7	18.5	0.3	0.5
4A	-2	-14	11	18.8	20.5	17.0	-15.3	-3.0	-27.5	-	-
4A	1	-13	16	18.6	20.4	16.8	4.3	10.5	-1.8	-	-
4A	16	0	34	20.3	21.8	18.9	22.9	24.1	21.8	3.1	0.5
4A	30	9	54	18.8	20.6	17.1	20.1	21.7	18.5	0.3	0.4
4A	34	11	63	19.3	20.9	17.6	21.1	22.5	19.7	1.3	0.4
4A	52	16	102	14.4	17.3	11.6	19.0	20.8	17.1	-0.8	0.4
4A	62	23	115	23.1	24.2	22.1	18.6	20.6	16.7	-1.2	0.4
4A	93	33	189	17.0	19.2	14.8	18.7	20.6	16.7	-1.1	0.4
4A	103	36	217	19.5	21.1	17.9	18.9	20.8	17.0	-0.9	0.4
4A	133	42	304	19.0	20.7	17.2	19.8	21.5	18.1	0.0	0.4
4A	207	72	424	18.1	20.0	16.2	20.0	21.6	18.3	0.2	0.4
4A	207	72	424	18.1	20.0	16.2	20.0	21.6	18.3	0.2	0.4
4A	249	85	513	17.6	19.6	15.6	17.3	19.6	15.0	-2.5	0.5
4A	309	124	593	19.7	21.3	18.2	21.6	22.9	20.3	1.7	0.5
4A	369	153	697	22.2	23.3	21.0	20.0	21.6	18.3	0.1	0.6

4A	435	188	766	21.2	22.5	19.9	20.7	22.2	19.2	0.8	0.6
4A	1311	736	1687	22.2	23.4	21.1	20.3	21.8	18.7	-1.3	0.5
4A	1348	867	1681	21.3	22.6	20.0	24.0	25.1	22.9	2.3	0.5
4A	1404	994	1680	25.1	26.3	24.0	22.1	23.3	20.9	0.2	0.5
4A	1502	1146	1748	20.8	22.2	19.5	22.1	23.3	20.9	-0.1	0.4
4A	1600	1309	1800	23.1	24.2	22.0	22.4	23.6	21.2	-0.2	0.4
4A	1699	1472	1851	22.5	23.6	21.4	22.1	23.4	20.9	-0.8	0.4
4A	1795	1652	1893	25.1	26.3	24.0	21.2	22.6	19.8	-2.2	0.4
4A	1867	1708	2002	23.4	24.5	22.3	24.1	25.2	22.9	0.4	0.4
4A	1932	1759	2110	24.0	25.1	22.9	23.8	25.0	22.7	-0.1	0.4
4A	1996	1813	2197	23.9	25.0	22.8	23.8	24.9	22.7	-0.3	0.4
4A	2057	1852	2274	27.0	28.4	25.6	20.9	22.4	19.5	-3.5	0.4
4A	2119	1902	2347	25.8	27.0	24.5	27.0	28.5	25.5	2.3	0.4
4A	2184	1947	2444	24.3	25.4	23.2	26.9	28.4	25.4	1.9	0.3
4A	2266	2005	2535	26.6	27.9	25.2	27.1	28.7	25.6	1.8	0.3
4A	2362	2076	2654	27.6	29.2	26.1	25.8	27.1	24.5	0.1	0.3
4A	2458	2164	2777	26.7	28.1	25.4	23.3	24.4	22.1	-2.9	0.3
4A	2513	2213	2830	29.1	31.0	27.2	25.8	27.1	24.6	-0.5	0.3
4A	2531	2221	2853	26.5	27.9	25.2	26.0	27.3	24.7	-0.5	0.3
4A	2531	2221	2853	26.5	27.9	25.2	26.0	27.3	24.7	1.5	0.3
4A	2531	2221	2853	26.0	27.2	24.7	26.0	27.3	24.7	-0.5	0.3
4A	2531	2221	2853	26.0	27.2	24.7	26.0	27.3	24.7	1.5	0.3
4A	2531	2221	2853	26.5	27.9	25.2	27.9	29.7	26.2	-0.5	0.3
4A	2531	2221	2853	26.5	27.9	25.2	27.9	29.7	26.2	1.5	0.3
4A	2531	2221	2853	26.0	27.2	24.7	27.9	29.7	26.2	-0.5	0.3
4A	2531	2221	2853	26.0	27.2	24.7	27.9	29.7	26.2	1.5	0.3
4A	2745	2396	3054	27.3	28.8	25.8	27.8	29.5	26.2	0.5	0.3
4A	2898	2568	3187	25.9	27.1	24.6	26.6	28.0	25.2	-1.4	0.3
4A	3033	2715	3297	31.2	33.6	28.7	26.8	28.2	25.3	-1.7	0.3

4A	3130	2845	3370	30.6	32.9	28.4	30.4	32.8	28.1	1.6	0.4
4A	3225	2974	3435	31.2	33.7	28.8	30.9	33.3	28.4	1.7	0.4
4A	3273	3034	3457	30.1	32.2	27.9	30.5	32.9	28.1	1.2	0.4
4A	3302	3062	3482	31.1	33.5	28.7	30.7	33.2	28.3	1.3	0.4
4A	3329	3107	3514	24.8	25.9	23.7	25.3	26.5	24.1	-4.2	0.4
4A	3394	3209	3597	30.5	32.8	28.3	30.5	32.9	28.1	0.8	0.4
4A	3425	3253	3633	32.2	34.9	29.5	31.7	34.4	29.0	2.0	0.4
4A	3492	3336	3701	30.9	33.3	28.6	30.4	32.7	28.0	0.5	0.4
4A	3825	3634	4023	30.7	32.9	28.4	30.5	32.9	28.1	-0.1	0.5
4A	4072	3897	4290	22.4	23.6	21.3	31.6	34.2	28.9	-	-
4A	4072	3897	4290	32.3	35.1	29.6	31.6	34.2	28.9	-	-
4A	4538	4217	4876	30.5	32.8	28.3	32.1	34.9	29.3	1.1	0.7
4A	4700	4370	5009	31.3	33.8	28.9	32.0	34.8	29.2	1.1	0.8
4A	4889	4583	5123	29.5	31.5	27.5	29.9	32.1	27.7	-0.9	0.8
4A	4953	4636	5156	29.0	30.9	27.1	29.5	31.5	27.4	-1.2	0.8
7A	-56	-58	-54	29.5	31.5	27.5	29.6	31.8	27.5	-	-
7A	-48	-54	-43	28.0	29.7	26.4	29.2	31.2	27.1	-	-
7A	-41	-50	-32	26.9	28.3	25.4	28.6	30.5	26.7	-	-
7A	-35	-44	-26	27.8	29.4	26.2	29.2	31.3	27.2	-	-
7A	-23	-36	-6	28.2	29.9	26.5	28.7	30.6	26.8	-	-
7A	-6	-26	17	25.8	27.0	24.6	27.7	29.3	26.0	-	-
7A	-3	-23	19	26.0	27.3	24.7	30.2	32.5	27.9	-	-
7A	13	-10	42	28.8	30.6	27.0	29.9	32.2	27.7	-	-
7A	198	71	415	28.6	30.4	26.8	30.5	32.8	28.1	-	-
7A	1899	970	2809	28.5	30.2	26.7	30.3	32.7	28.0	-	-
7A	2374	1527	3190	24.7	25.8	23.6	27.3	28.9	25.8	-	-
7A	2534	1714	3315	27.5	29.0	25.9	29.0	31.0	27.0	-	-
7A	2694	1911	3443	27.9	29.6	26.3	29.3	31.3	27.2	-	-
7A	3097	2431	3729	23.9	25.0	22.8	31.7	34.4	29.0	-	-

7A	3287	2714	3849	28.8	30.7	27.0	29.7	31.8	27.5	-	-
7A	3441	2926	4035	27.9	29.6	26.3	27.6	29.2	26.0	-	-
7A	3550	3063	4201	28.7	30.4	26.9	29.1	31.1	27.1	-	-
7A	3742	3183	4468	26.7	28.1	25.3	26.5	27.9	25.1	-	-
7A	3884	3272	4657	28.8	30.6	26.9	30.0	32.3	27.8	-	-
7A	4067	3396	4900	30.2	32.4	28.1	30.5	32.8	28.1	-	-
7A	4475	3526	5757	31.4	33.9	29.0	31.5	34.2	28.9	-	-
8A	-53	-54	-52	23.8	24.9	22.8	25.8	27.1	24.5	-2.0	0.3
8A	-53	-54	-52	26.2	27.5	24.9	25.8	27.1	24.5	-2.0	0.3
8A	-53	-54	-52	23.8	24.9	22.8	24.0	25.2	22.9	-2.0	0.3
8A	-53	-54	-52	26.2	27.5	24.9	24.0	25.2	22.9	-2.0	0.3
8A	-40	-44	-37	24.9	26.1	23.8	26.3	27.7	24.9	0.2	0.3
8A	-37	-41	-33	23.1	24.2	22.0	25.7	27.0	24.5	-0.4	0.3
8A	-34	-39	-29	26.3	27.6	25.0	25.0	26.2	23.8	-1.1	0.3
8A	-27	-34	-21	26.1	27.4	24.8	27.2	28.7	25.6	1.0	0.2
8A	-25	-30	-19	23.9	25.0	22.9	25.9	27.2	24.6	-0.3	0.2
8A	-17	-23	-10	23.1	24.1	22.0	27.3	28.9	25.7	1.1	0.2
8A	-14	-21	-6	25.2	26.4	24.0	24.3	25.4	23.1	-2.0	0.2
8A	-6	-17	6	24.2	25.3	23.2	26.9	28.4	25.4	0.7	0.2
8A	3	-10	16	26.0	27.3	24.7	24.7	25.9	23.6	-1.5	0.2
8A	6	-6	18	25.2	26.3	24.0	26.3	27.7	25.0	0.1	0.2
8A	15	3	26	25.0	26.1	23.8	25.4	26.7	24.2	-0.9	0.2
8A	18	5	30	23.8	24.9	22.7	27.1	28.6	25.6	0.8	0.2
8A	30	11	48	23.4	24.4	22.3	27.7	29.4	26.1	1.4	0.2
8A	32	16	50	24.4	25.5	23.3	26.2	27.5	24.8	-0.2	0.2
8A	41	26	56	24.0	25.1	22.9	27.6	29.3	26.0	1.3	0.2
8A	44	28	60	25.3	26.5	24.1	26.4	27.8	25.0	0.1	0.2
8A	53	34	73	25.0	26.1	23.9	26.9	28.3	25.4	0.5	0.2
8A	62	41	86	27.1	28.5	25.6	25.3	26.6	24.1	-1.1	0.2

8A	66	46	88	23.9	25.0	22.8	26.6	28.0	25.2	0.2	0.2
8A	77	53	100	24.8	25.9	23.7	26.2	27.6	24.9	-0.2	0.3
8A	81	55	105	24.0	25.0	22.9	26.6	28.0	25.1	0.1	0.3
8A	198	102	327	25.4	26.5	24.2	24.5	25.7	23.4	-1.9	0.4
8A	238	142	367	23.6	24.7	22.6	26.4	27.8	25.0	0.0	0.4
8A	703	284	1088	23.4	24.5	22.4	24.4	25.5	23.3	-1.2	0.4
8A	743	336	1118	24.3	25.4	23.2	24.7	25.8	23.5	-1.0	0.4
8A	803	394	1162	27.0	28.5	25.6	24.4	25.5	23.2	-1.3	0.4
8A	843	446	1185	24.5	25.6	23.4	26.2	27.5	24.8	0.5	0.4
8A	905	514	1242	24.9	26.1	23.8	25.4	26.6	24.2	-0.3	0.3
8A	946	572	1268	24.3	25.4	23.2	26.4	27.7	25.0	0.6	0.3
8A	1007	646	1315	26.1	27.3	24.8	25.8	27.0	24.5	0.0	0.3
8A	1046	709	1338	25.7	26.9	24.5	26.8	28.3	25.3	1.0	0.3
8A	1106	790	1390	25.3	26.5	24.1	26.8	28.3	25.3	0.9	0.3
8A	1146	857	1419	24.8	25.9	23.7	26.8	28.3	25.3	0.8	0.3
8A	1208	945	1464	27.4	28.9	25.9	26.0	27.3	24.7	-0.1	0.3
8A	1250	1039	1487	25.2	26.3	24.0	27.1	28.7	25.6	1.0	0.3
8A	1315	1143	1535	24.8	25.9	23.7	26.7	28.2	25.3	0.5	0.3
8A	1367	1232	1568	25.3	26.4	24.1	26.7	28.1	25.2	0.3	0.3
8A	1449	1293	1669	25.6	26.8	24.4	26.5	27.9	25.1	0.1	0.3
8A	1518	1339	1752	25.0	26.2	23.9	25.8	27.1	24.5	-0.7	0.3
8A	1621	1392	1930	25.5	26.6	24.3	25.4	26.7	24.2	-1.0	0.3
8A	1692	1439	1976	24.0	25.1	22.9	27.0	28.4	25.5	0.5	0.3
8A	1793	1492	2086	24.2	25.3	23.2	26.6	28.0	25.2	0.3	0.3
8A	1817	1516	2099	24.9	26.0	23.8	23.4	24.5	22.3	-2.9	0.3
8A	1842	1542	2113	25.2	26.3	24.0	26.9	28.4	25.4	0.7	0.3
8A	1891	1580	2157	26.1	27.3	24.8	29.0	31.0	27.0	2.9	0.3
8A	1910	1595	2177	25.1	26.2	23.9	25.6	26.8	24.3	-0.5	0.3
8A	1934	1627	2198	25.3	26.4	24.1	25.3	26.5	24.1	-0.7	0.3

8A	1970	1669	2235	25.4	26.5	24.2	24.2	25.4	23.1	-1.7	0.2
8A	2029	1733	2284	25.0	26.1	23.8	24.4	25.6	23.3	-1.3	0.3
8A	2052	1763	2295	26.6	28.0	25.2	25.1	26.3	23.9	-0.5	0.3
8A	2087	1802	2321	24.0	25.0	22.9	25.5	26.8	24.3	-0.1	0.3
8A	2111	1837	2335	24.4	25.5	23.3	25.4	26.6	24.1	-0.1	0.3
8A	2147	1881	2360	24.1	25.1	23.0	26.7	28.1	25.2	1.2	0.3
8A	2171	1923	2374	26.2	27.5	24.9	28.5	30.3	26.6	3.1	0.3
8A	2207	1973	2399	25.2	26.4	24.0	27.1	28.6	25.6	1.8	0.3
8A	2233	2013	2418	23.4	24.5	22.3	24.0	25.1	22.9	-1.2	0.3
8A	2273	2056	2464	25.1	26.3	24.0	25.5	26.7	24.2	0.3	0.3
8A	2306	2080	2533	25.2	26.4	24.0	23.4	24.5	22.3	-1.7	0.3
8A	2356	2107	2637	24.1	25.2	23.0	25.0	26.2	23.8	-0.1	0.4
8A	2524	2221	2879	24.0	25.0	22.9	25.6	26.9	24.4	0.0	0.5
8A	2557	2247	2916	25.3	26.5	24.2	25.6	26.9	24.3	-0.2	0.6
8A	2591	2267	2969	24.5	25.6	23.4	26.1	27.4	24.8	0.0	0.7
UL-5	1844	1252	2362	24.5	25.7	23.4	23.7	24.9	22.6	-	-
UL-5	2047	1457	2518	22.5	23.6	21.3	23.9	25.1	22.8	-	-
UL-5	2207	1653	2640	21.5	22.7	20.3	23.4	24.5	22.3	-	-
UL-5	2372	1872	2750	21.5	22.8	20.3	21.2	22.6	19.9	-	-
UL-5	2585	2164	2882	22.2	23.4	21.1	24.2	25.3	23.0	-	-
UL-5	2772	2489	2995	23.1	24.1	22.0	23.4	24.5	22.3	-	-
UL-5	2950	2823	3112	25.6	26.8	24.4	24.0	25.1	22.8	-	-
UL-5	3137	2946	3396	24.3	25.4	23.2	22.5	23.7	21.3	-	-
UL-5	3253	3005	3570	26.2	27.5	24.9	25.5	26.8	24.3	-	-
UL-5	3353	3078	3657	25.0	26.2	23.9	24.0	25.2	22.9	-	-
UL-5	3455	3159	3756	25.9	27.1	24.6	28.6	30.5	26.7	-	-
UL-5	3455	3159	3756	25.8	27.0	24.5	28.6	30.5	26.7	-	-
UL-5	3455	3159	3756	25.9	27.1	24.6	25.8	27.1	24.5	-	-
UL-5	3455	3159	3756	25.8	27.0	24.5	25.8	27.1	24.5	-	-

UL-5	3592	3265	3882	30.0	32.1	27.9	31.3	33.9	28.7	-	-
UL-5	4215	3932	4488	26.6	28.0	25.3	28.8	30.7	26.9	-	-

Chapter 4

Investigating $\delta^{11}B$ variability in shallow benthic foraminifera *Ammonia parkinsoniana* and potential application as a paleospring discharge proxy of low-pH springs in the Yucatan Peninsula, Mexico

4.1 Abstract

The boron isotope system ($\delta^{11}B$) has been used to reconstruct the pH of ocean surface and deep water on a variety of timescales and as an isotope tracer in groundwater studies but has not been utilized for tracing the input of low-pH water sources, such as groundwater springs, into coastal water. Here, we investigate the utility of $\delta^{11}B$ in the benthic foraminifera *Ammonia parkinsoniana* as a spring paleo-discharge proxy into a coastal lagoon system. Samples were collected from surface sediments and down core from the spring-dominated tropical estuary Celestun Lagoon, Yucatan, Mexico and analysed for $\delta^{11}B$, $\delta^{13}C$, $^{87}Sr/^{86}Sr$, B/Ca, and Mg/Ca. Isotope ratios were compared to ratios in samples of source-waters to the lagoon. No significant difference was found between the $\delta^{11}B$ values of lagoon (38.82 ± 0.16‰) and spring-water (38.24 ± 0.45‰) samples, suggesting groundwater discharging at this site does not have a unique isotopic signature influencing $\delta^{11}B$ of lagoon water. *A. parkinsoniana* B isotope ratios ($\delta^{11}B_{calcite}$) in surface (0-2 cm) sediments ranged from 8.06 to 18.53 ‰ and demonstrated greater variability near springs compared to seawater-dominated sample sites and near beds of seagrass. Over at least the past 3,000 years, $\delta^{11}B_{calcite}$ also exhibits greater variability in down core samples collected

near springs compared to down core samples located further away from springs. Long-term decrease in B/Ca ratios measured in the same samples as $\delta^{11}B_{calcite}$ correlate with Ba/Ca and $^{87}Sr/^{86}Sr$, indicating lagoon total B concentration [B_T] (which is derived from mixing of spring water and seawater) controls B/Ca ratios of foraminifera. The low-pH spring discharge also affects $\delta^{11}B_{calcite}$. Respiration of sediment organic matter traced using $\delta^{13}C_{organic}$ and $\delta^{13}C_{calcite}$ suggests respired CO_2 (and hence total dissolved inorganic carbon) is a secondary control on B/Ca of benthic foraminifera. No relation between $\delta^{13}C_{calcite}$ and $\delta^{11}B_{calcite}$ is observed, likely due to the loss of sensitivity of the $\delta^{11}B$ below pH 6.7. Despite the large variability, mean $\delta^{11}B_{calcite}$ of benthic *A. parkinsoniana* agrees well with published data of other symbiont-barren benthic specimens, bolstering the overall framework of $\delta^{11}B_{calcite}$ dependence on pH, even in marginal marine environments dominated by carbonate. When combined with other proxy data, $\delta^{11}B_{calcite}$ in coastal systems may provide insight into coastal groundwater discharge and improve understanding of pH and equilibrium controls on $\delta^{11}B_{calcite}$ in shallow marine carbonate records available in deep time sedimentary archives.

4.2 Introduction

4.2.1 Ocean acidification and paleoclimate

As ocean acidification progresses with anthropogenic CO_2 emissions, greater attention has been devoted to reconstructing past periods of ocean acidification and understanding the implications for mortality and extinction of calcareous fauna (Wootton et al., 2008; Hönisch et al., 2012; Babila et al., 2016; Foster and Rae, 2016). A promising proxy for reconstructing carbonate system systematics has emerged in boron (B), both for its relation with carbonate ions and its stable isotopes in dissolved polyatomic ions. However, several recent reviews of the B isotope ($\delta^{11}B$) proxy (Henehan et al., 2015; Foster and Rae, 2016; Branson, 2018; Rae, 2018; Hönisch et al., 2019) demonstrate that there are several important unknowns regarding the proxy, including temperature effects on the fractionation factor α, mechanism of incorporation into calcite versus aragonite, fractionation effects in the conversion of trigonal to tetrahedral borate, magnitude and controls on species-specific vital effects in foraminifera (including planktic and benthic, symbiont-bearing and symbiont-barren), and the influence of calcite saturation state. While lab culture studies are instrumental for providing greater understanding of specific processes that control the final preserved $\delta^{11}B$, field calibration studies have the advantage of best reflecting calcifying conditions foraminifera experience prior to sediment deposition and have proven to be a useful method of understanding the total effect of carbonate chemistry on foraminifera B isotopes ($\delta^{11}B_{calcite}$) (Rae et al., 2011; Rae, 2018; Hönisch et al., 2019) and on boron to calcium ratios (B/Ca) (Yu and Elderfield, 2007; Yu et al., 2010; Quintana Krupinski et al., 2017).

Field studies have focused primarily on open-ocean surface and deep environmental conditions because these best reflect interactions with the atmosphere and bottom water circulation, respectively (Foster and Rae, 2016; Hönisch et al., 2019). Much less work has occurred in shallow coastal ecosystems, particularly in carbonate environments (Zhang et al., 2017). Although variability in the carbonate system parameters in these shallow coastal systems is much higher than in the deep ocean due to greater physical mixing (upwelling, riverine inputs) and biogeochemical cycling (e.g., carbon cycling, sulfate reduction, methanogenesis), such systems can provide insight to $\delta^{11}B$ behavior in shallow habitats ubiquitous in present and past oceans. Improved understanding $\delta^{11}B$ systematics in these environments is particularly important in order to apply $\delta^{11}B$ in deep time where shallow marine settings are more abundant in the geological record. In addition, study of $\delta^{11}B$ in carbonate sedimentary environments can provide information about the sensitivity of $\delta^{11}B$ to unique environmental variables characteristic of these systems and assess the limitations of applying the $\delta^{11}B$ proxy.

Here we present a field study of $\delta^{11}B$ and B/Ca behavior in the symbiont-barren benthic foraminifera *Ammonia parkinsoniana* from an estuary with a broad range of pH values in the Yucatan Peninsula, Mexico, a marine carbonate platform renowned for abundant low-pH (< 7.5) groundwater discharge (Pope et al., 1993; Perry et al., 2003; Bauer-Gottwein et al., 2011). The infaunal *Ammonia* genus was identified by Rae et al. (2011) as a possible specimen that has promise for use in paleo pH studies.

Lack of symbionts in this genus removes one source of variability while its large geographical range around tropical and temperate coasts provides diverse sites for comparison (Poag, 2015). *Ammonia* is also the most abundant foraminifera for this field site, providing ample calcite for a multi-proxy geochemical approach. To better understand B measurements in this species at this field site, we review below the currently known biogeochemical and geologic context in which *A. parkinsoniana* produces calcite tests and provide a summary of terms in Table 4.1.

4.2.2 B incorporation into benthic foraminifera

The $\delta^{11}B$ and B/Ca proxies in marine biogenic calcite ($\delta^{11}B_{calcite}$ and B/Ca) are modified from the composition of B in the ambient calcifying fluid, typically seawater ($\delta^{11}B_{sw}$). In seawater, B is partitioned primarily between two aqueous molecules, borate and boric acid ($B(OH)_4^-$ and $B(OH)_3$, respectively, (Zeebe et al., 2001)), which are in equilibrium following the equations:

$$B(OH)_3 + H_2O \leftrightarrow B(OH)_4^- + H^+ \quad (4.1)$$

$$K_B = \frac{[B(OH)_4^-][H^+]}{[B(OH)_3]}, pK_B \approx 8.6 \quad (4.2)$$

where pK_B is the equilibrium constant for boric acid dissociation. Thus the proportions of $B(OH)_3$ (trigonal structure) and $B(OH)_4^-$ (tetrahedral structure) (Hemming and Hanson, 1992; Hemming and Hönisch, 2007) in a solution are

determined by ambient pH. For the pH range common in the present day ocean (7.8 to 8.1), boron is present dominantly as boric acid (~80%) with ~20% borate (Rae, 2018). At lower pH (6.5 to 7.5), B is found almost exclusively as boric acid (Zeebe and Wolf-Gladrow, 2001). In addition, the isotope ^{11}B is preferentially incorporated into $B(OH)_3$, when compared to $B(OH)_4^-$, due to thermodynamic bonding energy differences (Zeebe and Wolf-Gladrow, 2001). The fractionation value has been determined to be 27.2 ‰ (α_B = 1.0272, (Klochko et al., 2006)), in agreement with recent measurements made by Nir et al. (2015). The $\delta^{11}B_{calcite}$ proxy works on the assumption that only $B(OH)_4^-$ is incorporated into marine carbonate with no further fractionation (Hemming and Hanson, 1992, but see recent reviews by Foster and Rae (2017), Rae (2018) and Hönisch et al., (2019)). The isotopic composition of aqueous borate is described by the equation after Foster and Rae (2016):

$$\delta^{11}B_{borate} = \frac{\delta^{11}B_{sw} + (\delta^{11}B_{sw} - \varepsilon_B) \times 10^{pK_B^* - pH}}{1 + \alpha_B \times 10^{pK_B^* - pH}} \quad (4.3)$$

where $\delta^{11}B_{borate}$ is the isotopic composition of aqueous borate, α_B = 1.0272 is the fractionation factor of B isotopes into each borate and boric acid species (Klochko et al., 2006), $\varepsilon = (\alpha_B - 1)*1{,}000$ is the fractionation factor in per mille units (27.2 ‰), and pK^*_B is the conditional equilibrium constant for boric acid dissociation (which is dependent on temperature, salinity, pressure, and ion activity). Note that pH must be on the total scale which is the scale for which the constants α_B and pK^*_B are defined (Hönisch et al., 2019).

The B/Ca proxy is based on the observation that B/Ca increases with the $B(OH)_4^-$ /HCO_3^- ratio in water, however research results are controversial on whether borate/carbonate ratios or carbonate saturation state are more important for planktic or benthic foraminifera (Henehan et al., 2015; Hönisch et al., 2019).

Reviews of specific mechanisms of B incorporation into biogenic and inorganic calcite can be found elsewhere (Balan et al., 2016; Uchikawa et al., 2017; Branson, 2018; Rae, 2018), but the important point is that mechanisms incorporating both $[B(OH)_4^-]$ and $[B(OH)_3]$ and rate of calcification may influence the final $\delta^{11}B_{calcite,}$ resulting in variability between species and within a species when calcifying conditions change. In synthetic calcite lab studies, $\delta^{11}B_{calcite}$ depends only on the solution pH and mineralogy of the phase precipitated, either calcite or aragonite (Noireaux et al., 2015). B/Ca depends only on the total B concentration, $[B_T]$, and on the total dissolved inorganic carbonate (TIC), were $[B_T]$/TIC best predicts calcite B/Ca at high precipitation rates (Uchikawa et al., 2015).

In foraminifera, B incorporation mechanisms are not fully known but have been studied under lab culture. Foraminifera calcify from seawater by transporting [Ca] and $[CO_3^{2-}]$ needed for calcification, possibly to internal reservoirs (Erez, 2003; de Nooijer et al., 2014), while $[B(OH)_4^-]$ (and maybe $[B(OH)_3]$) diffuse across the calcifying zone or they may be actively transported (Zeebe and Wolf-Gladrow, 2001). Species-specific offsets occur between different species of planktic foraminifera (Rae

et al., 2011; Hönisch et al., 2019). In planktic foraminifera, B/Ca is more sensitive to the increase of borate via [B_T] (at constant pH, TIC) than to pH-driven [$B(OH)_4^-$]/[CO_3^{2-}] (Hönisch et al., 2019). Planktic culture studies and field observations also show that B/Ca is related to [HCO_3^-] independent of pH via [$B(OH)_4^-$]/[HCO_3^-] ratios (Henehan et al., 2015; Howes et al., 2017; Quintana Krupinski et al., 2017).

For deep sea benthic foraminifera, lab calibrations have so far been unsuccessful, so field studies have been employed instead. Some deep see epifaunal benthic foraminifera show a linear relationship between B/Ca and degree of saturation, or $\Delta[CO_3^{2-}]$ (Yu and Elderfield, 2007), but other deep sea foraminifera also show a relationship between B/Ca and [$B(OH)_4^-$]/[CO_3^{2-}] of deep seawater (Rae et al., 2011). The $\delta^{11}B_{calcite}$ of deep sea specimens appear directly related to pH rather than any other parameter (Yu et al., 2010). Furthermore, differences are noted between epifaunal and infaunal taxa where infaunal specimens are about 2 ‰ lower than expected $\delta^{11}B_{borate}$ of the overlying water column (Rae et al., 2011), suggesting lower pH of porewater and thus some influence of biogeochemical cycling within sediments (e.g., respiration, remineralization of organic matter, or sulfate reduction). For *Ammonia beccarii*, a $\delta^{11}B_{calcite}$ = 14.56 ‰ was measured which is offset from $\delta^{11}B_{borate}$ in the seawater by 1.68 ‰ (Rae et al., 2011). This is the only $\delta^{11}B$ measurement in the genus *Ammonia* of which we are aware.

Much of the variability of $\delta^{11}B_{calcite}$ and B/Ca in planktic and benthic foraminifera has been ascribed to "vital effects," or biological influences in the process of calcification particular to each species. These may also be thought of as microenvironmental effects and specifically refer to conditions within a few hundred micrometers of the foraminifera test, including photosynthesis (CO_2 consumption), respiration (CO_2 production), and calcification (proton acidification) effects on pH (Zeebe et al., 2003). These vital effects contribute to the observed variability in the open ocean where they are the main source of variability on short time scales. For estuaries and coasts, the range of environmental conditions may be much greater than the range of variability attributed to vital effects and thus provide insight into additional first order environmental controls of $\delta^{11}B_{calcite}$ and B/Ca in coastal benthic foraminifera. This adds insight to otherwise scarce literature on environmental conditions that affect B systematics in shallow benthic calcifying taxa (Rollion-Bard and Erez, 2010).

4.2.3 Geologic influence on ambient $\delta^{11}B$ of water

Assuming α_B (and thus ε) is constant in equation 4.3 (see Klochko et al., 2006 and Hönisch et al., 2019), the two parameters that affect $\delta^{11}B_{borate}$ independent of pH are $\delta^{11}B_{sw}$ and pK^*_B (Table 4.1). These two parameters vary with B source signature and ion complexation effects, and while changes in the these parameters in the open ocean occur on timescales of millions of years, in coastal settings they may change

seasonally or interannually, substantially impacting the $\delta^{11}B_{calite}$, as summarized below.

4.2.3.1 Evolution of seawater $\delta^{11}B$

Most studies focus on the pH control of $\delta^{11}B$ in foraminifera, but the final $\delta^{11}B_{calcite}$ also depends on the initial $\delta^{11}B$ of the calcifying fluid, typically seawater ($\delta^{11}B_{sw}$). Modern seawater $\delta^{11}B_{sw}$ is 39.61 ‰ (Foster et al., 2010). Long-term changes in $\delta^{11}B_{sw}$ and $[B_T]$ depend on weathering of continental crust and hydrothermal alteration of ocean crust (Lemarchand et al., 2000). The 10 million years residence time of B in the oceans means $\delta^{11}B_{sw}$ is relatively invariant in the open ocean on time periods less than this scale, thus change in $\delta^{11}B_{calcite}$ generally reflects change in pH (with superimposed vital effects). For these longer time scales, studies suggest that the $\delta^{11}B_{sw}$ (and $[B_T]$) exhibit small but significant change in the ocean with a range of estimates generally between 36 ‰ and 40 ‰ for the Cenozoic (Hönisch et al., 2019 and references therein). For example the Miocene, $\delta^{11}B_{sw}$ is estimated at 37.6 ‰ (Raitzsch and Hönisch, 2013). Precipitation of marine carbonates in the Miocene will thus occur in water with $\delta^{11}B_{sw}$ typically lower than today, resulting in final $\delta^{11}B_{carbonate}$ that is also lower relative to carbonates precipitating today (Perry et al., 2009b; Zhang et al., 2017).

4.2.3.2 Marine carbonate and groundwater $\delta^{11}B$

Most analyzed marine carbonates of Cenozoic age (66 Ma to present) fall in a relatively small range of $\delta^{11}B_{carbonate}$ between 15 and 25 ‰ (Hemming and Hanson, 1992; Hemming and Hönisch, 2007). Typical modern marine carbonate $\delta^{11}B_{carbonate}$ of ~22 ‰ (Branson, 2018), recording an offset of about 17 ‰ from $\delta^{11}B_{sw}$ representing primarily the incorporation of $\delta^{11}B_{borate}$ into marine carbonates, including limestone. Dissolving limestone bedrock would thus impart a signature of $\delta^{11}B_{carbonate}$ between 15 ‰ and 25 ‰ to groundwaters running through such bedrock, assuming no additional fractionation these values will characterize the groundwater $\delta^{11}B_{gw}$. Indeed groundwater $\delta^{11}B_{gw}$ derived from marine sandstones exhibit $\delta^{11}B_{gw}$ values of 10 to 22 ‰, based on the carbonate cements within the sandstone (Mather and Porteous, 2001; Négrel et al., 2012). For coastal estuaries, $\delta^{11}B_{water}$ of estuarine water will reflect some mixing between $\delta^{11}B_{sw}$ and $\delta^{11}B_{gw}$ (groundwater in this study, but also riverine water where rivers exist). Mixing carbonate-derived groundwater with modern seawater would thus result in bulk $\delta^{11}B_{water}$ between 10 and 39.61 ‰ with the final value skewed toward the source contributing the most [B_T].

4.2.3.3 Evaporite $\delta^{11}B$

Marine carbonates may be accompanied by marine evaporites which have their own $\delta^{11}B_{evaporite}$ signatures derived from $\delta^{11}B_{sw}$. The range reported for $\delta^{11}B_{evaporite}$ is larger than for marine carbonates, in part because $\delta^{11}B_{evaporite}$ can reflect both $\delta^{11}B_{borate}$ in the

precipitated minerals and $\delta^{11}B_{boric\ acid}$ in residual fluids (Vengosh et al., 1992; Paris et al., 2010; Liu et al., 2014). In general, $\delta^{11}B_{evaporite}$ ranges between 11 and 36 ‰, with values closer to $\delta^{11}B_{sw}$ of 39.61‰ indicating primarily a trapped fluid signature (Paris et al., 2010). As with marine carbonates, where evaporites are dissolved into groundwater, they will impart a $\delta^{11}B_{evaporite}$ signature to $\delta^{11}B_{gw}$ which, when discharged into a lagoon, results in the final mixed $\delta^{11}B_{water}$ reflecting the sources based on their relative $[B_T]$.

4.2.3.4 [Mg] and [Ca] impact on B acid-base equilibria

Seawater $\delta^{11}B_{sw}$ directly affects $\delta^{11}B_{carbonate}$, but changes in concentration of [Mg] and [Ca] also affect $\delta^{11}B_{carbonate}$ by changing the equilibrium constants of acid-base chemistry for the B and carbon systems (Hain et al., 2015). [Mg] and [Ca] in seawater change over the10 million year timescale similar to $[B_T]$ (Berner and Berner, 1996; Lemarchand et al., 2002), and increases in these two elements affect ion pairing with $[CO_3^{2-}]$and thus the buffering capacity of the ocean. Changes to carbonate buffering system also impact the buffering capacity of the borate system. K^*_B is the conditional equilibrium constant for boric acid dissociation, one of the primary variables influencing $\delta^{11}B_{borate}$ through B speciation (the other primary variable being α_B), and is expressed on the log scale as pK^*_B (Farmer et al., 2019). For modern surface seawater at 25 °C, 35 salinity, 10.3 mmolar [Ca], and 52.8 mmolar [Mg], pK^*_B has been experimentally determined as 8.5975 (DOE, 1994). For comparison, for Eocene

seas (~56 Ma) at the same temperature and salinity but with 20 mmolar [Ca] and 30 mmolar [Mg], pK^*_B is 8.722 (Rae, 2018). The difference in pK^*_B for these two time periods results in a $\delta^{11}B_{calcite}$ difference of about 2 ‰ which can translate to a pH difference of up to 0.27 units (Hain et al., 2015; Rae, 2018).

Ocean [Mg] and [Ca], and thus borate-boric acid equilibrium constants, change on long timescales, but these dissolved metal concentrations can change over diurnal, seasonal, or interannual timescales in estuaries, particularly where fresh surface and groundwaters low in [Ca] and [Mg] mix with modern seawater. Short-term variations in [Mg] and [Ca] may occur on the timescale of foraminifera lifecycle and calcification of about 2 months (Murray, 2006). Therefore, if [Mg] and [Ca] dissolved from carbonate bedrock and mixed with seawater produces a range of concentration on par with the range between Eocene and the modern ocean, the impact of [Mg] and [Ca] on pK^*_B will need to be accounted for using the MyAMI model of Hain et al. (2015), providing an opportunity to further test behavior of $\delta^{11}B_{calcite}$ in shallow coastal and estuarine ecosystems. Typically in such environments, the salinity of the mixed water is also impacted by the amount of groundwater discharge with lower salinity coinciding with greater proportions of fresh meteoric groundwater present in the estuary.

4.2.4 Geologic context for this study

The Yucatan Peninsula of Mexico is a karst terrain composed of carbonates of Eocene, Miocene, and Pliocene age (Perry et al., 2003; Perry et al., 2009b). No major rivers or lakes occur on the peninsula, as most precipitation seeps through the highly permeable bedrock directly into the extensive limestone and dolostone karst lithology of the platform (Perry et al., 2003). Evaporites are also common (celestite, anhydrite) and dissolution provides favorable flow paths and elevated concentrations of [Sr], [K], and [SO_4^-], and high alkalinity to groundwaters (Perry et al., 2002; Gonneea et al., 2014). Radiogenic strontium isotopes ($^{87}Sr/^{86}Sr$) provide chemostratigraphy of the aquifer rocks and a serve as a tracer for groundwater flow paths, with Miocene limestones having $^{87}Sr/^{86}Sr$ signatures of 0.70830 (Perry et al., 2009b) compared to modern seawater (and modern limestone) value of 0.70916 (Beck et al., 2013).

An extensive cave network in the carbonate bedrock directs groundwater toward the coastal plains where a thin (10 to 100s of meters) freshwater lens is underlain by seawater intrusion. Around the east, north, and west coasts, groundwater discharges from seeps and springs, locally known as "ojos" (eyes), with discharge rates ranging between 26 to 45 m^3 /m /d (Bauer-Gottwein et al., 2011; Null et al., 2014; Gonneea et al., 2014). Groundwater is persistently low in pH due to respiration of plants and detrital carbon farther inland (Gonneea et al., 2014), and these coastal discharge sites have been used as natural laboratories for ocean acidification (Martinez et al., 2018; Wall et al., 2019). On the eastern Caribbean side, spring pH has been observed to be 7.65 ± 0.24 (Hofmann et al., 2011) and on the northwestern side to be 7.25 ± 0.56

(Gonneea et al., 2014). Wall et al. (2019) measured groundwater discharge $\delta^{11}B_{gw}$ as 38.85 ± 0.17 ‰, indicating the contribution of $\delta^{11}B_{carbonate}$ and $\delta^{11}B_{evaporite}$ to $\delta^{11}B_{gw}$ although the groundwater has mixed with the seawater intrusion (based on salinity) hence $\delta^{11}B_{sw}$ is also contributing to the mixture. The $\delta^{11}B_{gw}$ of groundwater not mixed with seawater within the interior of the peninsula is currently unknown.

In the northwestern corner of the peninsula, the biosphere reserve Celestun Lagoon sits between the carbonate platform and a Holocene-age barrier island dune complex (Chapter 2; Lowery and Rankey, 2017). The lagoon is surrounded by a highly productive mangrove ecosystem and waters with abundant calcareous fauna and primary producer communities (Herrera-Silveira et al., 1998, p.199; Gonneea et al., 2004; Pech et al., 2007). Groundwater discharge into the lagoon results in seasonally persistent salinity gradients (Herrera-Silveira, 1994) which in turn provide persistently low pH_{tot} conditions close to the springs (6.69-6.82) and a large pH_{tot} range over the lagoon length (7.26-8.06). Several studies have quantified geochemical fluxes for this lagoon, including nutrient fluxes, sulfate reduction, methanogenesis, dissolved and particulate organic carbon export, radium sources, and spring-sourced trace metal concentrations (Chapter 3; Herrera-Silveira, 1996; Young, 2005; Young et al., 2008; Stalker et al., 2014; Gonneea et al., 2014; Chuang et al., 2016; Chuang et al., 2017).

.

4.2.5 Multi-proxy approach

Few coretop calibration studies span a large enough pH range to constrain the limits and sensitivities of the $\delta^{11}B$ proxy (Rae, 2018). The wide range of pH occurring at groundwater discharge sites in the Yucatan, accompanied by variation in TIC , [B_T], [Mg], and [Ca], provide a natural laboratory to observe extreme (relative to open ocean) carbonate chemistry effects on [$B(OH)_4^-$] and $\delta^{11}B_{borate}$. However, marginal marine settings have additional variability absent or less prominent in surface or deep ocean settings, such as extensive mixing from wind and bioturbation, high rates of macro-vegetation photosynthesis, high rates of respiration and carbon remineralization, and active biogeochemical cycling from microbes within sediment porewaters (Chuang et al., 2016; Chuang et al., 2017).

Some of these processes can be quantified by using additional proxies in conjunction with $\delta^{11}B_{calcite}$ and B/Ca and by comparing to measured modern parameters. Recent work in Chapters 2 and 3 provides a body of proxy work against which to compare the B data. Elemental ratios of Ba/Ca and Sr/Ca in lagoon water follow the salinity trend with high ratios in freshwater, hence we expect that low salinity (low pH) conditions will correlate with high Ba/Ca and Sr/Ca in calcite and low $\delta^{11}B_{calcite}$. Mg/Ca and $\delta^{18}O$ of the calcite provide insight into changes in temperature and evaporation which both impact degassing of CO_2 and thus TIC of water. The $^{87}Sr/^{86}Sr$ ratio also correlates to salinity but more specifically signifies aquifer source,

indicating the age of rocks (Perry et al., 2009) and constraining expected $\delta^{11}B_{gw}$ signatures. Bulk sediment weight percent carbon (wt% C), organic carbon isotopes ($\delta^{13}C_{organic}$), and foraminifera calcite carbon isotopes ($\delta^{13}C_{calcite}$) track respiration of terrestrial vegetation and thus relative changes of porewater TIC, and these should correlate with B/Ca of foraminiferal calcite.

This study provides new $\delta^{11}B_{calcite}$, B/Ca and Mg/Ca data of foraminifera to compare to proxies presented in Chapter 3 and to compare to abiotic $\delta^{11}B_{carbonate}$ in shallow marine carbonate environments of the Bahamas (Zhang et al., 2017). In addition to expanding understanding of the limitations of $\delta^{11}B_{calcite}$ and B/Ca in general, this study also provides the first look at $\delta^{11}B_{calcite}$ as a paleospring discharge proxy. Coastal spring discharge may have substantial impact on baseline pH of coastal waters where calcareous fauna of interest reside and hence baseline $\delta^{11}B_{calcite}$ or $\delta^{11}B_{aragonite}$ recorded in biogenic carbonates of shallow marine communities. In deep time, prior to the evolution of foraminifera or extant corals, many carbonate organisms such as sponges, corals, and brachiopods have lived in shallow carbonate environments (Benton and Harper, 2009). As we observe the effect of CO_2 emissions on modern carbonate reefs and reconstruct past ocean acidification, it is important to consider the hydrogeologic processes that may also impact $\delta^{11}B_{borate}$ and thus $\delta^{11}B_{calcite}$ in shallow/shelf environments adjacent to coastal groundwater discharge of the past.

4.3 Materials and methods

4.3.1 Field site

Celestun Lagoon is a long, narrow (21 km by 2 km) shallow (0.5 to 3 m depth) semi-protected mangrove estuary on the northwestern corner of the Yucatan Peninsula (Figure 4.1) (Herrera-Silveira, 1994). Sediments are ~ 95% calcium carbonate and consist of fine authigenic carbonate mud, moderate siliceous ooze, and abundant calcareous fauna including bivalves, gastropods, and foraminifera (Lowery and Rankey, 2017). Remaining sediment composition consists of organic carbon derived from mangroves that are fringing the lagoon banks, beds of seagrass in the northern lagoon and lagoon shallow banks, and marine particulate matter from the southern opening to the ocean (Gonneea et al., 2004), and minor amounts of clay and biogenic silica (Lowery and Rankey, 2017). Groundwater springs and seeps populate the northern lagoon, discharging fresh and brackish groundwater resulting in a seasonally variable but persistent salinity gradient that responds to rainfall inland (Herrera-Silveira, 1994; Young et al., 2008). There are at least two different source aquifers discharging groundwater into Celestun Lagoon, characterized by distinct $^{87}Sr/^{86}Sr$ values and enriched in metal and ion concentrations (normalized to salinity) of strontium, barium, and sulfate relative to seawater (Young et al., 2008; Perry et al., 2009b; Stalker et al., 2014), resulting from carbonate and evaporite dissolution in the aquifer. Groundwater in this system has high dissolved inorganic carbon (6630 ±

1230 µmol /kg), total alkalinity (6460 ± 1210 µeq /kg), dissolved calcium (when normalized to chlorine) (3.8 ± 0.9 mmol/kg), and has low pH (7.25 ± 0.56) (Gonneea et al., 2014).

Climate in the region is humid tropical with daily temperatures between 25 and 35 °C and annual precipitation between 600 and 1500 mm /yr divided between a dry season from January to May, a wet season from June to October, and a variable windy season from October to December (Herrera-Silveira, 1994; Giddings and Soto, 2003; Bauer-Gottwein et al., 2011). Evapotranspiration rates are high for the northwestern region of the Yucatan Peninsula (Bauer-Gottwein et al., 2011).

4.3.2 Field methods

Three field expeditions recovered sediment samples from Celestun Lagoon (June 2006, June 2009 and May 2015) and included short (30 cm) and long (262 cm) cores (Table 4.2, Figure 4.1). Short cores were immediately extruded and sectioned in 2 cm intervals. Long cores collected in 2006 and 2009 were recovered with piston, Bolivia, and Livingstone corers provided by the National Lacustrine Core Facility (Minneapolis, Minnesota, USA), split into working and archive halves for cold storage, and subsampled in 1 cm intervals and analyzed at 5 cm resolution. From each subsample of 2 g aliquot of bulk sediment was removed for bulk C and N concentrations and isotope analysis. The remaining sediment was wet-sieved to 63

μm, shaken in 15 mL 1% sodium hexametaphosphate for 6 hours to deflocculate fine sediment, thoroughly rinsed with deionized water, and air-dried. The dried coarse fraction was sieved to 250-500 μm from which approximately 3 mg (~100 individuals) of the foraminifera *Ammonia parkinsoniana* were picked and gently crushed in an agate mortar and pestle to open chambers for cleaning and analysis. From each sediment interval, an additional 300 μg of *A. parkinsoniana* was sampled for trace metal analysis and another 60 μg for inorganic carbon and oxygen isotope analysis.

Between 2001 and 2015, water salinity was measured in situ with a Yellow Springs Instrument Model 63 handheld sonde. In 2015, temperature and pH (NBS scale, error = 0.03 units) also were measured *in situ* with the same sonde. In May 2015, water samples were filtered through a 0.2 μm filters, collected in acid-washed (10% HCl for 3 hours) low density polyethylene vials, and acidified with 1 N ultra-pure nitric acid (Optima® grade), and were analyzed for trace metals and isotopes of B and oxygen, and water samples collected in ashed (400 °C for 3 hours) glass vials poisoned with 100 μL saturated mercuric (II) chloride were analyzed for nutrients, total alkalinity, and dissolved inorganic carbon.

Water and sediment data are presented on a distance transect to convert latitude to kilometers from the north lagoon central bank (0 km) to the south lagoon opening to the ocean (21km).

4.3.3 Geochemical analysis

4.3.3.1 TIC and TA

Total inorganic carbon (TIC) was measured on a UIC Carbon Coulometer Analyzer by acidifying 5 mL water samples with 2 N sulfuric acid. Instrument precision is ± 0.4%, and reproducibility was determined from repeated analysis of Dickson Standard Batch 121 (n = 6, sd = ± 95.3 µmol/kg). Total alkalinity (TA) was measured on an Orion 950 Titrator by adding 0.03 N hydrochloric acid to 15 mL of sample, and reproducibility was determined from repeated measurements of Dickson Standard Batch 121 (n = 5, sd = ± 45.1 µmol/kg).

4.3.3.2 Trace metal concentrations

[Ca], [Sr], and [Ba] concentrations in water in this study are the same as in Chapter 3 but presented together with [B_T] and [Mg] data of the same samples. An acidified (1 M nitric acid, Optima-grade) aliquot of water was diluted by a factor of 100 and analyzed for [B_T] and [Mg] concentrations on a Thermo Scientific Element XR using lab-prepared solution standards. Reproducibility was assessed with repeated measurements of a lab-prepared standard and is reported as ±1 standard deviation of each element measured, on the order of ±5% for [B_T] and < 1% for [Mg].

4.3.3.3 Water $\delta^{18}O$ and $\delta^{11}B$

Water oxygen isotopes were determined by equilibrium exchange of the water oxygen with 0.3% carbon dioxide gas analyzed on a ThermoFinnigan Delta Plus XP isotope ratio mass spectrometer. Lab-calibrated standards yield precision of ±0.06‰, and results are reported relative to Vienna Standard Mean Ocean Water.

Water B isotopes were determined using the microsublimation technique of Wang et al. (2010). Approximately 20 µL of lagoon water was diluted with B-free water to 1 mL for ~50 ppb [B_T], then 20 µL of this dilution was acidified with 10µL concentrated pure nitric acid and sublimated in conical Savillex vials for 12 hours. Condensate was diluted with 0.1 N pure nitric acid to 1 mL of solution for analysis on a Neptune multicollector inductively coupled plasma mass spectrometer.

4.3.3.4 Foraminifera used

Most analyses were performed on *Ammonia parkinsoniana*, and some $\delta^{11}B$ data was collected on *Elphidium poeyanum*. *A. parkinsoniana* is infaunal, inhabiting silty sand estuaries and coasts throughout the Gulf of Mexico in salinity ranges 4-31 (Murray 2006, Poag 2015). *Elphidium poeyanum* is epifaunal, inhabiting warm-temperate silty lagoons and estuaries around Gulf of Mexico in salinity ranges 25-35 (Sen Gupta, 1999; Murray, 2006).

4.3.3.5 δ11Bcalcite and element/calcium ratios

Approximately 3 mg of foraminifera sample and 9 mg of coral standards (JCp-1, JCt-1) were transferred into acid-washed (3 N HCl at 75 °C overnight) 1.5 mL conical centrifuge tubes and cleaned as follows: 1 mL B-free Milli-Q water (18.2 MΩ) was added to each vial, sonicated for 10 minutes at 65 °C, centrifuged at 7000 RPM for 10 minutes, and siphoned with a new acid-washed pipette tip for each vial, which was repeated three times; 1 mL 10% NaOCl was added to each vial, capped, allowed to react overnight to remove organics, then sonicated for 10 minutes at 65 °C, centrifuged for 10 minutes, and siphoned with a clean acid-washed pipette tip between each vial. The milli-Q cleaning step above was repeated again five times. Samples were acid-leached with 1 mL 0.0005 N HNO_3 (Optima grade), sonicated for 10 minutes, centrifuged for 10 minutes, and siphoned with a new acid-washed pipette tip for each vial. The milli-Q cleaning was then repeated 3 times.

Following the microsublimation technique of Wang et al. (2010), samples were dissolved in 50 µL 1 N HNO_3 with additional increments of 5 µL added until calcite was completely dissolved and no effervescence was observed. Samples were sonicated for 10 minutes and then centrifuged at 10,000 RPM. 50 µL of dissolved sample was added to the lid of acid-washed conical PFA vials (Savillex brand) and

heated cap-side down for 14 hours on a Teflon hotplate at 98 °C to sublimate B. Vials were then allowed to cool to 25 °C before dilution for analysis.

The sublimated B droplet of each was diluted in 350 µL 0.1 N HNO_3 and poured into a new acid-washed 1 mL centrifuge tube. Samples were analyzed on a Neptune multi-collector inductively coupled mass spectrometer using the standard-sample-standard bracketing technique (Wang et al., 2010). The boric acid standard NBS 951 (National Institute of Standards and Technology, Maryland, USA) was used to determine $\delta^{11}B$ of forams and coral standards, and reproducibility determined from JCp-1 (0.43 ‰) and JCt-1 (0.51 ‰). Remaining dissolved sample solution was analyzed for B/Ca, Mg/Ca, Sr/Ca, and Ba/Ca on a Thermo Scientific Element XR using lab-prepared standard gravimetric solutions, and additional foraminiferal samples of 300 µg were cleaned and analyzed following the methods of Barker et al. (2003) and Chapter 3.

4.3.3.6 Calcite $\delta^{18}O_{calcite}$, $\delta^{13}C_{calcite}$

Approximately 60 µg of foraminiferal calcite was used to measure $\delta^{18}O_{calcite}$ and $\delta^{13}C_{calcite}$ on a Kiel IV Carbonate Device connected to a ThermoScientific MAT-253 dual-inlet isotope ratio mass spectrometer. Results are reported relative to Vienna PeeDee Belemnite, and long-term reproducibility was determined with repeated measurements of standard reference material NBS-19 limestone (±0.08‰)**.**

4.3.3.7 $^{87}Sr/^{86}Sr$

The $^{87}Sr/^{86}Sr$ results reported here are the same samples (and method) presented in Chapter 3. Briefly, foraminiferal samples dissolved in 3 M nitric acid were passed through Sr-specific Eichrom resin and analyzed on a Neptune multi-collector inductively coupled plasm mass spectrometer. Reproducibility was determined from IAPSO seawater standard (±0.00007) and NIST 987 strontium carbonate standard (±0.00006). Average NIST 987 during the analyses was 0.71025 and IAPSO was 0.70919.

4.3.3.8 Bulk sediment organic carbon $\delta^{13}C$, wt% C

Bulk sediment organic matter $\delta^{13}C_{organic}$ and atomic weight percent organic carbon (wt% C) were analyzed simultaneously via gas-sourced Carlo Erba elemental analyzer isotope ratio mass spectrometry. Some data were originally presented in Chapter 3 and additional data presented here was obtained by taking a 2 mg bulk sediment sample from each sediment interval, acidifying with chilled 6% sulphurous acid following Verardo et al. (1990), and sonicating between acidifications to promote complete decarbonation. Values are reported in reference to VPDB with instrumental reproducibility of $\delta^{13}C_{organic}$ = 0.2‰ and wt%C = 1%, determined from Pugel bovine collagen standard.

4.3.4 B and carbonate speciation and pH calculations

The speciation of borate and boric acid, and the $\delta^{11}B_{borate}$ thereof (Table 4.3), was calculated for each water sample using the spreadsheet calculator provided in Rae (2018) with the following parameters: depth = 0 m, *in situ* temperature, salinity, and $[B_T]$ (Table 4.3), *in situ* lagoon water $\delta^{11}B_{lw}$ = 38.51 ‰ (Table 4.3), α_B = 1.0272 (Klochko et al. 2006), and pK^*_B using *in situ* [Mg] and [Ca] after Hain et al. (2015), as implemented in MATLAB code from Rae (2018). The measured pH_{NBS} was corrected using $pH_{tot} = pH_{NBS} - 0.14$ (Foster and Rae, 2016), and the pH probe error 0.03 was propagated to determine the lower and upper bounds of $\delta^{11}B_{borate}$ (Figure 4.3). In addition, curves of $\delta^{11}B_{borate}$ over the pH range 6.5 to 8.5 were generated for the north lagoon (<10.8 km), south lagoon (>10.8 km), and mean lagoon using the mean temperature, salinity, [Mg], and [Ca] of each region and the aforementioned values of α_B and $\delta^{11}B_{lw}$. The 10.8 km divide is based on biogeographic distribution of benthic foraminifera at this field site (Chapter 2).

Dissolved carbonate $[CO_3^{2-}]$ was calculated using CO_2 SYS spreadsheet (Pierrot et al., 2011) using *in situ* temperature, salinity, phosphate, silicate, and total pH (Table 4.3), K_1 and K_2 from Lueker et al. 2000, K_{SO4-} from Dickson (1990), and total B $[B_T]$ from Lee et al. (2010), which are the same constants applied in Hönisch et al. (2019). The parameters TIC and pH were used to calculate $[CO_3^{2-}]$ rather than using TIC and TA to calculate $[CO_3^{2-}]$ (or pH) because dissolved sulfate and dissolved organic

carbon measured in Celestun lagoon do not meet the spreadsheet's assumption of typical oceanic values scaled to salinity (Young, 2005; Young et al., 2008) and thus cause uncertainty in calculated pH values exceeding pH probe error of 0.03.

The pH of lagoon water was calculated from coretop foraminifera for comparison to measured pH values. The equation used is equation 23 from Foster and Rae (2016):

$$pH = pK_B^* - log\left(\frac{\delta^{11}B_{Lw} - \delta^{11}B_{calcite}}{\delta^{11}B_{Lw} - \alpha_B\delta^{11}B_{calcite} - \varepsilon_B}\right) \quad (4.4)$$

where lagoon water $\delta^{11}B_{lw}$ =38.51 ‰ (as opposed to $\delta^{11}B_{sw}$ = 39.61 ‰). The same equation was applied to downcore samples to calculate past lagoon pH. Calculated pH uncertainty was determined from the upper and lower bounds of $\delta^{11}B_{borate}$ (Table 4.3).

4.3.5 Statistical analysis

Principal component analysis was performed for water samples and foraminiferal calcite samples using a correlation matrix to account for different units of parameters. Pearson's correlation assessed relationships between variables, and linear least-squares regression determined predictive relationships between lagoon salinity and values of isotopes or trace metals. Hoteling T^2 test assessed difference in multi-

variate parameters between the northern and southern lagoon and between pairs of cores in each lagoon region. Welch t-tests and F-tests assessed statistical differences for $\delta^{11}B_{carbonate}$ mean and variability.

4.4 Results

4.4.1 Sediment descriptions

Coretop and downcore sediment of Celestun Lagoon consist of >95% carbonate sediment, primarily authigenic carbonate mud and calcareous bivalves, gastropods, and foraminifera. Greater abundance of fine mud was observed in the northern lagoon compared to the southern lagoon. Images of sediment cores can be found in Chapter 2. Within sediments from coretop and downcore samples, fossils appeared pristine with no noted dissolution, pitting, or discoloration, and calcite walls of *Ammonia parkinsoniana* were notably thick, exhibiting a mean mass and standard deviation of 38.2 ± 15.4 µg for the size fraction 250-500 µg (Table S4.5).

4.4.2 Hydrographic properties

4.4.2.1 Salinity, pH, TIC, TA, and trace metals

For samples measured in 2015, groundwater discharge had low salinity (6.1 ± 3.9, n = 2) compared to seawater in the Gulf of Mexico (salinity of 36.3), with a mean lagoon salinity of 22.5 ± 8.5, n = 16 (Table 4.3). Lagoon salinity measured between 2001 and 2015 has a mean of 24.8 ± 7.6 (n = 169, Supplemental Table S4.3), exhibits a gradient from low to high salinity from the north to the south of the lagoon, and varies with precipitation by a lag of one to two months (Figure 4.2a, 4.2b). Mean and standard deviations of measured [B_T], [Mg], [Ca], TIC and pH_{tot} are given in Table 4.3. Significant linear relationships between salinity and [B_T], [Mg], [Ca], TIC, and pH_{tot} are shown in Figure 4.2d-4.2i left panels (R^2 provided therein). Figure 4.2d-4.2i middle panels show predicted seasonal gradients in [B], [Mg], [Ca], TIC, pH, and $\delta^{11}B_{borate}$ along the lagoon based on the respective salinity regressions in Figure 4.2, and right panels show histograms of calculated annual values for these parameters. In comparison to measured values in Table 4.3, the calculated values for annual mean ± standard deviation (and range) predicted from regressions with salinity (Figure 4.2d-4.2h) for northern lagoon samples (Distance < 10.8 km, n = 76) where most groundwater discharge occurs are: [B_T] 255.7 ± 63.8 (117.9 - 395.8) µmolar, [Mg] 22.1 ± 6.4 (8.3 - 36.1) mmolar, [Ca] 8.9 ± 0.7 (7.3 - 10.5) mmolar, TIC 4324 ± 447 (3342 – 5289) µmol/kg, pH_{tot} 7.43 ± 0.13 (7.15 - 7.72). Distribution of measured total alkalinity (TA) values are nearly identical to measured TIC with a northern lagoon mean ± sd and range of 4486 ± 376 (3659 - 5299) µmol/kg. Groundwater discharge form spring and well samples is associated with low pH (6.69 ± 0.03, total scale), low salinity (3.4), low absolute values of [Ca], [Mg], and [B], and elevated TIC and TA

(>6600 µmol /kg for both) compared to seawater (Table 4.3). The range of pH and TIC is consistent with water samples previously measured at this site (Gonneea et al., 2014).

4.4.2.2 $\delta^{11}B$ of $[B_T]$ and borate in water

Mean lagoon water B isotope ratio ($\delta^{11}B_{lw}$) of total B is 38.51 ± 0.26 ‰ (Table 4.3). A welch t-test suggests a significant difference between groundwater $\delta^{11}B_{gw}$ (38.24 ‰) and lagoon water (38.62 ‰) (Welch t-test: t = 3.64, p = 0.016), although all values are within analytical uncertainty of each other (Table 4.3). There was no significant difference in variability between $\delta^{11}B_{gw}$ (sd = 0.05 ‰) and $\delta^{11}B_{lw}$ (0.22 ‰) (F(4,1) = 16.4, p = 0.37). The seawater sample (salinity 36.3) collected 1 km beyond the lagoon mouth has a $\delta^{11}B_{sw}$ of 38.26 ± 0.26 ‰ which is 1.35 ‰ below mean ocean $\delta^{11}B_{sw}$ of 39.61‰ (Foster et al., 2010).

Calculated $\delta^{11}B_{borate}$ is given in Table 4.3 and plotted against pH in Figure 4.4a. The $\delta^{11}B_{borate}$ values show notable divergence between the northern and southern lagoon (Figure 4.4a) resulting from divergent pK^*_B values calculated from temperature, salinity, [Mg], [Ca], and $\delta^{11}B_{lw}$ (Table 4.3). Mean and sd $\delta^{11}B_{borate}$ = 13.41 ± 1.42 ‰ (Table 4.3).

In Figure 4.4a we show $\delta^{11}B_{borate}$ that represents water samples from May 2015. To estimate seasonal changes in $\delta^{11}B_{borate}$, we use the ranges of salinity and calculated [B], [Mg], [Ca], and pH based on the relations shown in Figure 4.2 to calculate seasonal change in pK^*_B (Hain 2015, Rae 2018), producing a range of $\delta^{11}B_{borate}$ between 11.40 and 17.70 ‰ for the whole lagoon with a mean and standard deviation of 13.35 ± 1.49 ‰, n = 147 (Figure 4.2i middle panel).

4.4.2.3 Carbonate system parameters

Carbonate species concentrations calculated from CO_2SYS are given in Table 4.3. Water is undersaturated with respect to calcite in well water, spring water, and one lagoon water sample collected adjacent to the spring water sample ($\Omega_{calcite}$ 0.4 to 0.6, Table 4.3). Elevated pCO_2 in groundwater samples indicate substantial respiration and dissolution of carbonate bedrock, consistent with previous observations (Perry et al., 2003; Gonneea et al., 2014).

4.4.3 Foraminiferal calcite isotopes and trace metals

4.4.3.1 $\delta^{11}B$ of calcite

The $\delta^{11}B_{calcite}$ in coretop samples of the infaunal *Ammonia parkinsoniana* ranged between 8.06 to 18.53 ‰ (Table 4.4). $\delta^{11}B_{calcite}$ is significantly different between the

northern (mean = 14.54 ‰) and southern (mean = 11.21 ‰) lagoon (Welch t-test: t = 2.3, df = 11.3, p = 0.04). There was no significant difference in variability between the northern (sd = 2.62 ‰) and southern (sd = 3.62 ‰) lagoon (F(13,7) = 0.52, p = 0.3), and high variability characterizes all coretop $\delta^{11}B_{calcite}$ values (Figure 4.4a, 4.4b). The values for the mean and standard deviation of $\delta^{11}B_{calcite}$ for all coretop samples of *A. parkinsoniana* was 13.33 ± 3.36 ‰ (Figure 4.4c), a value derived from a cumulative amount of 71,500 µg of foraminiferal calcite representing approximately 3,000 foraminiferal specimens. For the epifaunal *Elphidium poeyanum*, $\delta^{11}B_{calcite}$ variability was also high (sd = 2.80 ‰, Figure 4.4a, 4b) with a mean $\delta^{11}B_{calcite}$ (16.12 ‰, n = 4) higher than that of *A. parkinsoniana* samples (Figure 4.4c). Neither species follows any trend between $\delta^{11}B_{calcite}$ and $\delta^{11}B_{borate}$ of the nearest water samples (Figure 4.4b), and the 2 ‰ offset for infaunal species noted by Rae (2018) is smaller than the full range of variability. However, both species have a $\delta^{11}B_{calcite}$ about 3 ‰ lower than benthic and planktic specimens from the open ocean (Figure 4.4c), qualitatively consistent with the lower than seawater pH measured in the lagoon (mean = 7.55, Table 4.3).

In downcore samples *A. parkinsoniana*, $\delta^{11}B_{calcite}$ ranged between 10.98 and 19.50 ‰ (Table 4.5). The mean $\delta^{11}B_{calcite}$ between downcore samples of the northern lagoon (4A and UL-1, 16.22 ‰) and the southern lagoon (8Aand ML-3-1, 14.55 ‰) was significantly different (Welch t-test: t = 2.4, df = 29, p = 0.02). There was no significant difference in variance between the northern (sd = 1.84 ‰) and southern

(sd = 2.87 ‰; F test, F(18,15) = 0.71, p = 0.48) regions. For individual cores in each region, there was no significant difference in $\delta^{11}B_{calcite}$ between 4A (mean = 16.39 ‰) and UL-1 (mean = 15.98 ‰) (Welch t-test: t = 0.41, df = 8.7, p = 0.7). However, there was a significant difference in variance between 4A (1.08 ‰) and UL-1 (2.64 ‰) (F(10,7) = 0.17, p = 0.01). There was a significant difference in mean $\delta^{11}B_{calcite}$ between 8A (13.81 ‰) and ML-3-1 (16.18 ‰) (t - -3.3, df = 8.6, p = 0.009), and there was a significant difference in variance between 8A (1.90 ‰) and ML-3-1 (0.56 ‰) (F(7,5,) = 11, p = 0.02). For replicate standards, JCp-1 (n = 10) values are mean = 24.32 ‰, sd = 0.43 ‰ compared to accepted value of 24.19 ‰ (Okai et al., 2002), and for JCt-1 (n = 5) the mean = 15.99 ‰ and sd = 0.51‰, also similar to accepted value of 16.17 ‰ (Inoue et al., 2004). Alfa-boron lab standard (n = 45) had a mean = -5.21‰, sd = 0.25 ‰, compared to measured value of -5.61‰ ± 0.37 ‰ of Wang et al. (2010).

4.4.3.2 B/Ca of calcite

Coretop sediment B/Ca ratios range between 18.78 and 37.47 µmol/mol (Table 4.4). There was a significant difference in B/Ca between the northern lagoon (20.48 µmol/mol) and southern lagoon (24.88 µmol/mol) (Welch t-test: t = -2.5, df = 76, p = 0.01) and no significant difference in variance between the northern lagoon (7.20 µmol/mol) and southern lagoon (9.45 µmol/mol) (F(54,42) = 0.58 p = 0.06). No

correlation was noted between B/Ca and $[B(OH)_4^-]/[HCO_3^-]$ (Pearson r = 0.10, p = 0.31) or between B/Ca and $\Delta[CO_3^{2-}]$ (Pearson r = 0.15, p = 0.13).

For downcore sediments, there is a significant difference in mean B/Ca between the northern lagoon (27.10 µmol/mol) and southern lagoon (17.25 µmol/mol) (Welch t-test: t= 8.1, df = 88, p < 0.01) and a significant difference in variance between the northern lagoon (12.65) and southern lagoon (5.17)(F(70,88) = 5.9, p < 0.01). For the combined all sample data (coretop and downcore), there is no significant correlation between foraminifera B/Ca and $\delta^{11}B_{calcite}$ *A. parkinsoniana* samples (Pearson r = 0.12, p = 0.45).

4.4.3.3 B versus temperature proxies (Mg/Ca)

No significant correlation is noted between $\delta^{11}B_{calcite}$ and Mg/Ca (r = -0.18, p = 0.24) (Figure 4.5e) for all sample data (coretop and downcore). B/Ca is significantly correlated with Mg/Ca (r = 0.63, p < 0.001) (Figure 4.5j) for all coretop and downcore data. In coretop samples, there is no significant difference in Mg/Ca between the northern lagoon (5.22 mmol/mol) and southern lagoon (5.14 mmol/mol) (Welch t-test: t = 0.34, p = 0.73). There was a significant difference in variance between the northern lagoon (1.01 mmol/mol) and southern lagoon (1.49 mmol/mol) (F(59,44) =0.46, p = 0.05). For downcore samples, Mg/Ca did not differ significantly between the northern lagoon (5.35 mmol/mol) and southern lagoon (5.10 mmol/mol)

(Welch t test: t = 1.60, df = 151, p = 0.11), and there was a significant difference in Mg/Ca variance between the northern lagoon (0.84 mmol/mol) and southern (1.08 mmol/mol) lagoon (F(72,79) = 0.61, p = 0.03).

4.4.3.4 B versus salinity proxies (Ba/Ca, Sr/Ca, $^{87}Sr/^{86}Sr$, $\delta^{18}O$)

$\delta^{11}B_{calcite}$ is significantly correlated with Ba/Ca (r = 0.26, p = 0.05) and inversely correlated with $^{87}Sr/^{86}Sr$ (r = -0.32, p - 0.02) (Figure 4.5) while no significant correlation is noted between $\delta^{11}B_{calcite}$ and $\delta^{18}O_{calcite}$, Sr/Ca, or Mg/Ca. High $^{87}Sr/^{86}Sr$ values (0.7090) derive from seawater while low values (0.7082) derive from groundwater, and the grayscale coloration identifies the northern lagoon (< 10.8 km) as the source of low-$^{87}Sr/^{86}Sr$ (and thus low salinity) water. Low salinity water is associated with low pH (Figure 4.2), yet $\delta^{11}B_{calcite}$ increases towards the springs in the northern lagoon (Figure 4.5a), a trend corroborated by increasing $\delta^{11}B_{calcite}$ with increasing Ba/Ca (salinity tracer without respect to aquifer type, Figure 4.5c). No clear pattern is observed between $\delta^{11}B_{calcite}$ and Sr/Ca (Figure 4.5d). Between cores, there was a significant difference in Mg/Ca between core 4A (5.23mmol/mol) and UL-1 (5.77 mmol/mol) (Welch t-test: t = -2.59, df = 34.8, p = 0.01 and no significant difference in variance between the core 4A (0.85 mmol/mol) and UL-1(0.76 mmol/mol) (f(53,18) = 1.24, - = 0.64). For the southern lagoon, there was a significant difference in Mg/Ca between core 8A (4.99 mmol/mol) and ML-3-1 (7.76 mmol/mol) (Welch t: t = -4.20, p = 0.05). There was not a significant difference in

variance between 8A (0.85 mmol/mol) and ML-3-1(0.76 mmol/mol) ($F(79,2) = 0.41$, $p = 0.18$). Epifaunal *Elphidium poeyanum* has a mean $\delta^{11}B_{calcite}$ (16.12 ‰) higher than that of *A. parkinsoniana* samples (Figure 4.4a, 4.4b).

B/Ca correlates significantly with $^{87}Sr/^{86}Sr$, Ba/Ca, and Sr/Ca (Figure 4.5, Pearson r given therein). Grayscale coloration highlights the significant differences between the northern and southern lagoon. B/Ca was not significantly correlated with $\delta^{18}O_{calcite}$ ($r = 0.15$, $p = 0.09$), though $\delta^{18}O_{calcite}$ values plot in two distinct clusters indicating the brackish (~-1.5 ‰) and fresh (~-3.0 ‰) groundwater endmembers determined in Chapter 3.

4.4.3.5 B versus respiration proxies ($\delta^{13}C$ of calcite and of organic carbon)

$\delta^{13}C_{calcite}$ for all sample data ranged between -8.50 ‰ and -3.02 ‰ with a mean of -6.39 ‰ and sd of 0.96 ‰. $\delta^{13}C_{organic}$ of organic carbon for all sample data ranged between -28.98 ‰ and -17.7 ‰ with a mean of -22.59 ‰ and sd of 1.80 ‰. $\delta^{13}C$ of calcite and organic carbon are significantly correlated ($r = 0.70$, $p < 0.01$) (Fig 6a.) indicating a clear relationship between the two. Weight percent of organic carbon (wt%C) ranged between 0.7 % and 9.9 % with a mean of 2.7 % and sd of 1.5 %.

There was no significant correlation between $\delta^{11}B_{calcite}$ and $\delta^{13}C_{calcite}$ or $\delta^{11}B_{calcite}$ and atomic weight % organic carbon (Figure 4.6b, 4.6c) for all sample data (coretop and

downcore). B/Ca exhibited the highest correlation with bulk sediment weight % organic carbon ($r = -0.36$, $p = 0.004$) in which B/Ca trends lower with increasing wt% C upcore (e.g., with time) (Figure 4.6f). B/Ca also significantly correlates with $\delta^{13}C_{calcite}$ ($r = 0.36$, $p < 0.01$), and B/Ca decreases with decreasing $\delta^{13}C_{calcite}$ of calcite up core (Figure 4.6e). Lastly, B/Ca correlates with $\delta^{13}C$ of organics ($r = 0.26$, $p = 0.02$) with B/Ca decreasing as $\delta^{13}C_{organic}$ decreases over time (Figure 4.6d). $\delta^{13}C_{calcite}$ of significantly correlates with $\delta^{18}O_{calcite}$ (Pearson $r = 0.289$, $p = 0.04$), and there is a significant but weak predictive relationship between $\delta^{13}C_{calcite}$ and $\delta^{18}O_{calcite}$ following approximately a 1:2 ratio (Supplemental Material Figure S4.4) which is expected if species vital effects are not important to the final test carbon isotopic composition (Ravelo and Hillaire-Marcel, 2007).

4.4.3.6 Multivariate statistical relationships and water and calcite samples (Hotelling, PCA)

Principal component analysis of measured water parameters from Table 4.3 are given in Figure 4.3a. Geochemical gradients observed in Figure 4.2 are again observed in Figure 4.3a, shown as arrows against samples colored by distance. Total pH is significantly correlated with $\delta^{18}O_{calcite}$ (Pearson $r = 0.89$, $p < 0.001$), significantly but more weakly correlated with salinity ($r = 0.50$, $p = 0.03$), and inversely correlated with TA and TIC ($r_{TIC} = -0.94$, $r_{TA} = -0.95$, $p < 0.001$ for both). The northern lagoon is characterized by greater spread (variability) along component 2 compared to the lower lagoon indicating that the second principal component explaining 19% of

variability has stronger influence in the northern lagoon compared to southern lagoon. For the parameters shown in Figure 4.3a, a multivariate Hotelling T^2 test indicates significant difference between the northern lagoon (<10.8 km, n = 9) and southern lagoon (>10.8 km, n= 10) (Hotelling $T^2 = 4.38$, $F(7,11) =$, $p = 0.015$). Means are given in Table 4.3.

For calcite, downcore plots indicate variability has been a feature of the lagoon for the 150 cm $\delta^{11}B_{calcite}$ record (Figure 4.7) which represents approximately the last 3,000 years (Chapters 2, 3).To increase sample size and produce a more robust dataset for analysis, all *A. parkinsoniana* coretop and downcore data are combined in principal component analysis.

Principal components 1 and 2 and 1 and 3 are shown in Figure 4.3. The greatest rates of change in $\delta^{11}B_{calcite}$ occur in direct relationship to Ba/Ca and inverse relationship to $^{87}Sr/^{86}Sr$, both of which are salinity tracers. The gradient in salinity is represented by the gray color along the lagoon, and the northern and southern lagoon data fall along principal component 1 (Figure 4.3b). $\delta^{11}B_{calcite}$ is roughly orthogonal to B/Ca in both Figure 4.3b and 3c, reflecting lack of correlation. There is variability in rates of change between $\delta^{11}B_{calcite}$, Mg/Ca, and $\delta^{13}C$ calcite. The distribution of northern and southern lagoon points along PC1, combined with the gradients in Ba/Ca, Sr/Ca, and $^{87}Sr/^{86}Sr$ suggest PC1 represents the salinity gradient from north lagoon to south. The long arrows of B/Ca and $\delta^{13}C$ calcite in Figure 4.3b suggest processes impacting $\delta^{13}C$

of TIC (e.g. carbon respiration) fall along PC2, and the arrows of Mg/Ca, B/Ca, and $\delta^{11}B_{calcite}$ arrow in Figure 4.3c suggest PC3 to be either temperature or pH, similar to the water PCA in Figure 4.3a. Changes in temperature would directly affect changes in pH and subsequent equilibria in borate and carbonate parameters.

In addition to the geochemical gradients indicated by PCA, the parameters in Figure 4.3b and 4.3c ($\delta^{11}B_{calcite}$, $\delta^{18}O_{calcite}$, $\delta^{13}C_{calcite}$, $^{87}Sr/^{86}Sr$, B/Ca, Mg/Ca, Sr/Ca, and Ba/Ca) were significantly different between the northern and southern lagoon (Hotelling T^2 test: $T^2 = 3.34$, $F(8,25)$, $p = 0.009$).

For the downcore parameters ($\delta^{11}B_{calcite}$, $\delta^{18}O_{calcite}$, $\delta^{13}C_{calcite}$, B/Ca, and Ba/Ca, n = 35) which have the most complete data set when excluding strontium data, there was no significant difference between downcore samples of 4A and UL-1 ((Hotelling T^2 test: $T^2 = 1.45$, $F(5,12)$, $p = 0.27$) (Table 4.5), and there was a significant difference for these parameters between 8A and ML-3-1 (Hotelling T^2 test: $T^2 = 6.627$, $F(5,7)$, $p = 0.01$). Means for all calcite geochemical variables are provided in Tables 4.3 and 4.4.

4.4.4 Calculated pH

For coretop samples (Figure 4.8a), the total-scale pH values calculated from $\delta^{11}B_{calcite}$ (pH_{cal}) range between 7.26 and 8.31 with a mean of 7.94 and sd of 0.34. This

compares to the measured pH (pH_{meas}) range of lagoon water samples from 6.76 to 8.06 with a mean of 7.65 and sd of 0.30. The mean values of pH_{cal} and pH_{meas} are significantly different (Welch t test: t= ,2.72 df = 34.0, p = 0.01), but there was no difference in variance between pH_{cal} (sd = 0.34) and pH_{meas} (sd = 0.30) (F(18,16)=1.31, p = 0.59).

For downcore samples (Figure 4.8b), pH_{cal} ranged from 6.94 to 8.38 with a mean of 8.00 and sd of 0.28. There was no significant difference between northern lagoon samples (mean 8.06) and southern lagoon samples (7.92) (Welch t test: t = 1.40, df = 13 p = 0.18, nor was there significant difference in the variance between the northern (sd = 0.24) and southern lagoon (sd = 0.32)(F(18,13)=0.56, p = 0.25). Within each site, there was no significant difference in long-term pH_{cal} between core 4A (8.10) and core UL-1 (8.00) (Welch t: t = 0.81, df = 8.2, p = 0.44), and there was a significant difference in variance between core 4A (sd = 0.12) and core UL-1 (sd = 0.35)(F(10,7) = 0.11, p = 0.003). For the southern region, there was no significant difference in pH_{cal} between 8A (7.79) and core ML-3-1 (8.09)(Welch t test: t = -2.19, df = 7.5, p = 0.06), and there was a significant difference in variance between core 8A (sd = 0.38) and core ML-3-1 (sd = 0.06)(F(7,5) = 40.9, p < 0.001).

4.5 Discussion

The goal of this work is to consider the various controls on $\delta^{11}B_{borate}$ in complex shallow coastal lagoon settings dominated by carbonate rocks and groundwater to improve the understanding of pH and equilibrium controls on $\delta^{11}B_{calcite}$ in these settings and to assess the utility of $\delta^{11}B_{calcite}$ as a proxy for low-pH groundwater discharge in these environments. Below we compare the data from Celestun Lagoon to records from open ocean settings and focus on interpreting the source of variability in shallow coastal waters. These may include abiotic factors (groundwater discharge and associated bulk $\delta^{11}B_{water}$ and salinity, pH, TIC, [Mg], [Ca]) and biotic factors (vital effects, calcification rates, proximal photosynthesis, organic matter respiration, dissolved organic carbon, sulfate reduction and B mechanisms of incorporation into biogenic carbonate), all of which will vary with seasonality in coastal settings.

4.5.1 Comparison with published B/Ca and δ^{11}B foraminifera values

The mean $\delta^{11}B_{calcite}$ of the shallow water benthic, symbiont-barren foraminifera *Ammonia parkinsoniana* in Celestun Lagoon reflects the mean $\delta^{11}B_{borate}$ for the water in the Lagoon (Figure 4.4c) while mean $\delta^{11}B_{calcite}$ of *Elphidium poeyanum* is 2.79 ‰ higher than *A. parkinsoniana*, possibly indicating differences in life habit or/and vital effects between the two species. When compared to other (deep sea) benthic or planktic foraminifera field studies, these data plot at lower $\delta^{11}B$ values for calcite, as expected based on the lower mean lagoon pH of 7.55 (Table 4.3) and in broad agreement with current understanding of the $\delta^{11}B$ proxy. The variance for both

$\delta^{11}B_{calcite}$ is higher than reported in other studies, with a $\delta^{11}B_{calcite}$ range of about 10 ‰ (Figure 4.4c), reflecting the variability in the shallow coastal lagoon. High variability of $\delta^{11}B_{calcite}$ may be common for other coastal margins with large changes in pH. Indeed, a recent field study using sediment trap samples noted a 10 ‰ change in $\delta^{11}B_{calcite}$ for planktic foraminifera off the upwelling-influenced coast of California (Mayk et al., 2020), a field site with a pH range of at least 0.7 units (Hofmann and Washburn, 2018) compared to the range of 1.37 pH units in Celestun Lagoon.

We note that our calculated $\delta^{11}B_{borate}$ values represent only a snapshot in time (two days where samples were collected only during the daytime) while *A. parkinsoniana* calcifies over a lifespan of about two months (Murray, 2006) and will experience more variable $\delta^{11}B_{borate}$ in response to the onset of wet and dry seasons and change in pH and pK^*_B (Figure 4.2i). At the same time, lagoon surface sediments are mixed in the top 5 cm by storms and bioturbation, accumulating at rates between 1.5 and 2.5 mm/yr (Chapter 2; Gonneea et al., 2004). Sediment mixing averages seasonal variation of lagoon pH and associated parameters, resulting in mean sediment chemistry values over the upper 2 cm representing about 10 years. Although our record is of relatively course age resolution, surface sediment geochemistry represents intermediate-term averages of hydrologic conditions, including average groundwater discharge volume, that is one of the major controls on the average $\delta^{11}B_{calcite}$ and the average calculated pH_{tot} of 7.70 for the lagoon based on data from *A.*

parkinsoniana reflects the average $\delta^{11}B_{borate}$ and measured pH_{tot} of the lagoon over the represented timescale.

In contrast to $\delta^{11}B_{calcite}$, B/Ca did not show the expected strong relationship with $[B(OH)_4^-]$/TIC or $\Delta[CO_3^{2-}]$ (Supplemental Material) but did show significant correlation with several salinity tracers including Ba/Ca, Sr/Ca, and $^{87}Sr/^{86}Sr$ (Figure 4.5) and with organic carbon respiration tracers (Figure 4.6). Low salinity groundwater discharge is high in TIC and low $[B_T]$ and in the metals [Ba] and [Sr] relative to seawater (Figure 4.2 and Chapter 3), thus a relationship between B/Ca and TIC likely exists but is obscured by the conservative properties of $[B_T]$ and salinity and thus appears to be related to salinity tracers Ba/Ca and Sr/Ca and is also affected by the overall variability of this system (Figure 4.7).

B/Ca and $\delta^{11}B_{calcite}$ thus appear to be controlled primarily by spring discharge, represented by PC1 in Figure 4.3a-c. Despite high variability in $\delta^{11}B_{calcite}$, it is striking that the mean value of $\delta^{11}B_{calcite}$ of *A. parkinsoniana* falls close to the 1:1 line with $\delta^{11}B_{borate}$, similar to deep sea benthic specimens from Rae et al. (2011) (Figure 4.4c open circles), and warrants a close look at each likely source of variability mentioned in the beginning of Section 4 above. To understand the broad findings for $\delta^{11}B_{calcite}$ and B/Ca ratios in *A. parkinsoniana* at this site, we consider the sources of B to the lagoon and triggers of change in pH and corresponding carbonate chemistry both as a result of seasonal change in the environment and specific biogeochemical processes.

4.5.2 Abiotic causes of variation in B/Ca and $\delta^{11}B_{calcite}$ of *A. parkinsoniana*

4.5.2.1 B sources and water mixing

The two primary sources of dissolved B to Celestun lagoon come from the springs (30 µmolar) and from the ocean (435 µmolar global average; Lemarchand et al., 2000), with atmospheric contributions playing a minimal role (Lemarchand et al., 2002). The initial $[B_T]$ and $\delta^{11}B_{water}$ would necessarily set the values ultimately recorded in carbonates precipitate, as observed in synthetic calcite precipitation studies and foraminifera culture studies (Uchikawa et al., 2015; Noireaux et al., 2015; Howes et al., 2017; Farmer et al., 2019). Groundwater discharge contributes about 80% of the water to Celestun northern lagoon (Young et al., 2008; Stalker et al., 2014), while water $[B_T]$ concentrations average 313 µmolar (Table 4.3), with simple mass balance indicating that the vast majority of B in Celestun Lagoon is contributed by seawater (~70%). The significant linear relationship between $[B_T]$ and salinity in water samples from the lagoon is consistent with the endmember mixing and is also manifested in foraminiferal calcite samples as a strong correlation between B/Ca and all of the salinity tracers except $\delta^{18}O$ (Figure 4.5). Water $\delta^{18}O$ is distinct between the two groundwater sources to the system, despite similar pH in both groundwater sources, and is also affected by evaporation in the northern lagoon (Chapter 3), thus it may be decoupled from $[B_T]$, particularly at sites further away from spring discharge

locations. These results suggest that [B_T] is a major control for the B/Ca of foraminiferal calcite, consistent with precipitation observations by Uchikawa et al. (2015) (implications for TIC discussed below).

Because groundwater is a source of about 30% of B to this system, there remains the possibility that it is also a source of $\delta^{11}B_{gw}$ values that are distinct from the present day seawater value of 39.61‰ (Foster et al., 2010). Indeed, $\delta^{11}B_{gw}$ signatures in groundwater have previously been used to trace sources of B in coastal aquifers (Vengosh et al., 1998; Vengosh, 1998). Groundwater B can be divided into natural and anthropogenic sources. Anthropogenic sources for this region are typically waste water, particularly sewage effluents or household water (Tapia González et al., 2008), which are expected to have high [B_T] and low $\delta^{11}B_{gw}$ values of -0.9 to 10 ‰, if sodium perborate detergents are present (Vengosh et al., 1994; Barth, 1998). No elevated B concentrations of such low $\delta^{11}B$ value were observed in our water or calcite samples. Elevated nitrogen in groundwater may indicate agricultural pollution entering the water table (Table 4.3, Tapia González et al., 2008), but we see no evidence of anthropogenic impact on the $\delta^{11}B_{gw}$ signature at our site. Natural sources of groundwater $\delta^{11}B_{gw}$ in the Yucatan derive from dissolution of Eocene- to Miocene-age marine carbonate ($\delta^{11}B_{sw}$ ~ 37.6 ‰ at time of deposition, Raitzsch and Hönisch, 2013) which would have a $\delta^{11}B_{carbonate}$ value of ~22.1‰ (Hemming and Hanson, 1992; Perry et al., 2009b) and from marine evaporites with $\delta^{11}B_{evaporite}$ values similar to those of seawater at time of deposition (Vengosh et al., 1992) . Assuming no

fractionation during carbonate dissolution, groundwater $\delta^{11}B_{gw}$ mixing with seawater $\delta^{11}B_{sw}$ in the aquifer prior to discharge would results in a $\delta^{11}B_{water}$ value between 22 and 39.61 ‰, depending on the $[B_T]$ of each endmember and the actual $\delta^{11}B_{gw}$ in this system.

The samples of well water (salinity of 3, representing nearly exclusively groundwater) and spring water (salinity 9, representing some mixing with seawater, Chapter 3; Young et al., 2008) exhibit $\delta^{11}B_{gw}$ values of 38.21± 0.39 and 38.28 ±0.22 ‰, respectively, which were significantly lower than lagoon mean $\delta^{11}B_{lw}$ value of 38.51±0.26 ‰ (see Section 3.2.2). These groundwater and lagoon water values are about 1.3 ‰ lower than mean global seawater which is a significant difference compared to the $\delta^{11}B$ measurement precision using the MC-ICP-MS method (~0.25 ‰, Hönisch et al., 2019). In addition, there are two sources of groundwater (fresh and brackish) to Celestun lagoon indicated by isotopes of radiogenic strontium, radium, and stable oxygen, as well as distinct [Sr], $[Cl^-]$, $[SO_4^-]$, and salinity data (Chapter 3; Young et al., 2008; Stalker et al., 2014), although $[B_T]$ does not differ between these endmembers when normalized to salinity. The difference in the dissolved ions in the two groundwater sources is likely from variable contribution of evaporites, particularly celestite and anhydrite (Perry et al., 2002; Perry et al., 2003), which can also be sources of B with distinct $\delta^{11}B_{gw}$ (Vengosh et al., 1994). Fortunately, we observe minimal difference in $\delta^{11}B_{gw}$ from the northern or middle lagoon springs (Table 4.3) that represent the two groundwater sources of discharge, suggesting that

the $\delta^{11}B_{evaporite}$ signature may be similar to the $\delta^{11}B_{limestone}$ and that [B_T] of both sources is similar, an intuitive result if the two lithologies precipitated during the same time period and from the same seawater chemistry. These observations based on isotope mass balance (38.21*X + [39.61* (1-X)] = 38.51) suggest that groundwater contributes ~79% of B to the system, consistent with previous estimates of discharge and salinity in the lagoon (Stalker et al., 2014) and in general agreement with mass balance of [B_T] alone. The measured groundwater $\delta^{11}B_{gw}$ of 38.21 ‰ may indicate some degree of seawater mixing with the freshwater lens within the aquifer, consistent with other geochemical evidence of shallow aquifer-seawater mixing on the coastal Yucatan (Perry et al., 2003; Gonneea et al., 2014). On the eastern coast of the Yucatan peninsula in the Caribbean, groundwater discharge $\delta^{11}B$ was measured to be 38.85 ±0.17 ‰ (Wall et al., 2019), suggesting that limestone and evaporite B sources contribution is smaller there but that it is pervasive around the Yucatan Peninsula coast. Values of $\delta^{11}B_{borate}$ lower than expected for seawater may explain discrepancies observed in $\delta^{11}B_{aragonite}$ of aragonitic reef cements (17.68 ‰) compared to expected $\delta^{11}B_{borate}$ of seawater (19.95 ‰) off the coast of Belize (Zhang et al., 2017). Zhang et al. (2017) used $\delta^{11}B_{sw}$ of 39.61 to calculate $\delta^{11}B_{borate}$, whereas a value of ~38.5 ‰ would result in $\delta^{11}B_{borate}$ of 18.84‰, which is closer to the observed $\delta^{11}B_{aragonite}$. The actual $\delta^{11}B_{borate}$ value should be directly measured for more precise calculations around the reefs which are affected by groundwater discharge.

For Celestun Lagoon, all else being equal, changes in groundwater discharge can potentially alter $\delta^{11}B_{borate}$ by about 1.4 ‰ on a seasonal basis (calculated based on seasonal variability in pK^*_B derived from seasonal change in pH, salinity, [Mg], and [Ca]) and to reach that range of variability (that is a $\delta^{11}B_{borate}$ of 38.21 to 39.61‰) would require contribution of 100% groundwater in the lagoon in the wet season and 0% during the dry season, which is not the case for Celestun based on salinity and other proxies (Herrera-Silveira, 1994). However, the observed range in $\delta^{11}B_{calcite}$ in the *A. parkinsoniana* coretop samples is much larger (10 ‰), accordingly, fluctuations in water source mixing alone do not fully the range of $\delta^{11}B_{calcite}$ (Figure 4.4c), thus variations in $\delta^{11}B_{calcite}$ and B/Ca are affected by other factors, specifically, changes in acid-base equilibria due to seasonal change to equilibrium conditions.

4.5.3 Seasonally-induced variation in lagoon hydrochemistry

4.5.3.1 Salinity, TIC, TA, pH, and temperature

Precipitation over the Yucatan Peninsula is seasonal with a distinct wet season (June-October) and dry season (January-May, Figure 4.2a, Bauer-Gottwein et al., 2011). Rainfall percolates through the karst landscape and discharges at springs and seeps in Celestun lagoon with a one to two month lag (Chapter 3; Perry et al., 2003), resulting in a persistent but seasonally variable salinity gradient (Figure 4.2b). Seasonal salinity variability is particularly high in the northern lagoon where most springs are located

(Herrera-Silveira, 1994; Young et al., 2008). This seasonal variability in salinity at any one location is larger than the variability throughout the lagoon recorded in a single sampling campaign (Table 4.3). Salinity is highly correlated with dissolved major and trace elements (Ca, Mg, B, Sr, Ba), TIC, TA, and pH (Figures 4.2d-4.2i). Assuming these linear relationships remain relatively constant between the wet and dry seasons, we can calculate the expected seasonal changes in select parameters important to the B proxy system (Figure 4.2d-4.2i).

The mean and standard deviation demonstrating total annual variability in these calculated parameters are shown as histograms in Figure 4.2, and variability in these parameters may impact B/Ca and $\delta^{11}B_{calcite}$ directly or indirectly (change in equilibrium constant). Salinity correlates with strontium isotopes and dissolved Sr and Ba in Celestun Lagoon (Chapter 3), thus $^{87}Sr/^{86}Sr$, Sr/Ca and Ba/Ca are salinity tracers for this system. B/Ca correlates well with these three parameters in foraminiferal calcite (Figure 4.5), yet salinity has been observed to directly affect planktic foraminifera B/Ca (Allen et al., 2011; Henehan et al., 2015), although impact on benthic foraminifera is unknown. Given that $[B_T]$ correlates with salinity and dissolved [Sr] and [Ba], correlations observed in Figure 4.5 between B/Ca and salinity are likely related directly to variation in $[B_T]$ rather than salinity itself (Uchikawa et al., 2017).

TIC is inversely related to salinity with the highest TIC values observed in groundwater samples (Table 4.3, Figure 4.2g). The linear relationship between [B_T] and salinity (Figure 4.2d) and the low [B_T] (31 µmolar) in groundwater compared to seawater we measured in the waters adjacent to this site (439 to 478 µmolar, Table 4.3), in conjunction with the high groundwater TIC (> 6500 µmol /kg) compared to seawater (~ 2,400 µmol /kg), this results in a [B_T]/TIC ratio of 0.0046 for groundwater and 0.197 for seawater entering the southern lagoon. The measured ratio in the northern lagoon is 0.070 (consistent with our previous mass balance calculation of ~80% contribution of groundwater). Though seasonal variability in both [B_T] and TIC are high, the strong correlation with salinity nevertheless imply that the [B_T]/TIC ratio will oscillate with seasonal or interannual spring discharge, yet as long as there is some discharge it will be persistently low compared to seawater values for this groundwater dominated system. Changing [B_T]/TIC as a control of B/Ca variability is consistent with the observations of Uchikawa et al. (2015) in which synthetic calcite B/Ca increased with increasing [B_T]/TIC. However, since the groundwater we sampled is slightly undersaturated with respect to calcite due to elevated TIC (Table 4.3), and the lowest B/Ca ratios of foraminifera occur near the largest sources of groundwater discharge (Table 4.4, distance 10.7 km), an impact of $\Delta[CO_3^{2-}]$ on B/Ca (Table 4.3) (Yu and Elderfield, 2007) in *A. parkinsoniana* cannot be ruled out. It has been shown that $\delta^{11}B_{calcite}$ correlates with TIC in inorganic calcite precipitation (Farmer et al., 2019). Mean annual TIC of Celestun is calculated to be about 3700 µmol/kg (Figure 4.2g), 33% higher than typical seawater values (2,400 µmol/kg) and

is consistent with in the low mean annual pH of the lagoon water (7.6, Figure 4.2h). Carbonate precipitation rates may be rapid in sediments in this environment, evidenced by the authigenic carbonate mud sedimentation rates between 1.5 and 2.5 mm/yr (despite water column undersaturation). Rates of calcification for *A. parkinsoniana* are unknown, but the thick calcite walls produced over the 2 months lifespan for this infaunal species suggest biogenic calcification rates are also high.

Alkalinity may also play a role because it is one of the controls of speciation of $[HCO_3^-]$, $[CO_3^{2-}]$, and $[B(OH)_4^-]$. Dickson formulated TA as follows, presented in DOE (1994):

$$TA = [HCO_3^-] + 2[CO_3^{2-}] + [B(OH)_4^-] + [OH^-] + [HPO_4^{2-}] + 2[PO_4^{3-}] + [H_3SiO_4^-] + [NH_3] + [HS^-] + [H^+]_F + [HSO_4^-] + [HF] + [H_3PO_4] \quad (4.5)$$

In Celestun, alkalinity is closely correlated with TIC (Pearson $r = 0.94$, $p < 0.001$), thus its relationship with salinity and seasonal range look nearly identical to that of TIC (Figure 4.2g, Table 4.3, Supplemental Material), suggesting that carbonate and bicarbonate provide most of the alkalinity in this lagoon. However, sulfur sources of alkalinity may also be important (SO_4^-, HS^-) in this system complicating interpretation. Groundwater in Celestun Lagoon is enriched in sulfate relative to seawater due to the dissolution of evaporites (celestite, anhydrite) (Perry et al., 2003; Young et al., 2008; Gonneea et al., 2014). Springs are more variable in sulfate

concentration between the wet and dry season compared to the lagoon as a whole (Young et al., 2008, Supplemental Figure S4.1). Culturing studies will be needed to directly determine the impact of sulfate on $\delta^{11}B_{calcite}$ and B/Ca. We note that B/Ca has been linked to PO_4^- concentrations in the planktic foraminifera *Globigerinoides ruber* (Henehan et al., 2015), which may be an expression of the impact of phosphate on TA, thus a similar impact by sulfate may occur. Note that the Dickson formulation of TA in equation 4.5 also contains reduced sulfide [HS-], which is abundant in sediment porewaters of Celestun Lagoon due to microbially-mediated sulfate reduction (Chuang et al., 2016, 2017).

In addition, dissolved organic matter (DOM) and specifically dissolved organic carbon (DOC) in estuarine systems is observed to significantly affect total alkalinity of these systems (Kim and Lee, 2009). DOM in Celestun northern lagoon (12 to 26 mg/L and as high as 52 mg/L) is about double that of the southern lagoon (4- 9 mg/L) and higher than typical seawater surrounding the western Yucatan (~3 mg/L, Young et al., 2005). Average annual values are 20.69 mg/L for the northern lagoon, 9.01 mg/L for the southern lagoon, 3.53 mg/L for the coast, and 3.13 mg/L for groundwater (Young et al., 2005). The total effect of DOM on TA in Celestun lagoon is observable (Gonneea et al., 2014) but unknown on seasonal scales, and because of the uncertainty introduced by DOM and sulfate, we prefer to use measured pH values in conjunction with TIC to calculate carbonate speciation, rather than using TIC and

TA to calculate pH and carbonate species, as is generally preferred in open ocean sites (Rae, 2018).

The most important parameter, pH_{tot}, varied similarly to TIC and TA. The calculated mean and range of annual pH_{tot} (based regression between pH and salinity, Figure 4.2h) is 7.6 ± 0.2 with greater variability in the northern lagoon, roughly 0.5 units (Figure 4.2h). The measured mean and range of pH_{tot} for Celestun Lagoon was 7.55 with a total range of 1.01, though excluding spring values brings the range down to 0.8. Our calculated and measured results compare well with pH_{tot} values reported from springs in the Eastern Yucatan Puerto Morelos (mean = 7.65 with range from 7.143 to 8.048 and sd = 0.241) (Hofmann et al., 2011) and the springs in the northern Yucatan Coast (mean and sd 7.25 ± 0.56) (Gonneea et al., 2014). In the springs at Puerto Morelos, pH was extremely variable and lacked detectable periodicity over a 30 day period with rates of pH change as high as 0.3 pH units/hr (Hofmann et al., 2011). The standard deviation of calculated seasonal pH in Celestun (0.23) is nearly identical to that of Puerto Morelos (0.24), thus variable pH from springs is likely a first-order control of $\delta^{11}B_{calcite}$ variability in foraminifera in Celestun Lagoon (Figure 4.4c). With such variability it is possible that a much larger number of individual tests is needed to capture average conditions and reduce the variability in the data. Our data range between approximately 40 and 160 individuals per $\delta^{11}B_{calcite}$ measurement while the sum of individual foraminiferal tests in all coretop measurements (whose mean $\delta^{11}B_{calcite}$ approaches $\delta^{11}B_{borate}$) is approximately 3,000 individuals, a high value

for any sediment sample. An optimal value likely lies in between, and for coastal B isotope studies we suggest a target of 300 individuals used conventionally in assemblage studies to assess statistical significance (Schönfeld et al., 2012).

Temperature indirectly impacts B/Ca and $\delta^{11}B_{calcite}$ through changes in calcite precipitation rate based on experimental work (Mavromatis et al., 2015; Uchikawa et al., 2017), although in these experiments the temperature range is large (5 to 25 °C) relative to the temperature range of Celestun Lagoon (24 to 33 °C) with most samples between 27 and 30 °C (Table 4.3). The tropics have relatively small temperature variations relative to temperature latitudes (Haug et al., 2001), thus direct temperature influence on $\delta^{11}B_{calcite}$ and B/Ca is likely small. Temperature does impact equilibrium constant pK^*_B, however, and there is evidence that the B fractionation factor α_B may be temperature dependent (Hönisch et al., 2019), but additional field studies are needed to elucidate the precise impact of temperature on $\delta^{11}B_{calcite}$ in our system and in other natural settings.

4.5.3.2 [Mg], [Ca], and pK^*_B equilibrium

The concentrations of [Mg] and [Ca] correlate well with salinity (Figures 4.2e, 4.2f), and because these are considered conservative ions, seasonal change in salinity would result in a large calculated range of [Mg] (8.3 to 36.1 mmolar) and of [Ca] (7.3 to 10.5 mmolar) (based on extrapolations from salinity). Both [Mg] and [Ca] complex

with [CO_3^{2-}], altering the saturation state of and effective alkalinity of seawater (Hain et al., 2015), and thus are factors controlling the conditional equilibrium speciation of carbonate and borate. While the study of Hain et al. (2015) focused on deep time changes between the Eocene (56 Ma, [Ca] = 20 mmolar, [Mg] = 30 mmolar) and the present ([Ca] = 10.3 mmolar, [Mg] = 52.8 mmolar), the range noted in the northern lagoon between wet and dry season, and between the north and south lagoon (Figure 4.2e, 4.2f), are on par with ranges of concentration over the last 56 Ma and thus need to be accounted for in equilibrium chemistry of [CO_3^{2-}] and [$B(OH)_4^-$], particularly because low Mg concentrations increase pK^*_B and reduce the sensitivity of $\delta^{11}B_{calcite}$ to pH change (Rae, 2018). Because pK^*_B is formulated on ionic strength rather than concentration (Hain et al., 2015), and because lagoon water has a lower ionic strength than seawater, there may be additional unconstrained uncertainty in $\delta^{11}B_{borate}$ curves presented in Figure 4.4a, although their effect on $\delta^{11}B_{borate}$ is likely small for the relatively low concentrations of [Mg] and [Ca]. Overall, seasonal change in [Mg] and [Ca] translate to $\delta^{11}B_{borate}$ variability of 1.3 ‰ along the length of the lagoon (Figure 4.4a) and results in 2 ‰ variability between wet and dry seasons through their impact on $\delta^{11}B_{borate}$ (Figure 4.2i).

Change in [Mg] and [Ca] also influences Mg/Ca in *A. parkinsoniana* which has a range of 4.7 to 18.7 in coretop sediments (Table 4.4). Using the temperature equation determined by de Noojier et al. (2014):

$$Mg/Ca_{calcite} = 0.167e^{0.121T} \quad (4.6)$$

where T is temperature in °C, coretop Mg/Ca results in a mean and sd calculated temperature of 31.5 ± 4.05 with a min of 27.6 and max of 39.0. This overestimates observed mean lagoon temperatures by about 2 °C and suggests warmer temperature (>32 °C) near spring sites where we in fact observe cooler temperatures (< 25 °C, Table 4.3, Supplemental Figure S4.5). Mg/Ca increases near the largest spring site which discharges the coolest water (Table 4.3), giving the appearance of the warmest temperatures adjacent the spring (Supplemental Figure S4.5). This may be caused by a higher Mg/Ca is the spring water relative to seawater or possibly by low pH of the discharged groundwater. Recent work suggests pH may influence Mg/Ca by as much has 9% per 0.2 pH unit for planktic foraminifera (Gray and Evans, 2019), perhaps through the same complexation and change in effective alkalinity that affects pK^*_B. The pH is most variable in the central lagoon with measured variability of 0.2 to 0.3 units (Table 4.3), suggesting an Mg/Ca-apparent temperature variability of about 3 °C, (Supplemental Figure S4.5). This finding is also consistent with work by Raitzsch et al., (2010) that observed an increasing concentration of Mg/Ca with increasing saturation for *A. tepida*, although this should be accompanied by increase in B/Ca rather than decrease (Supplemental Figure S4.5). This finding conflicts with work by Dissard et al., (2010a) on *A. tepida*, however, that indicates that changes to $[CO_3^{2-}]$ or TIC have no impacted on test Mg/Ca. Springs are sources of low [Mg] water and if [Ca] does not play a role, the increase of Mg/Ca of *A. parkinsoniana* may indeed be

related to pH or [CO_3^{2-}] for this field site. Significant correlation between Mg/Ca and B/Ca (Figure 4.5j) indicates possible similar underlying control of both proxies, in this case, either total amount of [B_T] and [Mg], relative high TIC (which would drive relatively high [CO_3^{2-}]) provided by spring discharge sites, or relatively cold (24 °C) groundwater compared to mean lagoon conditions (29 °C) are at play. Mg/Ca decrease with temperature in the southern lagoon, as expected, but variability near groundwater discharge sites and increases in Mg/Ca despite cooler water temperature suggest that temperature is not the main control at the spring sites.

In summary, for ambient lagoon waters in which benthic foraminifera calcify, primary influences on B/Ca appear to be relatively low [B_T] discharged from springs (which happens to be a relatively low ratio of [B_T]/TIC due to carbonate lithology), and primary influences of $\delta^{11}B_{borate}$ appear to be $\delta^{11}B$ of the sources (controlled by mixing between $\delta^{11}B_{sw}$ and $\delta^{11}B_{gw}$), pH (controlled by flux of high TIC discharged from groundwater), and pK^*_B (controlled by salinity, temperature, [Mg], and [Ca]). Direct controls by temperature are unclear. On average, $\delta^{11}B_{calcite}$ of the symbiont-barren benthic foraminifera *A. parkinsoniana* resembles $\delta^{11}B_{borate}$ of the water column, similar to observations of other deep sea benthic foraminifera (Rae et al., 2011). Because springs mediate the amount of $\delta^{11}B_{gw}$, TIC, [Mg], and [Ca] to this setting, the first order control of $\delta^{11}B_{calcite}$ of foraminifera is probably spring discharge, demonstrated by principal component 1 that explains nearly half of the

geochemical variability of this system (Figure 4.3b), and we interpret PC1 as proximity of samples to springs.

4.5.4 Biotic causes of variation in B/Ca and $\delta^{11}B_{calcite}$ of *A. parkinsoniana*

If half of the variability in $\delta^{11}B_{calcite}$ is explained by (abiotic) spring discharge controlling ambient conditions that affect $\delta^{11}B_{calcite}$, the remaining variability may be explained by biological influences on precipitation conditions. Overprinting of environmental pH conditions can come from changes in $[B(OH)_4^-]$ by altering pH due to photosynthesis (usually by symbionts), respiration, and calcification rates (Hönisch et al., 2003; Henehan et al., 2016; Rae, 2018), collectively termed "vital effects."

4.5.4.1 Lagoon vegetation photosynthesis

Symbiont-bearing foraminifera exhibit offsets between $\delta^{11}B_{calcite}$ and $\delta^{11}B_{borate}$ as the process of photosynthesis utilizes dissolved CO_2 with a concomitant increase in pH and an expected increase in $\delta^{11}B_{borate}$ (Rollion-Bard and Erez, 2010; Foster and Rae, 2016). *Ammonia parkinsoniana* lacks symbionts (Murray, 2006), but its habitat in the upper sediments of the lagoon places it in proximity to abundant primary producers. Seagrass and macroalgae cover approximately 65% of the lagoon floor (Herrera-Silveira et al., 1998; Gonneea et al., 2004), while more than 100 algal species reside in the water column and sediment surface (Herrera-Silveira et al., 1998). High rates of

photosynthesis by micro and macroalgae and seagrass could have similar effects as that of photosynthesis by symbionts, which is to consume CO_2 and raise the pH. Relatively high pH (7.79 to 8.06 compared to the spring values < 7) is observed in the northern lagoon where abundant seagrass beds exist, despite the low pH water supplied by springs in this area of the lagoon. Furthermore, all but one sample of $\delta^{11}B_{calcite}$ collected in the northern lagoon fall above the expected $\delta^{11}B_{borate}$ (Figure 4.4b), suggesting that seagrass and algae photosynthesis contributes to microenvironmental change in pH which is experienced by *A. parkinsoniana*, specifically photosynthesis is raising pH and thus $\delta^{11}B_{borate}$ in the water in proximity to *A. parkinsoniana* (Zeebe et al., 2003).

Variability in photosynthesis will contribute to variability in $\delta^{11}B_{borate}$. Macroalgae photosynthesis and respiration can change pH on diurnal cycle by 0.24 units during a typical day (Wootton et al., 2008). Local heterogeneity in distribution of macroalgae and seagrass beds likely also contribute to variable CO_2 drawdown and pH increase, particularly in the absence of discrete spring discharge like the one in middle lagoon. Higher calcite saturation states typically also occur in seagrass-dominated coastal settings with estuarine input of [Ca] (Beckwith et al., 2019), and the highest saturation states (6.4 and 8.5) were observed in the northern lagoon (Table 4.3). Photosynthetic impacts on CO_2 also plays a role in driving authigenic precipitation of micritic carbonate sediments (Zhang et al., 2017), and the highest sediment accumulation rates (2.5 mm/yr) occur in the protected northern lagoon (Chapter 2;

Gonneea et al., 2004), although overall physical energy is lower here. Authigenic precipitation would remove [Ca] and [CO_3^{2-}] from the water as well as [Mg] and $B(OH)_4^-$. The residual lagoon water TIC is unlikely to change much due to the large TIC reservoir (Table 4.3), but borate may decrease appreciably given that [B_T] is already low in the northern lagoon relative to seawater values (Table 4.3). Authigenic precipitation of calcite or aragonite would incorporate [$B(OH)_4^-$] and decrease the remaining dissolved B and further contribute to the variability of B/Ca observed in the northern lagoon.

4.5.4.2 Respiration and carbon remineralization in sediments

Foraminifera respiration releases CO_2, lowering pH of water surrounding the foraminifera test (Zeebe et al., 2003; Hönisch et al., 2003; Foster and Rae, 2016), and culture studies are needed to determine the significance of respiration for individual species. A more substantial source of CO_2 in mangrove lagoon sediments would be microbial respiration during the remineralization of organic matter since the organic content of mangrove lagoon sediments is generally high (>5%, (Alongi, 2012)), as is the case for Celestun (Table 4.4). Microbial remineralization of organic matter releases CO_2 into sediment, decreasing the pH and increasing TIC. The $\delta^{13}C_{TIC}$ value of TIC will reflect the $\delta^{13}C_{organic}$ of the organic matter being respired plus some fractionation factor (Deines et al., 1974). Celestun Lagoon organic matter derives from mangroves ($\delta^{13}C$ organic = -28 ‰), seagrasses (-16 ‰), and marine particulate

matter (-22 ‰) (Gonneea et al., 2004), with respiration resulting in a mean $\delta^{13}C_{TIC}$ of ~ -5 ‰ for the lagoon (Pérez et al., 2011) compared to carbonate-derived $\delta^{13}C_{TIC}$ values which are typically in the range of 0 to +2 ‰ (Ravelo and Hillaire-Marcel, 2007) and the foraminiferal $\delta^{13}C_{calcite}$ derives from $\delta^{13}C$ of TIC. Respired CO_2 results in a strong correlation between $\delta^{13}C_{organic}$ and $\delta^{13}C_{calcite}$ for *A. parkinsoniana* (Figure 4.6a), suggesting that microbial remineralization of carbon is an important process in the lagoon, but more specifically that the $\delta^{13}C_{TIC}$ fluid from which *A. parkinsoniana* calcifies is mediated by high rates of respiration of organic matter in the sediment, suggesting low pH and change in concentrations of carbonate and borate species.

The B/Ca ratio of *A. parkinsoniana* significantly correlates with $\delta^{13}C_{organic}$, $\delta^{13}C_{calcite}$, and weight % organic carbon of sediments (Figure 4.6). Respiration does not change $[B_T]$ but does change total TIC, thus driving the ratio of $[B_T]$/TIC downward in favor of less borate incorporation. Indeed, the highest content of sediment bulk organic matter (4 to 6 %) is associated with the lowest values of $\delta^{13}C_{org}$ and $\delta^{13}C_{TIC}$, which in turn are associated with the lowest B/Ca values (10 to 20 µmol/mol). This strong relationship is demonstrated by the arrows corresponding to B/Ca and $\delta^{13}C$ in Figure 4.3b, suggesting that PC2, which explains 18.2% of lagoon variability, may represent sediment organic matter respiration.

Respiration control over porewater pH suggests $\delta^{11}B_{calcite}$ should also correlate with $\delta^{13}C_{calcite}$, $\delta^{13}C_{organic}$ or wt%C, but no significant relationship is noted among these

parameters (Figure 4.6), despite the observed relationship between B/Ca and carbon isotope data. The reason is likely due to the limit of sensitivity of $\delta^{11}B$ at the *in situ* conditions. Below pH of 6.7, nearly all B occurs as boric acid (Rae, 2018) with a $\delta^{11}B_{boric\ acid}$ approaching that of the bulk fluid $\delta^{11}B$. B isotopes thus no longer record the fractionation between borate and boric acid species, but $\delta^{13}C_{TIC}$ values are still free to change, decoupling the expected relationship.

A caveat to respiration-driven change in $\delta^{13}C_{calcite}$ and B/Ca is that, as with $[B_T]$ and $\delta^{11}B_{water}$, a unique source of TIC with distinct $\delta^{13}C_{TIC}$ can alter $\delta^{13}C_{calcite}$ of foraminifera. For other carbonate bedrock geology in the region, $\delta^{13}C_{TIC}$ of groundwaters was recorded as -13.68 ‰ in Belize (Marfia et al., 2004) and ranges between -10.20 and -15.10 ‰ in the Upper Floridan Aquifer (Katz et al., 1997). In contrast, $\delta^{13}C_{TIC}$ of Celestun Lagoon is -5 ‰ (Pérez et al., 2011), in the range of $\delta^{13}C_{calcite}$ and thus indicating that $\delta^{13}C_{TIC}$ derives primarily from organic matter respiration in this system rather than from distinct $\delta^{13}C_{TIC}$ signatures from the groundwater aquifer supplying Celestun Lagoon. Measurements of $\delta^{13}C_{TIC}$ from the northwestern Yucatan aquifer are needed to confirm this.

Although biologic controls affect $\delta^{11}B_{calcite}$ through changes in TIC, this may only represent about 18% of variability of all geochemical data measured in Celestun Lagoon, including $\delta^{11}B_{calcite.}$ Biologically-induced change in ambient water pH adds

variability about the mean pH which, for this system, appears to be controlled primarily by spring discharge.

4.5.5 Application of $\delta^{11}B$ as a paleospring discharge proxy

The mean values of pH measured in situ (7.55) and calculated from $\delta^{11}B_{calcite}$ for coretop sediments (7.94) are significantly different from each other (Figure 4.8a) with no significant difference in variance, despite the similarity between $\delta^{11}B_{calcite}$ and $\delta^{11}B_{borate}$. Mean pH calculated for all downcore samples (8.00) was even higher. These results suggest $\delta^{11}B$ is not reliable for determining absolute paleo-pH values for this lagoon system, but relative difference between the north and south lagoon and between cores in each area imply $\delta^{11}B_{calcite}$ may record changes in pH relative to spring discharge sites.

Previous work with the conservative tracers, Ba/Ca and $^{87}Sr/^{86}Sr$, establishes a well-constrained paleosalinity record in Celestun Lagoon as well as the relative contributions from different groundwater sources (Chapter 3). For the northern lagoon (core 4A), the down-core record indicates increasing proportions of groundwater through time resulting in a trend toward higher Ba/Ca and lower $^{87}Sr/^{86}Sr$ (reproduced in Figure 4.7). The freshening trend is caused by continually reduced input of seawater as barrier island formation on the west bank progresses since about 5,000 years BP (263 cm core depth) to the present restricting seawater

input (Chapter 2; Lowery and Rankey, 2017). Seawater [B_T] is expected to be constant over this relatively short time interval (Lemarchand et al., 2000), and assuming the groundwater sources did not change in composition over that time period (the aquifer rocks have not changed), the lagoon would also be characterized by rising TIC, decreasing [B_T], a general shift toward lower pH, and thus decreasing $\delta^{11}B_{borate}$ (and thus $\delta^{11}B_{calcite}$) values from the past to present. Abundance of *A. parkinsoniana* was only sufficient (~ 3 mg calcite) for $\delta^{11}B_{calcite}$ analysis from the depth of 150 to 0 cm (about 60% of the sedimentary record, or the last 3,000 years), suggesting that the brackish (low pH) protected lagoon conditions in which *Ammonia* proliferate were established during this time interval (Chapter 2). Thus, the geochemical gradients observed in the modern lagoon would likely exist for the duration of our $\delta^{11}B_{calcite}$ record, manifested as a distinct geochemical differences between the northern (<10.8 km) and southern (> 10.8 km) parts of the lagoon.

The significant correlations between B/Ca and Ba/Ca and $^{87}Sr/^{86}Sr$ (Figure 4.5) support the interpretation that groundwater discharge is a first-order control of B in *A. parkinsoniana*, either through direct control of [B_T], control of TIC and thus [$B(OH)_4^-$], or both (Uchikawa et al., 2015). Over short timescales, variability imposed by TIC and mixing common in the coretop sediments (Chapter 2; Gonneea et al., 2004) may explain the lack of significant difference in B/Ca between the northern and southern lagoon despite the difference in [B_T] from groundwater along the lagoon. On longer time scales (e.g. downcore), there is a significant difference in B/Ca between the

northern and southern lagoon (B/Ca = 26.22 and 17.07 µmol/mol, respectively). The difference in mean B/Ca can be observed most easily between cores 4A and 8A, and the long-term decrease in B/Ca is apparent in core 4A (Figure 4.7). The effect is less pronounced for core 8A which would have less time to experience isolation from the ocean given the unidirectional nature of barrier island accumulation at this site (Lowery and Rankey, 2017 and Supplemental Figure S4.6).

The $\delta^{11}B_{calcite}$ for coretop samples was significantly different between the northern (14.59 ‰) and southern (10.98 ‰) lagoon both are impacted by groundwater discharge but differ in the abundance of seagrass vegetation (more in the north). Within each area, $\delta^{11}B_{calcite}$ varied significantly between core sites, and in the southern lagoon mean $\delta^{11}B_{calcite}$ differed significantly between site 8A and ML-3-1 (Figure 4.7). Middle lagoon core 8A is within 1.3 km of a large point-source spring discharge compared to core ML-3-1 which is about 3 km away from the spring. Over this distance, values of the paleosalinity tracers Ba/Ca and $^{87}Sr/^{86}Sr$ are not significantly different in *A. parkinsoniana* (Table 4.5). While there is little difference in the spring water tracers Ba/Ca and $^{87}Sr/^{86}Sr$ between cores 8A and ML-3-1, yet significant difference in both mean $\delta^{11}B_{calcite}$ and $\delta^{11}B_{calcite}$ variance (Figure 4.7) when translated to pH, there is no significant difference in pH between 8A and ML-3-1, likely reflecting the myriad other dissolved ions and temperature that influence final pH values. Unlike dissolved [Ba] and $^{87}Sr/^{86}Sr$, pH and TIC do not necessarily behave conservatively due to loss of CO_2 to the atmosphere or photosynthesis or gain from

respiration. [B_T] mixes conservatively in the lagoon over the course of our days-long sampling campaign (Figure 4.2d), but over month-long timescales, [$B(OH)_4^-$] likely does not behave conservatively because it is part of the total alkalinity system and related to equilibrium chemistry of TIC and to the pK^*_B from other dissolved constituents (Section 1.3.4). The $\delta^{11}B_{calcite}$ proxy, then, may only be sensitive to groundwater discharge in the very close vicinity of springs and become increasingly variable with distance from discharge as locally heterogeneous conditions (e.g. seagrass beds, organic matter respiration, CO_2 off-gassing) that can alter pH become more prevalent.

Overall, $\delta^{11}B_{calcite}$ measured in the benthic symbiont-barren foraminifera *Ammonia parkinsoniana* may be useful as indicator of low-pH spring discharge (particularly close to the discharge site) but lose some of the sensitivity when converted to pH measurements, so $\delta^{11}B_{calcite}$ may best be used in conjunction with other isotope systems ($^{87}Sr/^{86}Sr$, $\delta^{13}C$). It is clear, however, that low-pH conditions prevalent in groundwater discharge in Celestun Lagoon impose a first-order control over final $\delta^{11}B_{calcite}$ values despite the variability in a range of parameters affecting equilibrium constant pK^*_B. We note a high variability in $\delta^{11}B_{calcite}$ for this shallow marine carbonate environment was observed in others studies (Zhang et al., 2017) (Wall et al., 2019; Mayk et al., 2020), and the relative agreement between $\delta^{11}B_{calcite}$ of *A. parkinsoniana* and foraminifera measured in other studies of similar setting, despite the high variability, is encouraging. Future work should include more calibration

studies of benthic taxa common to shallow marine environments and particularly focus on multi-proxy analysis to better understand controls of final $\delta^{11}B_{calcite}$ composition. Similarly, a multi-proxy approach is needed for shallow carbonate field studies, and additional measurements of porewater geochemistry and micritic carbonate muds will be useful to understand $\delta^{11}B_{borate}$ in situ and final $\delta^{11}B_{calcite}$ expression.

4.6 Conclusion

This study presents the first multi-proxy approach carried out with a goal of understanding boron isotopes in calcite ($\delta^{11}B_{calcite}$) in the benthic shallow-infaunal symbiont-barren foraminifera *Ammonia parkinsoniana* in a carbonate sediment coastal lagoon affected by groundwater discharge. Despite high variability in parameters that control pH (salinity, temperature, [Mg], [Ca], TIC, TA), mean $\delta^{11}B_{borate}$ is reflected by mean $\delta^{11}B_{calcite}$ and plots lower than $\delta^{11}B_{calcite}$ measured in other symbiont-barren foraminifera in deep sea settings with "normal" open ocean pH (Rae et al. 2011). Mean conditions determining $\delta^{11}B_{borate}$ are set by low-pH springs discharging into Celestun lagoon, and spring discharge explains about 76% of variability seen across parameters measured in lagoon water and about 44% of variability in trace metal and isotope values measured in foraminiferal calcite. Another 18% of the variability in foraminiferal geochemistry is explained by respiration of organic matter in this productive mangrove estuary ecosystem, with

respiration impacting the $\delta^{13}C_{TIC}$ of foraminifera and B/Ca but with no impact on $\delta^{11}B_{calcite}$, possibly due to the loss of sensitivity around pH 6.7. Applying the $\delta^{11}B$ proxy downcore shows that pH at this shallow coastal site has likely been as variable over the last 3,000 years as is observed at present. Paleo-pH calculations over time are not clearly related to spring discharge or any other single process, but $\delta^{11}B_{calcite}$ measurements alone show greater sensitivity to spring discharge when within 1 km of large spring sites. This supports our hypothesis that low-pH spring discharge is a first-order control of $\delta^{11}B_{calcite}$ of benthic foraminifera and suggests $\delta^{11}B_{calcite}$ may offer some utility as a tracer for paleospring discharge in coastal environments, provided that $\delta^{11}B_{calcite}$ measurements are paired with multiple proxies of other environmental factors to understand impacts of salinity, temperature, sources of B, photosynthesis, and microbially-mediated respiration of organic matter. In particular, variability of [Mg] and [Ca] in discharging terrestrial waters require correction of pK^*_B equilibrium constants using the MyAMI model of Hain et al. (2015), and additional data on $[SO_4^-]$ and DOC may be needed to fully model changes in alkalinity and subsequent impacts on $\delta^{11}B_{borate}$ in coastal systems. These results suggest that $\delta^{11}B_{calcite}$ may also be useful for understanding pH controls from microbially-mediated processes in sediments (e.g., sulfate reduction, methanogenesis) if used in tandem with isotopes specific to those elements. The lower than seawater pH setting of this study site illustrates the lower sensitivity of $\delta^{11}B_{calcite}$ at low pH but nevertheless suggests that even under extreme marginal marine conditions, the pH-$\delta^{11}B$ relationship is robust, which may also be true for marginal marine carbonate environments in deep time.

4.7 Acknowledgements

This work was supported by UCMEXUS [grant numbers SC20080859, 2009; ST271201, 2017]. Thanks to the NSF EAPSI Fellowship to Taiwan and NSF Graduate Research Fellowship awarded to Kyle Broach. Thank you to the helpful technical lab staff at NCKU, particularly Bear and Arrien Liu, and to Lucy for ensuring a smooth summer. Thank you to CJ Vigil, Brendan Chapman, Katie Roberts, and Colin Carney for lab assistance. Special thanks to Rob Franks for mass spectrometer magic and Dustin Harper and Tali Babila for assistance with boron lab work.

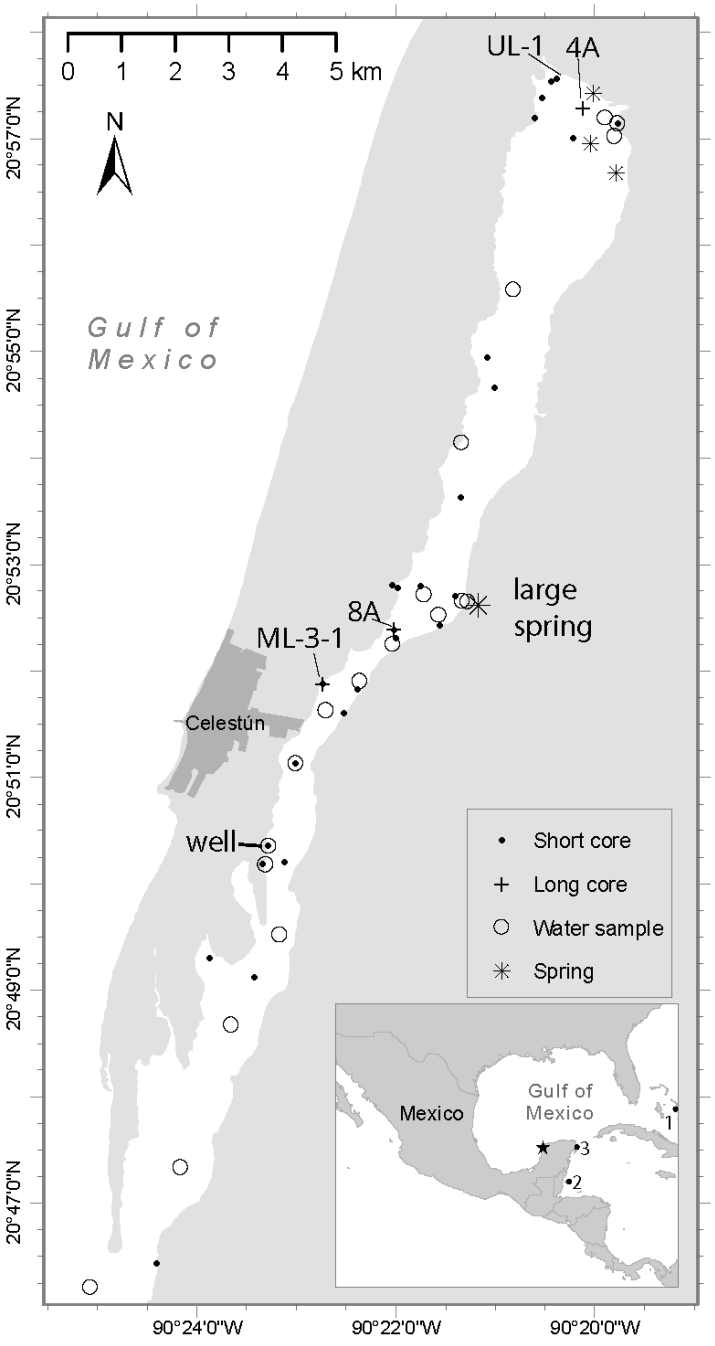

Figure 4.1
Map of Celestun Lagoon field site and sampling locations for water and sediment core samples from Table 4.1. Long sediment cores used for paleo-pH measurements are named. Inset: regional map with location of Celestun Lagoon (star) and other sites with $\delta^{11}B$ data for water or calcite. 1) Bahamas (Zhang et al., 2017), 2) Belize (Zhang et al., 2017), 3) Puerto Morelos (Wall et al., 2019).

Figure 4.2
(a) Ten-year average of monthly precipitation over the Yucatan Peninsula from TRMM-3B42 project (Bauer-Gottwein et al. 2011). **(b)** Salinity measured along Celestun Lagoon during different months between 2001 and 2015, colored to match months sampled. **(c)** Histogram of salinity data from (b) with mean (dash) and standard deviation (dotted) given in the lower corner. Geochemistry and salinity measured in lagoon water sampled in 2015 (Table 4.2) show linear relationships between salinity and dissolved **(d)** total boron [B_T] **(e)** magnesium [Mg] **(f)** calcium [Ca] **(g)** total inorganic carbon TIC **(h)** pH on the total scale, corrected from the NBS scale by -0.14 units (note 4 points above regression line which are from northern lagoon) **(i)** and $\delta^{11}B_{borate}$ of lagoon water. Middle panels of (d) through (h) show predicted variability of each parameter using linear regressions of monthly salinity observations in (b), and right panels show the distribution and mean ± standard deviation of parameter estimates. Note that $\delta^{11}B_{borate}$ regressions (i. middle panel) were calculated directly from salinity and predicted [B], [Ca], [Mg], and pH_{tot} (at constant temperature 25 °C) using the code provided by Rae 2018. Total alkalinity is not shown but looks nearly identical to TIC (Supplemental Material).

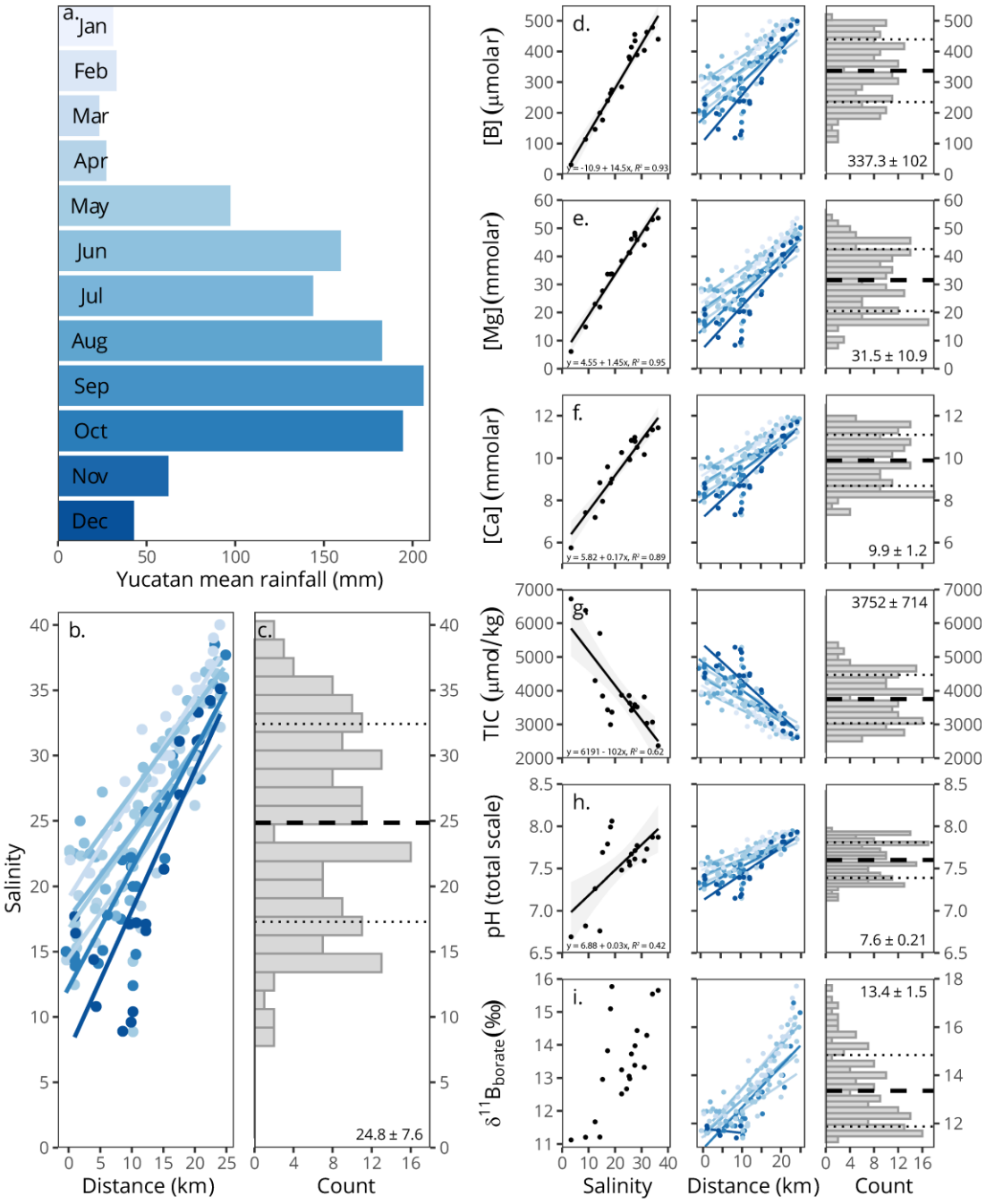
a.
Jan
Feb
Mar
Apr
May
Jun
Jul
Aug
Sep
Oct
Nov
Dec
0
50
100
150
200
Yucatan mean rainfall (mm)
b.
c.
Salinity
Distance (km)
Count
24.8 ± 7.6
d.
[B] (µmolar)
y = -10.9 + 14.5x, R² = 0.93
337.3 ± 102
e.
[Mg] (mmolar)
y = 4.55 + 1.45x, R² = 0.95
31.5 ± 10.9
f.
[Ca] (mmolar)
y = 5.82 + 0.17x, R² = 0.89
9.9 ± 1.2
g.
TIC (µmol/kg)
y = 6191 - 102x, R² = 0.62
3752 ± 714
h.
pH (total scale)
y = 6.88 + 0.03x, R² = 0.42
7.6 ± 0.21
i.
δ11Bborate (‰)
13.4 ± 1.5
Salinity
Distance (km)
Count

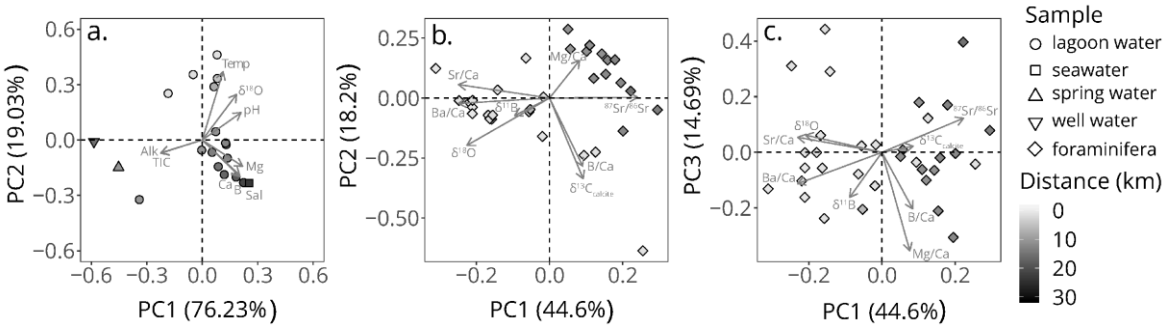

Figure 4.3

Principal component analysis of **(a)** water sample geochemistry (Table 4.2) excluding $\delta^{11}B_{water}$. **(b)** Principal components 1 and 2 of all benthic foraminifera *A. parkinsoniana* data (coretop and downcore) and **(c)** principal components 1 and 3 of the same data. All panels are colored by distance sampled along the lagoon (Figure 4.1).

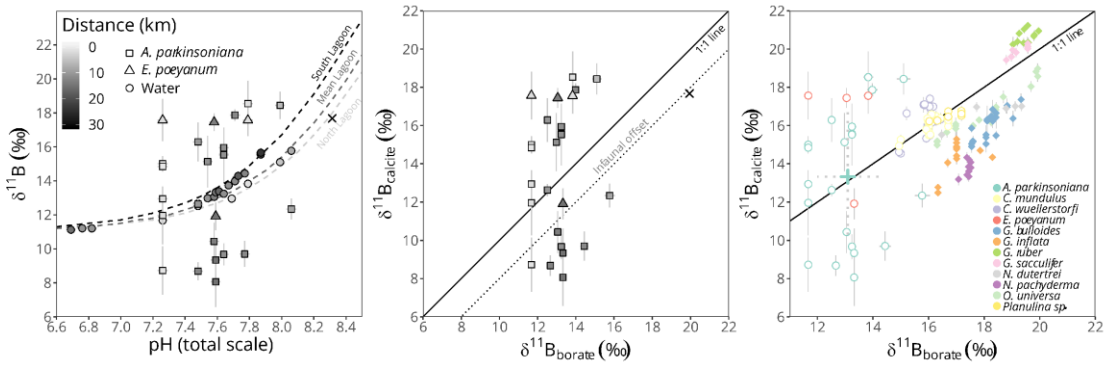

Figure 4.4

(a) Coretop comparison between foraminiferal calcite $\delta^{11}B_{calcite}$, calculated $\delta^{11}B_{borate}$, and total pH measured *in situ* (corrected using $pH_{tot} = pH_{NBS} - 0.14$ after Rae and Foster (2017)). Curves are theoretical $\delta^{11}B_{borate}$ values at a given pH_{tot}, calculated after Rae (2018) using measured $\delta^{11}B_{lagoon} = 38.51$, $\alpha_B = 1.0272$, and [Mg] and [Ca] (Hain et al., 2015, as implemented by Rae (2018); Table 4.2) measured for the northern (Distance < 10.8 km) and southern (Distance > 10.8 km) lagoon. X marks $\delta^{11}B_{aragonite}$ of aragonitic cements measured in Belize (Zhang et al, 2017). Error bars for $\delta^{11}B$ values of borate and calcite represent 95% confidence intervals. **(b)** $\delta^{11}B_{borate}$ calculated from Rae (2018) versus measured $\delta^{11}B_{calcite}$ of coretop foraminifera. Symbols and X are as in (a). Dotted line represents expected infaunal offset $\delta^{11}B_{calcite} - \delta^{11}B_{borate} = -2.0$ ‰ (Rae et al., 2011). **(c)** Comparison of benthic *Ammonia parkinsoniana* and *Elphidium poeyanum* from this study with benthic (open circle) foraminifera (Rae et al., 2011), and planktic (closed diamonds) foraminifera (Foster, 2008; Yu et al. 2013; Martinez-Boti et al., 2015; Henehan et al., 2013, 2016). Note that $\delta^{11}B_{borate}$ for this study was calculated as in (a) while $\delta^{11}B_{borate}$ for other species uses ambient seawater $\delta^{11}B_{SW} = 39.61$. Cross with dotted lines are the mean and standard deviation of values for *A. parkinsoniana*. All data was collected using MC-CIP-MS, thus minimizing instrument offsets (Hönisch 2019).

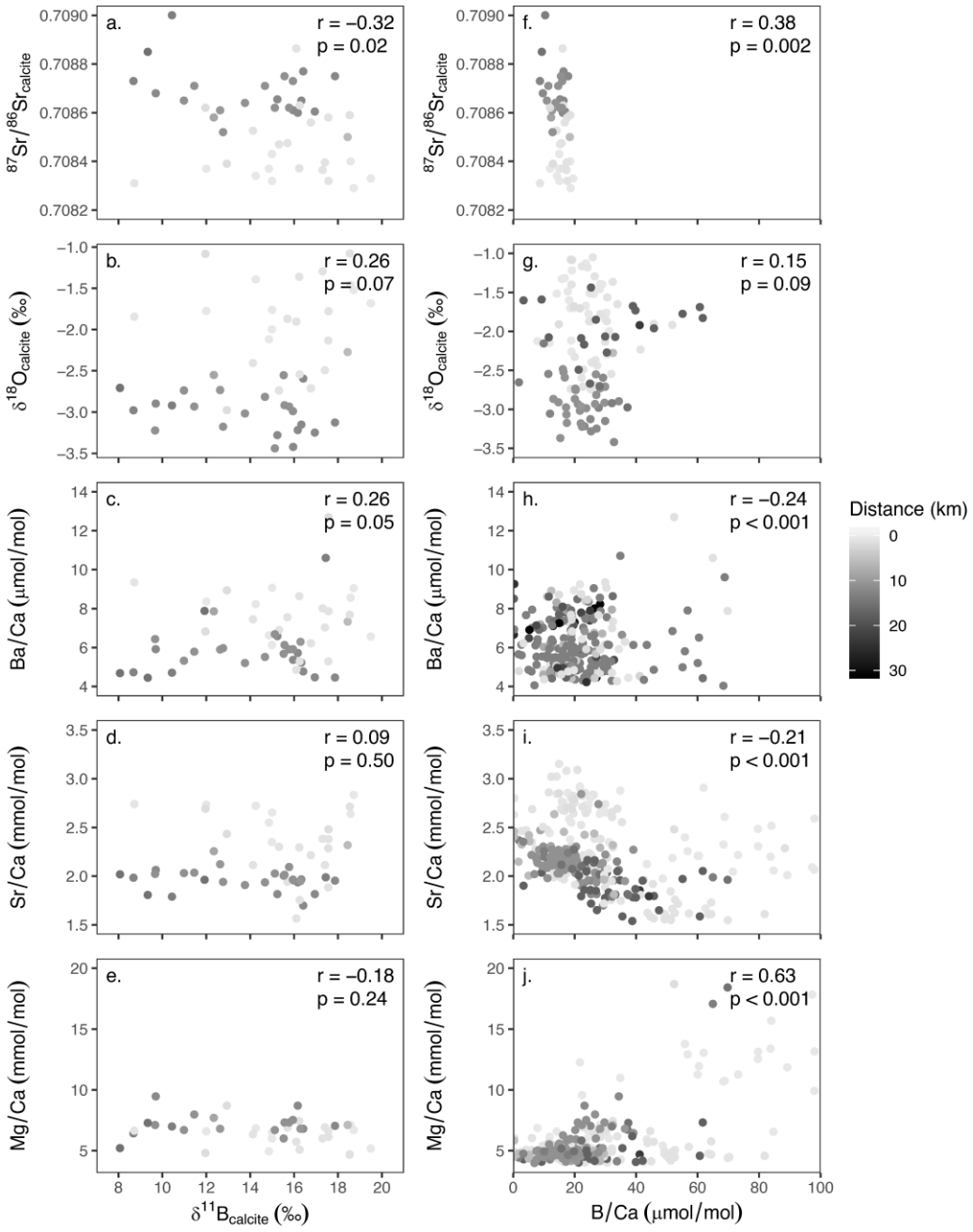

Figure 4.5
Foraminiferal $\delta^{11}B_{calcite}$ **(a-e)** and B/Ca **(f-j)** of *A. parkinsoniana* compared to salinity and temperature proxies for coretop and downcore samples. Each panel is colored by sediment core distance along the lagoon. Pearson correlation coefficients and p-values are given in the upper corners.

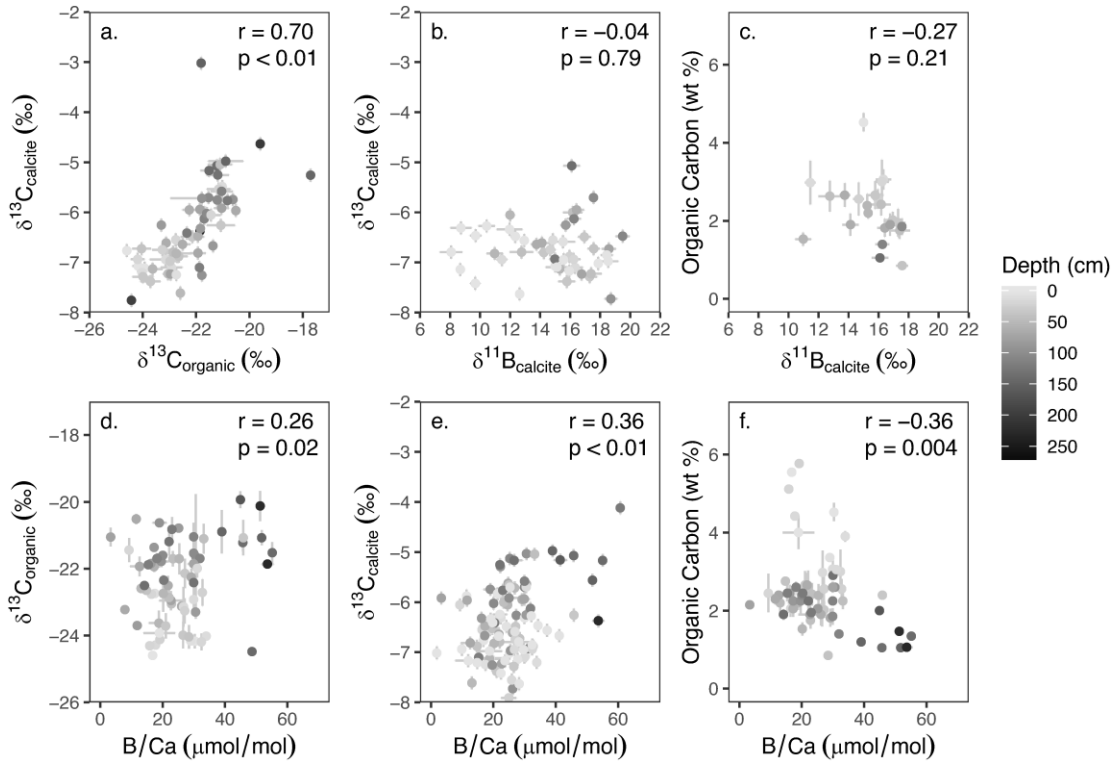

Figure 4.6
$\delta^{11}B_{calcite}$ and B/Ca of *A. parkinsoniana* compared to respiration proxies in combined coretop and downcore samples. **(a)** Carbon isotope data for bulk sediment organics and foraminiferal calcite. **(b)** Boron and carbon isotope data for foraminiferal calcite. **(c)** Boron and bulk sediment organic carbon. **(d)** Boron/calcium ratio of foraminiferal calcite and carbon isotope of bulk sediment organics. **(e)** Boron/calcium ratio and carbon isotopes of foraminiferal calcite. **(f)** Boron/calcium ratio of foraminiferal calcite and bulk sediment organic carbon. Each panel is colored by sediment core total depth and shows the Pearson correlation coefficient and p-value in the upper corner.

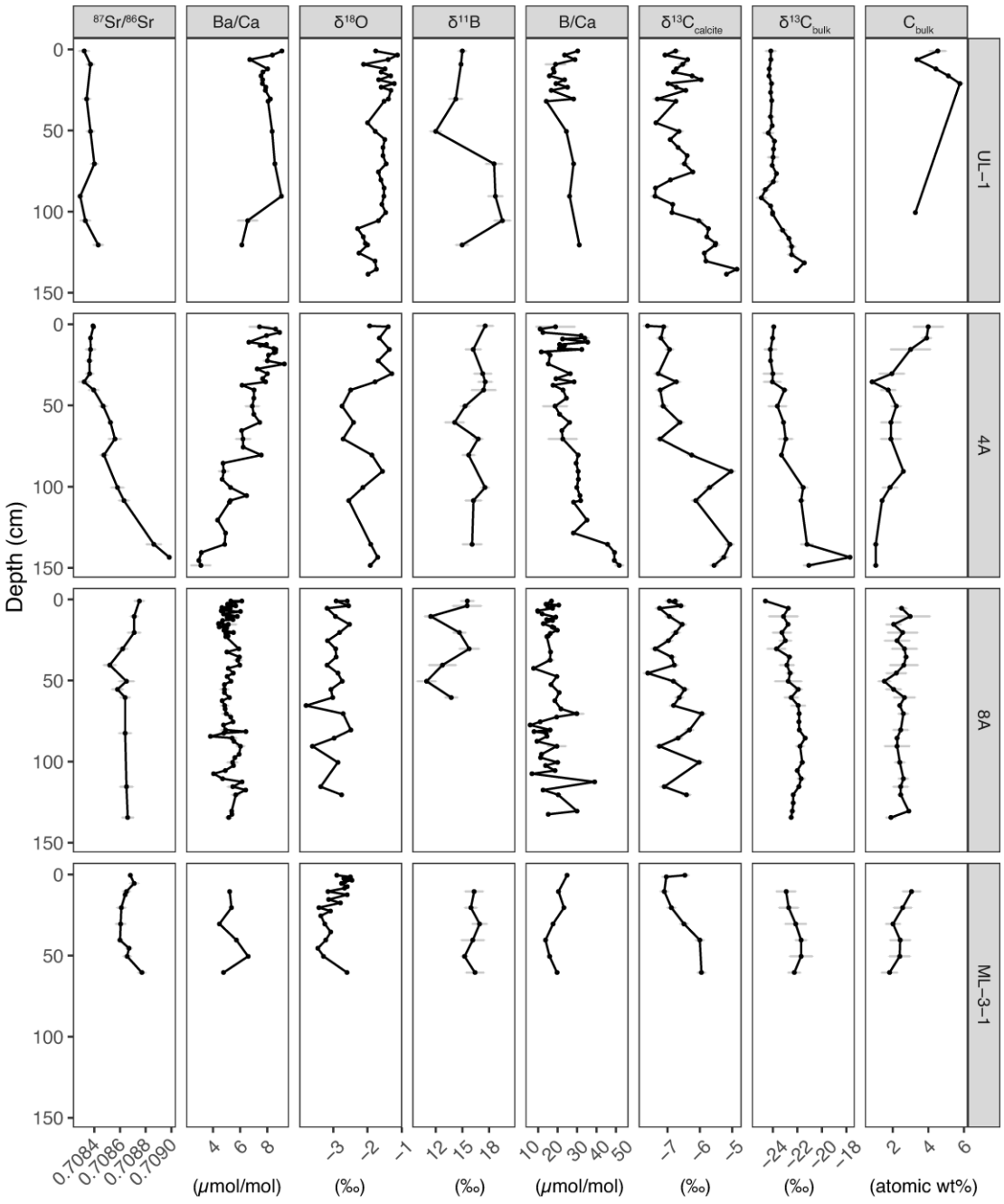

Figure 4.7
Comparison of downcore data between the northern lagoon (UL-1, 4A) and southern lagoon (8A, ML-3-1), organized by distance along the lagoon (UL-1, 4A, 8A, ML-3-1Figure 4.1). Strontium, barium, and oxygen isotope date are from Chapter 3.

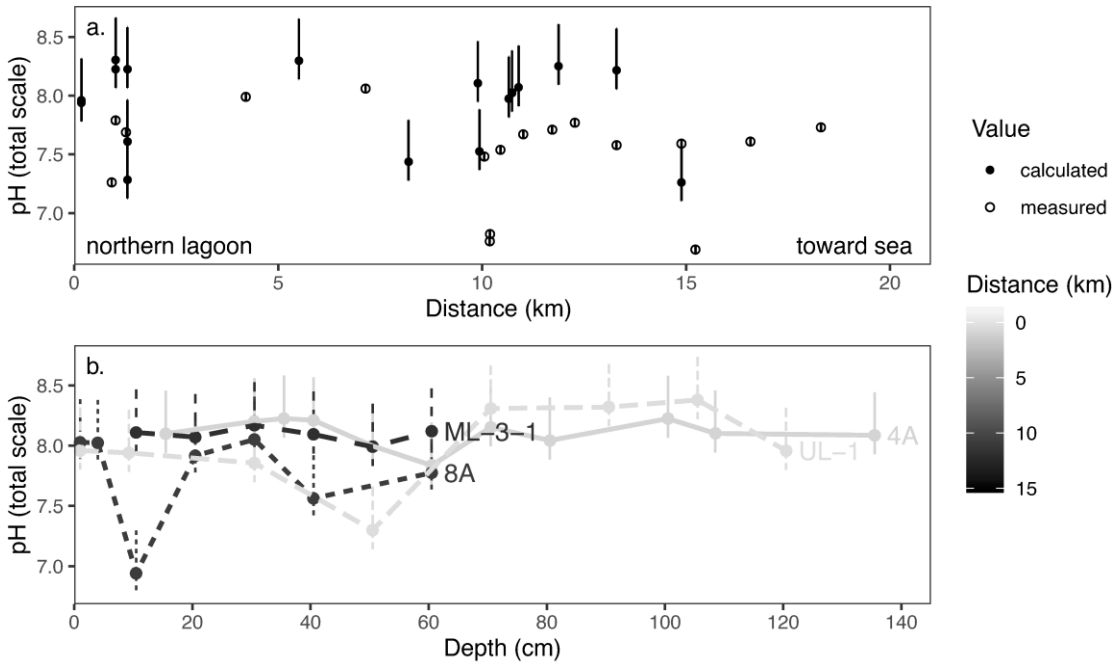

Figure 4.8
(a) Measured and $\delta^{11}B_{calicte}$ -derived pH_{tot} of coretop samples from the modern system (Table 4.3). **(b)** $\delta^{11}B_{calicte}$ -derived pH for downcore samples (Table 4.4). Calculated pH uncertainty is propagated from $\delta^{11}B_{calite}$ uncertainty and change in pK^{*}_{B}. Both panels are colored by distance sediment was sampled along the lagoon (Figure 4.1).

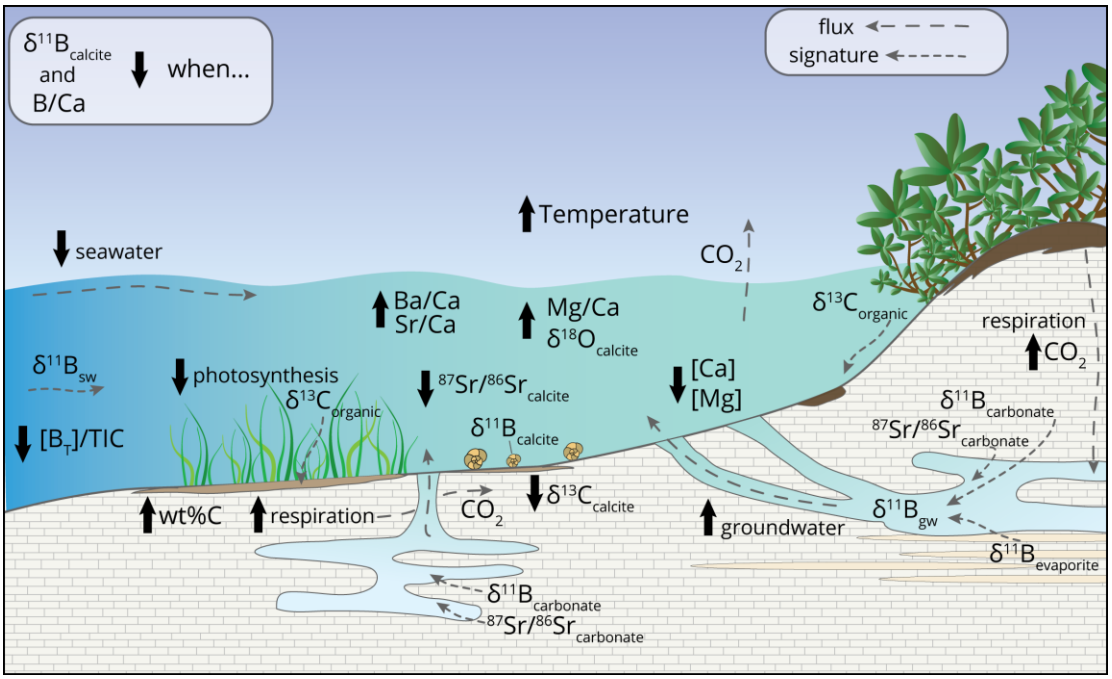

Figure 4.9
Conceptual diagram of dominant controls of foraminiferal $\delta^{11}B_{calcite}$ in *A. parkinsoniana*. Thick black arrows mark direction of change in proxy value, for example, $\delta^{11}B_{calcite}$ decreases when seawater contribution decreases. Major fluxes are seawater and groundwater into the lagoon and CO2 from sediments into water and water into the atmosphere (and vice versa). Signatures refer to isotopic signatures distinct to each water source (seawater, groundwater) and geologic materials contributing to water signatures (evaporites, inorganic and organic carbon). Primary controls of $\delta^{11}B_{calcite}$ are the mixing of seawater (sw) and groundwater (gw) $\delta^{11}B$ signatures (sources of $\delta^{11}B_{borate}$) and chemistry (TIC, [Mg], [Ca]) that impact pH (causes of change to pK^{*}_{B} conditional equilibrium). Secondary controls are biologic photosynthesis and respiration altering TIC (and thus pH), and vital effects within *A. parkinsoniana*.

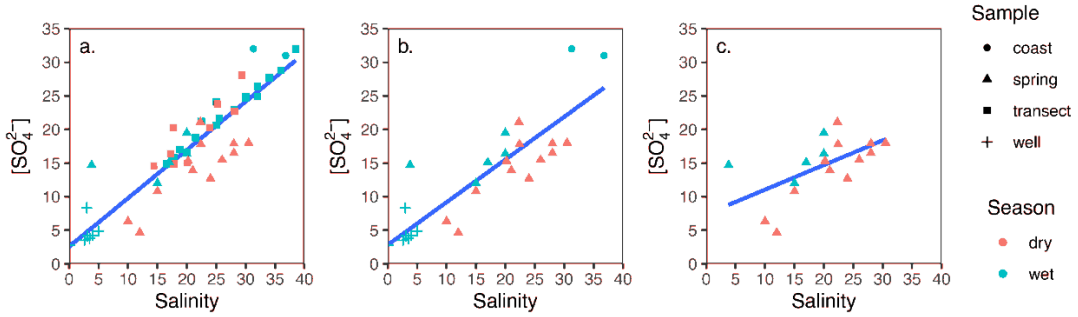

Figure S4.1
Celestun Lagoon salinity and dissolved sulfate data from Young et al. (2008). **(a)** Data compared between coastal seawater, spring water, lagoon water along a transect, and well water. **(b)** Remove of the lagoon transect data to show only seawater, spring water, and well water. **(c)** Salinity and sulfate of spring water only.

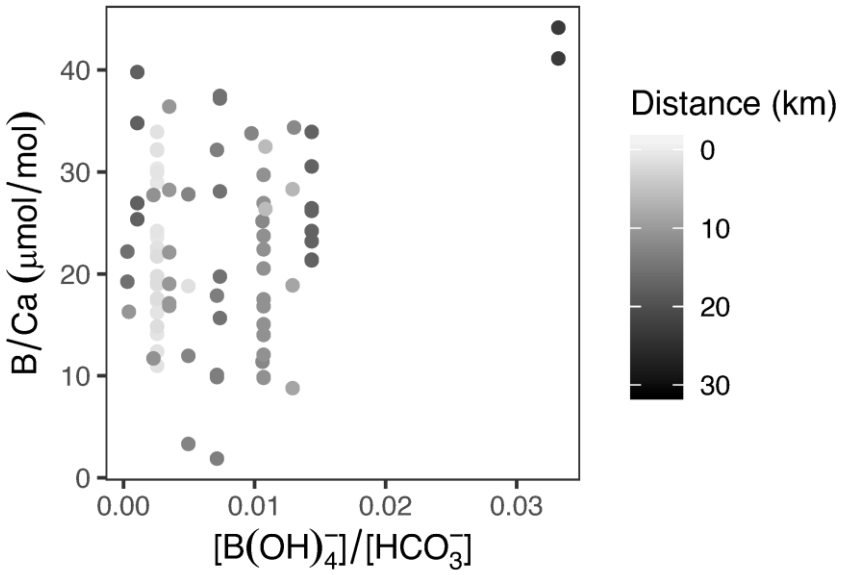

Figure S4.2
Calculated borate/carbonate of lagoon water compared to the nearest coretop foraminiferal calcite measurement of boron/calcium, colored by distance sampled along the lagoon (Figure 4.1).

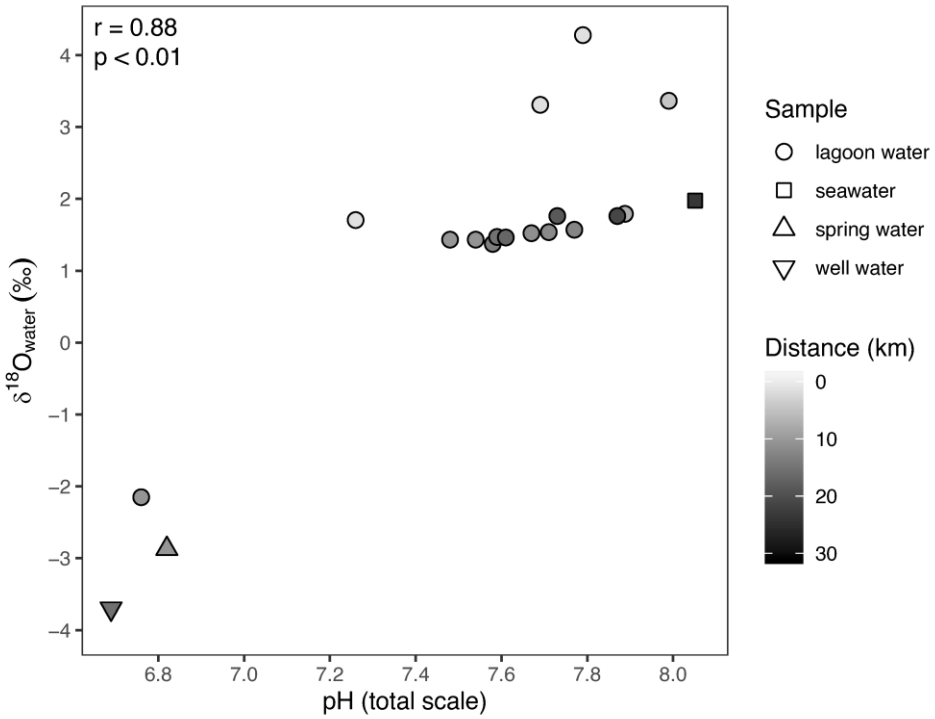

Figure S4.3
Total-scale pH and oxygen isotope values for water sampled in the lagoon and at groundwater discharge sites (Table 2). Colored by distance sampled along the lagoon (Figure 4.1).

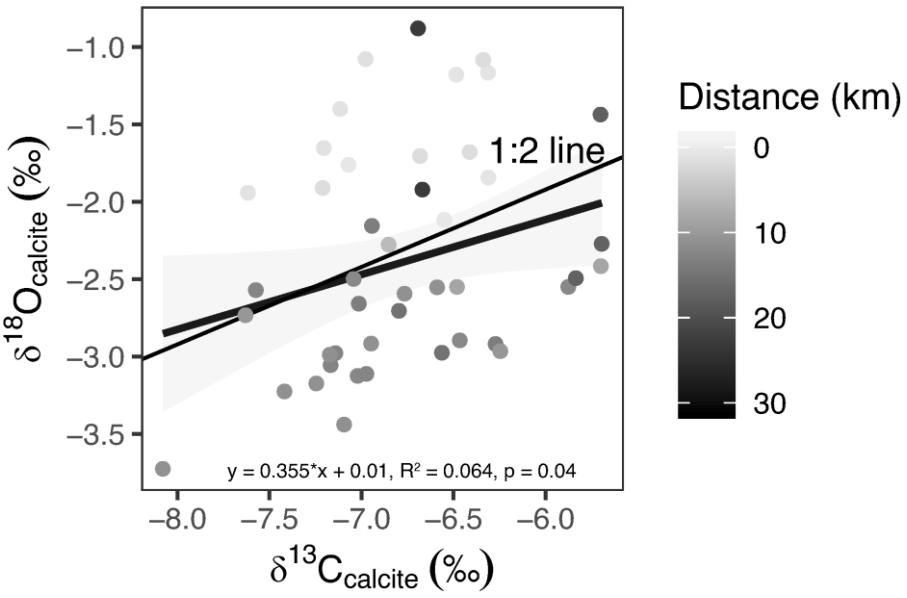

Figure S4.4
Carbon and oxygen isotopes for foraminiferal calcite in *A. parkinsoniana* coretop samples, colored by distance sampled along the lagoon (Figure 4.1). Regression equation is for least-squares fit to the data.

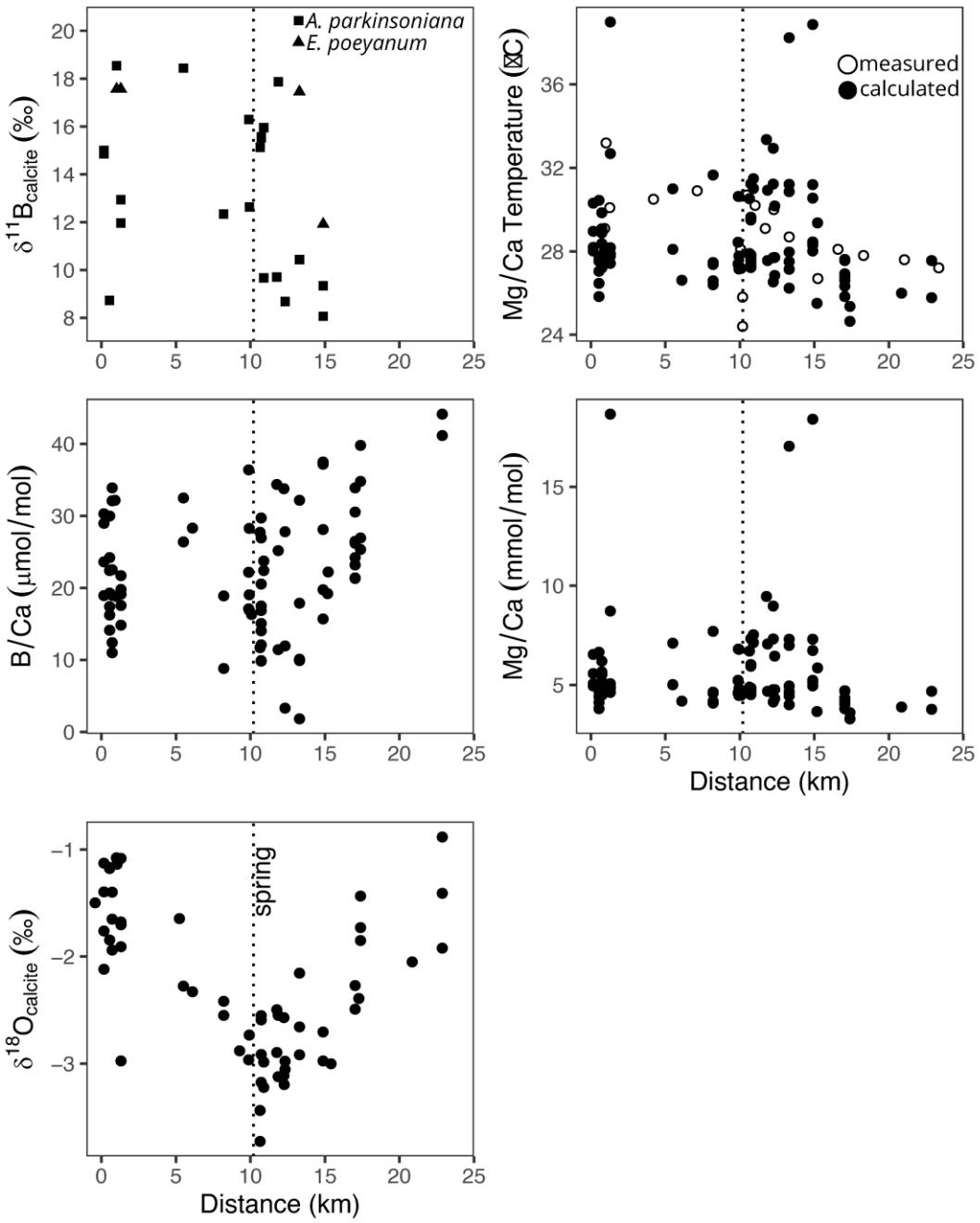

Figure S4.5
Comparison of foraminiferal $\delta^{11}B_{calcite}$, B/Ca, $\delta^{18}O_{calcite}$, Mg/Ca, and temperature calculated from Mg/Ca, plotted against distance sampled along the lagoon (Figure 4.1). Note that $\delta^{18}O_{calcite}$ is lowest adjacent to the spring while B/Ca and Mg/Ca values are not at the lowest until 2 to 3 km farther south (>10.2 km) toward the ocean. Open circles are measured temperatures of *in situ* water samples.

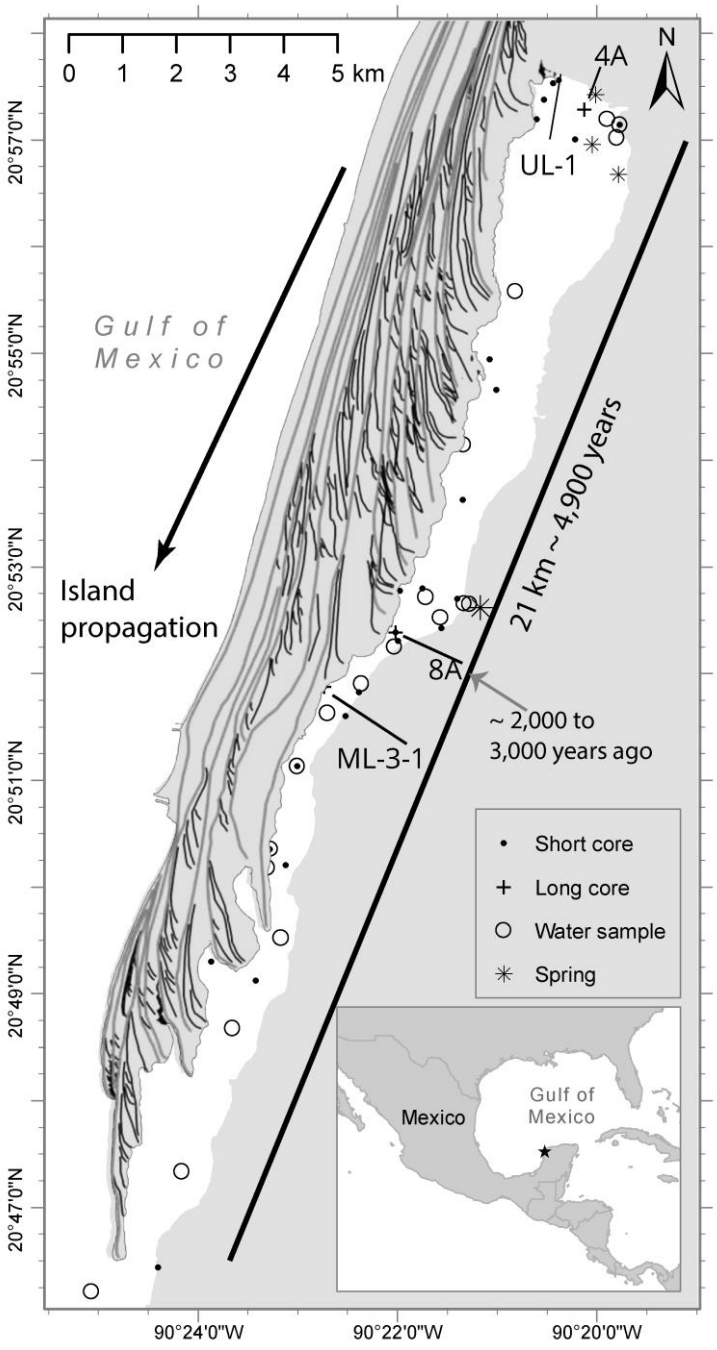

Figure S4.6
Barrier island growth formation adapted from Lowery and Rankey (2017). Close-spaced gray and black lines are outlines of major island-dune complexes. Ages are from Chapter 2 and show that sites 4A and UL-1 developed in a protected lagoon before sites 8A and ML-3-1.

Table 4.1 Terms used throughout this chapter

Term	Definition	Equation
α_B	Aqueous fractionation factor of boron isotopes between borate and boric acid. Value is equal to 1.0727 (Klochko et al., 2006).	4.3, 4.4
ε_B	Aqueous fractionation factor expressed in ‰ units.	4.3, 4.4
$\delta^{11}B$	Boron isotopic composition of a material, expressed as ‰ referenced to NIST951 boric acid standard. Used to refer abstractly to the boron isotope system and theory.	
$\delta^{11}B_{water}$	Boron isotopic composition	
$\delta^{11}B_{sw}$	Boron isotopic composition of modern seawater, taken as 39.61 ‰ (Foster et al., 2010).	4.3
$\delta^{11}B_{calcite}$	Boron isotopic composition, whether synthetic, authigenic, or biogenic with repeatability compared to JcP-t and Jct-1 coral standards.	4.4
$\delta^{11}B_{gw}$	Boron isotopic composition of ground water.	
$\delta^{11}B_{lw}$	Boron isotopic composition of lagoon water for this study, taken to be a mixture between $\delta^{11}B_{sw}$ and $\delta^{11}B_{gw}$.	4.4
$\delta^{11}B_{borate}$	Boron Isotopic composition of aqueous borate ion.	4.3
$\delta^{11}B_{evaporite}$	Boron Isotopic composition of evaporites.	
$\delta^{13}C_{calcite}$	Stable carbon isotopic composition of calcite (whether authigenic or biogenic), expressed as ‰ relative to VPDB standard with repeatability compared to NBS-19 limestone.	
$\delta^{13}C_{organic}$	Stable carbon isotopic composition of bulk sediment organic carbon.	
$\delta^{13}C_{TIC}$	Stable carbon isotopic composition of total inorganic carbon dissolved in water.	
$\delta^{18}O_{calcite}$	Stable oxygen isotopic composition of calcite, whether authigenic or biogenic.	
$\delta^{18}O_{water}$	Stable oxygen isotopic composition of water.	
$\Delta[CO_3^{2-}]$	Difference between carbonate ion concentration and saturation state of calcifying fluid.	
B/Ca	Boron to calcium molar ratio of calcite.	
$[B_T]$	Aqueous total boron µmol/kg, comprised of borate and boric acid (negligible polyatomic ions).	
$[B(OH)_3]$	Aqueous boric acid which dominates $[B_T]$ at low pH (< 7).	4.1, 4.2
$[B(OH)_4^-]$	Aqueous borate, generally believed to be the primary B incorporated into calcite.	4.1, 4.2
DOM, DOC	Dissolved organic matter and dissolved organic carbon. Terms used collectively to refer to influence on total alkalinity.	
[Ca]	Aqueous calcium of any isotope or ionic form.	
[Mg]	Aqueous magnesium of any isotope or ionic form.	
pH_{tot}	pH on the total scale. Includes activity of [H+] and $[HSO_4^-]$. $pH_{tot} \approx pH_{NBS} - 0.14$	
pH_{NBS}	pH on the National Bureau of Standards scale. Includes activity of $[H^+]$ only. Here, refers to instrument-measured pH calibrated to NBS standards of pH 4.01, 7.0 and 10.01.	
pK^*_B	Conditional (on temperature, salinity, pressure) equilibrium constant of boric acid dissociation. General equilibrium constant expressed as K_B .	4.2, 4.3, 4.4
TA	Total alkalinity of water as formulated by Dickson (DOE, 1994).	4.5
TIC	Total inorganic carbon dissolved in water. $TIC = [CO_2 + H_2CO_3] + [HCO_3^-] + [CO_3^{2-}]$.	
$^{87}Sr/^{86}Sr$	Radiogenic strontium isotopic composition, primarily of calcite in this manuscript.	

Table 4.2 Sediment and water sampling locations

Site	Type	Distance km	Latitude	Longitude	Year
UL-1	sediment core	0.2	20.9593	-90.3398	2006
3A	sediment core	0.5	20.9562	-90.3422	2009
4A	sediment core	0.7	20.9548	-90.3354	2009
FIC3	sediment core	1.0	20.9524	-90.3296	2015
FIC1	sediment core	1.3	20.9501	-90.3370	2015
2A	sediment core	5.5	20.9157	-90.3513	2009
5A	sediment core	8.2	20.8938	-90.3558	2009
7 CEL	sediment core	9.9	20.8799	-90.3626	2001
9A	sediment core	9.9	20.8796	-90.3663	2009
8-1 CEL	sediment core	10.7	20.8737	-90.3594	2001
8A	sediment core	10.7	20.8731	-90.3670	2009
FIC21	sediment core	10.9	20.8718	-90.3666	2015
ML-3-1	sediment core	11.8	20.8646	-90.3790	2006
MS-2-1	sediment core	11.9	20.8638	-90.3732	2006
MS-1-2	sediment core	12.3	20.8600	-90.3754	2006
FIC19	sediment core	13.3	20.8522	-90.3835	2015
FIC18	sediment core	14.9	20.8392	-90.3880	2015
FIC2	lagoon water	0.9	20.9532	-90.3317	2015
FIC3	lagoon water	1.0	20.9524	-90.3296	2015
FIC4	lagoon water	1.3	20.9503	-90.3300	2015
FIC5	lagoon water	4.2	20.9263	-90.3470	2015
FIC6	lagoon water	7.1	20.9024	-90.3557	2015
FIC22	lagoon water	10.1	20.8786	-90.3620	2015
FIC8	lagoon water	10.2	20.8775	-90.3556	2015
FIC7	spring	10.2	20.8775	-90.3546	2015

FIC9	lagoon water	10.5	20.8754	-90.3596	2015
FIC10	lagoon water	11.0	20.8708	-90.3672	2015
FIC11	lagoon water	11.7	20.8651	-90.3727	2015
FIC12	lagoon water	12.3	20.8605	-90.3784	2015
FIC19	lagoon water	13.3	20.8522	-90.3835	2015
FIC18	lagoon water	14.9	20.8392	-90.3880	2015
FIC17	well	15.2	20.8364	-90.3885	2015
FIC16	lagoon water	16.6	20.8254	-90.3863	2015
FIC15	lagoon water	18.3	20.8113	-90.3943	2015
FIC14	lagoon water	21.0	20.7889	-90.4028	2015
FIC13	seawater	23.3	20.7701	-90.4178	2015

Table 4.3 Water samples taken from Celestun Lagoon

Site	Type	Distance km	Temperature °C	Salinity	pH_{tot}	TIC µmol/kg	Alkalinity µmol/kg	[Ca] mmolar	[Mg] mmolar	[B] µmolar	$\delta^{18}O_{water}$ ‰	pK^*_B	$\delta^{11}B_{borate}$ ‰	$\delta^{11}B_{water}$ ‰
FIC2	lagoon	0.9	29.1	12.5	7.26 ± 0.03	4298 ± 174	4503 ± 45	7.2 ± 0.1	23.1 ± 0.2	146.1 ± 0.3	1.70 ± 0.04	8.867	11.67 ± 0.04	
FIC3	lagoon	1.0	33.2	17.1	7.79 ± 0.03	3430 ± 130	3746 ± 45	9.6 ± 0.9	33.7 ± 0.4	239.5 ± 0.3	4.28 ± 0.05	8.730	13.83 ±0.17	
FIC4	lagoon	1.3	30.1	15.3	7.69 ± 0.03	3843 ± 156	3980 ± 45	8.0 ± 0.1	27.7 ± 0.3	176.7 ± 0.3	3.31 ± 0.06	8.806	12.95 ±0.12	
FIC5	lagoon	4.2	30.5	18.3	7.99 ± 0.03	2990 ± 114	3378 ± 45	8.8 ± 0.1	33.7 ± 0.7	262.8 ± 0.3	3.36 ± 0.04	8.746	15.50 ±0.26	
FIC6	lagoon	7.1	30.9	18.8	8.06 ± 0.03	3363 ± 128	3548 ± 45	9.0 ± 0.1	33.8 ± 0.9	275.0 ± 0.3	2.03 ± 0.06	8.737	15.10 ±0.24	38.69 ± 0.23
FIC22	lagoon	10.1	28.1	22.5	7.48 ± 0.03	3871 ± 157	4338 ± 45	10.3 ± 0.1	38.4 ± 0.8	284.5 ± 0.3	1.43 ± 0.05	8.716	15.77 ± 0.27	
FIC8	lagoon	10.2	24.4	14.3	6.76 ± 0.03	5699 ± 231	5497 ± 45	8.8 ± 0.1	22.0 ± 0.2	199.6 ± 0.3	-2.15 ± 0.04	8.899	12.51 ± 0.10	
FIC7	spring	10.2	25.8	8.9	6.82 ± 0.03	6378 ± 259	6059 ± 45	7.4 ± 0.1	14.9 ± 0.2	113.9 ± 0.3	-2.87 ± 0.03	8.971	11.21 ± 0.01	38.28 ± 0.22
FIC9	lagoon	10.5	30.7	25.5	7.54 ± 0.03	3633 ± 148	3941 ± 45	9.9 ±0.1	41.3 ± 1.1	375.7 ± 0.3	1.43 ± 0.06	8.651	11.20 ± 0.01	
FIC21	lagoon	10.9	28.2	22.5	7.50 ± 0.03									
FIC10	lagoon	11.0	30.2	26.2	7.67 ± 0.03	3415 ± 139	3828 ± 45	10.8 ± 0.1	46.1 ± 1.2	414.4 ± 0.3	1.54 ± 0.04	8.628	13.24 ± 0.14	
FIC11	lagoon	11.7	29.1	27.6	7.71 ± 0.03	3530 ± 134	3710 ± 45	10.8 ± 0.1	47.4 ± 1.3	434.9 ± 0.3	1.57 ± 0.04	8.625	13.73 ± 0.17	38.60 ± 0.20
FIC20	lagoon	12.2	27.9	24.4	7.34 ± 0.03									
FIC12	lagoon	12.3	30	28.3	7.77 ± 0.03	3519 ± 134	3872 ± 45	10.5 ± 0.1	45.9 ± 1.3	388.7 ± 0.3	1.47 ± 0.03	8.615	12.67 ± 0.11	
FIC19	lagoon	13.3	28.7	25.3	7.58 ± 0.03	3853 ± 156	4001 ± 45	10.0 ± 0.1	41.4 ± 1.1	382.3 ± 0.3	-3.70 ± 0.02	8.674	14.43 ± 0.21	
FIC18	lagoon	14.9	28.3	31.1	7.59 ± 0.03	3810 ± 155	4016 ± 45	10.2 ± 0.1	44.0 ± 1.1	403.9 ± 0.3	1.46 ± 0.04	8.625	13.05 ± 0.13	38.80 ± 0.18
FIC17	well	15.2	26.7	3.4	6.69 ± 0.03	6720 ± 373	6698 ± 45	5.8 ± 0.1	6.2 ± 0.1	31.0 ± 0.3	1.76 ± 0.06	9.075	13.32 ± 0.15	38.21 ± 0.39
FIC16	lagoon	16.6	28.1	27.4	7.61 ± 0.03	3582 ± 145	3967 ± 45	11.0 ± 0.1	48.3 ± 1.4	455.3 ± 0.3	1.76 ± 0.05	8.633	11.12 ± 0.01	
FIC15	lagoon	18.3	27.8	32.0	7.73 ± 0.03	3034 ± 115	3506 ± 45	11.1 ± 0.1	49.8 ± 1.4	462.5 ± 0.3	1.79 ± 0.05	8.596	13.38 ± 0.15	
FIC14	lagoon	21.0	27.6	34.1	7.87 ± 0.03	3069 ± 117	3223 ± 45	11.3 ± 0.1	53.1 ± 1.4	478.2 ± 0.3	1.70 ± 0.04	8.572	14.29 ± 0.20	38.77 ± 0.15
FIC13	seawater	23.3	27.2	36.3	7.87 ± 0.03	2365 ± 90	2890 ± 45	11.4 ± 0.1	53.6 ± 1.3	439.7 ± 0.3	4.28 ± 0.05	8.560	15.55 ± 0.26	38.26 ± 0.18
Means	Northern		29.2	17.0	7.49	4167	4332	8.8	29.8	230.4	1.39	8.791	13.02	38.49
	Southern		28.3	26.6	7.60	3690	3971	10.3	43.5	389.1	1.06	8.660	13.85	38.53
	All Water		28.8	22.5	7.55	3916	4142	9.6	37.0	313.9	1.22	8.722	13.46	38.51
Standard deviations	Northern		2.7	5.1	0.47	1135	902	1.1	8.6	80.4	2.43	0.102	1.63	0.29
	Southern		1.0	8.3	0.31	1152	1026	1.7	13.7	129.8	1.68	0.149	1.30	0.28
	All water		1.9	8.5	0.38	1138	961	1.6	13.3	140.2	2.01	0.136	1.42	0.26
Maximum	All water		33.2	36.3	8.06	6720	6698	11.4	53.6	511.1	4.28	9.075	15.76	38.80
Minimum	All water		24.4	3.4	6.69	2365	2890	5.8	6.2	30.5	-3.70	8.56	11.12	38.21
Range	All water		8.8	32.9	1.37	4355	3808	5.6	47.4	460.6	7.98	0.515	4.65	0.59

Northern < 10.8 km, Southern > 10.8 km

calculated pK^*_B and $\delta^{11}B_{borate}$ (Rae, 2018) using temperature, salinity, [Ca], and [Mg], $\alpha_B = 1.0272$, $\delta^{11}B_{water} = 38.51$‰, and depth = 0 m

Table 4.3 (cont.)

Site	Type	Distance km	$[B(OH)_4^-]$ µmol/kg	*p*CO2 uatm	$[CO_2]$ µmol/kg	$[HCO_3^-]$ µmol/kg	$[CO_3^{2-}]$ µmol/kg	Ω calcite	Δ $[CO_3^{2-}]$ µmol/kg	$[NO_3^-]$ µmol/kg	$[PO_4^{3-}]$ µmol/kg	$[SiO_4^{4-}]$ µmol/kg
FIC2	lagoon	0.9	10.4 ± 1.4	6934 ± 309	199 ± 99	4051 ± 5	48 ± 9	1.4 ± 0.1	15	32.93	0.29 ± 0.02	26.40
FIC3	lagoon	1	15.9 ± 2	1562 ± 69	40 ± 80	3214 ± 17	176 ± 2	5.1 ± 0.5	142	2.31	0.24 ± 0.02	13.61
FIC4	lagoon	1.3	15 ± 1.9	2243 ± 102	62 ± 85	3648 ± 12	134 ± 3	3.9 ± 0.4	99	13.2	0.21 ± 0.02	14.04 ± 0.02
FIC5	lagoon	4.2	29.7 ± 3.5	816 ± 34	22 ± 74	2744 ± 22	225 ± 1	6.4 ± 0.6	189	1.18 ± 0.05	0.4 ± 0.02	14.72
FIC6	lagoon	7.1	39.3 ± 4.5	767 ± 36	20 ± 68	3041 ± 28	302 ± 1	8.5 ± 0.8	266	3.29 ± 0.05	0.49 ± 0.02	14.09
FIC22	lagoon	10.1	12.8 ± 1.7	3334 ± 149	93 ± 90	3681 ± 9	97 ± 4	2.6 ± 0.2	60	5.1	0.21 ± 0.02	14.6
FIC8	lagoon	10.2	2 ± 0.3	24965 ± 1071	800 ± 128	4883 ± 2	17 ± 34	0.5 ± 0	-19	139.1	0.12 ± 0.02	13.2
FIC7	spring	10.2	1.2 ± 0.2	26880 ± 1213	853 ± 132	5506 ± 2	19 ± 39	0.6 ± 0.1	-14	145.9	88.4 ± 0.02	267
FIC9	lagoon	10.5	7.9 ± 1	2684 ± 118	70 ± 86	3439 ± 12	125 ± 3	3.3 ± 0.3	87	7.94 ± 0.14	0.26 ± 0.02	22.20
FIC21	lagoon	10.9										
FIC10	lagoon	11	31.3 ± 3.9	1841 ± 80	48 ± 82	3210 ± 15	157 ± 2	4.1 ± 0.4	119	7.11	0.29 ± 0.02	14.1
FIC11	lagoon	11.7	35.1 ± 4.3	1702 ± 76	45 ± 80	3308 ± 17	177 ± 2	4.6 ± 0.4	138	8.75	0.34 ± 0.02	15.22 ± 0.54
FIC20	lagoon	12.2										
FIC12	lagoon	12.3	42.6 ± 5.2	1466 ± 67	38 ± 77	3269 ± 20	212 ± 2	5.5 ± 0.5	173	6.64 ± 0.03	0.2 ± 0.02	13.9
FIC19	lagoon	13.3	26.1 ± 3.3	2570 ± 117	70 ± 86	3649 ± 12	134 ± 3	3.5 ± 0.3	96	7.67	0.33 ± 0.02	14.10 ± 0.42
FIC18	lagoon	14.9	26.5 ± 3.3	2375 ± 109	63 ± 84	3592 ± 14	155 ± 3	3.9 ± 0.4	115	8.41 ± 0.05	0.14 ± 0.02	14.50
FIC17	well	15.2	1.6 ± 0.2	39813 ± 1672	1270 ± 147	5438 ± 1	12 ± 53	0.4 ± 0	-21	160.45	0.07 ± 0.02	13.08 ± 0.09
FIC16	lagoon	16.6	3.6 ± 0.5	2182 ± 96	60 ± 85	3384 ± 13	138 ± 3	3.6 ± 0.3	100	18.01	0.13 ± 0.02	14.75 ± 0.35
FIC15	lagoon	18.3	40.6 ± 4.9	1345 ± 55	36 ± 80	2828 ± 17	169 ± 2	4.2 ± 0.4	129	4.83	0.82 ± 0.02	17.20
FIC14	lagoon	21.0	65.5 ± 7.6	956 ± 41	26 ± 73	2802 ± 23	242 ± 1	5.9 ± 0.6	201	1.59 ± 0.02	0.19 ± 0.02	16.00
FIC13	seawater	23.3	71.5 ± 8.2	729 ± 25	19 ± 76	2153 ± 20	193 ± 1	4.6 ± 0.5	151	3.29 ± 0.05	0.28 ± 0.02	14.37
Means	Northern		14.9	7798	240	3801	127	3.6	92	39.0	10.07	44.43
	Southern		34.4	5498	168	3363	159	4.0	120	22.68	0.28	14.72
	All water		25.2	6588	202	3571	144	3.8	107	30.41	4.92	28.79
Standard deviations	Northern		12.47	10450	337	891	96	2.7	95	59.50	29.37	83.60
	Southern		22.64	12071	389	852	61	1.5	59	48.61	0.21	1.17
	All water		20.64	11081	357	875	79	2.1	78	53.15	20.22	57.78
Maximum	All water		71.5	39813	1270	5506	302	8.5	266	160.45	88.4	267
Minimum	All water		1.2	729	19	2153	12	0.4	-21	1.18	0.07	13.08
Range	All water		70.3	39084	1251	3353	290	8.1	287	159.27	88.33	253.92

Table 4.4 Coretop sample data with associated $\delta^{11}B$

Site	Distance km	pH_{tot} (nearest)	$\delta^{11}B_{borate}$ ‰	$\delta^{11}B_{borate}$ upper ‰	$\delta^{11}B_{borate}$ lower ‰	$\delta^{11}B_{calcite}$ ‰	$\delta^{18}O_{calcite}$ ‰	$\delta^{13}C_{calcite}$ ‰	B/Ca µmol/mol	Mg/Ca mmol/mol	Sr/Ca mmol/mol	Ba/Ca µmol/mol	$^{87}Sr/^{86}Sr$
UL-1	0.2	7.26 ± 0.03	11.67	11.72	11.63	15 ± 0.22	-1.76 ± 0.06	-7.07 ± 0.13	30.32 ± 0.6	6.53 ± 0.06	2.65 ± 0	9.07 ± 0.39	0.70832 ± 0.00002
UL-1	0.2	7.26 ± 0.03	11.67	11.72	11.63	14.85 ± 0.02	-2.12 ± 0.42	-6.55 ± 0.13	18.92 ± 0.21	4.95 ± 0.11	2.55 ± 0.07	6.63 ± 0.14	0.70837 ± 0.000015
3A	0.5	7.26 ± 0.03	11.67	11.72	11.63	8.73 ± 0.7	-1.84 ± 0.06	-6.31 ± 0.13	29.97 ± 0.6	6.65 ± 0.06	2.74 ± 0.01	9.35 ± 0.39	0.70831 ± 0.000015
FIC3	1	7.79 ± 0.03	13.83	14.01	13.66	18.53 ± 0.67	-1.08 ± 0.06	-6.98 ± 0.13	18.78 ± 0.18	4.71 ± 0.1	2.71 ± 0.08	7.69 ± 0.17	0.70859 ± 0.000015
FIC3[e]	1	7.79 ± 0.03	13.83	14.01	13.66	17.56 ± 0.46			88.42 ± 1.33		2.29 ± 0.01	14.03 ± 0.39	
FIC1	1.3	7.26 ± 0.03	11.67	11.72	11.63	11.96 ± 0.85	-1.08 ± 0.06	-6.34 ± 0.13	19.1 ± 0.18	4.82 ± 0.1	2.69 ± 0.08	6.83 ± 0.14	0.70862 ± 0.000025
FIC1[e]	1.3	7.26 ± 0.03	11.67	11.72	11.63	17.57 ± 0.62			52.42 ± 0.6	18.69 ± 0.06	2.48 ± 0.01	12.7 ± 0.39	
FIC1	1.3	7.26 ± 0.03	11.67	11.72	11.63	12.94 ± 0.27	-2.97 ± 0.06	-6.56 ± 0.13		8.71 ± 0.06	2.43 ± 0.01	8.94 ± 0.39	0.70839 ± 0.00002
2A	5.5	7.99 ± 0.03	15.10	15.34	14.86	18.44 ± 0.4	-2.28 ± 0.06	-6.85 ± 0.13	32.47 ± 0.6	7.11 ± 0.06	2.32 ± 0.01	7.33 ± 0.22	0.7085 ± 0.00001
5A	8.2	8.06 ± 0.03	15.77	16.05	15.5	12.34 ± 0.31	-2.55 ± 0.06	-6.48 ± 0.13		7.7 ± 0.06	2.26 ± 0.01	7.86 ± 0.22	0.70858 ± 0.000015
7 CEL	9.9	7.48 ± 0.03	12.51	12.61	12.42	16.29 ± 0.57			36.41 ± 0.6	6.8 ± 0.06	1.95 ± 0.01	6.29 ± 0.22	0.70909 ± 0.00006
9A	9.9	7.48 ± 0.03	12.51	12.61	12.42	12.63 ± 0.16	-2.73 ± 0.06	-7.63 ± 0.13	28.24 ± 0.6	6.8 ± 0.06	2.12 ± 0.01	5.9 ± 0.22	0.70861 ± 0.00003
8-1 CEL	10.7	7.54 ± 0.03	12.98	13.11	12.86	15.13 ± 0.76	-3.44 ± 0.06	-7.09 ± 0.13		6.71 ± 0.06	2.03 ± 0.01	6.68 ± 0.22	0.70862 ± 0.000015
8A	10.7	7.64 ± 0.03	13.24	13.39	13.1	15.57 ± 0.38	-2.91 ± 0.06	-6.95 ± 0.13	29.72 ± 0.6	7.32 ± 0.06	2.01 ± 0.01	6.13 ± 0.22	0.70875 ± 0.00002
8A	10.7	7.64 ± 0.03	13.24	13.39	13.1	15.57 ± 0.38	-2.91 ± 0.06	-6.95 ± 0.13	29.72 ± 0.6	7.32 ± 0.06	2.01 ± 0.01	6.13 ± 0.22	0.70875 ± 0.00002
8A	10.7	7.64 ± 0.03	13.24	13.39	13.1	15.53 ± 0.8	-2.55 ± 0.06	-6.59 ± 0.13	26.92 ± 0.6	6.02 ± 0.06	2.01 ± 0.01	5.67 ± 0.22	
FIC21	10.9	7.64 ± 0.03	13.24	13.39	13.1	9.67 ± 0.32	-3.22 ± 0.06	-7.42 ± 0.13	22.41 ± 0.6	7.12 ± 0.06	2.02 ± 0.01	6.43 ± 0.22	
FIC21	10.9	7.64 ± 0.03	13.24	13.39	13.1	15.95 ± 0.32	-2.99 ± 0.06	-7.17 ± 0.13	23.73 ± 0.6	7.53 ± 0.06	1.96 ± 0.01	5.92 ± 0.22	0.70873 ± 0.00002
ML-3-1	11.8	7.77 ± 0.03	14.43	14.65	14.23	9.7 ± 0.38	-2.9 ± 0.06	-6.47 ± 0.13	34.37 ± 0.6	9.46 ± 0.06	2.06 ± 0.01	5.92 ± 0.22	0.70868 ± 0.000007
MS-2-1	11.9	7.71 ± 0.03	13.98	14.17	13.8	17.86 ± 0.17	-3.12 ± 0.06	-7.02 ± 0.13	25.18 ± 0.6	7.06 ± 0.06	1.95 ± 0.01	4.45 ± 0.17	0.70875 ± 0.00002
MS-1-2	12.3	7.48 ± 0.03	12.67	12.78	12.56	8.68 ± 0.26	-2.98 ± 0.06	-7.14 ± 0.13	27.81 ± 0.6	6.43 ± 0.06	1.98 ± 0.01	4.72 ± 0.22	0.70873 ± 0.00001
FIC19	13.3	7.58 ± 0.03	13.05	13.19	12.92	10.44 ± 0.55	-2.92 ± 0.06	-6.27 ± 0.13	32.16 ± 0.6	6.99 ± 0.06	1.79 ± 0.01	4.7 ± 0.17	0.709 ± 0.00003
FIC19[e]	13.3	7.58 ± 0.03	13.05	13.19	12.92	17.45 ± 0.26			64.93 ± 0.6	17.06 ± 0.06	1.99 ± 0.01	10.61 ± 0.39	
FIC18	14.9	7.59 ± 0.03	13.32	13.47	13.18	8.06 ± 0.74	-2.7 ± 0.06	-6.79 ± 0.13	28.11 ± 1.99	5.22 ± 0.09	2.02 ± 0.01	4.69 ± 0.1	0.70904 ± 0.00003
FIC18[e]	14.9	7.59 ± 0.03	13.32	13.47	13.18	11.92 ± 0.4			69.75 ± 0.6	18.43 ± 0.06	1.96 ± 0.01	7.88 ± 0.22	
FIC18	14.9	7.59 ± 0.03	13.32	13.47	13.18	9.34 ± 0.64			37.47 ± 0.6	7.29 ± 0.06	1.81 ± 0.01	4.44 ± 0.17	0.70885 ± 0.00002
Means	Northern	7.54	12.91	13.03	12.80	14.54	-2.13	-6.82	20.48	5.22	2.45	7.16	0.70852
	Southern	7.63	13.41	13.56	13.26	11.21	-2.45	-6.61	24.88	5.14	2.06	4.17	0.70883
	All *A. park.*	7.57	13.09	13.23	12.07	13.33	-2.28	-6.73	22.4	5.18	2.28	5.86	0.70863
Standard deviations	Northern	0.27	1.31	1.38	1.23	2.62	0.74	0.50	7.20	1.01	0.30	2.90	0.00019
	Southern	0.09	0.55	0.58	0.52	3.62	0.60	0.61	9.45	1.49	0.16	0.95	0.00016
	All *A. park.*	0.22	1.10	1.17	1.04	3.36	0.67	0.38	5.57	1.16	0.31	1.46	0.00022
Maximum	All *A. park.*	8.06	15.77	16.05	15.50	18.53	-1.08	-6.27	37.47	9.46	2.74	9.35	0.70909
Minimum	All *A. park.*	7.26	11.67	11.72	11.63	8.06	-3.44	-7.63	18.78	4.71	1.79	4.44	0.70831
Range	All *A. park.*	0.80	4.10	4.33	3.87	8.06	2.36	1.36	18.69	4.75	0.95	4.91	0.00078

[e]*E. poeyanum* sample, all others *A. parkinsoniana*. Summary statistics for *A. parkinsoniana* only. Means and standard deviations of columns $\delta^{18}O$ through $^{87}Sr/^{86}Sr$ include data from supplemental tables

Table 4.5 Downcore sample data with associated $\delta^{11}B$

Site	Core	Interval cm	Depth cm	$\delta^{11}B_{calcite}$ ‰	$\delta^{18}O_{calcite}$ ‰	$\delta^{13}C_{calcite}$ ‰	$\delta^{13}C_{organic}$ ‰	C wt%	B/Ca µmol/mol	Mg/Ca mmol/mol	Sr/Ca mmol/mol	Ba/Ca µmol/mol	$^{87}Sr/^{86}Sr$
UL-1	UL-1	0-2	1	15.00 ± 0.23	-1.76 ± 0.06	-6.75 ± 0.13	-24.17 ± 0.22	4.5	30.32 ± 0.60	6.53 ± 0.06	2.65 ± 0.01	9.07 ± 0.35	0.70832 ± 0.00002
UL-1	UL-1	7.5-11	9.25	14.85 ± 0.02	-2.12 ± 0.06	-6.54 ± 0.13		0.0	18.92 ± 0.21	4.95 ± 0.11	2.55 ± 0.04	6.63 ± 0.35	0.70837 ± 0.00002
UL-1	UL-1	30-31	30.5	14.25 ± 0.38	-1.39 ± 0.06	-7.31 ± 0.13		0.0	28.30 ± 0.60	6.85 ± 0.06	2.72 ± 0.01	8.23 ± 0.35	0.70834 ± 0.00002
UL-1	UL-1	50-51	50.5	12.00 ± 0.31	-1.77 ± 0.06	-6.65 ± 0.13		0.0	24.53 ± 0.60	6.60 ± 0.06	2.73 ± 0.01	8.36 ± 0.35	0.70837 ± 0.00002
UL-1	UL-1	70-71	70.5	18.57 ± 0.48	-1.46 ± 0.06	-6.48 ± 0.13		0.0	28.21 ± 0.60	7.12 ± 0.06	2.64 ± 0.01	8.56 ± 0.35	0.70840 ± 0.00002
UL-1	UL-1	90-91	90.5	18.72 ± 0.43	-1.52 ± 0.06	-7.38 ± 0.13		0.0	26.20 ± 0.60	6.71 ± 0.06	2.83 ± 0.01	9.05 ± 0.35	0.70829 ± 0.00001
UL-1	UL-1	105-106	105.5	19.50 ± 0.47	-1.68 ± 0.06	-6.04 ± 0.13		0.0		5.19 ± 0.04		6.56 ± 0.35	0.70833 ± 0.00002
UL-1	UL-1	120-121	120.5	14.98 ± 0.37	-2.00 ± 0.06	-5.52 ± 0.13		0.0	31.21 ± 0.60	6.00 ± 0.06	2.35 ± 0.01	6.12 ± 0.35	0.70843 ± 0.00002
ML-3-1	ML-3-1	10-11	10.5	16.33 ± 0.52	-3.15 ± 0.06	-7.10 ± 0.13	-22.92 ± 0.40	3.1	20.50 ± 0.60		1.97 ± 0.01	5.23 ± 0.35	0.70865 ± 0.00002
ML-3-1	ML-3-1	20-21	20.5	15.96 ± 0.34	-3.42 ± 0.06	-6.88 ± 0.13	-22.71 ± 0.40	2.6	23.30 ± 0.60		1.96 ± 0.01	5.36 ± 0.35	0.70861 ± 0.00002
ML-3-1	ML-3-1	30-31	30.5	16.94 ± 0.43	-3.25 ± 0.06	-6.49 ± 0.13	-22.14 ± 0.44	2.0	17.66 ± 0.60		1.81 ± 0.01	4.47 ± 0.35	0.70861 ± 0.00002
ML-3-1	ML-3-1	40-41	40.5	16.17 ± 0.64	-3.22 ± 0.06	-6.00 ± 0.13	-21.70 ± 0.23	2.4	13.80 ± 0.60	8.71 ± 0.06	1.93 ± 0.01	5.73 ± 0.35	0.70860 ± 0.00001
ML-3-1	ML-3-1	50-51	50.5	15.24 ± 0.18	-3.28 ± 0.06		-21.70 ± 0.47	2.4	15.88 ± 0.60		1.81 ± 0.01	6.59 ± 0.35	0.70866 ± 0.00002
ML-3-1	ML-3-1	60-61	60.5	16.42 ± 0.51	-2.59 ± 0.06	-5.95 ± 0.13	-22.25 ± 0.26	1.8	19.72 ± 0.60	6.81 ± 0.06	1.70 ± 0.01	4.78 ± 0.35	0.70877 ± 0.00002
4A	4A-1P-1	15-16	15.5	16.23 ± 0.45	-1.36 ± 0.06	-6.94 ± 0.13	-24.19 ± 0.26	3.0	32.44 ± 0.60	7.44 ± 0.06	2.30 ± 0.01	8.63 ± 0.35	0.70837 ± 0.00002
4A	4A-1P-1	30-31	30.5	17.30 ± 0.50	-1.29 ± 0.06	-7.29 ± 0.13	-23.99 ± 0.40	2.0	26.56 ± 0.60	6.02 ± 0.06	2.38 ± 0.01	8.02 ± 0.35	0.70836 ± 0.00002
4A	4A-1P-1	35-36	35.5	17.57 ± 0.40	-1.78 ± 0.06	-6.73 ± 0.13	-24.04 ± 0.36	0.9	28.45 ± 0.60	6.14 ± 0.06	2.38 ± 0.01	7.87 ± 0.35	0.70832 ± 0.00002
4A	4A-1P-1	40-41	40.5	17.40 ± 0.69	-2.49 ± 0.06	-7.23 ± 0.13	-23.06 ± 0.14	1.8	22.79 ± 0.60	6.92 ± 0.06	2.11 ± 0.01	7.03 ± 0.35	0.70839 ± 0.00002
4A	4A-1P-1	50-51	50.5	15.31 ± 0.26	-2.74 ± 0.06	-7.13 ± 0.13	-23.63 ± 0.38	2.2	18.76 ± 1.9		2.30 ± 0.01	6.90 ± 0.35	0.70847 ± 0.00002
4A	4A-1P-1	60-61	60.5	14.12 ± 0.55	-2.41 ± 0.06	-6.61 ± 0.13	-23.13 ± 0.08	1.9	26.12 ± 0.60	6.36 ± 0.06	2.11 ± 0.01	7.45 ± 0.35	0.70853 ± 0.00001
4A	4A-1P-1	70-71	70.5	16.76 ± 0.27	-2.71 ± 0.06	-7.23 ± 0.13	-22.96 ± 0.29	1.9	22.65 ± 1.9		2.21 ± 0.01	6.22 ± 0.35	0.70856 ± 0.00003
4A	4A-1P-1	80-81	80.5	15.70 ± 0.35	-1.87 ± 0.06	-6.26 ± 0.13	-23.30	0.0	30.51 ± 0.60	6.91 ± 0.06	1.94 ± 0.01	7.56 ± 0.35	0.70848 ± 0.00002
4A	4A-1P-1	100-101	100.5	17.55 ± 0.24	-2.13 ± 0.06	-5.70 ± 0.13	-21.53 ± 0.19	1.9	29.94 ± 0.60	6.62 ± 0.06	1.88 ± 0.01	5.29 ± 0.35	0.70858 ± 0.00003
4A	4A-1P-1	108-109	108.5	16.25 ± 0.46	-2.55 ± 0.06	-6.13 ± 0.13	-21.70 ± 0.14	1.4	31.90 ± 0.60	5.09 ± 0.06	1.75 ± 0.01	5.28 ± 0.35	0.70863 ± 0.00002
4A	4A-1P-1	135-136	135.5	16.10 ± 0.55	-1.90 ± 0.06	-5.07 ± 0.13	-21.22 ± 0.26	1.1	45.74 ± 0.60	5.73 ± 0.06	1.56 ± 0.01	4.86 ± 0.35	0.70886 ± 0.00003
8A	8A-1P-1	10-11	10.5	11.45 ± 0.36	-2.93 ± 0.06	-6.94 ± 0.13	-23.14 ± 0.60	3.0	17.22 ± 0.60	7.97 ± 0.06	2.04 ± 0.01	5.79 ± 0.35	0.70871 ± 0.00002
8A	8A-1P-1	20-21	20.5	14.67 ± 0.36	-2.82 ± 0.06	-6.75 ± 0.13	-23.26 ± 0.38	2.6	17.62 ± 0.60		1.94 ± 0.01	5.52 ± 0.35	0.70871 ± 0.00003
8A	8A-1P-1	30-31	30.5	15.77 ± 0.56	-2.93 ± 0.06	-7.38 ± 0.13	-23.71 ± 0.38	2.7	11.56 ± 0.60	7.31 ± 0.06	2.09 ± 0.01	5.9 ± 0.35	0.70862 ± 0.00002
8A	8A-1P-1	40-41	40.5	12.76 ± 0.78	-3.18 ± 0.06	-6.79 ± 0.13	-22.86 ± 0.30	2.6	12.55 ± 0.60		1.94 ± 0.01	5.97 ± 0.35	0.70852 ± 0.00003
8A	8A-1P-1	50-51	50.5	10.98 ± 0.54	-2.74 ± 0.06	-6.82 ± 0.13	-22.74 ± 0.55	1.5	10.73 ± 0.60	6.7 ± 0.06	2.03 ± 0.01	5.32 ± 0.35	0.70865 ± 0.00003
8A	8A-1P-1	60-61	60.5	13.76 ± 0.37	-3.02 ± 0.06	-6.64 ± 0.13	-22.50 ± 0.285	2.7	12.28 ± 0.60		1.91 ± 0.01	5.20 ± 0.35	0.70864 ± 0.00002
8A	SPC8	0-2	1	15.57 ± 0.38	-2.91 ± 0.06	-6.95 ± 0.13		0.0	20.25 ± 0.60	7.32 ± 0.06	2.01 ± 0.01	6.13 ± 0.35	0.70875 ± 0.00002
8A	SPC8	0-8	4	15.53 ± 0.81	-2.55 ± 0.06	-6.59 ± 0.13		0.0	17.45 ± 0.60	6.02 ± 0.06	2.01 ± 0.01	5.67 ± 0.35	
Means		UL-1		15,98	-1.67	-6.44	-24.17	4.4	23.00	5.77	2.70	7.78	0.70836
		4A		16.39	-1.88	-6.37	-22.22	2.5	31.20	5.23	2.19	6.43	0.70857
		8A		13.81	-2.95	-6.78	-22.49	2.5	16.01	4.99	2.15	5.24	0.70865
		ML-3-1		16.18	-3.06	-6.58	-22.24	2.4	18.48	7.76	1.86	5.36	0.70865
Standard deviations		UL-1		2.64	0.29	0.64	0.11	0.97	5.47	0.76	0.13	0.83	0.00005
		4A		1.08	0.52	0.92	2.32	2.14	13.7	0.85	0.45	3.48	0.00031
		8A		1.90	0.33	0.4	0.74	0.72	5.37	0.89	0.13	0.53	0.00007

	ML-3-1	0.56	0.36	0.51	0.51	0.43	3.41	1.35	0.11	0.75	0.00006
Maximum	UL-1	19.50	-1.39	-6.05	-24.17	4.5	31.2	7.12	2.83	9.07	0.70843
	4A	17.57	-1.29	-5.07	-21.22	3.0	45.7	7.44	2.38	8.63	0.70886
	8A	15.77	-2.55	-6.59	-22.5	3.0	29.7	7.97	2.09	6.13	0.70875
	ML-3-1	16.94	-2.59	-5.95	-21.7	3.1	32.8	8.71	1.93	5.73	0.70877
Minimum	UL-1	12.00	-2.12	-7.72	-24.17	4.5	18.9	4.95	2.35	6.12	0.70829
	4A	14.12	-2.74	-7.29	-24.19	0.8	18.8	5.09	1.56	4.86	0.70832
	8A	10.98	-3.18	-7.38	-23.71	1.5	20.2	6.7	2.01	5.32	0.70862
	ML-3-1	15.24	-3.42	-7.1	-22.92	1.8	23.3	6.81	1.70	4.78	0.7086
Range	UL-1	7.50	0.73	1.67	0	0	12.3	2.16	0.48	2.95	0.00014
	4A	3.45	1.44	2.22	2.97	2.1	27.0	2.35	0.82	3.77	0.00054
	8A	4.79	0.63	0.79	1.21	1.4	9.5	1.26	0.08	0.8	0.00013
	ML-3-1	1.70	0.83	1.15	1.22	1.2	9.5	1.91	0.24	0.95	0.00017

All samples are *A. parkinsoniana*. Means and standard deviations of columns $\delta^{18}O$ through $^{87}Sr/^{86}Sr$ include data from supplemental tables

Table S4.1 Downcore sample isotope data for *A. parkinsoniana* without associated $\delta^{11}B$

Site	Core	Interval cm	Depth cm	$\delta^{18}O_{calcite}$ ‰	$\delta^{13}C_{calcite}$ ‰	$\delta^{13}C_{organic}$ ‰	C wt%	$^{87}Sr/^{86}Sr$
4A	SPC4	0-2	1	-1.94 ± 0.06	-7.62 ± 0.13			0.70839 ± 0.000005
4A	4A-1P-1	1-2	1.5	-1.40 ± 0.06	-7.12 ± 0.13	-23.93 ± 0.09	4.0	0.708393 ± 0.000005
4A	4A-1P-1	8-9	8.5	-1.65 ± 0.06	-7.20 ± 0.13	-24.02 ± 0.08	3.9	0.70837 ± 0.0000035
4A	4A-1P-1	90-91	90.5	-1.56 ± 0.06	-5.04 ± 0.13	-21.63 ± 1.87	2.6	
4A	4A-2B-1	5-6	143.5	-1.70 ± 0.06	-5.26 ± 0.13	-17.71 ± 0.01		0.708984 ± 0.000007
4A	4A-1P-1	148-149	148.5	-1.92 ± 0.06	-5.56 ± 0.13	-21.07 ± 0.23	1.1	
4A	4A-2B-1	14-15	165.5			-19.93 ± 0.26	2.0	0.708983 ± 0.000006
4A	4A-2B-1	25-26	176.5			-19.42 ± 0.06	1.6	
4A	4A-2B-1	35-36	186.5			-20.08 ± 0.01	1.6	0.70903 ± 0.0000035
4A	4A-2B-1	50-51	201.5	-1.46 ± 0.06	-4.63 ± 0.13	-19.59 ± 0.06	1.8	0.709036 ± 0.000007
4A	4A-2B-1	60-61	211.5			-19.37 ± 0.16	1.8	
4A	4A-2B-1	70-71	221.5			-20.12 ± 0.45	1.5	0.709056 ± 0.000007
4A	4A-2B-1	76-77	227.5	-0.85 ± 0.06	-6.37 ± 0.13	-21.86 ± 0.01	1.1	
4A	4A-2B-1	88-89	239.5			-27.28 ± 0.09	9.9	0.708035 ± 0.000007
4A	4A-2B-1	106-107	257.5			-26.84 ± 0.06	7.5	0.708065 ± 0.000007
8A	8A-1P-1	0-2	1	-2.59 ± 0.06	-6.76 ± 0.13	-24.6 ± 0.02	5.6	
8A	8A-1P-1	5-6	5.5	-3.17 ± 0.06	-7.24 ± 0.13	-22.74 ± 0.01	2.5	
8A	8A-1P-1	15-16	15.5	-2.52 ± 0.06	-6.55 ± 0.13	-22.76 ± 0.04	2.1	
8A	8A-1P-1	25-26	25.5	-3.16 ± 0.06	-6.98 ± 0.13	-22.98 ± 0.25	2.3	
8A	8A-1P-1	35-36	35.5	-2.91 ± 0.06	-6.88 ± 0.13	-22.65 ± 0.12	2.8	
8A	8A-1P-1	45-46	45.5	-2.87 ± 0.06	-7.61 ± 0.13	-22.59 ± 0.14	2.2	
8A	8A-1P-1	55-56	55.5	-3.07 ± 0.06	-6.48 ± 0.13	-21.94 ± 0.16	2.1	0.70858 ± 0.000022
8A	8A-1P-1	65-66	65.5	-3.79 ± 0.06	-6.81 ± 0.13	-21.93 ± 0.3	2.4	
8A	8A-1P-1	70-71	70.5	-2.71 ± 0.06	-5.94 ± 0.13	-21.86 ± 0.09	2.6	
8A	8A-1P-1	80-81	80.5	-2.49 ± 0.06	-6.32 ± 0.13	-21.85 ± 0.04	2.5	
8A	8A-1P-1	85-86	85.5	-2.97 ± 0.06	-6.67 ± 0.13	-21.37 ± 0.08	2.3	
8A	8A-1P-1	90-91	90.5	-3.61 ± 0.06	-7.25 ± 0.13	-21.78 ± 0.17	2.3	
8A	8A-1P-1	100-101	100.5	-2.87 ± 0.06	-6.02 ± 0.13	-21.6 ± 0.11	2.4	
8A	8A-1P-1	110-111	110.5			-21.7 ± 0.16	2.6	
8A	8A-1P-1	115-116	115.5	-3.37 ± 0.06	-7.1 ± 0.13	-21.88 ± 0.1	2.5	0.70865 ± 0.000025
8A	8A-1P-1	120-121	120.5	-2.75 ± 0.06	-6.41 ± 0.13	-22.35 ± 0.01	2.5	
8A	8A-1P-1	130-131	130.5			-22.41 ± 0.1	2.9	
8A	8A-1P-1	134-135	134.5			-22.51 ± 0.09	1.9	0.70866 ± 0.000023
UL-1	UL-1	2-5	3.5	-1.13 ± 0.06	-7.08 ± 0.13			
UL-1	UL-1	5-7.5	6.25	-1.4 ± 0.06	-6.38 ± 0.13	-24.16 ± 0.09	3.4	

UL-1	UL-1	11-13	12	-1.49 ± 0.06	-6.73 ± 0.13	-24.29 ± 0.07	4.4
UL-1	UL-1	13-15	14	-1.6 ± 0.06	-6.81 ± 0.13		
UL-1	UL-1	15-17.5	16.25	-1.33 ± 0.06	-6.24 ± 0.13	-24.31 ± 0.04	5.1
UL-1	UL-1	17.5-20	18.75	-1.67 ± 0.06	-5.96 ± 0.13		
UL-1	UL-1	20-22	21	-1.22 ± 0.06	-6.99 ± 0.13	-24.11 ± 0.1	5.8
UL-1	UL-1	22-22.5	23.25	-1.6 ± 0.06	-6.73 ± 0.13		
UL-1	UL-1	24.5-26	25.25	-1.32 ± 0.06	-6.44 ± 0.13		
UL-1	UL-1	32-33	32	-1.52 ± 0.06	-6.75 ± 0.13		
UL-1	UL-1	44.5-46	45.25	-2.00 ± 0.06	-7.36 ± 0.13		
UL-1	UL-1	55-56	55.5	-1.49 ± 0.06	-6.92 ± 0.13		
UL-1	UL-1	60-61	60.5	-1.55 ± 0.06	-6.67 ± 0.13		
UL-1	UL-1	65-66	65.5	-1.55 ± 0.06	-6.39 ± 0.13		
UL-1	UL-1	75-76	75.5	-1.68 ± 0.06	-6.22 ± 0.13		
UL-1	UL-1	80-81	80.5	-1.61 ± 0.06	-6.91 ± 0.13		
UL-1	UL-1	85-86	85.5	-1.52 ± 0.06	-7.37 ± 0.13		
UL-1	UL-1	95-96	95.5	-1.58 ± 0.06	-6.84 ± 0.13		
UL-1	UL-1	100-101	100.5	-1.47 ± 0.06	-6.86 ± 0.13	-24.01 ± 0.1	3.3
UL-1	UL-1	110-111	110.5	-2.29 ± 0.06	-5.73 ± 0.13		
UL-1	UL-1	115-116	115.5	-2.12 ± 0.06	-5.79 ± 0.13		
UL-1	UL-1	119-120	119.5	-2.07 ± 0.06	-5.52 ± 0.13		
UL-1	UL-1	125-126	125.5	-2.25 ± 0.06	-5.86 ± 0.13		
UL-1	UL-1	130-131	130.5	-1.78 ± 0.06	-5.81 ± 0.13		
UL-1	UL-1	135-136	135.5	-1.74 ± 0.06	-4.86 ± 0.13		
UL-1	UL-1	138-139	138.5	-1.99 ± 0.06	-5.18 ± 0.13		
ML-3-1	ML-3-1	1-2	1.5	-2.5 ± 0.06	-7.04 ± 0.13		

Table S4.2 Downcore trace metal data for *A. parkinsoniana* without associated $\delta^{11}B$

Site	Core	Interval cm	Depth cm	B/Ca µmol/mol	Mg/Ca mmol/mol	Sr/Ca mol/mol	Ba/Ca µmol/mol
4A	4A-1P-1	1-2	1.5	18.94 ± 3.4	4.49 ± 0.05	2.8 ± 0.01	7.43 ± 0.05
4A	4A-1P-1	8-9	8.5	33.92 ± 3.4	6.18 ± 0.05	2.69 ± 0.01	24.42 ± 0.05
4A	4A-1P-1	12-13	12.5	21.11 ± 6.81	5.05 ± 0.03	2.69 ± 0.02	7.94 ± 0.08
4A	4A-1P-1	17-18	17.5	15.21 ± 6.81	4.94 ± 0.03	2.63 ± 0.02	8.51 ± 0.08
4A	4A-1P-1	22-23	22.5		5.24 ± 0.03	2.76 ± 0.01	8.01 ± 0.08
4A	4A-1P-1	24-25	24.5	15.29 ± 6.81	6.05 ± 0.03	2.8 ± 0.02	9.26 ± 0.36
4A	4A-1P-1	27-28	27.5		5.81 ± 0.03	2.61 ± 0.02	7.26 ± 0.08
4A	4A-1P-1	33-34	33.5	19.14 ± 6.81	5.09 ± 0.03	2.47 ± 0.02	7.67 ± 0.08
4A	4A-1P-1	37-38	37.5	17.64 ± 6.81	4.91 ± 0.03	2.46 ± 0.02	6.14 ± 0.08
4A	4A-1P-1	45-46	45.5	24.6 ± 6.81	5.43 ± 0.03	2.51 ± 0.02	7.02 ± 0.08
4A	4A-1P-1	55-56	55.5	21.05 ± 6.81	6.03 ± 0.03	2.35 ± 0.02	7.01 ± 0.08
4A	4A-1P-1	65-66	65.5	22.21 ± 6.81	4.84 ± 0.03	2.27 ± 0.02	6.11 ± 0.08
4A	4A-1P-1	75-76	75.5		4.82 ± 0.03	2.23 ± 0.02	6.23 ± 0.08
4A	4A-1P-1	85-86	85.5	29.56 ± 6.81	4.37 ± 0.07	2.06 ± 0.02	4.73 ± 0.08
4A	4A-1P-1	90-91	90.5	30.62 ± 3.4	3.63 ± 0.05	2.19 ± 0.01	4.80 ± 0.05
4A	4A-1P-1	95-96	95.5	30.68 ± 6.81	4.65 ± 0.07	1.98 ± 0.02	4.69 ± 0.08
4A	4A-1P-1	105-106	105.5	31.48 ± 6.81	3.85 ± 0.07	1.97 ± 0.02	6.48 ± 0.08
4A	4A-1P-1	109-110	109.5	28.22 ± 6.81	4.8 ± 0.03	1.99 ± 0.02	5.21 ± 0.08
4A	4A-1P-1	120-121	120.5	35.09 ± 6.81	4.0 ± 0.07	1.91 ± 0.02	4.35 ± 0.08
4A	4A-1P-1	128-129	128.5	28.17 ± 6.81	4.89 ± 0.03	2.05 ± 0.02	4.92 ± 0.08
4A	4A-1P-1	140-141	140.5	49.27 ± 6.81	4.94 ± 0.03	1.61 ± 0.02	3.15 ± 0.08
4A	4A-1P-1	145-146	145.5	49.21 ± 6.81	4.77 ± 0.03	1.56 ± 0.02	2.95 ± 0.08
4A	4A-1P-1	148-149	148.5	51.77 ± 6.81	4.91 ± 0.05	1.66 ± 0.02	3.1 ± 0.08
4A	4A-1P-1	150-151	150.5	50.57 ± 6.81	4.42 ± 0.07	1.57 ± 0.02	3.01 ± 0.08
4A	4A-2B-1	2-3	153.5	7.65 ± 6.81	4.74 ± 0.03	2.14 ± 0.02	5.53 ± 0.08
4A	4A-2B-1	10-11	161.5	43.72 ± 6.81	5.64 ± 0.03	1.62 ± 0.02	3.12 ± 0.08
4A	4A-2B-1	14-15	165.5	44.92 ± 6.81	4.13 ± 0.07	1.47 ± 0.02	2.55 ± 0.08
4A	4A-2B-1	20-21	171.5	44.53 ± 6.81	6.62 ± 0.03	1.59 ± 0.02	3.17 ± 0.08

4A	4A-2B-1	39-40	190.5	64.44 ± 6.81	5.77 ± 0.03	1.61 ± 0.02	3.12 ± 0.08
4A	4A-2B-1	50-51	201.5			2.36 ± 0.02	
4A	4A-2B-1	50-51	201.5	50.52 ± 1.6	4.55 ± 0.04	1.46 ± 0.02	2.63 ± 0.04
4A	4A-2B-1	65-66	216.5	52.57 ± 6.81	4.49 ± 0.07	1.62 ± 0.02	2.37 ± 0.08
4A	4A-2B-1	70-71	221.5	51.24 ± 6.81	4.20 ± 0.07	1.55 ± 0.02	2.41 ± 0.08
4A	4A-2B-1	76-77	227.5	53.64 ± 3.72		1.72 ± 0.02	3.39 ± 0.04
4A	4A-2B-1	78-79	229.5	52.68 ± 6.81	5.06 ± 0.03	1.76 ± 0.02	3.60 ± 0.08
4A	SPC4	2-4	3	10.99 ± 0.63	5.50 ± 0.1	2.48 ± 0.02	8.61 ± 0.07
4A	SPC4	4-6	5	12.39 ± 0.63	5.55 ± 0.1	3.02 ± 0.02	8.91 ± 0.08
4A	SPC4	6-8	7	32.13 ± 0.63	5.17 ± 0.1	2.66 ± 0.02	7.94 ± 0.07
4A	SPC4	8-10	9	22.52 ± 0.63	5.64 ± 0.1	2.71 ± 0.02	15.29 ± 0.08
4A	SPC4	10-12	11	35.45 ± 0.63	3.84 ± 0.06	2.55 ± 0.02	6.64 ± 0.07
4A	SPC4	12-14	13	23.55 ± 0.63	5.09 ± 0.10	2.65 ± 0.02	7.47 ± 0.07
4A	SPC4	14-16	15	20.93 ± 0.63	4.83 ± 0.10	3.09 ± 0.02	8.49 ± 0.07
4A	SPC4	16-18	17	11.62 ± 0.63	5.71 ± 0.10	2.86 ± 0.02	8.62 ± 0.07
4A	SPC4	18-20	19	16.13 ± 0.63	4.77 ± 0.10	2.68 ± 0.02	8.10 ± 0.07
8A	8A-1P-1	0-2	1	16.82 ± 6.2	4.65 ± 0.02	2.23 ± 0.02	5.30 ± 0.03
8A	8A-1P-1	3-4	3.5	20.52 ± 1.6	5.93 ± 0.05	2.30 ± 0.02	5.34 ± 0.14
8A	8A-1P-1	5-6	5.5	17.48 ± 6.2	4.53 ± 0.02	2.22 ± 0.02	5.27 ± 0.03
8A	8A-1P-1	7-8	7.5	9.89 ± 1.6	4.5 ± 0.04	2.11 ± 0.02	6.02 ± 0.14
8A	8A-1P-1	12-13	12.5	14.42 ± 1.6	4.66 ± 0.04	2.13 ± 0.02	5.47 ± 0.14
8A	8A-1P-1	15-16	15.5	16.42 ± 2.31	4.76 ± 0.03	2.18 ± 0.01	5.13 ± 0.09
8A	8A-1P-1	17-18	17.5	18.13 ± 1.6	4.77 ± 0.05	2.10 ± 0.02	5.01 ± 0.14
8A	8A-1P-1	22-23	22.5	15.3 ± 1.6	4.86 ± 0.05	2.14 ± 0.02	5.11 ± 0.14
8A	8A-1P-1	25-26	25.5		6.94 ± 0.04	2.91 ± 0.01	
8A	8A-1P-1	32-33	32.5	16.4 ± 1.6	4.68 ± 0.04	2.25 ± 0.02	5.02 ± 0.14
8A	8A-1P-1	35-36	35.5	14.73 ± 2.31	5.51 ± 0.03	2.27 ± 0.01	5.95 ± 0.08
8A	8A-1P-1	37-38	37.5	16.1 ± 1.6	4.38 ± 0.04	2.19 ± 0.02	5.83 ± 0.14
8A	8A-1P-1	42-43	42.5	7.65 ± 1.6	4.28 ± 0.04	2.17 ± 0.02	5.12 ± 0.14
8A	8A-1P-1	45-46	45.5	13.09 ± 2.31	4.54 ± 0.04	2.13 ± 0.01	5.49 ± 0.08
8A	8A-1P-1	47-48	47.5	19.62 ± 1.6	4.57 ± 0.04	2.19 ± 0.02	5.04 ± 0.14

8A	8A-1P-1	52-53	52.5	16.57 ± 1.6	4.31 ± 0.04	2.06 ± 0.02	4.84 ± 0.14
8A	8A-1P-1	55-56	55.5	17.29 ± 2.31	4.99 ± 0.03	2.1 ± 0.01	4.84 ± 0.09
8A	8A-1P-1	57-58	57.5	20.84 ± 1.6	4.98 ± 0.05	2.14 ± 0.02	4.84 ± 0.14
8A	8A-1P-1	62-63	62.5	18.63 ± 1.6	5.98 ± 0.05	2.11 ± 0.02	4.68 ± 0.04
8A	8A-1P-1	65-66	65.5	12.58 ± 2.31	4.76 ± 0.03	2.15 ± 0.01	4.86 ± 0.09
8A	8A-1P-1	67-68	67.5	21.68 ± 1.6	4.8 ± 0.05	2.1 ± 0.02	4.9 ± 0.14
8A	8A-1P-1	70-71	70.5	29.92 ± 3.4	4.82 ± 0.05	2.07 ± 0.01	4.97 ± 0.05
8A	8A-1P-1	72-73	72.5	19.58 ± 1.6	4.85 ± 0.05	2.12 ± 0.02	5.31 ± 0.14
8A	8A-1P-1	75-76	75.5	11 ± 1.6	4.72 ± 0.04	2.08 ± 0.02	5.47 ± 0.14
8A	8A-1P-1	77-78	77.5	5.96 ± 1.6	3.61 ± 0.04	2.22 ± 0.02	4.77 ± 0.14
8A	8A-1P-1	80-81	80.5	16.17 ± 3.4	3.97 ± 0.05	2.19 ± 0.01	4.92 ± 0.05
8A	8A-1P-1	81-82	81.5	7.95 ± 1.6	5.03 ± 0.05	2.13 ± 0.02	6.42 ± 0.14
8A	8A-1P-1	82-83	82.5	14.07 ± 3.4	5.07 ± 0.05	2.11 ± 0.01	4.79 ± 0.05
8A	8A-1P-1	84-85	84.5	14.49 ± 1.6	4.73 ± 0.05	2.03 ± 0.02	3.81 ± 0.04
8A	8A-1P-1	85-86	85.5	17.23 ± 2.31	4.74 ± 0.04	2.12 ± 0.01	5.42 ± 0.08
8A	8A-1P-1	87-88	87.5	9.46 ± 1.6	4.93 ± 0.05	2.1 ± 0.02	5.54 ± 0.14
8A	8A-1P-1	90-91	90.5	19.62 ± 3.4	5.33 ± 0.05	2.09 ± 0.01	6.03 ± 0.05
8A	8A-1P-1	95-96	95.5	11.74 ± 1.6	5.53 ± 0.05	2.13 ± 0.02	5.93 ± 0.14
8A	8A-1P-1	97-98	97.5	11.22 ± 1.6	3.74 ± 0.04	1.98 ± 0.02	5.61 ± 0.14
8A	8A-1P-1	100-101	100.5	20.05 ± 3.4	4.5 ± 0.05	2.22 ± 0.01	5.43 ± 0.05
8A	8A-1P-1	102-103	102.5	13.77 ± 1.6	4.69 ± 0.04	2.18 ± 0.02	5.5 ± 0.14
8A	8A-1P-1	105-106	105.5	18.78 ± 1.6	4.66 ± 0.04	2.21 ± 0.02	4.91 ± 0.14
8A	8A-1P-1	107-108	107.5	6.91 ± 1.6	4.01 ± 0.04	2.02 ± 0.02	4.05 ± 0.04
8A	8A-1P-1	110-111	110.5	18.15 ± 2.31	4.97 ± 0.03	2.11 ± 0.01	4.7 ± 0.07
8A	8A-1P-1	112-113	112.5	39.06 ± 1.6	6.45 ± 0.05	2.27 ± 0.02	6.14 ± 0.14
8A	8A-1P-1	115-116	115.5	15.35 ± 2.31	4.56 ± 0.03	2.11 ± 0.01	5.46 ± 0.08
8A	8A-1P-1	117-118	117.5	12.59 ± 1.6	4.53 ± 0.04	2.11 ± 0.02	6.42 ± 0.14
8A	8A-1P-1	120-121	120.5	20.35 ± 3.4	4.39 ± 0.05	2.21 ± 0.01	5.69 ± 0.05
8A	8A-1P-1	130-131	130.5	29.99 ± 1.6	4.45 ± 0.04	2.22 ± 0.02	5.38 ± 0.14
8A	8A-1P-1	132-133	132.5	15.28 ± 1.6	4.7 ± 0.04	2.09 ± 0.02	5.39 ± 0.14
8A	8A-1P-1	134-135	134.5	14.2 ± 2.31	4.97 ± 0.03	2.17 ± 0.01	5.16 ± 0.08

8A	SPC8	2-4	3	14.01 ± 0.63	4.79 ± 0.1	2.13 ± 0.02	5.07 ± 0.07
8A	SPC8	4-6	5	15.03 ± 0.63	4.84 ± 0.1	2.03 ± 0.02	4.67 ± 0.01
8A	SPC8	6-8	7	9.79 ± 0.63	4.61 ± 0.06	2.3 ± 0.02	4.61 ± 0.01
8A	SPC8	8-10	9	12.06 ± 0.63	4.73 ± 0.1	2.19 ± 0.02	4.77 ± 0.07
8A	SPC8	10-12	11	19.07 ± 0.63	3.84 ± 0.06	2.11 ± 0.02	5.05 ± 0.07
8A	SPC8	12-14	13	17.44 ± 0.63	5.85 ± 0.1	2.24 ± 0.02	4.70 ± 0.01
8A	SPC8	14-16	15	12.62 ± 0.63	4.93 ± 0.1	2.28 ± 0.02	4.41 ± 0.01
8A	SPC8	16-18	17	17.17 ± 0.63	4.12 ± 0.06	2.22 ± 0.02	4.46 ± 0.01
8A	SPC8	18-20	19	19.88 ± 0.63	4.70 ± 0.06	2.13 ± 0.02	4.81 ± 0.07
8A	SPC8	20-22	21	16.25 ± 0.63	6.27 ± 0.1	2.23 ± 0.02	4.95 ± 0.07
8A	SPC8	22-24	23	14.47 ± 0.63	3.97 ± 0.06	2.22 ± 0.02	4.95 ± 0.07
UL-1	UL-1	2-5	3.5	23.62 ± 0.13	5.55 ± 0.01	2.73 ± 0.01	8.39 ± 0.15
UL-1	UL-1	5-7.5	6.25	28.97 ± 0.13	5.06 ± 0.01	2.68 ± 0.01	6.72 ± 0.15
UL-1	UL-1	11-13	12	17.78 ± 0.13	5.08 ± 0.01	2.85 ± 0.01	8.03 ± 0.15
UL-1	UL-1	13-15	14	18.23 ± 0.13	5.11 ± 0.01	2.59 ± 0.01	7.69 ± 0.15
UL-1	UL-1	15-17.5	16.25	15.85 ± 0.13	4.96 ± 0.01	2.77 ± 0.01	7.54 ± 0.15
UL-1	UL-1	17.5-20	18.75	23.59 ± 0.13	5.95 ± 0.01	2.65 ± 0.01	7.66 ± 0.15
UL-1	UL-1	20-22	21	19.16 ± 0.13	5.07 ± 0.01	2.81 ± 0.01	7.65 ± 0.15
UL-1	UL-1	22-24.5	23.25	25.08 ± 0.13	5.27 ± 0.01	2.8 ± 0.01	7.90 ± 0.15
UL-1	UL-1	24.5-26	25.25	16.74 ± 0.13	5.30 ± 0.01	2.67 ± 0.01	7.86 ± 0.15
UL-1	UL-1	32-33	32	14.23 ± 0.13	6.58 ± 0.01	2.84 ± 0.01	8.06 ± 0.15

Table S4.3 Lagoon salinity measured *in situ*

Year	Month	Distance km	Latitude	Longitude	Salinity
2000	Dec	0.95	20.95292	-90.34322	17.7
2000	Dec	1.08	20.95187	-90.34367	16.4
2000	Dec	3.96	20.92832	-90.35025	14.4
2000	Dec	4.37	20.92503	-90.34545	10.8
2000	Dec	8.54	20.89095	-90.35665	8.9
2000	Dec	9.65	20.88188	-90.36467	17.1
2000	Dec	9.89	20.87992	-90.36257	9.6
2000	Dec	10.19	20.87750	-90.35550	10.4
2000	Dec	10.72	20.87318	-90.35918	17.2
2000	Dec	12.21	20.86105	-90.37763	17.1
2000	Dec	12.24	20.86080	-90.37490	16.6
2000	Dec	15.11	20.83735	-90.38550	21.3
2000	Dec	17.54	20.81750	-90.39083	31.1
2000	Dec	17.57	20.81723	-90.38850	27.0
2000	Dec	20.37	20.79443	-90.40992	31.1
2000	Dec	20.52	20.79318	-90.40245	33.3
2000	Dec	20.73	20.79147	-90.39707	31.2
2000	Dec	22.45	20.77742	-90.40882	34.2
2000	Dec	24.03	20.76455	-90.41302	35.1
2001	Oct	-0.42	20.96410		15.0
2001	Oct	-0.42	20.96410	-90.34192	15.0
2001	Oct	0.92	20.95320		14.7
2001	Oct	0.92	20.95320	-90.34345	14.7
2001	Oct	1.00	20.95250		14.0
2001	Oct	1.04	20.95218		14.3
2001	Oct	1.04	20.95217		13.9

2001	Oct	1.05	20.95213		14.2
2001	Oct	1.05	20.95213	-90.34367	14.3
2001	Oct	4.70	20.92235		14.1
2001	Oct	5.39	20.91667	-90.34825	15.1
2001	Oct	5.39	20.91667		15.1
2001	Oct	6.10	20.91090		17.8
2001	Oct	6.10	20.91090	-90.35012	17.8
2001	Oct	8.26	20.89327		17.5
2001	Oct	8.48	20.89148		22.0
2001	Oct	8.59	20.89057		20.0
2001	Oct	9.88	20.88002	-90.36722	22.2
2001	Oct	9.88	20.88002		22.4
2001	Oct	9.94	20.87952		21.5
2001	Oct	10.18	20.87760		20.0
2001	Oct	10.19	20.87750		12.4
2001	Oct	10.65	20.87373		14.8
2001	Oct	10.65	20.87373	-90.35935	14.8
2001	Oct	10.74	20.87298		20.0
2001	Oct	12.20	20.86107		25.7
2001	Oct	12.27	20.86057		25.5
2001	Oct	12.27	20.86055		25.4
2001	Oct	14.26	20.84427		26.0
2001	Oct	15.06	20.83772		30.0
2001	Oct	15.19	20.83673		27.0
2001	Oct	15.19	20.83673	-90.38540	27.0
2001	Oct	15.22	20.83642		22.1
2001	Oct	16.49	20.82608		30.0
2001	Oct	17.57	20.81728		32.0
2001	Oct	20.46	20.79372		30.0

2001	Oct	20.46	20.79368		30.0
2001	Oct	20.85	20.79047	-90.39705	28.2
2001	Oct	20.85	20.79047		28.2
2001	Oct	22.44	20.77753		34.0
2001	Oct	23.17	20.77158		38.5
2001	Oct	24.89	20.75752		37.7
2002	Jul	0.86	20.95367		22.5
2002	Jul	1.83	20.94573		25.0
2002	Jul	3.41	20.93283		22.5
2002	Jul	4.25	20.92602		22.2
2002	Jul	5.82	20.91313		19.8
2002	Jul	7.48	20.89958		17.7
2002	Jul	9.71	20.88143		18.9
2002	Jul	9.86	20.88020		17.3
2002	Jul	11.31	20.86833		17.1
2002	Jul	12.53	20.85837		25.0
2002	Jul	14.45	20.84270		27.0
2002	Jul	16.63	20.82492		29.4
2002	Jul	18.18	20.81232		32.7
2002	Jul	20.25	20.79537		34.2
2002	Jul	22.86	20.77412		35.5
2003	Mar	0.24	20.95873		22.0
2003	Mar	3.21	20.93447		21.0
2003	Mar	3.36	20.93327		21.0
2003	Mar	5.69	20.91425		21.0
2003	Mar	5.75	20.91378		24.0
2003	Mar	8.92	20.88785		26.0
2003	Mar	8.93	20.88778		28.0
2003	Mar	11.62	20.86582		32.0

2003	Mar	12.70	20.85700	28.0
2003	Mar	13.31	20.85205	28.0
2003	Mar	13.92	20.84708	29.0
2003	Mar	14.51	20.84227	29.0
2003	Mar	14.97	20.83850	30.0
2003	Mar	15.38	20.83513	30.0
2003	Mar	15.41	20.83487	33.0
2003	Mar	15.57	20.83357	30.0
2003	Mar	16.08	20.82947	30.0
2003	Mar	16.75	20.82400	31.0
2003	Mar	17.15	20.82067	32.0
2003	Mar	17.20	20.82028	31.0
2003	Mar	17.22	20.82008	35.0
2003	Mar	17.70	20.81618	32.0
2003	Mar	18.26	20.81163	32.0
2003	Mar	18.78	20.80737	33.0
2003	Mar	19.33	20.80288	33.0
2003	Mar	19.98	20.79760	34.0
2003	Mar	20.11	20.79655	36.0
2003	Mar	20.20	20.79577	34.0
2003	Mar	20.37	20.79440	35.0
2003	Mar	20.93	20.78985	35.0
2003	Mar	21.48	20.78533	34.0
2003	Mar	21.96	20.78143	35.0
2003	Mar	22.44	20.77752	37.0
2003	Mar	22.91	20.77372	38.0
2003	Mar	22.91	20.77368	39.0
2003	Mar	23.96	20.76515	40.0
2003	Apr	-0.36	20.96363	14.4

2003	Apr	1.36	20.94958	16.4
2003	Apr	1.61	20.94750	19.3
2003	Apr	4.26	20.92593	15.7
2003	Apr	4.48	20.92412	18.7
2003	Apr	8.33	20.89265	20.1
2003	Apr	11.43	20.86740	16.8
2003	Apr	11.44	20.86732	18.5
2003	Apr	13.94	20.84690	21.0
2003	Apr	13.96	20.84670	26.8
2003	Apr	17.64	20.81672	30.5
2003	Apr	19.99	20.79753	26.2
2003	Apr	20.02	20.79723	30.0
2003	Apr	24.03	20.76455	32.2
2006	May	0.15	20.95942	22.6
2006	May	0.17	20.95925	22.7
2006	May	0.17	20.95925	22.7
2006	May	1.96	20.94464	22.3
2006	May	5.31	20.91736	22.4
2006	May	8.48	20.89147	22.8
2006	May	8.48	20.89147	20.0
2006	May	11.29	20.86853	24.9
2006	May	12.63	20.85761	25.0
2006	May	15.54	20.83386	26.3
2006	May	19.56	20.80100	28.7
2006	May	24.01	20.76472	34.6
2009	Jun	2.47	20.94055	23.3
2009	Jun	5.31	20.91732	27.2
2009	Jun	7.59	20.89875	24.6
2009	Jun	10.19	20.87752	21.5

2009	Jun	11.80	20.86435	29.1
2009	Jun	13.83	20.84783	30.6
2009	Jun	16.13	20.82905	31.7
2009	Jun	17.03	20.82164	28.6
2009	Jun	18.81	20.80715	34.2
2009	Jun	21.67	20.78380	36.4
2009	Jun	23.59	20.76813	37.2
2009	Jun	24.59	20.75995	36.0
2015	May	0.92	20.95318	12.5
2015	May	1.02	20.95237	17.1
2015	May	1.27	20.95030	15.3
2015	May	1.30	20.95005	16.1
2015	May	4.21	20.92632	18.3
2015	May	7.14	20.90238	18.8
2015	May	10.05	20.87863	22.5
2015	May	10.19	20.87753	14.3
2015	May	10.19	20.87750	8.9
2015	May	10.45	20.87537	25.5
2015	May	11.01	20.87083	26.2
2015	May	11.72	20.86505	27.6
2015	May	12.27	20.86052	28.3
2015	May	13.29	20.85218	25.3
2015	May	14.88	20.83918	31.1
2015	May	16.58	20.82535	27.4
2015	May	18.31	20.81127	32.0
2015	May	21.04	20.78893	34.1
2015	May	23.35	20.77012	36.3

Table S4.4 Crushed mass of *A. parkinsoniana* 250-500 µm fraction used to generate coretop $\delta^{11}B$

Site	Interval cm	$\delta^{11}B_{calcite}$ ‰	Depth cm	Crushed mass mg
UL-1	0-2	15.00	1	4.1
UL-1	7.5-11	14.85	9.25	6.1
3A	0-2	8.73	1	4.2
FIC3	0-2	18.53	1	3.2
FIC1	0-2	11.96	1	3.1
FIC1	1-2	12.94	1.5	3.9
2A	0-2	18.44	1	4.0
5A	0-2	12.34	1	3.4
CEL.7	0-2	16.29	1	3.8
9A	0-2	12.63	1	3.6
CEL.8-1	0-2	15.13	1	
8A	0-8	15.53	4	3.4
8A	0-2	15.57	1	3.5
FIC21	0-1	9.67	0.5	2.8
FIC21	1-2	15.95	1.5	3.5
ML-3-1	0-1	9.70	0.5	3.3
MS-2-1	0-1	17.86	0.5	3.6
MS-1-2	1-2	8.68	1.5	3.3
FIC19	0-2	10.44	1	2.0
FIC18	0-2	8.06	1	2.1
FIC18	0-1	9.34	0.5	1.6

Table S4.5 *A. parkinsoniana* counts and masses within the top 20 cm of sediments

Site	Fraction µm	Count	Mass µg
ML-3-1	250-355	20	426
3SPC	355-425	12	444
3SPC	355-425	14	461
4SPC	355-425	11	421
4SPC	355-425	37	1166
4SPC	355-425	37	1126
4SPC	355-425	30	1333
4SPC	355-425	27	1155
5SPC	250-355	20	460
5SPC	250-355	23	492
5SPC	355-425	11	411
5SPC	355-425	13	482
5SPC	355-425	33	1254
5SPC	355-425	34	1185
5SPC	425-500	8	471
5SPC	425-500	6	425
6SPC	250-355	19	440
6CEL	355-425	9	428
6SPC	250-355	33	432
6SPC	355-425	38	1102
6SPC	355-425	33	1097
6SPC	355-425	33	1152
6SPC	425-500	25	1139
7SPC	250-355	46	286
8SPC	355-425	11	451
8SPC	425-500	7	478

8CEL	355-425	11	467
8SPC	250-355	18	381
8SPC	355-425	12	373
8SPC	355-425	30	1232
8SPC	355-425	30	1130
8SPC	355-425	32	1147
8SPC	355-425	33	1142
CEL6	250-355	18	434
CEL6	355-425	9	379
CEL6	425-500	7	418
CEL8-1	250-355	17	411
CEL8-1	355-425	8	368
CEL8-1	425-500	6	406
FIC2	250-355	20	450
FIC2	250-355	16.5	375
FIC2	250-355	18	415
FIC2	250-355	15	345
FIC2	355-425	9	364
FIC2	355-425	12	533
FIC2	355-425	10	385
FIC2	355-425	10	471
FIC2	425-500	8	487
FIC2	425-500	6	376
FIC2	425-500	6	447
FIC2	425-500	6	440
FIC18	250-355	14	336
FIC18	250-355	20	413
FIC18	250-355	22	411
FIC18	250-355	21	449

FIC18	355-425	10	328
FIC18	355-425	11	381
FIC18	355-425	11	421
FIC18	355-425	12	459
FIC18	425-500	9	386
FIC18	425-500	7	324
FIC18	425-500	7	352
FIC18	425-500	7	349
FIC19	250-355	15	371
FIC19	250-355	16	355
FIC19	250-355	18.5	300
FIC19	250-355	24	427
FIC19	355-425	12	388
FIC19	355-425	12	447
FIC19	355-425	12	441
FIC19	355-425	12	434
FIC19	425-500	8	418
FIC19	425-500	8	404
FIC19	425-500	8	452
FIC19	425-500	7	463
FIC3	250-355	19	389
FIC3	250-355	18	374
FIC3	250-355	18	399
FIC3	250-355	17	368
FIC3	355-425	11	339
FIC3	355-425	12	437
FIC3	355-425	13	401
FIC3	355-425	12	395
FIC3	425-500	7	404

FIC3	425-500	7	391
FIC3	425-500	9	416
FIC3	425-500	8	441
UL-1	250-355	18	491
UL-1	250-355	12	346
UL-1	355-425	8	371
UL-1	355-425	8	340
UL-1	425-500	7	448
UL-1	425-500	6	461

5 Data Repository

All data presented in this dissertation are provided in the supplemental tables at the end of each chapter. In addition, all data have been deposited in the Paleoclimatology Database managed by the National Centers for Environmental Information (formerly the National Climatic Data Center), a division of the United States National Oceanic and Atmospheric Administration (NOAA). As of June 2020, data can be accessed from [ncdc.noaa.gov/paleo-search] using the search terms Broach, Yucatan, Celestun, or by searching for specific geochemical proxies mentioned in this text. Sediment cores are stored at the National Lacustrine Core Facility (LacCore, University of Minnesota, Minnesota, USA), and cores, core images, metadata, and bulk physical properties can be retrieved by using the project code FLAM-CEL09 when requesting materials archived by LacCore.

6 Bibliography

Akaike H. (1974) A new look at the statistical model identification. *IEEE Transactions on Automatic Control* **19**, 716–723.

Akers P. D., Brook G. A., Railsback L. B., Liang F., Iannone G., Webster J. W., Reeder P. P., Cheng H. and Edwards R. L. (2016) An extended and higher-resolution record of climate and land use from stalagmite MC01 from Macal Chasm, Belize, revealing connections between major dry events, overall climate variability, and Maya sociopolitical changes. *Palaeogeography, Palaeoclimatology, Palaeoecology* **459**, 268–288.

Allen K. A., Hönisch B., Eggins S. M., Yu J., Spero H. J. and Elderfield H. (2011) Controls on boron incorporation in cultured tests of the planktic foraminifer Orbulina universa. *Earth and Planetary Science Letters* **309**, 291–301.

Alongi D. M. (2012) Carbon sequestration in mangrove forests. *Carbon Management* **3**, 313–322.

Anderson M. J. (2001) A new method for non-parametric multivariate analysis of variance: Non-parametric MANOVA for ecology. *Austral Ecology* **26**, 32–46.

Anderson M. J., Ellingsen K. E. and McArdle B. H. (2006) Multivariate dispersion as a measure of beta diversity. *Ecology Letters* **9**, 683–693.

Appendini C. M., Salles P., Mendoza E. T., López J. and Torres-Freyermuth A. (2012) Longshore Sediment Transport on the Northern Coast of the Yucatan Peninsula. *Journal of Coastal Research* **285**, 1404–1417.

Aragón-Moreno A. A., Islebe G. A., Roy P. D., Torrescano-Valle N. and Mueller A. D. (2018) Climate forcings on vegetation of the southeastern Yucatán Peninsula (Mexico) during the middle to late Holocene. *Palaeogeography, Palaeoclimatology, Palaeoecology* **495**, 214–226.

Aragón-Moreno A. A., Islebe G. A. and Torrescano-Valle N. (2012) A ~ 3800-yr, high-resolution record of vegetation and climate change on the north coast of the Yucatan Peninsula. *Review of Palaeobotany and Palynology* **178**, 35–42.

Arellano-Torres E., Correa-Metrio A., López-Dávila D., Escobar J., Curtis J. H. and Cordero-Oviedo M. C. (2019) Mid to late Holocene hydrological and sea-level change reconstructions from La Mancha coastal lagoon, Veracruz, Mexico. *Palaeogeography, Palaeoclimatology, Palaeoecology* **520**, 150–162.

Babila T. L., Rosenthal Y., Wright J. D. and Miller K. G. (2016) A continental shelf perspective of ocean acidification and temperature evolution during the Paleocene-Eocene Thermal Maximum. *Geology* **44**, 275–278.

Balan E., Pietrucci F., Gervais C., Blanchard M., Schott J. and Gaillardet J. (2016) First-principles study of boron speciation in calcite and aragonite. *Geochimica et Cosmochimica Acta* **193**, 119–131.

Barker S., Greaves M. and Elderfield H. (2003) A study of cleaning procedures used for foraminiferal Mg/Ca paleothermometry. *Geochemistry, Geophysics, Geosystems* **4**, 8407.

Barth S. (1998) Application of boron isotopes for tracing sources of anthropogenic contamination in groundwater. *Water Research* **32**, 685–690.

Bauer-Gottwein P., Gondwe B. R. N., Charvet G., Marín L. E., Rebolledo-Vieyra M. and Merediz-Alonso G. (2011) Review: The Yucatán Peninsula karst aquifer, Mexico. *Hydrogeology Journal* **19**, 507–524.

Beach T., Luzzadder-Beach S., Dunning N., Jones J., Lohse J., Guderjan T., Bozarth S., Millspaugh S. and Bhattacharya T. (2009) A review of human and natural changes in Maya Lowland wetlands over the Holocene. *Quaternary Science Reviews* **28**, 1710–1724.

Beck A. J., Charette M. A., Cochran J. K., Gonneea M. E. and Peucker-Ehrenbrink B. (2013) Dissolved strontium in the subterranean estuary – Implications for the marine strontium isotope budget. *Geochimica et Cosmochimica Acta* **117**, 33–52.

Beckwith S. T., Byrne R. H. and Hallock P. (2019) Riverine Calcium End-Members Improve Coastal Saturation State Calculations and Reveal Regionally Variable Calcification Potential. *Frontiers in Marine Science*, **6**.

Benton M. J. and Harper D. A. T. (2009) *Introduction to Paleobiology and the Fossil Record*. Wiley-Blackwell. Chichester, United Kingdom.

Berner E. and Berner R. (1996) *Global environment water, air, and geochemical cycles* Prentice-Hall. Englewood Cliffs, NewJersey.

Bhattacharya T., Chiang J. C. H. and Cheng W. (2017) Ocean-atmosphere dynamics linked to 800–1050 CE drying in mesoamerica. *Quaternary Science Reviews* **169**, 263–277.

Blaauw M. and Christen J. A. (2011) Flexible paleoclimate age-depth models using an autoregressive gamma process. *Bayesian Anal.* **6**, 457–474.

Blum M. D., Carter A. E., Zayac T. and Goble R. (2002) Middle Holocene Sea-Level and Evolution of The Gulf of Mexico Coast (USA). *Journal of Coastal Research* **36**, 65–80.

Bond G., Kromer B., Beer J., Muscheler R., Evans M. N., Showers W., Hoffmann S., Lotti-Bond R., Hajdas I. and Bonani G. (2001) Persistent Solar Influence on North Atlantic Climate During the Holocene. *Science* **294**, 2130–2136.

Branson O. (2018) Boron incorporation into marine CaCO 3. In *Boron Isotopes* Springer. pp. 71–105.

Brenner M., Rosenmeier M. F., Hodell D. A. and Curtis J. H. (2002) Paleolimnology of the Maya lowlands. *Ancient Mesoamerica* **13**, 141–157.

Buzas M. A. and Hayek L.-A. C. (1998) SHE analysis for biofacies identification. *Journal of Foraminiferal Research* **28**, 233–239.

Carnero-Bravo V., Sanchez-Cabeza J.-A., Ruiz-Fernández A. C., Merino-Ibarra M., Corcho-Alvarado J. A., Sahli H., Hélie J.-F., Preda M., Zavala-Hidalgo J., Díaz-Asencio M. and Hillaire-Marcel C. (2018) Sea level rise sedimentary record and organic carbon fluxes in a low-lying tropical coastal ecosystem. *CATENA* **162**, 421–430.

Carrillo-Bastos A., Islebe G. A. and Torrescano-Valle N. (2013) 3800 Years of Quantitative Precipitation Reconstruction from the Northwest Yucatan Peninsula. *PLOS ONE* **8**, e84333.

Chou C., Chiang J. C. H., Lan C.-W., Chung C.-H., Liao Y.-C. and Lee C.-J. (2013) Increase in the range between wet and dry season precipitation. *Nature Geoscience* **6**, 263–267.

Chou C. and Lan C.-W. (2012) Changes in the Annual Range of Precipitation under Global Warming. *Journal of Climate* **25**, 222–235.

Chuang P.-C., Young M. B., Dale A. W., Miller L. G., Herrera-Silveira J. A. and Paytan A. (2016) Methane and sulfate dynamics in sediments from mangrove-dominated tropical coastal lagoons, Yucatán, Mexico. *Biogeosciences* **13**, 2981–3001.

Chuang P.-C., Young M. B., Dale A. W., Miller L. G., Herrera-Silveira J. A. and Paytan A. (2017) Methane fluxes from tropical coastal lagoons surrounded by mangroves, Yucatán, Mexico: Methane Fluxes from Coastal Lagoons. *Journal of Geophysical Research Biogeosciences* **122**, 1156–1174.

Coffey M., Dehairs F., Collette O., Luther G., Church T. and Jickells T. (1997) The Behaviour of Dissolved Barium in Estuaries. *Estuarine, Coastal and Shelf Science* **45**, 113–121.

Collins E. S., Scott D. B. and Gayes P. T. (1999) Hurricane records on the South Carolina coast: Can they be detected in the sediment record? *Quaternary International* **56**, 15–26.

Collins S. V., Reinhardt E. G., Werner C. L., Le Maillot C., Devos F. and Rissolo D. (2015) Late Holocene mangrove development and onset of sedimentation in the Yax Chen cave system (Ox Bel Ha) Yucatan, Mexico: Implications for using cave sediments as a sea-level indicator. *Palaeogeography, Palaeoclimatology, Palaeoecology* **438**, 124–134.

Cuevas E., Liceaga-Correa M. de los Á., Rincón-Sandoval L. A., Mexicano-Cíntora G., Arellano-Méndez L., Euán-Ávila J., Hernández-Núñez H. and Mulsow S. (2013) Morphological and sedimentological assessment of submarine dune fields on the coast of Yucatan, Mexico. *Ciencas Marinas* **39**, 83–99.

Culver S. J. (1990) Benthic Foraminifera of Puerto Rican Mangrove-Lagoon Systems: Potential for Paleoenvironmental Interpretations. *PALAIOS* **5**, 34–51.

Culver S. J. and Buzas M. A. (1982) Recent benthic foraminiferal provinces between Newfoundland and Yucatan. *Geological Society of America Bulletin* **93**, 269–277.

Curtis J. H., Brenner M., Hodell D. A., Balser R. A., Islebe G. A. and Hooghiemstra H. (1998) A multi-proxy study of Holocene environmental change in the Maya Lowlands of Peten, Guatemala. *Journal of Paleolimnology* **19**, 139–159.

Davis J. C. (2002) *Statistics and data analysis in geology*., John Wiley & Sons, New York.

Debenay J.-P., Beck Eichler B., Duleba W., Bonetti C. and Eichler-Coelho P. (1998) Water stratification in coastal lagoons: its influence on foraminiferal assemblages in two Brazilian lagoons. *Marine Micropaleontology* **35**, 67–89.

Debenay J.-P. and Guillou J.-J. (2002) Ecological transitions indicated by foraminiferal assemblages in paralic environments. *Estuaries* **25**, 1107–1120.

Debenay J.-P., Guillou J.-J., Redois F. and Geslin E. (2000) Distribution Trends of Foraminiferal Assemblages in Paralic Environments. In *Environmental Micropaleontology* (ed. R. E. Martin). Springer US, Boston, MA. pp. 39–67.

Debenay J.-P., Guiral D. and Parra M. (2002) Ecological Factors Acting on the Microfauna in Mangrove Swamps. The Case of Foraminiferal Assemblages in French Guiana. *Estuarine, Coastal and Shelf Science* **55**, 509–533.

Deines P., Langmuir D. and Harmon R. S. (1974) Stable carbon isotope ratios and the existence of a gas phase in the evolution of carbonate ground waters. *Geochimica et Cosmochimica Acta* **38**, 1147–1164.

Díaz K. A., Pérez L., Correa-Metrio A., Franco-Gaviria J. F., Echeverría P., Curtis J. and Brenner M. (2017) Holocene environmental history of tropical, mid-altitude Lake Ocotalito, México, inferred from ostracodes and non-biological indicators. *The Holocene* **27**, 1308–1317.

Dickson A. G. (1990) Standard potential of the reaction: AgCl(s) + 12H2(g) = Ag(s) + HCl(aq), and and the standard acidity constant of the ion HSO4− in synthetic sea water from 273.15 to 318.15 K. *The Journal of Chemical Thermodynamics* **22**, 113–127.

Dissard D., Nehrke G., Reichart G. J. and Bijma J. (2010a) The impact of salinity on the Mg/Ca and Sr/Ca ratio in the benthic foraminifera Ammonia tepida: Results from culture experiments. *Geochimica et Cosmochimica Acta* **74**, 928–940.

Dissard D., Nehrke G., Reichart G.-J. and Bijma J. (2010b) Impact of seawater pCO2 on calcification and Mg/Ca and Sr/Ca ratios in benthic foraminifera calcite: results from culturing experiments with Ammonia tepida. *Biogeosciences* **7**, 81–93.

Diz P., Barras C., Geslin E., Reichart G.-J., Metzger E., Jorissen F. and Bijma J. (2012a) Incorporation of Mg and Sr and oxygen and carbon stable isotope fractionation in cultured Ammonia tepida. *Marine Micropaleontology* **92–93**, 16–28.

Diz P., Barras C., Geslin E., Reichart G.-J., Metzger E., Jorissen F. and Bijma J. (2012b) Incorporation of Mg and Sr and oxygen and carbon stable isotope fractionation in cultured Ammonia tepida. *Marine Micropaleontology* **92–93**, 16–28.

Diz P., Jorissen F. J., Reichart G. J., Poulain C., Dehairs F., Leorri E. and Paulet Y.-M. (2009) Interpretation of benthic foraminiferal stable isotopes in subtidal estuarine environments. *Biogeosciences* **6**, 2549–2560.

DOE (1994) *Handbook of methods for the analysis of the various parameters of the carbon dioxide system in sea water. Version 2*., Oak Ridge National Lab., TN (United States).

Doney S., Bopp L. and Long M. (2014) Historical and Future Trends in Ocean Climate and Biogeochemistry. *Oceanography* **27**, 108–119.

Douglas P. M. J., Brenner M. and Curtis J. H. (2016a) Methods and future directions for paleoclimatology in the Maya Lowlands. *Global and Planetary Change* **138**, 3–24.

Douglas P. M. J., Demarest A. A., Brenner M. and Canuto M. A. (2016b) Impacts of Climate Change on the Collapse of Lowland Maya Civilization. *Annual Review of Earth and Planetary Sciences* **44**, 613–645.

Douglas P. M. J., Pagani M., Canuto M. A., Brenner M., Hodell D. A., Eglinton T. I. and Curtis J. H. (2015) Drought, agricultural adaptation, and sociopolitical collapse in the Maya Lowlands. *Proceedings of the National Academy of Sciences* **112**, 5607–5612.

Dueñas-Bohórquez A., Raitzsch M., de Nooijer L. J. and Reichart G.-J. (2011) Independent impacts of calcium and carbonate ion concentration on Mg and Sr incorporation in cultured benthic foraminifera. *Marine Micropaleontology* **81**, 122–130.

Enriquez C., Mariño-Tapia I. J. and Herrera-Silveira J. A. (2010) Dispersion in the Yucatan coastal zone: Implications for red tide events. *Continental Shelf Research* **30**, 127–137.

Erez J. (2003) The Source of Ions for Biomineralization in Foraminifera and Their Implications for Paleoceanographic Proxies. *Reviews in Mineralogy and Geochemistry* **54**, 115–149.

Escolero O. A., Marin L. E., Steinich B. and Pacheco J. (2000) Delimitation of a hydrogeological reserve for a city within a karstic aquifer: the Merida, Yucatan example. *Landscape and Urban Planning* **51**, 53–62.

Farmer J. R., Branson O., Uchikawa J., Penman D. E., Hönisch B. and Zeebe R. E. (2019) Boric acid and borate incorporation in inorganic calcite inferred from B/Ca, boron isotopes and surface kinetic modeling. *Geochimica et Cosmochimica Acta* **244**, 229–247.

Feely R. A., Doney S. C. and Cooley S. R. (2009) Ocean acidification: present conditions and future changes in a high-CO2 world. *Oceanography* **22**(4), 36-47.

Fletcher W. J., Zielhofer C., Mischke S., Bryant C., Xu X. and Fink D. (2017) AMS radiocarbon dating of pollen concentrates in a karstic lake system. *Quaternary Geochronology* **39**, 112–123.

Foster G. L., Pogge von Strandmann P. a. E. and Rae J. W. B. (2010) Boron and magnesium isotopic composition of seawater. *Geochemistry, Geophysics, Geosystems* **11**, Q08015.

Foster G. L. and Rae J. W. B. (2016) Reconstructing Ocean pH with Boron Isotopes in Foraminifera. *Annual Reviews of Earth and Planetary Science* **44**, 207–237.

Fox J. and Weisberg S. (2018) *An R companion to applied regression*. Sage Publications, Thousand Oaks, California.

Gabriel J. J., Reinhardt E. G., Peros M. C., Davidson D. E., Hengstum P. J. van and Beddows P. A. (2009) Palaeoenvironmental evolution of Cenote Aktun Ha (Carwash) on the Yucatan Peninsula, Mexico and its response to Holocene sea-level rise. *Journal of Paleolimnology* **42**, 199–213.

Geerken E., de Nooijer L. J., van Dijk I. and Reichart G.-J. (2018) Impact of salinity on element incorporation in two benthic foraminiferal species with contrasting magnesium contents. *Biogeosciences* **15**, 2205–2218.

Giddings L. and Soto M. (2003) Rhythms of precipitation in the Yucatan Peninsula. *The lowland Maya: three millennia at the human-wildland interface.* Haworth Press, Binghamton, New York, 77–90.

Gill R. B. (2001) *The great Maya droughts: water, life, and death*. University of New Mexico Press, Albuquerque, New Mexico.

Gischler E. and Hudson J. H. (2004) Holocene development of the Belize Barrier Reef. *Sedimentary Geology* **164**, 223–236.

Gleick P. H. (2000) A Look at Twenty-first Century Water Resources Development. *Water International* **25**, 127–138.

Gonneea M. E., Charette M. A., Liu Q., Herrera-Silveira J. A. and Morales-Ojeda S. M. (2014) Trace element geochemistry of groundwater in a karst subterranean estuary (Yucatan Peninsula, Mexico). *Geochimica et Cosmochimica Acta* **132**, 31–49.

Gonneea M. E., Paytan A. and Herrera-Silveira J. A. (2004) Tracing organic matter sources and carbon burial in mangrove sediments over the past 160 years. *Estuarine, Coastal and Shelf Science* **61**, 211–227.

Gray W. R. and Evans D. (2019) Nonthermal Influences on Mg/Ca in Planktonic Foraminifera: A Review of Culture Studies and Application to the Last Glacial Maximum. *Paleoceanography and Paleoclimatology* **34**, 306–315.

Hain M. P., Sigman D. M., Higgins J. A. and Haug G. H. (2015) The effects of secular calcium and magnesium concentration changes on the thermodynamics of seawater acid/base chemistry: Implications for Eocene and Cretaceous ocean carbon chemistry and buffering. *Global Biogeochemical Cycles* **29**, 517–533.

Hallock P. and Peebles M. W. (1993) Foraminifera with chlorophyte endosymbionts: Habitats of six species in the Florida Keys. *Marine Micropaleontology* **20**, 277–292.

Hart A. M. and Kaesler R. L. (1986) Temporal changes in Holocene lagoonal assemblages of foraminifera from northeastern Yucatan Peninsula, Mexico. *Journal of Foraminiferal Research* **16**, 98–109.

Haug G. H., Günther D., Peterson L. C., Sigman D. M., Hughen K. A. and Aeschlimann B. (2003) Climate and the Collapse of Maya Civilization. *Science* **299**, 1731–1735.

Haug G. H., Hughen K. A., Sigman D. M., Peterson L. C. and Röhl U. (2001) Southward Migration of the Intertropical Convergence Zone Through the Holocene. *Science* **293**, 1304–1308.

Havach S. M., Chandler G. T., Wilson-Finelli A. and Shaw T. J. (2001) Experimental determination of trace element partition coefficients in cultured benthic foraminifera. *Geochimica et Cosmochimica Acta* **65**, 1277–1283.

Hawkes A. D. and Horton B. P. (2012) Sedimentary record of storm deposits from Hurricane Ike, Galveston and San Luis Islands, Texas. *Geomorphology* **171–172**, 180–189.

Hayward B. W., Holzmann M., Grenfell H. R., Pawlowski J. and Triggs C. M. (2004) Morphological distinction of molecular types in Ammonia – towards a taxonomic revision of the world's most commonly misidentified foraminifera. *Marine Micropaleontology* **50**, 237–271.

Hemming N. G. and Hanson G. N. (1992) Boron isotopic composition and concentration in modern marine carbonates. *Geochimica et Cosmochimica Acta* **56**, 537–543.

Hemming N. G. and Hönisch B. (2007) Chapter Seventeen Boron Isotopes in Marine Carbonate Sediments and the pH of the Ocean. In *Developments in Marine Geology* Elsevier. pp. 717–734.

Henderson G. M. (2002) New oceanic proxies for paleoclimate. *Earth and Planetary Science Letters* **203**, 1–13.

Henehan M. J., Foster G. L., Bostock H. C., Greenop R., Marshall B. J. and Wilson P. A. (2016) A new boron isotope-pH calibration for Orbulina universa, with implications for understanding and accounting for 'vital effects.' *Earth and Planetary Science Letters* **454**, 282–292.

Henehan M. J., Foster G. L., Rae J. W. B., Prentice K. C., Erez J., Bostock H. C., Marshall B. J. and Wilson P. A. (2015) Evaluating the utility of B/Ca ratios in planktic foraminifera as a proxy for the carbonate system: A case study of *Globigerinoides ruber*: Investigating controls on *G. ruber* B/Ca. *Geochemistry, Geophysics, Geosystems* **16**, 1052–1069.

van Hengstum P. J., Reinhardt E. G., Beddows P. A. and Gabriel J. J. (2010) Linkages between Holocene paleoclimate and paleohydrogeology preserved in a Yucatan underwater cave. *Quaternary Science Reviews* **29**, 2788–2798.

van Hengstum P. J., Scott D. B., Gröcke D. R. and Charette M. A. (2011) Sea level controls sedimentation and environments in coastal caves and sinkholes. *Marine Geology* **286**, 35–50.

Herrera-Silveira J. A. (1996) Salinity and nutrients in a tropical coastal lagoon with groundwater discharges to the Gulf of Mexico. *Hydrobiologia* **321**, 165–176.

Herrera-Silveira J. A. (1994) Spatial heterogeneity and seasonal patterns in a tropical coastal lagoon. *Journal of Coastal Research*, 738–746.

Herrera-Silveira J. A. and Morales-Ojeda S. M. (2010) 13 Subtropical Karstic Coastal Lagoon Assessment, Southeast Mexico. In *Coastal lagoons: critical habitats of environmental change.* CRC Press, Boca Raton, Florida. pp. 307–333.

Herrera-Silveira J. A., R. J. R. and J. A. Z. (1998) Overview and characterization of the hydrology and primary producer communities of selected coastal lagoons of Yucatán, México. *Aquatic Ecosystem Health & Management* **1**, 353–372.

Higuera-Gundy A., Brenner M., Hodell D. A., Curtis J. H., Leyden B. W. and Binford M. W. (1999) A 10,300 14C yr Record of Climate and Vegetation Change from Haiti. *Quaternary Research* **52**, 159–170.

Hippensteel S. P. and Martin R. E. (1999) Foraminifera as an indicator of overwash deposits, Barrier Island sediment supply, and Barrier Island evolution: Folly Island, South Carolina. *Palaeogeography, Palaeoclimatology, Palaeoecology* **149**, 115–125.

Hodell D. A., Brenner M., Curtis J. H. and Guilderson T. (2001) Solar Forcing of Drought Frequency in the Maya Lowlands. *Science* **292**, 1367–1370.

Hodell D. A., Brenner M., Curtis J. H., Medina-González R., Ildefonso-Chan Can E., Albornaz-Pat A. and Guilderson T. P. (2005) Climate change on the Yucatan Peninsula during the Little Ice Age. *Quaternary Research* **63**, 109–121.

Hodell D. A., Curtis J. H. and Brenner M. (1995) Possible role of climate in the collapse of Classic Maya civilization. *Nature* **375**, 391–394.

Hodell D. A., Curtis J. H., Jones G. A., Higuera-Gundy A., Brenner M., Binford M. W. and Dorsey K. T. (1991) Reconstruction of Caribbean climate change over the past 10,500 years. *Nature* **352**, 790–793.

Hofmann G. E., Smith J. E., Johnson K. S., Send U., Levin L. A., Micheli F., Paytan A., Price N. N., Peterson B., Takeshita Y., Matson P. G., Crook E. D., Kroeker K. J., Gambi M. C., Rivest E. B., Frieder C. A., Yu P. C. and Martz T. R. (2011) High-Frequency Dynamics of Ocean pH: A Multi-Ecosystem Comparison. d. W.-C. Chin. *PLoS ONE* **6**, e28983.

Holmes J. A. (1996) Trace-element and stable-isotope geochemistry of non-marine ostracod shells in Quaternary palaeoenvironmental reconstruction. *Journal of Paleolimnology* **15**, 223–235.

Hönisch B., Allen K. A., Russell A. D., Eggins S. M., Bijma J., Spero H. J., Lea D. W. and Yu J. (2011) Planktic foraminifers as recorders of seawater Ba/Ca. *Marine Micropaleontology* **79**, 52–57.

Hönisch B., Bijma J., Russell A. D., Spero H. J., Palmer M. R., Zeebe R. E. and Eisenhauer A. (2003) The influence of symbiont photosynthesis on the boron isotopic composition of foraminifera shells. *Marine Micropaleontology* **49**, 87–96.

Hönisch B., Eggins S. M., Haynes L. L., Allen K. A., Holland K. D. and Lorbacher K. (2019) *Boron Proxies in Paleoceanography and Paleoclimatology*., Wiley-Blackwell, Chichester, United Kingdom.

Hönisch B., Ridgwell A., Schmidt D. N., Thomas E., Gibbs S. J., Sluijs A., Zeebe R., Kump L., Martindale R. C., Greene S. E., Kiessling W., Ries J., Zachos J. C., Royer D. L., Barker S., Marchitto T. M., Moyer R., Pelejero C., Ziveri P., Foster G. L. and Williams B. (2012) The Geological Record of Ocean Acidification. *Science* **335**, 1058–1063.

Howes E. L., Kaczmarek K., Raitzsch M., Mewes A., Bijma N., Horn I., Misra S., Gattuso J.-P. and Bijma J. (2017) Decoupled carbonate chemistry controls on the incorporation of boron into Orbulina universa. *Biogeosciences* **14**, 415–430.

Hsieh Y.-T. and Henderson G. M. (2017) Barium stable isotopes in the global ocean: Tracer of Ba inputs and utilization. *Earth and Planetary Science Letters* **473**, 269–278.

Hughen K. A., Overpeck J. T., Peterson L. C. and Anderson R. F. (1996) The nature of varved sedimentation in the Cariaco Basin, Venezuela, and its palaeoclimatic significance. *Geological Society, London, Special Publications* **116**, 171–183.

Ingram B. L. and Sloan D. (1992) Strontium Isotopic Composition of Estuarine Sediments as Paleosalinity-Paleoclimate Indicator. *Science* **255**, 68–72.

Inoue M., Nohara M., Okai T., Suzuki A. and Kawahata H. (2004) Concentrations of Trace Elements in Carbonate Reference Materials Coral JCp-1 and Giant Clam JCt-1 by Inductively Coupled Plasma-Mass Spectrometry. *Geostandards and Geoanalytical Research* **28**, 411–416.

Islebe G. A., Carrillo-Bastos A., Aragón-Moreno A. A., Valdez-Hernández M., Torrescano-Valle N. and Cabanillas-Terán N. (2019) Holocene Paleoecology and Paleoclimatology of South and Southeastern Mexico: A Palynological and Geospatial Approach. In *The Holocene and Anthropocene Environmental History of Mexico: A Paleoecological Approach on Mesoamerica* (eds. N. Torrescano- Valle, G. A. Islebe, and P. D. Roy). Springer International Publishing, Cham. pp. 195–207.

Islebe G. and Sánchez O. (2002) History of late Holocene vegetation at Quintana Roo, Caribbean coast of Mexico. *Plant Ecology* **160**, 187–192.

Javaux E. J. and Scott D. B. (2003) Illustration of modern benthic foraminifera from Bermuda and remarks on distribution in other subtropical/tropical areas. *Palaeontologia Electronica* **6**, 29.

Jones M. D., Metcalfe S. E., Davies S. J. and Noren A. (2015) Late Holocene climate reorganisation and the North American Monsoon. *Quaternary Science Reviews* **124**, 290–295.

Katz B. G., Coplen T. B., Bullen T. D. and Davis J. H. (1997) Use of Chemical and Isotopic Tracers to Characterize the Interactions Between Ground Water and Surface Water in Mantled Karst. *Groundwater* **35**, 1014–1028.

Kennett D. J., Breitenbach S. F. M., Aquino V. V., Asmerom Y., Awe J., Baldini J. U. L., Bartlein P., Culleton B. J., Ebert C., Jazwa C., Macri M. J., Marwan N., Polyak V., Prufer K. M., Ridley H. E., Sodemann H., Winterhalder B. and Haug G. H. (2012) Development and Disintegration of Maya Political Systems in Response to Climate Change. *Science* **338**, 788–791.

Keul N., Langer G., Thoms S., de Nooijer L. J., Reichart G.-J. and Bijma J. (2017) Exploring foraminiferal Sr/Ca as a new carbonate system proxy. *Geochimica et Cosmochimica Acta* **202**, 374–386.

Khan N. S., Ashe E., Horton B. P., Dutton A., Kopp R. E., Brocard G., Engelhart S. E., Hill D. F., Peltier W. R., Vane C. H. and Scatena F. N. (2017) Drivers of Holocene sea-level change in the Caribbean. *Quaternary Science Reviews* **155**, 13–36.

Kim H.-C. and Lee K. (2009) Significant contribution of dissolved organic matter to seawater alkalinity. *Geophysical Research Letters* **36**.

Klochko K., Kaufman A. J., Yao W., Byrne R. H. and Tossell J. A. (2006) Experimental measurement of boron isotope fractionation in seawater. *Earth and Planetary Science Letters* **248**, 276–285.

Koutsoyiannis D., Montanari A., Lins H. F. and Cohn T. A. (2009) Climate, hydrology and freshwater: towards an interactive incorporation of hydrological experience into climate research. *Hydrological Sciences Journal* **54**, 394–405.

Lambeck K., Rouby H., Purcell A., Sun Y. and Sambridge M. (2014) Sea level and global ice volumes from the Last Glacial Maximum to the Holocene. *Proceedings of the National Academy of Sciences* **111**, 15296–15303.

Langer G., Sadekov A., Thoms S., Keul N., Nehrke G., Mewes A., Greaves M., Misra S., Reichart G.-J., de Nooijer L. J., Bijma J. and Elderfield H. (2016) Sr partitioning in the benthic foraminifera Ammonia aomoriensis and Amphistegina lessonii. *Chemical Geology* **440**, 306–312.

Laskar J., Robutel P., Joutel F., Gastineau M., Correia A. C. M. and Levrard B. (2004) A long-term numerical solution for the insolation quantities of the Earth. *Astronomy & Astrophysics* **428**, 261–285.

Lea D. W. and Spero H. J. (1994) Assessing the reliability of paleochemical tracers: Barium uptake in the shells of planktonic foraminifera. *Paleoceanography* **9**, 445–452.

Lee K., Kim T.-W., Byrne R. H., Millero F. J., Feely R. A. and Liu Y.-M. (2010) The universal ratio of boron to chlorinity for the North Pacific and North Atlantic oceans. *Geochimica et Cosmochimica Acta* **74**, 1801–1811.

Lemarchand D., Gaillardet J., Lewin É. and Allègre C. J. (2002) Boron isotope systematics in large rivers: implications for the marine boron budget and paleo-pH reconstruction over the Cenozoic. *Chemical Geology* **190**, 123–140.

Lemarchand D., Gaillardet J., Lewin É. and Allègre C. J. (2000) The influence of rivers on marine boron isotopes and implications for reconstructing past ocean pH. *Nature* **408**, 951–954.

Leng M. J. and Marshall J. D. (2004) Palaeoclimate interpretation of stable isotope data from lake sediment archives. *Quaternary Science Reviews* **23**, 811–831.

Leyden B., Brenner M., Curtis J. H., Piperno D., Whitmore T. and Dahlin B. H. (1996) A Record of Long-and Short-Term Climatic Variation from NorthwestYucatán: Cenote San José Chulchaca. In *The Managed Mosaic: Ancient Maya Agriculture and Resource Use*. (ed. Scott L. Fedick). University of Utah Press, Salt Lake City, Utah.

Liu H.-C., You C.-F., Huang K.-F. and Chung C.-H. (2012) Precise determination of triple Sr isotopes (δ87Sr and δ88Sr) using MC-ICP-MS. *Talanta* **88**, 338–344.

Liu Q., Charette M. A., Henderson P. B., McCorkle D. C., Martin W. and Dai M. (2014) Effect of submarine groundwater discharge on the coastal ocean inorganic carbon cycle. *Limnology and Oceanography* **59**, 1529–1554.

Lowery J. G. and Rankey E. C. (2017) Nearshore Influences of Upwelling, Waves, and Currents On A Tropical Carbonate Ramp: Holocene, Northwestern Yucatán Shelf, Mexico. *Journal of Sedimentary Research* **87**, 546–566.

LTER S. B. C., Hofmann G. E. and Washburn L. (2018) SBC LTER: Ocean: Time-series: Mid-water SeaFET pH and CO2 system chemistry with surface and bottom Dissolved Oxygen at Santa Barbara Harbor/Stearns Wharf (SBH), ongoing since 2012-09-15.

Lutz W., Prieto L. and Sanderson W. (2000) Population, development and environment on the Yucatan Peninsula. *International Institute for Applied Systems Analysis. Research Report RR-00-14*.

Marfia A. M., Krishnamurthy R. V., Atekwana E. A. and Panton W. F. (2004) Isotopic and geochemical evolution of ground and surface waters in a karst dominated geological setting: a case study from Belize, Central America. *Applied Geochemistry* **19**, 937–946.

Martin P. A. and Lea D. W. (2002) A simple evaluation of cleaning procedures on fossil benthic foraminiferal Mg/Ca. *Geochemistry, Geophysics, Geosystems* **3**, 1–8.

Martinez A., Hernández-Terrones L., Rebolledo-Vieyra M. and Paytan A. (2018) Impact of carbonate saturation on large Caribbean benthic foraminifera assemblages. *Biogeosciences* **15**, 6819–6832.

Mather J. D. and Porteous N. C. (2001) The geochemistry of boron and its isotopes in groundwaters from marine and non-marine sandstone aquifers. *Applied Geochemistry* **16**, 821–834.

Mavromatis V., Montouillout V., Noireaux J., Gaillardet J. and Schott J. (2015) Characterization of boron incorporation and speciation in calcite and aragonite from co-precipitation experiments under controlled pH, temperature and precipitation rate. *Geochimica et Cosmochimica Acta* **150**, 299–313.

Mayewski P. A., Rohling E. E., Curt Stager J., Karlén W., Maasch K. A., David Meeker L., Meyerson E. A., Gasse F., van Kreveld S., Holmgren K., Lee-Thorp J., Rosqvist G., Rack F., Staubwasser M., Schneider R. R. and Steig E. J. (2004) Holocene climate variability. *Quaternary Research* **62**, 243–255.

Mayk D., Fietzke J., Anagnostou E. and Paytan A. (2020) LA-MC-ICP-MS study of boron isotopes in individual planktonic foraminifera: A novel approach to obtain seasonal variability patterns. *Chemical Geology* **531**, 119351.

McCorkle D. C., Martin P. A., Lea D. W. and Klinkhammer G. P. (1995) Evidence of a dissolution effect on benthic foraminiferal shell chemistry: δ13C, Cd/Ca, Ba/Ca, and Sr/Ca results from the Ontong Java Plateau. *Paleoceanography* **10**, 699–714.

Medina-Elizalde M., Burns S. J., Lea D. W., Asmerom Y., von Gunten L., Polyak V., Vuille M. and Karmalkar A. (2010) High resolution stalagmite climate record from the Yucatán Peninsula spanning the Maya terminal classic period. *Earth and Planetary Science Letters* **298**, 255–262.

Medina-Elizalde M., Burns S. J., Polanco-Martínez J. M., Beach T., Lases-Hernández F., Shen C.-C. and Wang H.-C. (2016) High-resolution speleothem record of precipitation from the Yucatan Peninsula spanning the Maya Preclassic Period. *Global and Planetary Change* **138**, 93–102.

Méndez M. and Magaña V. (2010) Regional Aspects of Prolonged Meteorological Droughts over Mexico and Central America. *Journal of Climate* **23**, 1175–1188.

Metcalfe S. E., Barron J. A. and Davies S. J. (2015) The Holocene history of the North American Monsoon: 'known knowns' and 'known unknowns' in understanding its spatial and temporal complexity. *Quaternary Science Reviews* **120**, 1–27.

Mewes A., Langer G., Reichart G.-J., de Nooijer L. J., Nehrke G. and Bijma J. (2015) The impact of Mg contents on Sr partitioning in benthic foraminifers. *Chemical Geology* **412**, 92–98.

Molinari R. L. and Morrison J. (1988) The separation of the Yucatan Current from the Campeche Bank and the intrusion of the Loop Current into the Gulf of Mexico. *Journal of Geophysical Research: Oceans* **93**, 10645–10654.

Moore W. S. (2003) Sources and fluxes of submarine groundwater discharge delineated by radium isotopes. *Biogeochemistry* **66**, 75–93.

Mueller A. D., Islebe G. A., Hillesheim M. B., Grzesik D. A., Anselmetti F. S., Ariztegui D., Brenner M., Curtis J. H., Hodell D. A. and Venz K. A. (2009) Climate drying and associated forest decline in the lowlands of northern Guatemala during the late Holocene. *Quaternary Research* **71**, 133–141.

Murray J. W. (2006) *Ecology and applications of benthic foraminifera*., Cambridge University Press, Cambridge, United Kingdom.

Murray J. W. and Alve E. (1999) Taphonomic experiments on marginal marine foraminiferal assemblages: how much ecological information is preserved? *Palaeogeography, Palaeoclimatology, Palaeoecology* **149**, 183–197.

Négrel P., Millot R., Guerrot C., Petelet-Giraud E., Brenot A. and Malcuit E. (2012) Heterogeneities and interconnections in groundwaters: Coupled B, Li and stable-isotope variations in a large aquifer system (Eocene Sand aquifer, Southwestern France). *Chemical Geology* **296–297**, 83–95.

Nir O., Vengosh A., Harkness J. S., Dwyer G. S. and Lahav O. (2015) Direct measurement of the boron isotope fractionation factor: Reducing the uncertainty in reconstructing ocean paleo-pH. *Earth and Planetary Science Letters* **414**, 1–5.

Noireaux J., Mavromatis V., Gaillardet J., Schott J., Montouillout V., Louvat P., Rollion-Bard C. and Neuville D. R. (2015) Crystallographic control on the boron isotope paleo-pH proxy. *Earth and Planetary Science Letters* **430**, 398–407.

de Nooijer L. J., Brombacher A., Mewes A., Langer G., Nehrke G., Bijma J. and Reichart G.-J. (2017) Ba incorporation in benthic foraminifera. *Biogeosciences* **14**, 3387–3400.

de Nooijer L. J., Hathorne E. C., Reichart G. J., Langer G. and Bijma J. (2014) Variability in calcitic Mg/Ca and Sr/Ca ratios in clones of the benthic foraminifer Ammonia tepida. *Marine Micropaleontology* **107**, 32–43.

Null K. A., Knee K. L., Crook E. D., de Sieyes N. R., Rebolledo-Vieyra M., Hernández-Terrones L. and Paytan A. (2014) Composition and fluxes of submarine groundwater along the Caribbean coast of the Yucatan Peninsula. *Continental Shelf Research* **77**, 38–50.

Okai T., Suzuki A., Kawahata H., Terashima S. and Imai N. (2002) Preparation of a New Geological Survey of Japan Geochemical Reference Material: Coral JCp-1. *Geostandards Newsletter* **26**, 95–99.

Paris G., Gaillardet J. and Louvat P. (2010) Geological evolution of seawater boron isotopic composition recorded in evaporites. *Geology* **38**, 1035–1038.

Pech D., Ardisson P.-L. and Hernández-Guevara N. A. (2007) Benthic community response to habitat variation: A case of study from a natural protected area, the Celestun coastal lagoon. *Continental Shelf Research* **27**, 2523–2533.

Pérez L., Bugja R., Lorenschat J., Brenner M., Curtis J., Hoelzmann P., Islebe G., Scharf B. and Schwalb A. (2011) Aquatic ecosystems of the Yucatán Peninsula (Mexico), Belize, and Guatemala. *Hydrobiologia* **661**, 407–433.

Pérez-Cruz L. (2013) Hydrological changes and paleoproductivity in the Gulf of California during middle and late Holocene and their relationship with ITCZ and North American Monsoon variability. *Quaternary Research* **79**, 138–151.

Peros M. C., Gregory B., Matos F., Reinhardt E. and Desloges J. (2015) Late Holocene record of lagoon evolution, climate change, and hurricane activity from southeastern Cuba. *The Holocene* **25**(9), 1483-1497.

Peros M. C., Reinhardt E. G. and Davis A. M. (2007a) A 6000-year record of ecological and hydrological changes from Laguna de la Leche, north coastal Cuba. *Quaternary Research* **67**, 69–82.

Peros M. C., Reinhardt E. G., Schwarcz H. P. and Davis A. M. (2007b) High-resolution paleosalinity reconstruction from Laguna de la Leche, north coastal Cuba, using Sr, O, and C isotopes. *Palaeogeography, Palaeoclimatology, Palaeoecology* **245**, 535–550.

Perry E., Marin L., McClain J. and Velazquez G. (1995) Ring of Cenotes (sinkholes), northwest Yucatan, Mexico: Its hydrogeologic characteristics and possible association with the Chicxulub impact crater. *Geology* **23**, 17–20.

Perry E., Paytan A., Pedersen B. and Velazquez-Oliman G. (2009a) Groundwater geochemistry of the Yucatan Peninsula, Mexico: Constraints on stratigraphy and hydrogeology. *Journal of Hydrology* **367**, 27–40.

Perry E., Paytan A., Pedersen B. and Velazquez-Oliman G. (2009b) Groundwater geochemistry of the Yucatan Peninsula, Mexico: Constraints on stratigraphy and hydrogeology. *Journal of Hydrology* **367**, 27–40.

Perry E., Swift J., Gamboa J., Reeve A., Sanborn R., Marin L. and Villasuso M. (1989) Geologic and environmental aspects of surface cementation, north coast, Yucatan, Mexico. *Geology* **17**, 818–821.

Perry E., Velazquez-Oliman G. and Marin L. (2002) The Hydrogeochemistry of the Karst Aquifer System of the Northern Yucatan Peninsula, Mexico. *International Geology Review* **44**, 191–221.

Perry, Velazquez-Oliman G. and Socki R. A. (2003) Hydrogeology of the Yucatán Peninsula. In *The Lowland Maya area: three millennia at the human-wildland interface* (eds. A. Gómez-Pompa, M. F. Allen, S. L. Fedick, and J. J. Jiménez-Osornio). Food Products Press, New York. pp. 115–138.

Peterson L. C. and Haug G. H. (2005) Climate and the Collapse of Maya Civilization: A series of multi-year droughts helped to doom an ancient culture. *American Scientist*, **93**(4), 322-329.

Phleger F. B. and Ayala-Castanares A. (1971) Processes and History of Terminos Lagoon, Mexico. *American Association of Petroleum Geology Bulletin* **55**, 2130–2140.

Pierrot, Wallace, Lewis, Pierrot D., Lewis E., Wallace R., Wallace D., Wallace W. and Wallace D. W. R. (2011) MS Excel Program Developed for CO2 System Calculations. Available at: https://www.scienceopen.com/document?vid=1e7ee0bc-d9d2-439e-8d00-c1ca560e2979 [Accessed January 15, 2020].

Poag C. W. (2015) *Benthic foraminifera of the Gulf of Mexico: distribution, ecology, paleoecology*. Texas A&M University Press, College Station, Texas.

Polk J. S., van Beynen P. E. and Reeder P. P. (2007) Late Holocene environmental reconstruction using cave sediments from Belize. *Quaternary Research* **68**, 53–63.

Poore R., Verardo S., Caplan J., Pavich K. and Quinn T. (2009) Planktic foraminiferal relative abundance and trends in Gulf of Mexico holocene sediments records of climate variability. In *Gulf of Mexico Origin, Waters, and Biota: Volume III, Geology* Texas A&M University Press. pp. 367–379.

Poore R. Z., Dowsett H. J., Verardo S. and Quinn T. M. (2003) Millennial- to century-scale variability in Gulf of Mexico Holocene climate records. *Paleoceanography* **18**, 1048.

Poore R. Z., Quinn T. M. and Verardo S. (2004) Century-scale movement of the Atlantic Intertropical Convergence Zone linked to solar variability. *Geophysical Research Letters* **31**, L12214.

Pope K. O., Ocampo A. C. and Duller C. E. (1993) Surficial geology of the Chicxulub impact crater, Yucatan, Mexico. *Earth Moon Planet* **63**, 93–104.

Quintana Krupinski N. B., Russell A. D., Pak D. K. and Paytan A. (2017) Core-top calibration of B/Ca in Pacific Ocean Neogloboquadrina incompta and Globigerina bulloides as a surface water carbonate system proxy. *Earth and Planetary Science Letters* **466**, 139–151.

Rae J. W. (2018) Boron isotopes in foraminifera: Systematics, biomineralisation, and CO2 reconstruction. In *Boron Isotopes* Springer. pp. 107–143.

Rae J. W. B., Foster G. L., Schmidt D. N. and Elliott T. (2011) Boron isotopes and B/Ca in benthic foraminifera: Proxies for the deep ocean carbonate system. *Earth and Planetary Science Letters* **302**, 403–413.

Raitzsch M., Dueñas-Bohórquez A., Reichart G.-J., de Nooijer L. J. and Bickert T. (2010) Incorporation of Mg and Sr in calcite of cultured benthic foraminifera: impact of calcium concentration and associated calcite saturation state. *Biogeosciences* **7**, 869–881.

Raitzsch M. and Hönisch B. (2013) Cenozoic boron isotope variations in benthic foraminifers. *Geology* **41**, 591–594.

Ravelo A. C. and Hillaire-Marcel C. (2007) Chapter Eighteen The Use of Oxygen and Carbon Isotopes of Foraminifera in Paleoceanography. In *Developments in Marine Geology* (eds. C. Hillaire–Marcel and A. De Vernal). Proxies in Late Cenozoic Paleoceanography. Elsevier. pp. 735–764.

Reinhardt E. G., Stanley D. J. and Patterson R. T. (1998) Strontium isotopic-paleontological method as a high-resolution paleosalinity tool for lagoonal environments. *Geology* **26**, 1003–1006.

Rollion-Bard C. and Erez J. (2010) Intra-shell boron isotope ratios in the symbiont-bearing benthic foraminiferan Amphistegina lobifera: Implications for δ11B vital effects and paleo-pH reconstructions. *Geochimica et Cosmochimica Acta* **74**, 1530–1536.

Rosenmeier M. F., Hodell D. A., Brenner M., Curtis J. H. and Guilderson T. P. (2002) A 4000-Year Lacustrine Record of Environmental Change in the Southern Maya Lowlands, Petén, Guatemala. *Quaternary Research* **57**, 183–190.

Rosenthal Y., Boyle E. A. and Slowey N. (1997) Temperature control on the incorporation of magnesium, strontium, fluorine, and cadmium into benthic foraminiferal shells from Little Bahama Bank: Prospects for thermocline paleoceanography. *Geochimica et Cosmochimica Acta* **61**, 3633–3643.

Roy P. D., Torrescano-Valle N., Islebe G. A. and Gutiérrez-Ayala L. V. (2017) Late Holocene hydroclimate of the western Yucatan Peninsula (Mexico). *Journal of Quaternary Science* **32**, 1112–1120.

Schönfeld J., Alve E., Geslin E., Jorissen F., Korsun S. and Spezzaferri S. (2012) The FOBIMO (FOraminiferal BIo-MOnitoring) initiative—Towards a standardised protocol for soft-bottom benthic foraminiferal monitoring studies. *Marine Micropaleontology* **94–95**, 1–13.

Sen Gupta B. K. (2003) Foraminifera in marginal marine environments. In *Modern Foraminifera* (ed. B. K. Sen Gupta). Springer Netherlands, Dordrecht. pp. 141–159.

Sen Gupta B. K. (1999) *Modern Foraminifera*. (ed. B. K. Sen Gupta). Kluwer Academic Publishers, Boston, Massachusetts.

Smith D. E., Harrison S. and Jordan J. T. (2013) Sea level rise and submarine mass failures on open continental margins. *Quaternary Science Reviews* **82**, 93–103.

Stalker J. C., Price R. M., Rivera-Monroy V. H., Herrera-Silveira J., Morales S., Benitez J. A. and Alonzo-Parra D. (2014) Hydrologic Dynamics of a Subtropical Estuary Using Geochemical Tracers, Celestún, Yucatan, Mexico. *Estuaries and Coasts* **37**, 1376–1387.

Steinhilber F., Beer J. and Fröhlich C. (2009) Total solar irradiance during the Holocene. *Geophysical Research Letters* **36**.

Sutton R. T. and Hodson D. L. R. (2005) Atlantic Ocean Forcing of North American and European Summer Climate. *Science* **309**, 115–118.

Swarzenski P. W. (2014) 210Pb Dating. In *Encyclopedia of Scientific Dating Methods* (eds. W. J. Rink and J. Thompson). Springer Netherlands, Dordrecht. pp. 1–11.

Swarzenski P. W., Baskaran M., Rosenbauer R. J. and Orem W. H. (2006) Historical trace element distribution in sediments from the Mississippi River delta. *Estuaries and Coasts* **29**, 1094–1107.

Tapia González F. U., Herrera-Silveira J. A. and Aguirre-Macedo M. L. (2008) Water quality variability and eutrophic trends in karstic tropical coastal lagoons of the Yucatán Peninsula. *Estuarine, Coastal and Shelf Science* **76**, 418–430.

Toscano M. A. and Macintyre I. G. (2003) Corrected western Atlantic sea-level curve for the last 11,000 years based on calibrated 14C dates from Acropora palmata framework and intertidal mangrove peat. *Coral Reefs* **22**, 257–270.

Toyofuku T., Suzuki M., Suga H., Sakai S., Suzuki A., Ishikawa T., de Nooijer L. J., Schiebel R., Kawahata H. and Kitazato H. (2011) Mg/Ca and δ18O in the brackish shallow-water benthic foraminifer Ammonia 'beccarii.' *Marine Micropaleontology* **78**, 113–120.

Uchikawa J., Harper D. T., Penman D. E., Zachos J. C. and Zeebe R. E. (2017) Influence of solution chemistry on the boron content in inorganic calcite grown in artificial seawater. *Geochimica et Cosmochimica Acta* **218**, 291–307.

Uchikawa J., Penman D. E., Zachos J. C. and Zeebe R. E. (2015) Experimental evidence for kinetic effects on B/Ca in synthetic calcite: Implications for potential B(OH)4− and B(OH)3 incorporation. *Geochimica et Cosmochimica Acta* **150**, 171–191.

Urey H. C., Epstein S., Buchsbaum R. and Lowenstam H. (1951) Carbonate-water isotopic temperature scale. *Geological Society of America Bulletin* **62**, 417–426.

Vela-Pelaez A. A., Torrescano-Valle N., Islebe G. A., Mas J. F. and Weissenberger H. (2018) Holocene precipitation changes in the Maya forest, Yucatán peninsula, Mexico. *Palaeogeography, Palaeoclimatology, Palaeoecology* **505**, 42–52.

Vengosh A. (1998) The isotopic composition of anthropogenic boron and its potential impact on the environment. *Biological Trace Element Research* **66**, 145–151.

Vengosh A., Heumann K. G., Juraske S. and Kasher R. (1994) Boron isotope application for tracing sources of contamination in groundwater. *Environmental science and technology* **28**(11), 1968-1974.

Vengosh A., Kolodny Y. and Spivack A. J. (1998) Ground-water pollution determined by boron isotope systematics. No. IAEA-TECDOC--1046. International Atomic Energy Agency.

Vengosh A., Starinsky A., Kolodny Y., Chivas A. R. and Raab M. (1992) Boron isotope variations during fractional evaporation of sea water: New constraints on the marine vs. nonmarine debate. *Geology* **20**, 799–802.

Verardo D. J., Froelich P. N. and McIntyre A. (1990) Determination of organic carbon and nitrogen in marine sediments using the Carlo Erba NA-1500 analyzer. *Deep Sea Research Part A. Oceanographic Research Papers* **37**, 157–165.

Wahl D., Byrne R. and Anderson L. (2014) An 8700 year paleoclimate reconstruction from the southern Maya lowlands. *Quaternary Science Reviews* **103**, 19–25.

Wahl D., Byrne R., Schreiner T. and Hansen R. (2006) Holocene vegetation change in the northern Peten and its implications for Maya Prehistory. *Quaternary Research* **65**, 380–389.

Wall M., Fietzke J., Crook E. D. and Paytan A. (2019) Using B isotopes and B/Ca in corals from low saturation springs to constrain calcification mechanisms. *Nature Communications* **10**, 3580.

Wang B.-S., You C.-F., Huang K.-F., Wu S.-F., Aggarwal S. K., Chung C.-H. and Lin P.-Y. (2010) Direct separation of boron from Na- and Ca-rich matrices by sublimation for stable isotope measurement by MC-ICP-MS. *Talanta* **82**, 1378–1384.

Webster J. W., Brook G. A., Railsback L. B., Cheng H., Edwards R. L., Alexander C. and Reeder P. P. (2007) Stalagmite evidence from Belize indicating significant droughts at the time of Preclassic Abandonment, the Maya Hiatus, and the Classic Maya collapse. *Palaeogeography, Palaeoclimatology, Palaeoecology* **250**, 1–17.

Weidie A. E. (1985) Part I: Geology of Yucatan Platform. (ed. W. Ward). *Geology and hydrogeology of the Yucatan and Quaternary geology of Northeastern Yucatan Peninsula*. New Orleans Geological Society, New Orleans, Louisiana.

Whitmore T. J., Brenner M., Curtis J. H., Dahlin B. H. and Leyden B. W. (1996) Holocene climatic and human influences on lakes of the Yucatan Peninsula, Mexico: an interdisciplinary, palaeolimnological approach. *The Holocene* **6**, 273–287.

Wootton J. T., Pfister C. A. and Forester J. D. (2008) Dynamic patterns and ecological impacts of declining ocean pH in a high-resolution multi-year dataset. *Proceedings of the National Academy of Sciences* **105**, 18848–18853.

Young M., Gonneea M. E., Herrera-Silveira J. and Paytan A. (2005) Export of dissolved and particulate carbon and nitrogen from a mangrove-dominated lagoon, Yucatan Peninsula, Mexico. *International Journal of Ecology and Environmental Sciences* **31**, 189–202.

Young M. B., Gonneea M. E., Fong D. A., Moore W. S., Herrera-Silveira J. and Paytan A. (2008) Characterizing sources of groundwater to a tropical coastal lagoon in a karstic area using radium isotopes and water chemistry. *Marine Chemistry* **109**, 377–394.

Young M., Gonneea M. E., Herrera-Silveira J. and Paytan A. (2005) Export of dissolved and particulate carbon and nitrogen from a mangrove-dominated lagoon, Yucatan Peninsula, Mexico. *International Journal of Ecology and Environmental Sciences* **31**, 189–202.

Yu J. and Elderfield H. (2007) Benthic foraminiferal B/Ca ratios reflect deep water carbonate saturation state. *Earth and Planetary Science Letters* **258**, 73–86.

Yu J., Foster G. L., Elderfield H., Broecker W. S. and Clark E. (2010) An evaluation of benthic foraminiferal B/Ca and δ11B for deep ocean carbonate ion and pH reconstructions. *Earth and Planetary Science Letters* **293**, 114–120.

Zeebe R. E., Sanyal A., Ortiz J. D. and Wolf-Gladrow D. A. (2001) A theoretical study of the kinetics of the boric acid–borate equilibrium in seawater. *Marine Chemistry* **73**, 113–124.

Zeebe R. E. and Wolf-Gladrow D. (2001) *CO2 in seawater: equilibrium, kinetics, isotopes*., Gulf Professional Publishing.

Zeebe R. E., Wolf-Gladrow D. A., Bijma J. and Hönisch B. (2003) Vital effects in foraminifera do not compromise the use of δ11B as a paleo-pH indicator: Evidence from modeling. *Paleoceanography* **18**.

Zhang S., Henehan M. J., Hull P. M., Reid R. P., Hardisty D. S., Hood A. V. S. and Planavsky N. J. (2017) Investigating controls on boron isotope ratios in shallow marine carbonates. *Earth and Planetary Science Letters* **458**, 380–393.